

A Theoretical Three Dimensional Electromagnetic Eye

Advances towards the Optimisation of Electroretinographic Signal Recovery

By

Helen Marah Gill

Thesis submitted to the University of Glasgow
for the degree of Doctor of Philosophy

This research was conducted in the
Department of Clinical Physics and Bio-engineering,
Tennent Institute of Ophthalmology,
University of Glasgow,
North Glasgow Hospitals University NHS Trust,
Glasgow

October 2000

ProQuest Number: 13818482

All rights reserved

INFORMATION TO ALL USERS

The quality of this reproduction is dependent upon the quality of the copy submitted.

In the unlikely event that the author did not send a complete manuscript and there are missing pages, these will be noted. Also, if material had to be removed, a note will indicate the deletion.



ProQuest 13818482

Published by ProQuest LLC (2018). Copyright of the Dissertation is held by the Author.

All rights reserved.

This work is protected against unauthorized copying under Title 17, United States Code
Microform Edition © ProQuest LLC.

ProQuest LLC.
789 East Eisenhower Parkway
P.O. Box 1346
Ann Arbor, MI 48106 – 1346

GLASGOW
UNIVERSITY
LIBRARY:

12428
copy 1

Summary

Ocular electrophysiology is the study of electrical signals produced by the retina. In the past many different techniques have been used to provide indirect, non-invasive, objective measurements of retinal function. These measurements are routinely used to predict, and confirm diagnoses of, a wide range of retinal disorders. Electrophysiology has many shortcomings and new developments are currently addressing these. In recent years, advances have been made in the simultaneous stimulation of multiple focal areas of the retina. This has led to the production of three-dimensional topographical maps of visual function from signals of only nano-volt initial amplitude.

A numerical three-dimensional computer program designed to calculate the electromagnetic potential distribution within the human eye has been developed from existing two-dimensional numerical models. This has been validated against two-dimensional analytical findings and various experiments to assess its robustness have been conducted. Modifications to the three-dimensional numerical model have enabled a more accurate retinal source photoreceptor distribution to be incorporated. Focal and ring stimulation of the three-dimensional retina has been performed and characteristic corneal distributions have been found.

A possible application for investigation using this model has been found. It is known that diseases affecting the photoreceptors of the retina may often be detected using electrophysiology. Predictions of corneal potential changes following simulated retinal scotomas by the three-dimensional model may therefore prove of use. By 'mapping' the potential distribution over the corneal surface optimal recording sites for a number of retinal stimulation parameters may be found.

A new type of electrode has been designed and built. Measurements made using this electrode have enabled further validation of theoretical potential distribution predictions. Further adaptation of the three-dimensional model is required including the provision of a mechanism by which the model may take account of the position of a reference electrode. Additional modification of the correction for retinal

photoreceptor density is also needed due to the known variation of photoreceptor density changes in all dimensions.

This three-dimensional model enables predictions to be made regarding the potential distribution at the electrode measurement site. This work shows in detail the variation in potential over the corneal / scleral surface. This insight should lead to further investigations regarding more accurate measurement techniques to facilitate optimal signal recovery. In future work it may be necessary for correction factors to be applied to various parts of the field if mono electrode recording is taking place when wide field peripheral stimulation is used.

List of Contents

Chapter 1 Background

- 1.0 Introduction
- 1.1 Anatomy of the Human Eye
 - 1.1.1 The Fibrous Layer
 - 1.1.2 The Vascular Layer
 - 1.1.3 The Nervous Layer
 - 1.1.4 The Interior Eyeball
- 1.2 The Mechanism of Vision
- 1.3 Measurement of Visual Function
 - 1.3.1 Electroretinography
 - 1.3.2 Electro-oculography
 - 1.3.3 Pattern Evoked Electroretinograms
 - 1.3.4 The Multifocal Electroretinogram
- 1.4 Electrodes
 - 1.4.1 Contact Lens Electrodes
 - 1.4.2 Gold Foil Electrodes
 - 1.4.3 DTL Fibre Electrodes
 - 1.4.4 Skin Electrodes
- 1.5 Summary and Conclusions

Chapter 2 Basic Theories and Current Practice

- 2.0 Introduction
- 2.1 Modelling Electromagnetic Events in the body
- 2.2 Analytical Modelling
- 2.3 Numerical Modelling
- 2.4 Delphi Programming in two dimensions
- 2.5 Summary and Conclusions

Chapter 3 Three Dimensional Modelling

- 3.0 Introduction
- 3.1 Theory
- 3.2 Validation of the model
 - 3.2.1 Comparisons with the two dimensional model
 - 3.2.2 Convergence of the three dimensional model
 - 3.2.3 Parameter Variation
 - 3.2.4 Frequency Considerations
 - 3.2.5 Physiological Comparisons
- 3.3 Summary and Conclusions

Chapter 4 Applications of the Three Dimensional Model

- 4.0 Introduction
- 4.1 Photoreceptor density scaling
- 4.2 Focal and ring stimulation
- 4.3 Focal and ring scotoma stimulation
- 4.4 Summary and Conclusions

Chapter 5 Topographical Potential Measurements *in vivo*

- 5.0 Introduction
- 5.1 Anterior surface measurement
- 5.2 Examination of the anterior surface potential distribution
- 5.3 Multifocal stimulation of the eye
- 5.4 Comparison of recordings using multifocal stimulation
- 5.5 Summary and Conclusions

Chapter 6 Discussion and Further Work

- 6.0 Introduction
- 6.1 Discussion
- 6.2 Further work

Appendices

- Appendix A** Original development of a two-dimensional analytical model along with the associated complex mathematics.
- Appendix B** Original development of two-dimensional 'passive node' algorithms.
- Appendix C** Original development of two-dimensional 'active node' algorithms.
- Appendix D** Original development of the two-dimensional algorithms to calculate the potential at the origin.
- Appendix E** Source code for the two-dimensional numerical model.
- Appendix F** Full mathematical progression of the 'passive node' algorithms for the three-dimensional numerical model.
- Appendix G** Source code for the three-dimensional numerical model.

List of Illustrations

Figure

- 1.1 Basic anatomy of the human eyeball.
- 1.2 Meridional section through the human cornea.
- 1.3 The uvea (shown in red), between the sclera and retina.
- 1.4 A three-dimensional cross section of the human retina.
- 1.5 Digital fundus image.
- 1.6 Human cones in cross section.
- 1.7 Human rods in cross section.
- 1.8 The Interior Cavities of the Eye.
- 1.9 A Normal Rod Dominated ERG response.
- 1.10 A Normal Maximal Response in a Dark Adapted Eye.
- 1.11 Normal Oscillatory Response in a Dark Adapted Eye.
- 1.12 Normal single flash cone mediated response.
- 1.13 Normal Flicker Response.
- 1.14 Waveforms from saccadic eye movements for EOG Arden Ratio.
- 1.15 PERG waveform (negativity appears here as downward deflection).
- 1.16 The multifocal stimulus.
- 1.17 MFERG waveforms over the stimulus area.
- 1.18 MFERG functional plot.
- 1.19 A Burian Allen Contact Lens Electrode.
- 1.20 A Gold Foil Electrode.
- 1.21 A DTL Fibre Electrode.
- 1.22 A Skin Electrode.

- 2.1 Two point current sources in a homogeneous conducting sphere.
- 2.2 Illustration of equipotentials in an equatorial plane
- 2.3 Construction of the Analytical Model
- 2.4 Numerical and analytical potentials along the circumference and midline of the eyeball.
- 2.5 Diagram showing the six different regions of the two-dimensional model.
- 2.6 Nodal arrangement for the two-dimensional numerical model.

- 3.1 Three-dimensional construction of model showing how two dimensional model is reproduced to make the three dimensional globe.
- 3.2 Nearest neighbour cubes over which the integral is evaluated.
- 3.3 Graph showing axial plot of data from two and three-dimensional numerical data plotted against two-dimensional analytical data for Conductivity Set A.
- 3.4 Graph showing axial plot of data from two and three-dimensional numerical data plotted against two-dimensional analytical data for Conductivity Set B.
- 3.5 Graph showing axial plot of data from two and three-dimensional numerical data plotted against two-dimensional analytical data for Conductivity Set C.
- 3.6 Graph showing axial plot of data from two and three-dimensional numerical data plotted against two-dimensional analytical data for Conductivity Set D.
- 3.7 Graph showing axial plot of data from two and three-dimensional numerical data plotted against two-dimensional analytical data for Conductivity Set E.
- 3.8 Graph showing axial plot of data from two and three-dimensional numerical data plotted against two-dimensional analytical data for Conductivity Set F.
- 3.9 Graph showing circumference plot of data from two and three-dimensional numerical data against two-dimensional analytical data for Conductivity Set A
- 3.10 Graph showing circumference plot of data from two and three-dimensional numerical data against two-dimensional analytical data for Conductivity Set B
- 3.11 Graph showing circumference plot of data from two and three-dimensional numerical data against two-dimensional analytical data for Conductivity Set C
- 3.12 Graph showing circumference plot of data from two and three-dimensional numerical data against two-dimensional analytical data for Conductivity Set D
- 3.13 Graph showing circumference plot of data from two and three-dimensional numerical data against two-dimensional analytical data for Conductivity Set E
- 3.14 Graph showing circumference plot of data from two and three-dimensional numerical data against two-dimensional analytical data for Conductivity Set F
- 3.15 Graph showing convergence of axial potentials to analytical solution for an increasing number of iterations with Conductivity Set A.
- 3.16 Graph showing convergence of axial potentials to analytical solution for an increasing number of iterations with Conductivity Set B.
- 3.17 Graph showing convergence of axial potentials to analytical solution for an increasing number of iterations with Conductivity Set C.

- 3.18 Graph showing convergence of axial potentials to analytical solution for an increasing number of iterations with Conductivity Set D.
- 3.19 Graph showing convergence of axial potentials to analytical solution for an increasing number of iterations with Conductivity Set E.
- 3.20 Graph showing convergence of axial potentials to analytical solution for an increasing number of iterations with Conductivity Set F.
- 3.21 Graph showing convergence of circumference potentials to analytical solution for an increasing number of iterations with Conductivity Set A.
- 3.22 Graph showing convergence of circumference potentials to analytical solution for an increasing number of iterations with Conductivity Set B.
- 3.23 Graph showing convergence of circumference potentials to analytical solution for an increasing number of iterations with Conductivity Set C.
- 3.24 Graph showing convergence of circumference potentials to analytical solution for an increasing number of iterations with Conductivity Set D.
- 3.25 Graph showing convergence of circumference potentials to analytical solution for an increasing number of iterations with Conductivity Set E.
- 3.26 Graph showing convergence of circumference potentials to analytical solution for an increasing number of iterations with Conductivity Set F.
- 3.27 Graph showing the potential magnitude along the axis of the eyeball when $\sigma_1 = 1$, $\sigma_2 = 0.15$, $\sigma_3 = 0.005$, $\sigma_4 = 0.19$, $\sigma_5 = 0.44$, $\sigma_6 = 0$, $RR = 1.67$, $RC = 58.8$ and frequency = 20Hz.
- 3.28 Graph showing the phase along the axis of the eyeball when $\sigma_1 = 1$, $\sigma_2 = 0.15$, $\sigma_3 = 0.005$, $\sigma_4 = 0.19$, $\sigma_5 = 0.44$, $\sigma_6 = 0$, $RR = 1.67$, $RC = 58.8$ and frequency = 20Hz.
- 3.29 Graph showing the potential magnitude around the circumference of the eyeball.
- 3.30 Graph showing the phase around the circumference of the eyeball.
- 3.31 Physiological Comparisons (The isolated eye)
The potential magnitude around the circumference when $\sigma_1 = 1$, $\sigma_2 = 0.01$, $\sigma_3 = 0$, $\sigma_4 = 0.19$, $\sigma_5 = 0.445$, $\sigma_6 = 0$, $RR = 1.67$, $RC = 43.3$ and frequency = 5Hz.
- 3.32 Physiological Comparisons (The isolated eye)
The potential magnitude around the circumference when $\sigma_1 = 1$, $\sigma_2 = 0.01$, $\sigma_3 = 0$, $\sigma_4 = 0.19$, $\sigma_5 = 0.445$, $\sigma_6 = 0$, $RR = 6.25$, $RC = 43.3$ and frequency = 5Hz.

3.33 Physiological Comparisons (The isolated eye)

The potential magnitude around the circumference when $\sigma_1 = 1$, $\sigma_2 = 0.15$, $\sigma_3 = 0$, $\sigma_4 = 0.19$, $\sigma_5 = 0.445$, $\sigma_6 = 0$, $RR = 1.67$, $RC = 43.3$ and frequency = 5Hz.

3.34 Physiological Comparisons (The isolated eye)

The potential magnitude around the circumference when $\sigma_1 = 1$, $\sigma_2 = 0.15$, $\sigma_3 = 0$, $\sigma_4 = 0.19$, $\sigma_5 = 0.445$, $\sigma_6 = 0$, $RR = 6.25$, $RC = 43.3$ and frequency = 5Hz.

3.35 Physiological Comparisons (The eye in situ)

Potential magnitude along the axis when $\sigma_1 = 1$, $\sigma_2 = 0.01$, $\sigma_3 = 0.005$, $\sigma_4 = 0.19$, $\sigma_5 = 0.445$, $\sigma_6 = 0$, $RR = 1.67$, $RC = 43.3$ and frequency = 5Hz.

3.36 Physiological Comparisons (The eye in situ)

Potential magnitude along the axis when $\sigma_1 = 1$, $\sigma_2 = 0.01$, $\sigma_3 = 0.005$, $\sigma_4 = 0.19$, $\sigma_5 = 0.445$, $\sigma_6 = 0$, $RR = 6.25$, $RC = 43.3$ and frequency = 5Hz.

3.37 Physiological Comparisons (The eye in situ)

Potential magnitude along the axis when $\sigma_1 = 1$, $\sigma_2 = 0.01$, $\sigma_3 = 0.06$, $\sigma_4 = 0.19$, $\sigma_5 = 0.445$, $\sigma_6 = 0$, $RR = 1.67$, $RC = 43.3$ and frequency = 5Hz.

3.38 Physiological Comparisons (The eye in situ)

Potential magnitude along the axis when $\sigma_1 = 1$, $\sigma_2 = 0.01$, $\sigma_3 = 0.06$, $\sigma_4 = 0.19$, $\sigma_5 = 0.445$, $\sigma_6 = 0$, $RR = 6.25$, $RC = 43.3$ and frequency = 5Hz.

3.39 Physiological Comparisons (The eye in situ)

Potential magnitude along the axis when $\sigma_1 = 1$, $\sigma_2 = 0.15$, $\sigma_3 = 0.005$, $\sigma_4 = 0.19$, $\sigma_5 = 0.445$, $\sigma_6 = 0$, $RR = 1.67$, $RC = 43.3$ and frequency = 5Hz.

3.40 Physiological Comparisons (The eye in situ)

Potential magnitude along the axis when $\sigma_1 = 1$, $\sigma_2 = 0.15$, $\sigma_3 = 0.005$, $\sigma_4 = 0.19$, $\sigma_5 = 0.445$, $\sigma_6 = 0$, $RR = 6.25$, $RC = 43.3$ and frequency = 5Hz.

3.41 Physiological Comparisons (The eye in situ)

Potential magnitude along the axis when $\sigma_1 = 1$, $\sigma_2 = 0.15$, $\sigma_3 = 0.06$, $\sigma_4 = 0.19$, $\sigma_5 = 0.445$, $\sigma_6 = 0$, $RR = 1.67$, $RC = 43.3$ and frequency = 5Hz.

3.42 Physiological Comparisons (The eye in situ)

Potential magnitude along the axis when $\sigma_1 = 1$, $\sigma_2 = 0.15$, $\sigma_3 = 0.06$, $\sigma_4 = 0.19$, $\sigma_5 = 0.445$, $\sigma_6 = 0$, $RR = 6.25$, $RC = 43.3$ and frequency = 5Hz.

- 4.1 Graph showing photoreceptor density variations with eccentricity (Osterberg, 1935).
- 4.2 Graph showing photoreceptor density variations with eccentricity (Curcio, 1987).
- 4.3 Cone response along axis of the three-dimensional model when $\sigma_1 = 1$, $\sigma_2 = 0.01$, $\sigma_3 = 0.005$, $\sigma_4 = 0.19$, $\sigma_5 = 0.445$, $\sigma_6 = 0$, RR = 1.67, RC = 43.3 and frequency = 5Hz.
- 4.4 Cone response around circumference of the three-dimensional model when $\sigma_1 = 1$, $\sigma_2 = 0.01$, $\sigma_3 = 0.005$, $\sigma_4 = 0.19$, $\sigma_5 = 0.445$, $\sigma_6 = 0$, RR = 1.67, RC = 43.3 and frequency = 5Hz.
- 4.5 Rod response along axis of the three-dimensional model when $\sigma_1 = 1$, $\sigma_2 = 0.01$, $\sigma_3 = 0.005$, $\sigma_4 = 0.19$, $\sigma_5 = 0.445$, $\sigma_6 = 0$, RR = 1.67, RC = 43.3 and frequency = 5Hz.
- 4.6 Rod response around circumference of the three-dimensional model when $\sigma_1 = 1$, $\sigma_2 = 0.01$, $\sigma_3 = 0.005$, $\sigma_4 = 0.19$, $\sigma_5 = 0.445$, $\sigma_6 = 0$, RR = 1.67, RC = 43.3 and frequency = 5Hz.
- 4.7 Three-dimensional heat map showing calculated surface potentials following homogeneous retinal global stimulation.
- 4.8 Three-dimensional heat map showing calculated surface potentials following photoreceptor density scaled retinal stimulation.
- 4.9 Heat map with graph showing electromagnetic potential variation over the cornea following photoreceptor density scaled global retinal stimulation.
- 4.10 Heat map with graph showing electromagnetic potential variation over the cornea following central 10-degree focal stimulation.
- 4.11 Heat map with graph showing electromagnetic potential variation over the cornea following peripheral 10-degree focal stimulation.
- 4.12 Surface heat map with graph demonstrating corneal potential changes due to a central ring stimulus.
- 4.13 Surface heat map with graph demonstrating corneal potential changes due to a peripheral ring stimulus.
- 4.14 Surface heat-map with graph illustrating the change in corneal potential distribution following central focal scotoma simulation.

- 4.15 Surface heat-map with graph illustrating the change in corneal potential distribution following peripheral ring scotoma simulation.
- 5.1 Four gold foil electrodes positioned on a 'post operative haptic' shell producing a quadrupole scleral electrode.
- 5.2 The Multi-focal Stimulus.
- 5.3 System display showing localised ERG signals one from each area stimulated.
- 5.4 Three dimensional response density plot.
- 5.5 Surface heat plot and graph showing electrical topography changes following single 10-degree peripheral stimulation.
- 5.6 Raw data traces from the four electrode sites.
- 5.7 Normalised trace arrays giving equal amplitudes at the central element.

List of Tables

Table

- 2.1 Table showing co-ordinates of nodes for Doslak's two-dimensional model.
- 3.1 Table of ranges of values used for each of the regions of the model.
- 3.2 Conductivity Sets and their Values.
- 3.3 The percentage deviation in two and three-dimensional numerical axial data from calculated analytical axial potential values.
- 3.4 The percentage deviation in two and three-dimensional numerical circumference data from calculated analytical circumference potential values.
- 3.5 Table showing convergence of the three dimensional model potentials to the analytical model potentials.
- 3.6 Table showing the order in which conductivity values for each region were modified for the parameter variation experiments.
- 3.7 Table showing changes in potential along the axis of the eye.
- 3.8 Table showing changes in potential over the whole surface of the eye.
- 3.9 Table showing changes in potential over the surface of the cornea.
- 3.10 Table showing values of conductivity parameters used in frequency effects experiments.
- 3.11 Table showing combinations for 0 Hz frequency experiments.
- 3.12 Table showing combinations for 20 Hz frequency experiments.
- 3.13 Table showing changes in potential over the corneal surface for parameter variations for a frequency of 0 Hz.
- 3.14 Table showing changes in potential over the corneal surface for parameter variations for a frequency of 20 Hz.
- 4.1 Table showing data comparison (Osterberg (1935), Curcio (1987)).
- 5.1 Amplitude values for summed traces for superior, inferior, nasal and temporal fields for the four electrode sites.

Authors Declaration

The material presented in this thesis is the author's own work with the following exceptions

The development of the two dimensional analytical and numerical models was undertaken by Doslak M.J and is referenced as such in the text.

The development of the display units in the programs to calculate electromagnetic potentials was largely undertaken by Dr D Keating. His assistance is very much appreciated.

The wide field multifocal ERG technique employed was designed and developed by Dr S Parks. His assistance in the technical aspects of it use is very much appreciated.

October 2000

List of Publications

Publications

Job H.M, Keating D, Evans A.L, Parks S

‘A Three Dimensional Electromagnetic Model of the Human Eye : The Optimisation of Electroretinographic Signal Detection’ *Medical and Biological Engineering & Computing* 1999: 37 (6):

Gill H.M, Keating D, Parks S.W, Evans A.L, Dutton G.N, ‘Topographical Electrophysiology : Theoretical and Practical Measurements of Corneal Potential Topography’ *submitted to Vision Research*

Poster Presentations

H M Job, D Keating, A L Evans, S W Parks & W L Lee

‘A Three Dimensional Mathematical Model of the Human Eye : A Tool for optimising signal recovery of focal stimuli ?’

The Association for Research in Vision and Ophthalmology, Fort Lauderdale, Florida, USA, 15th March 1998.

H.M Gill, D. Keating, S.W Parks, A.L Evans, G.N Dutton

‘Theoretical and Practical Measurements of Corneal Potential Topography for wide field multi-focal ERG stimulation’

The Association for Research in Vision and Ophthalmology, Fort Lauderdale, Florida, USA, 2nd May 2000.

Oral Presentations

‘The Three Dimensional Electromagnetic Eye’

Registrars and Research Workers Meeting, Tennent Institute, Glasgow,

16th April 1997.

‘A Model of the Human Eye to Optimise Electroretinographic Stimuli’

IPEM Northern Group Meeting, Royal Victoria Infirmary, Newcastle-Upon-Tyne,
24th October 1997.

‘Electrodiagnosis of the Visual System’

Registrars and Research Workers Meeting, Tennent Institute, Glasgow,
15th April 1998.

‘Functional, Anatomical and Mathematical Modelling of the Retina’

Department of Cardiac Electrophysiology, Duke University, North Carolina, USA,
27th April 1998.

‘Corneal Potential Topography Measurements using Three Dimensional
Electromagnetics’

Registrars and Research Workers Meeting, Tennent Institute, Glasgow
23rd June 1999.

‘Three Dimensional Theoretical Modelling of Ocular Potentials’

5th Annual Meeting of The Institute of Physics and Engineering in Medicine,
Nottingham
7th September 1999.

‘3D Imaging of the Electromagnetic Potentials within the Human Eye’

14th Annual Conference, British Ophthalmic Photographic Association, York
20th November 1999.

Grants awarded

Bursary Committee of West Glasgow Hospitals NHS Trust

Title : 'Three Dimensional Ocular Modelling for the Optimisation of Recording Techniques in Electroretinographic Stimuli' January 1998 (£1,760).

This grant enabled travel to the USA to visit centres of electrophysiology excellence

These included :-

Duke University, North Carolina

Fort Lauderdale, Florida

Columbia and New York Universities, New York

Ophthalmology Directorate of West Glasgow Hospitals NHS Trust

Title : 'Theoretical Optimisation of Electroretinographic Recording Sites Using a Three Dimensional Electromagnetic Model & an Integrated Computing Environment' 1998 (£1000)

This grant enabled the purchase of a Matlab 5.2 software which was used to 'visualise' the results from this research in three dimensions. It also paid for high quality colour printer.

Acknowledgement

The author wishes to thank the following people for their assistance and encouragement throughout the undertaking of this work.

- Dr David Keating** Principal Physicist, Electrodiagnostic Imaging Unit, Gartnavel General Hospital, Glasgow.
- Dr Aled Evans** Principal Physicist, Department of Clinical Physics and Bioengineering, Southern General Hospital, Glasgow.
- Dr Stuart Parks** Principal Physicist, Electrodiagnostic Imaging Unit, Gartnavel General Hospital, Glasgow.
- Mr Gordon Dutton** Consultant Ophthalmologist, Gartnavel General Hospital, Glasgow.
- Prof Alex Elliott** Head of Department, Department of Clinical Physics and Bioengineering, Western Infirmary, Glasgow.
- Dr Craig Henriquez** Associate Professor of Biomedical Engineering, Duke University North Carolina, USA.
- Prof Robert Plonsey** Assistant Professor, University of California (Berkeley),
Assistant Professor, Case Western Reserve University,
Professor BME Duke University, USA.
- John McCormick** Ophthalmic photographer, Gartnavel General Hospital, Glasgow.
- Jo McDonagh** Research Scientist, Gartnavel General Hospital, Glasgow.

I would like to thank **Anna, Mum, Dad, Gillian, Carolyn, Ma and Pa** for their encouragement, support and love over the years.

But mostly to **Howard** my husband for his continued vision, enthusiasm, interest, and participation in my work and his love, devotion and friendship in my life.

‘For with much wisdom comes much sorrow; the more knowledge, the more grief’

Ecclesiastes 1:18 (New International Version)

‘I can do everything through him who gives me strength’

Philippians 4:23 (New International Version)

‘Now to the King eternal, immortal, invisible, to God who alone is wise, be honour and glory forever and ever. Amen’

1 Timothy 1:17 (New King James Version)

Chapter 1

Background

1.0 Introduction

Since the discovery of the electroretinogram, (Dewar, 1877) many researchers have directed their attention towards optimising the recovery of electrical signals produced by the retina. Ocular electrophysiology is the study of these signals recorded from the eye and surrounding skin. Many techniques have been developed to provide indirect yet objective measurements of retinal function. Electrophysiological measurements of this kind are routinely used to predict, and confirm diagnoses of, a wide range of retinal disorders. Electrophysiology, like any branch of science, has its limitations, the boundaries of which are constantly being expanded. In recent years the development of techniques to stimulate multiple focal areas of the retina simultaneously has led to the production of topographical maps of visual function (Sutter *et al*, 1992). Multifocal electroretinography of this nature requires the ability to record signals of only nano-volt initial amplitude. Advancements in allied electronic sciences, specifically in amplification technology therefore, have a significant impact on signal recovery in this field.

Research has previously been conducted on the measurement of electromagnetic potentials produced by the retina and the discovery of specific cells responsible for resultant waveforms (Tomita *et al*, 1981). However, accurate analysis of the electromagnetic potential distribution inside the eye has by no means been exhaustively attempted. Preliminary work in two-dimensions has been performed by a number of investigators. Analytical analysis (Frank, 1952) of the potential produced by two point current sources in a homogeneous conducting sphere has provided the basis for other numerical models, (Doslak, 1978), (Plonsey, 1984). These numerical models depict the retina as an axially symmetric double layer incorporating regions of specific conductivity to represent the lens, cornea etc. These two-dimensional models however consider only full field retinal stimulation.

This work attempts to model the three-dimensional electromagnetic potential distribution within the human eye. It is hoped that these findings will go some way to increasingly optimise recording techniques in diagnostic electrophysiology. It is believed that existing techniques in clinical electrophysiology may be improved by theoretically modelling the physical phenomena known to exist. In this way a more accurate analysis of the electromagnetic potential field within the eye may be predicted. The aims of this work are therefore to

- Design and construct a three-dimensional mathematical model of the human eye.
- Validate this model against an existing two-dimensional model (Doslak, 1978).
- Simulate specific disorders of the retina in an attempt to predict changes in the potential field that may occur as a result of the disease.
- Ascertain optimal recording sites for a number of retinal stimulation parameters.

1.1 Anatomy of the Human Eye

The adult human eyeball is a globe of approximately 2.5cm in diameter (<http://webvision.med.utah.edu/anatomy.html>). Its posterior surface fits snugly into the orbital cavity of the skull where additional structures such as fat, muscles, nerve and blood vessels supply the necessary nutrients and cushion damaging impacts to this delicate sense organ. The anterior surface of the globe is protected from extremes of light, heat, cold and small foreign debris by the eyelids, lashes and the conjunctival membrane.

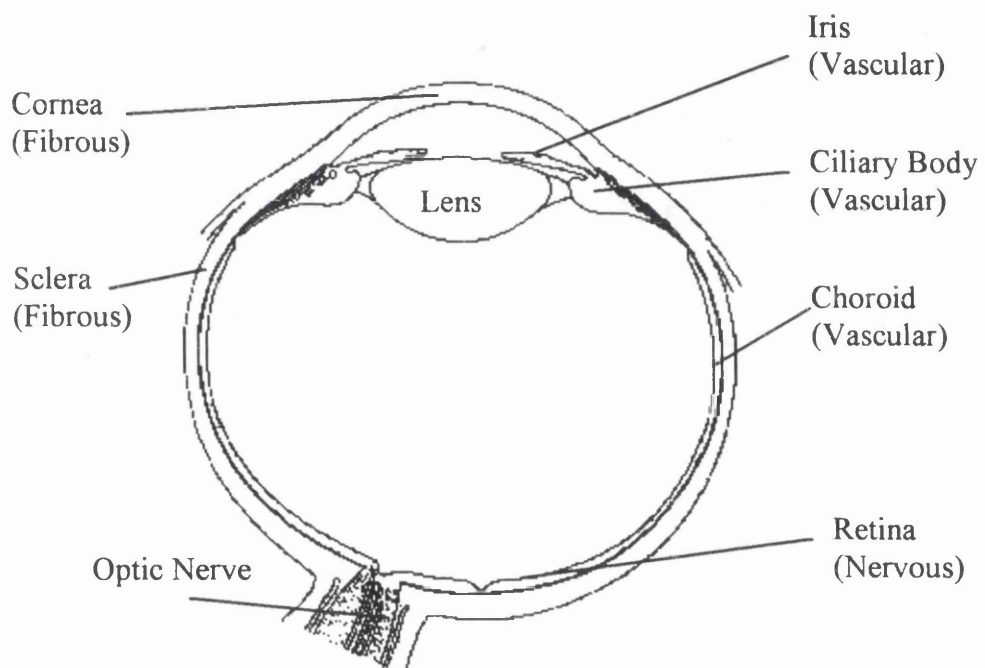
Most mathematical models of the eye assume its geometry to be a radially symmetrical sphere. Structurally, however it has a spherical posterior surface and a smaller and more prominent sphere as its anterior surface. The asymmetric exit point of the optic nerve incorporates other asymmetric nasal/temporal differences in the shape and structure of the eye. These differences are of fundamental functional significance, some of which are still awaiting explanation. Retinal location dependent waveform variations in monkeys and humans have recently been found, (Hood *et al.* 1999), (Sutter *et al.* 1999) and are the subject of continuing study in this field. This on going research has substantial implications on a simplified model of the eye. It is hoped that the outcome of this research will eventually be incorporated into

subsequent mathematical models. The model developed in this work has been constructed in such a way as to make asymmetrical calculations of the electromagnetic potential within the eye a possibility. It is hoped therefore that future work will address these new discoveries.

Although the geometry of the eye is assumed to be a relatively simple sphere, it is an inhomogeneous structure containing other regions such as the lens and cornea. Structurally the eye may be divided into three-distinct functional layers, (Figure 1.1).

Figure 1.1 Basic anatomy of the human eyeball

(adapted from 'Physiology of the Eye', Davson ; pp 3)



The fibrous layer provides the eye with a degree of rigidity. The vascular layer is essential for the supply of nutrients and the nervous layer is where incident light is converted into electrical impulses to initiate perception.

1.1.1 The Fibrous Layer

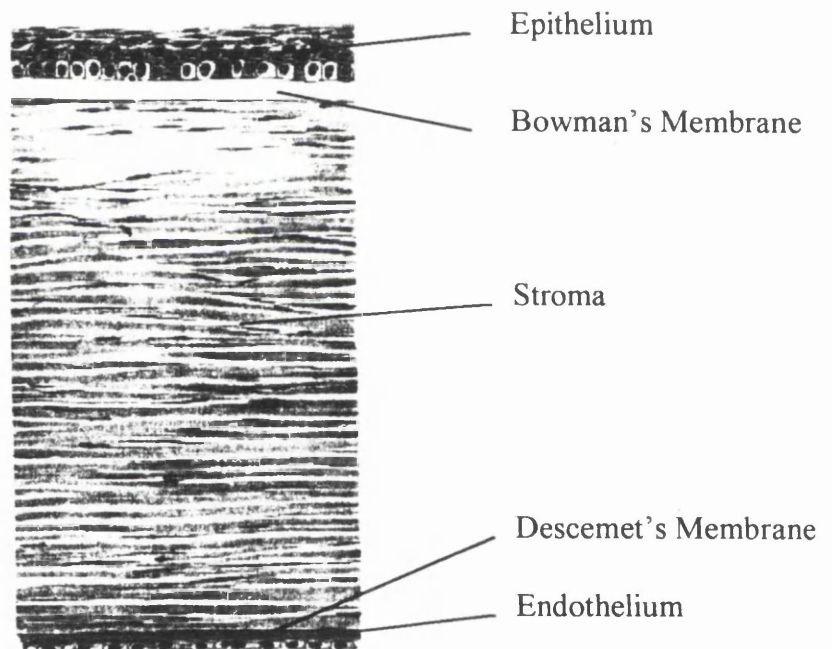
The function of the outer fibrous layer is to maintain the shape and ensure the optics of the eye are satisfactorily aligned. The fibrous layer incorporates anteriorly the transparent cornea and posteriorly the opaque sclera.

The Cornea

The cornea is the transparent, avascular structure on the front surface of the eye. While the cornea provides protection of the anterior globe its other function is to provide light transmission and focussing with the minimum amount of absorption and distortion. It has a thickness in the central region of approximately 0.5mm (Kanski, 1988) and focuses the light on the retina using refraction at the air to pre-corneal tear film boundary. The refractive power of the cornea is approximately 43 dioptres. The majority of the thickness of the cornea (up to 90%) is made up of the stroma (Spalton, 1994) and is bounded externally by Bowman's membrane and internally by Descemet's membrane, (Figure 1.2).

Figure 1.2 Meridional section through the human cornea

(adapted from 'Physiology of the Eye', Davson ; pp 105)



Bowman's Membrane is a thin (10 – 20 μm) layer of cells separating the corneal epithelium from the stroma (Kanski, 1988). The stroma provides the mechanical strength of the cornea and is made from collagen and muco-protein fibrils. The fibrils are of uniform size and extend across the cornea in parallel bundles each layer crossing at 90 degrees. A construction of this kind enables corneal transparency. Descemet's membrane is a strong, elastic layer approximately 10 – 12 μm thick (Kanski, 1988). It is made up of collagen fibres and forms the basal lamina of the

corneal endothelium. The endothelium itself is made up of a mono-layer of hexagonal cells and gap-junctions providing selective ionic permeability.

The external surface of the cornea is covered by corneal epithelium made up of basal columnar, wing and squamous cells. This epithelium acts as a permeability barrier though remains the site of ion transport. It is considered to be a 'semi-permeable' membrane to pure water but is relatively impermeable to the solutes of tears on the surface of the eye. Previous studies (Klyce 1972) have shown that the corneal epithelium accounts for almost 60% of the total corneal electrical resistance.

The corneal endothelium covering the internal surface of the cornea has been found to be 100 times more permeable to the Sodium ion (Na^+) than the corneal epithelium, (Maurice, 1967). Human endothelial resistance has been calculated to be approximately $13.3\Omega\text{cm}^2$ (Hodson *et al.*, 1983). Furthermore permeation of sodium chloride and bicarbonate across corneal endothelia is found to account for 89 % of the measured electrical conductance of the tissue (Hodson *et al.*, 1983). The corneal structure as a whole *in vivo* has been found to have a measurable potential of between 10 to 40 mV, (Modrell *et al.* 1959), (Maurice, 1967).

The Sclera

The sclera is the tough, avascular 'white' of the eye protecting the posterior part of the globe. It is made from collagen and elastin from which extrinsic muscles are attached to allow specific movements of the eyeball within the orbit (Rosen *et al* 1997). However, unlike the cornea it is opaque due to the irregularity in arrangement and diameter of the scleral fibres. The posterior surface of the sclera is pierced by the optic foramen encircling the optic nerve along which nerve impulses travel to the brain.

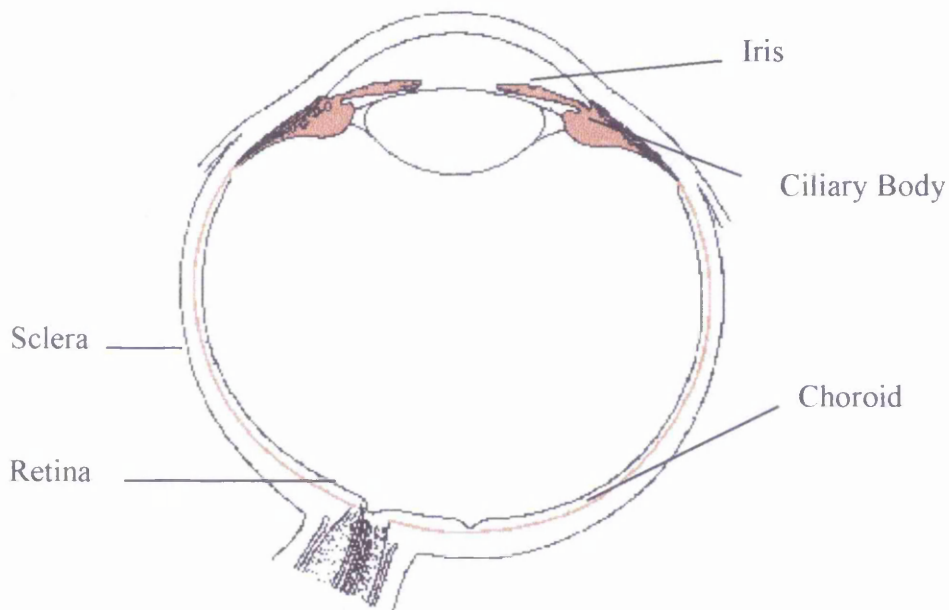
1.1.2 The Vascular Layer

The vascular layer provides the eye with nutrition. It incorporates the choroid, ciliary body and iris. These structures are collectively known as the uvea (Figure 1.3). The conjunctival membrane is also vascular and covers the posterior eyeball and the surfaces of the eyelids.

The Choroid

The choroid is supplied by ciliary arteries, which divide to form a structured capillary layer, the choriocapillaris. This is separated from the retina by Bruch's membrane, a single layer of cells responsible for the nutrition of the outer layers of the retina and the retinal pigment epithelium (RPE). This membrane is not a barrier to the flow of ions and provides structural support to the choroid (Spalton *et al* 1994).

Figure 1.3 The uvea (shown in red), between the sclera and retina
(adapted from 'Physiology of the Eye', Davson ; pp 7)



The Ciliary Body

The ciliary body is found anteriorly and is made up of ciliary processes and the ciliary muscle. Ciliary processes are folds on the internal surface of the ciliary body lined with ciliary epithelium. The epithelium separates the ciliary body from the aqueous chamber and vitreous body and secretes aqueous humour that fills the anterior chamber of the eye. The ciliary muscle is a circular band of smooth muscle that alters the shape of the lens.

The Iris

The iris is the most anterior part of the uvea and surrounds the circular opening of the choroid, the pupil. It is a coloured smooth muscular annulus and is attached at its outer margin to the ciliary processes, suspended between the cornea and lens. The anterior epithelium is also termed the myo-epithelium, as the specialised basal processes behave like muscle fibres. The iris therefore controls pupil size thus limiting the amount of light entering the eye.

The Conjunctiva

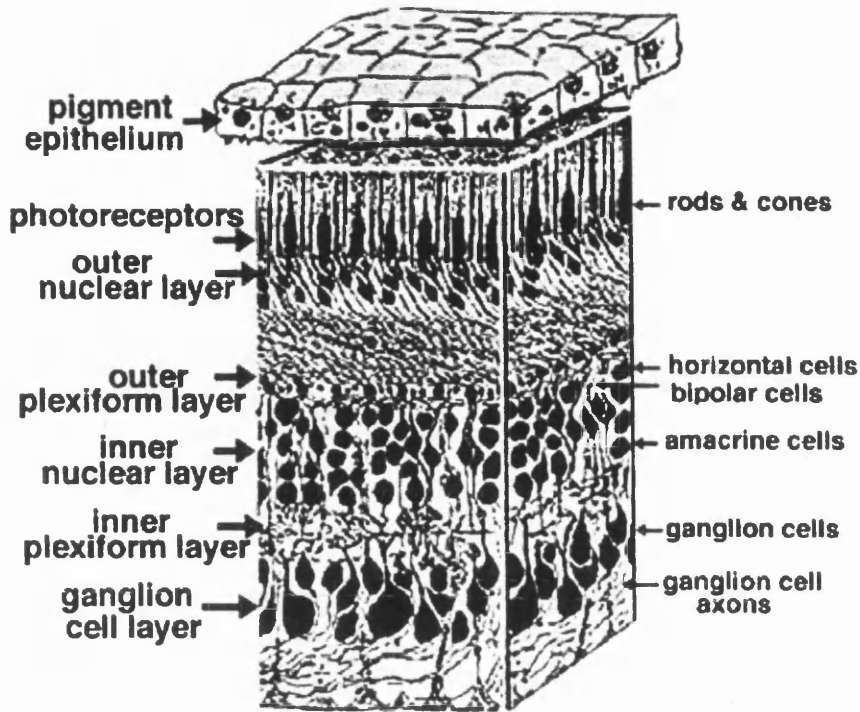
The conjunctiva is a transparent, mucous membrane that lines the outer surface of the eyeball and the posterior surface of the eyelids. Structurally it is continuous with the epithelium of the cornea and allows movement of the eyeball in all directions. Accessory lacrimal glands, provide the majority of fluid in which the eyeball and conjunctiva is bathed. This fluid provides lubrication, oxygen and protection against environmental pollutants (Klyce 1972). It has been found to contain 'lyzome', a natural antibiotic that helps protect the eye from infection, and drains via the naso-lacrimal duct into the nose (Whitnall, 1979).

1.1.3 The Nervous Layer (Retina)

The function of the retina is the conversion of light photons into electrical impulses. These impulses travel via the optic nerve to the occipital lobe of the brain where they are interpreted providing visual perception. The retina is approximately 32mm in diameter along the horizontal meridian and lines the inner surface of the eyeball (Polyak, 1941), (Van Buren, 1963), (Kolb, 1991). If, for example the average dimensions of the human eye are 22mm from anterior to posterior poles and approximately 72% of the inside of the globe is retina (Michels *et al.* 1990), then the area may be calculated to be 1094 mm². It is a complex structure containing detailed stratification (Figure 1.4).

Figure 1.4 A three-dimensional cross-section of the human retina

(from the website <http://webvision.med.utah.edu/sretina/html>)



The Retinal Pigment Epithelium (RPE)

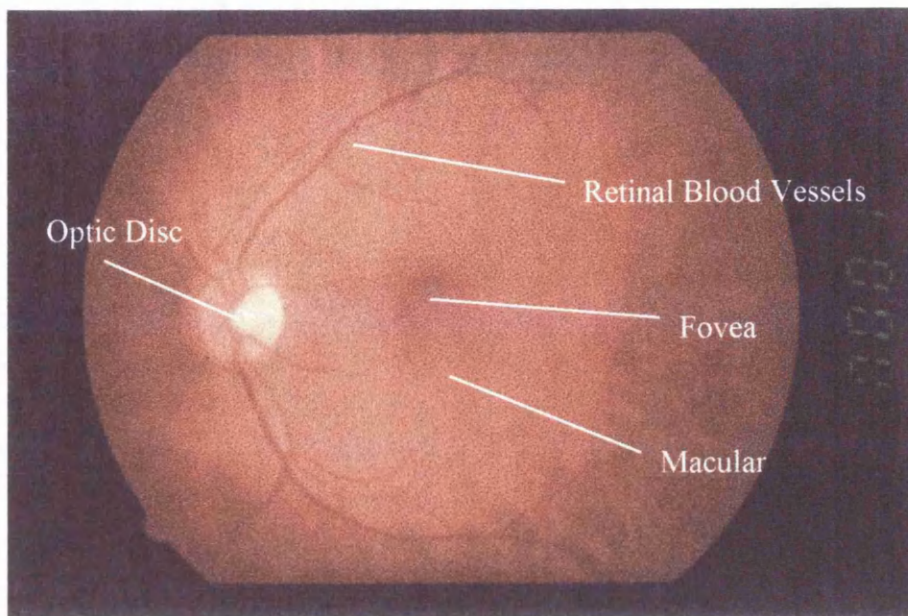
The retinal pigment epithelium (RPE) is a single layer of hexagonocuboidal cells bounded on one side by the capillary rich choriocapillaris and on the other the outer layer of the neural retina. It therefore has two membranes between which 'tight junctions' exist. Active transport of ions between these membranes induces the development of a potential across it. Compared with the retina the RPE has a high resistivity, (Heyen *et al.* 1985). As the membranes are actively held at different potentials, current flows through the RPE from the apical to the basal membrane. The action of this current depolarises the apical membrane and hyperpolarises the basal membrane (Steinberg *et al.* 1983). The steady potential existing across the RPE tissue is called the transepithelial potential (TEP). It is therefore best described as a 'selectively permeable' membrane existing between the blood and neural retina selectively allowing solutes from the plasma to pass through it. Direct control of the composition of the subretinal fluid thereby maintains the resting potentials of photoreceptors in the retina. Thus the delicate micro-electrical environment of the photoreceptors is directly controlled by the RPE.

The other main functions of the RPE are to absorb light, provide nutrients and digest ageing visual pigments from the retina. It is rich in melanin in order to absorb stray light and prevent excessive scatter. This helps sharpen the resultant image on the retina. Nutrients including metabolites such as Vitamin A are actively transported across the blood retinal barrier and mature visual pigments from the photoreceptors are broken down by phagocytosis. Each RPE cell is known to 'service' up to forty photoreceptors. Though there are no anatomical connections between them they interact via changes in potassium ion concentration. Absorbed light therefore hyperpolarises the apical membrane of the RPE. When the light stimulation ceases, the reverse occurs and the apical membrane depolarises.

The Retina

Anatomically the retina consists of many layers of cells each contributing to a measurable retinal resistance. The retina lines the posterior three-quarters of the eyeball, attaching only at the optic disc and ora serrata, where it is bound to the pigment epithelium (Van Buren, 1963). Its thickness varies from approximately 100 μm at the ora serrata to approximately 300 μm at the macula due to the increased packing density of the photoreceptors (<http://webvision.med.utah.edu/sretina/html>). Functionally it is a highly specialised, well-defined anatomical structure. It responds very efficiently to light stimulation, converting photons into nerve impulses. The retina may be viewed using an ophthalmoscope. The optic nerve leaves the posterior eyeball at the optic disc, a circular yellow structure (Figure 1.5). The impulses are conveyed via the optic nerve to visual centres in the occipital cortex of the brain. Branches of the central retinal artery that provide the anterior surface of the retina with nutrients are also visible. This is the only place in the human body where blood vessels may be examined directly. This enables assessment of systemic vascular pathological changes (e.g. diabetes).

Figure 1.5 Digital Fundus image



The macular is the foveal area, which contains the foveal pit, foveal slope, parafovea and perifovea. The foveal pit is less than a quarter of a millimetre across and contains densely packed cone photoreceptors arranged a hexagonal mosaic to ensure efficient packing. In cross section, light enters the eye and passes through the cornea and lens. It then penetrates the complete thickness of the transparent retina before striking the photoreceptors that lie on the external surface next to the RPE.

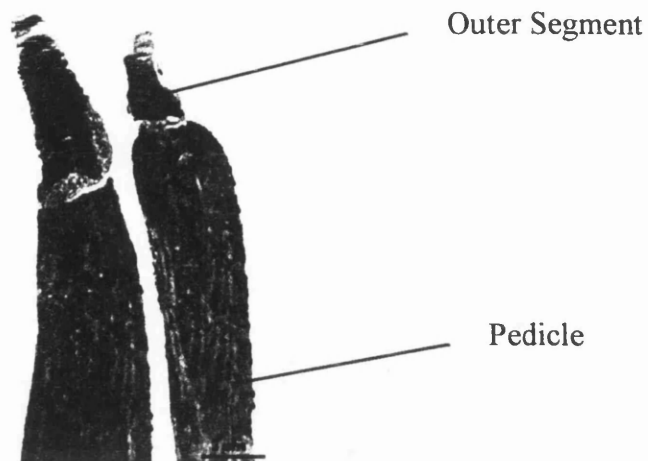
Photoreceptors

Any perception of light is initiated by specific photoreceptors of which there are two main types, rods and cones. Although they are dimensionally dissimilar, the two structures have many similarities. In both cases light sensitive pigment is contained within the 'outer segment' of the structure. This is in contact with the RPE. A 'synaptic body' (rod spherule or cone pedicle) forms the second part of the structure, (<http://webvision.med.utah.edu/photo1.html>). The effects of light on the receptor are transmitted through the 'synaptic body' to bipolar or horizontal cells that perform complex visual processing.

The human retina may typically contain six million cones (Østerberg, 1935). Cones are robust conical-shaped structures, specially adapted for daylight and colour vision. They are highly concentrated in the central fovea (Figure 1.6).

Figure 1.6 Human cones in cross section

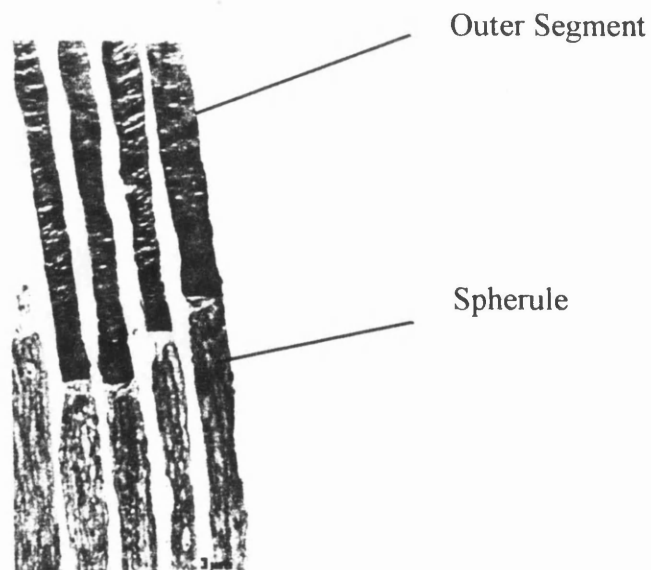
(adapted from <http://webvision.med.utah.edu/photo1.html>)



At the very centre of the fovea (i.e. an area $50 \times 50 \mu\text{m}$) the density may be on average $147,000/\text{mm}^2$ (Østerberg, 1935). More peripherally, cones quickly become outnumbered by rod photoreceptors. There are typically 120 million rods in the human retina and therefore far outnumber cone photoreceptors (Østerberg, 1935). They are slim rod-shaped structures specially adapted for night and peripheral vision. Their inner and outer segments fill the space between the larger cones in the sub-retinal space and the RPE cells (Figure 1.7)

Figure 1.7 Human rods in cross section

(adapted from <http://webvision.med.utah.edu/photo1.html>)



Incident light on the photoreceptive membranes of cones and rods causes changes in electrical membrane potentials (<http://webvision.med.utah.edu/photo1.html>). These are transmitted through layers of nerve cells and synapses in direct contact with each other both electrically and nutritionally. Electrical impulses produced in the outer segments of each photoreceptor travel via synaptic connections through the inner segments and outer limiting membrane to the outer nuclear layer.

Outer Limiting Membrane (OLM)

The outer limiting membrane is the boundary between photoreceptor cell inner segments and the outer nuclear layer. It is formed from junctions between the inner segments and Müller cells. Müller cells provide the primary structural support for the retina and extend radially from the OLM to the inner limiting membrane (ILM). Their cell bodies lie in the inner nuclear layer (INL) and their processes penetrate between the neurones in other layers.

In addition to their structural role their metabolic role includes acting as highly efficient potassium pumps essential for maintaining the micro-electrical environment of the retina (<http://webvision.med.utah.edu/sretina.html>).

Outer Nuclear Layer (ONL)

The outer nuclear layer lies between the photoreceptors and the outer plexiform layer (IPL) (Figure 1.4). It is known that a small amount of visual processing occurs in the ONL.

The Outer Plexiform Layer (OPL) -or Outer Synaptic Layer

The outer plexiform layer divides the outer and inner nerve cell layers. It is within this layer that synaptic connections are made. The two most important connections cause the visual signal to split into separate 'channels' for detecting objects lighter or darker than background (<http://webvision.med.utah.edu/OPL1.html>). They create pathways to simultaneously detect contrast of visual objects. Cone axons form a layer of their own in the OPL known as the Henlé fibre layer.

The Inner Nuclear Layer (INL) -or Bipolar Cell Layer

The inner nuclear layer forms the inner surface of the neural retina. It contains the cell bodies of bipolar, horizontal and amacrine cells. The INL is thicker in the central retina compared with the peripheral retina due to a higher density of cone connecting second order neurones. Cone connected circuits of neurones are less convergent (i.e. fewer cones impinge on second order neurones than rods in rod connected pathways).

The Inner Plexiform Layer (IPL) - or Inner Synaptic Layer

The inner plexiform layer again divides nerve cell layers. It contains nerve processes and synapses between neurons connecting to ganglion cells in the ganglion cell layer. In addition horizontally and vertically directed amacrine cells interact in further networks to influence and integrate the ganglion cell signals (<http://webvision.med.utah.edu/IPL.html>).

The Ganglion Cell Layer (GCL)

The ganglion cell layer is made up of ganglion cell bodies. A large amount of pre-processing of the visual signal has already been done before it reaches the ganglion cells. They are therefore sometimes referred to as the brains 'ultimate signaller' of retinal information (<http://webvision.med.utah.edu/GC1.html>). Ganglion cell processes converge to form a layer of nerve fibres that run along the inner limiting membrane. This is the nerve fibre layer, eventually becoming the optic nerve where it leaves the posterior of the globe at the optic disc.

The Inner Limiting Membrane (ILM)

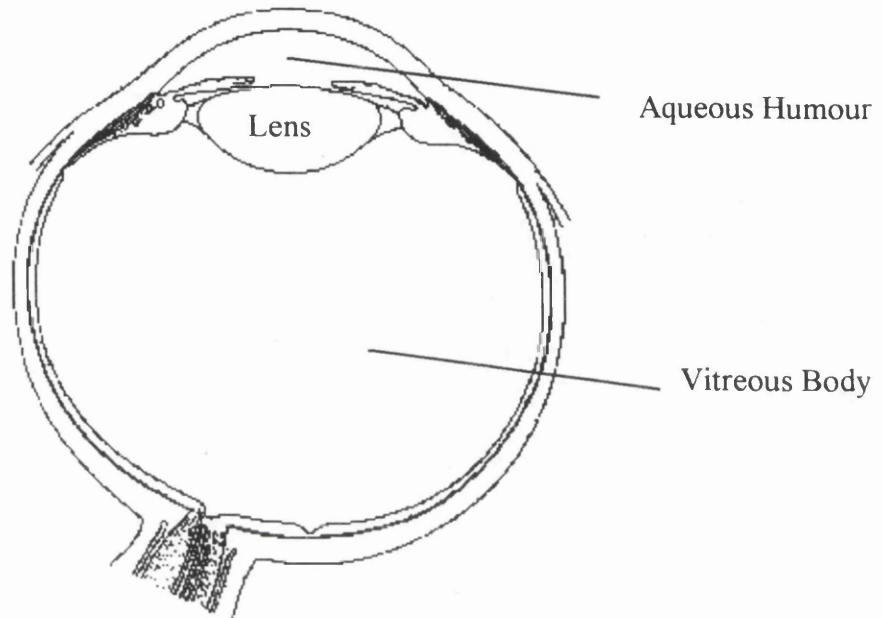
The inner limiting membrane is composed of laterally contacting Müller cell end feet and associated basement membrane constituents. It is the inner surface of the retina and forms a relative diffusion barrier between the neural retina and vitreous humour.

1.1.4 The Interior Eyeball

The interior of the eyeball is divided into two cavities (Figure 1.8), the anterior cavity and vitreous chamber. Their function is to maintain the rigidity of the globe, whilst being completely transparent to allow the passage of light to the retina.

Figure 1.8 The Interior Cavities of the Eye

(adapted from 'Physiology of the Eye', Davson ; pp 3).



The Anterior Cavity

The anterior cavity lies anterior to the lens and is divided into two chambers. The anterior chamber lies behind the cornea in front of the iris, and the posterior chamber behind the iris and in front of the suspensory ligaments and lens. The entire anterior cavity is filled with aqueous humour, a colourless fluid continually secreted by the ciliary processes for nourishment of the lens and cornea.

The chemical composition of the aqueous humour differs considerably from that of blood. The most obvious difference being its protein content. While blood plasma contains 6 – 7g / 100ml of protein, aqueous humor only contains 5 – 15mg / 100ml (<http://alpha.ipfw.edu/histo-embryo/histeye.html>). These different concentrations of ions in the aqueous may have a significant effect on its electrical conductivity.

The Lens

The lens is a transparent bi-convex, avascular, epithelial body and lies just behind the pupil and iris. The lens is normally perfectly transparent, enclosed in a clear connective tissue capsule, held in position by suspensory ligaments.

The Vitreous Chamber

The vitreous chamber containing the vitreous body gives rigidity to the eyeball and dampens strains caused by sudden eye movements. It is a colourless, near structureless, gelatinous mass and is approximately 99% water, (<http://alpha.ipfw.edu/histo-embryo/histeye.html>).

1.2 The Mechanism of Vision

The mechanism of vision is rather complex and there remain processes that are not fully understood. Fortunately for the purposes of this work, detailed physiology is not required. However, it is expected that the model of the human eye developed may be used and adapted to incorporate further physiological discoveries.

Photons of light are focussed on the retina and stimulate individual photoreceptors. These efficiently assimilate light energy into a receptor potential. Rods and cones are uniquely adapted to function optimally in different levels of light. They therefore contain different types of photo-pigment. Rods contain 'rhodopsin' which splits to form 'retinene' and 'scotopsin'. This structural change is believed to trigger off nerve impulses (<http://webvision.med.utah.edu/photo1.html>). In bright light, following a shift in the order of 7 to 9 log units of light intensity, rhodopsin is broken down very rapidly and bleaching occurs. In darkness retinene and scotopsin are recombined to form rhodopsin.

Cones exist as three-different types giving trichromatic vision. Each type has a different photo-pigment sensitive to a select band of wavelengths that changes its structure. All cone photopigments contain retinene plus a protein. The proteins are different for each cone type. Red cones respond maximally to yellow/orange light (565nm) green cones respond maximally to green light (535nm) and blue cones to blue light (440nm), (<http://webvision.med.utah.edu/photo2.html>).

As receptor potentials are induced following light absorption they spread through the inner segments of the photoreceptors to their synaptic terminals where neurotransmitters are released. This induces graded local potentials in both bipolar and horizontal cells. The membrane potential of these cells is a result of their selective permeability. This potential is maintained by the sodium-potassium (Na-K) pump, the energy for this being supplied by adenosine triphosphate (ATP).

In the dark, channels on the surface membrane of the outer segments remain open and allow the passage of cations across an electrochemical gradient. This inward current keeps the cell depolarised. The absorption of light by the visual pigment causes the channels on the outer segment to close. This suppresses the inward 'dark' current and causes the visual cell to hyperpolarise. This means that in the light the inside of the cell becomes more negative with respect to the outside. This is the exact reverse of the process in the dark.

Horizontal cells, as their name suggests, have horizontal connections within the retina and transmit inhibitory signals to bipolar cells in areas lateral to both rods and cones. This lateral inhibition enhances contrasts in areas adjacent to or weakly stimulated. Bipolar cells excite amacrine cells and these synapse with ganglion cells. They transmit information to the ganglion cells to indicate a change in the level of illumination. When bipolar or amacrine cells transmit excitatory signals to ganglion cells, they become depolarised and initiate nerve impulses. The axons of ganglion cells form the optic nerve. At the optic chiasma some fibres cross to the contra-lateral side of the brain while others remain on the same side. The nerve fibres terminate in the lateral geniculate nucleus in the thalamus of the brain.

The small changes in retinal potential may be measured. If standard stimulus conditions are employed and the small currents generated at the retina are summed together, characteristic waveform shapes are found. Many scientists believe that the generated current spreads outwards from the retina over the outer area of the eye after which it flows homogeneously through the sclera, choroid and back to the retina. It has previously been proved that radial current flow in an isolated retina is uniform (Arden, 1977). This proof has been corroborated *in vivo* using resistivity depth profiles (Heyen *et al.* 1985).

1.3 Measurement of Visual Function

Measurement of the electromagnetic potentials produced by the eye may be performed using any type of non-invasive electrode. A method of this kind allows an indirect measurement of retinal activity to be made. The actual potentials produced by the retina are assumed to be considerably attenuated. None-the-less, the combined sum of potentials produced from the photoreceptor cells of the retina is measurable. When a retinal cell is stimulated it becomes negative with respect to surrounding cells and positive current flows into it. A distant electrode at the cornea will then record a more positive phase of the characteristic waveform relative to the surrounding cells. If the electrode used were to penetrate the retina the recordings would be of the opposite polarity as the ERG would be reversed (Levett, 1974).

1.3.1 Electroretinography

Electroretinography is the measurement of the bio-electric activity of the retina at the anterior surface of the eye. Currents generated at the retina produce an electromagnetic field that is measured with an active electrode placed on the cornea. A ground electrode is positioned on the subjects' forehead and a reference electrode is placed on the temple or earlobe. The signals produced by the subject depend on the viability of the retina, the stimulus parameters, the recording technique and the presence of any other structures within the eye. Some important stimulus parameters to be considered when recording ERG's are, the amount of prior adaptation, the duration, intensity and frequency of the stimulus, and the amount of retina stimulated (Carr, *et al* 1990).

The electroretinogram (ERG) consists of three components the 'a', 'b', and 'c' waves. The initial 'a' wave is a negative deflection believed to be produced by sodium channels closing (Carr *et al* 1990). This reduces sodium transport into photoreceptor cells causing hyperpolarisation. The consequence of this is a reduction in the release of neurotransmitter at the photoreceptor synaptic terminals. A reduction in neurotransmitter causes the adjacent bipolar and horizontal cells to become either depolarised or hyperpolarised, (depending on their type). Depolarisation of bipolar cells causes an increase in extra-cellular potassium. This potassium enters and depolarises Müller cells. The depolarisation of Müller cells is detectable at the cornea as the positive 'b' wave of the ERG. Any decrease in extra-cellular potassium of this

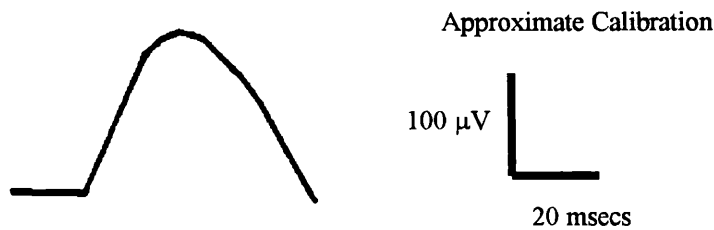
kind alters the standing electrical potential that exists between the surfaces of the RPE. The 'c' wave is believed to represent the algebraic summation of the positive component generated at the RPE and a corneal negative component generated by hyperpolarisation at the distal portion of the Müller cells.

A published standard of the International Society for Clinical Electrophysiology of Vision (ISCEV) (Marmor *et al.* 1995) ensures that electrophysiology is carried out in safe, standard conditions throughout the world. They also ensure that comparisons may be made of data collected from different electrophysiology centres. A Ganzfeld dome is used to provide standard optimal full field stimulation for the testing procedure. The stimulus strength at the surface of the Ganzfeld bowl is set to be between 1.5 – 3.0 cdm^{-2}s . This is referred to as the 'standard flash' (SF). In addition to producing flashes, the Ganzfeld dome is also capable of producing a constant, even background luminance of between 17 – 34 cdm^{-2} over the full field. A standard, full field ERG is designed to measure the following responses (Marmor *et al.* 1995),

- A response developed by the rods in the dark-adapted eye, (stimulating just rods),
- A maximal response in the dark-adapted eye, (stimulating both rods and cones),
- Oscillatory potentials (believed to be produced by horizontal and amacrine cells),
- A response developed by the cones, (stimulating just cones),
- Responses obtained to a rapidly repeated stimulus, flicker (produced by cones).

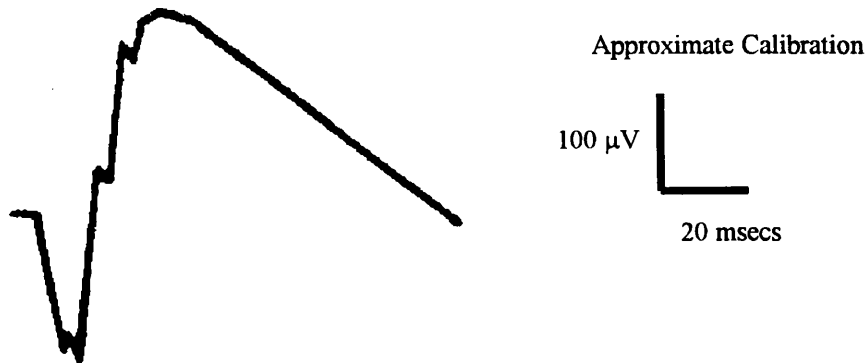
The rod-dominated response is initiated following at least 20 minutes dark adaptation. The extended period of dark adaptation ensures a relatively stable physiologic condition to obtain maximal scotopic responses. The stimulus used is a dim white flash of 2.5 log units below the standard flash, with a minimum of 2 seconds between flashes. (Figure 1.9) shows the shape of a typical rod dominated response (Marmor *et al.* 1995).

Figure 1.9 A Response Developed by the Rods (in the dark adapted eye)
(adapted from Marmor *et al* 1995)



The maximal response is produced using a standard flash on a dark-adapted eye. The response is a combination of both rod and cone systems. (Figure 1.10) shows the characteristic maximal waveform shape (Marmor *et al* 1995).

Figure 1.10 A Maximal Response (in the dark adapted eye)
(adapted from Marmor *et al* 1995)



Oscillatory potentials may also be produced using a standard flash. In this case the pre-amplifier high pass filter is set to 75 to 100 Hz. The eye is stimulated every 15 seconds and only the second or subsequent responses are averaged. Oscillatory potentials are small and believed to be produced by horizontal and amacrine cells, (Figure 1.11) shows a typical example, (Marmor *et al* 1995).

Figure 1.11 Oscillatory Potentials
(adapted from Marmor *et al* 1995)



For a cone mediated response a white standard flash is used following at least 10 minutes light adaptation. (Figure 1.12) shows the normal response, (Marmor *et al* 1995).

Figure 1.12 Normal single flash cone mediated response
(adapted from Marmor *et al* 1995)



To elicit flicker responses, a standard flash stimulus is used again under rod suppressing, light background conditions. Flashes are presented to the eye at 30 Hz. (Figure 1.13) shows the characteristic flicker response, (Marmor *et al* 1995).

Figure 1.13 Normal Flicker Response
(adapted from Marmor *et al* 1995)



Throughout all of these tests the subject's pupils are usually maximally dilated using 0.5% Tropicamide. This chemical temporarily dilates the pupil and paralyses the ciliary muscle.

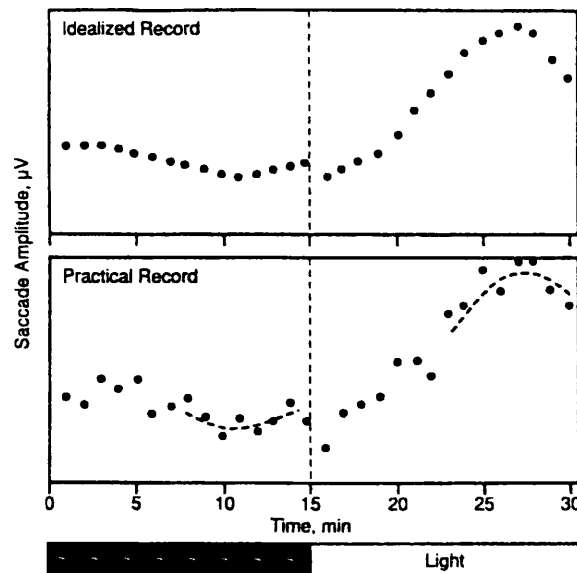
The ERG may be used to assess the progression of many ocular disorders and some types of cone dystrophy. Night blindness diseases such as retinitis pigmentosa (RP) may be discovered and diabetic retinopathy, retinal detachments, vascular degeneration and other circulatory disturbances of the retina may be assessed using the ERG. It is therefore a widely used generic test and may be used in a variety of ways.

1.3.2 Electro-oculography

The electro-oculogram (EOG) measures the standing potential of the eye generated by the RPE. It may vary from one to several millivolts depending on the retinal illumination (Marmor *et al* 1993). It is a mass response and has constant amplitude relative to the light or dark adaptation of the eye. The eye is effectively a dipole, with the cornea positive in relation to the posterior of the globe. Current flow around the orbit is proportional to the magnitude of the standing potential within the eye. Saccadic eye movements therefore result in relative changes in the recorded potential that are recorded as square waves. These changes can be measured from skin electrodes placed at the nasal and temporal canthal regions of the eye. Measurement of the increase or decrease in amplitude of the square waves generated by the saccades during dark and then light adaptation allows evaluation of the function of the retinal pigment epithelium.

ISCEV standards recommend that the fixation targets be 30 degrees of visual angle in the horizontal meridian apart to induce eye movements in constant defined saccades. The Ganzfeld bowl is used to produce even illumination of the retina for the light adaptation part of the test (Figure 1.14), (Marmor *et al* 1993).

Figure 1.14 Waveforms from saccadic eye movements for EOG Arden Ratio
(adapted from Marmor *et al* 1993)



Light adaptation is a time dependent process in which light leads to desensitisation of the retina. There appears to be a gain control mechanism of the retina by which the gain varies with the intensity of the ambient light. It occurs in both rods and cones by a negative feedback mechanism. The EOG is a clinically significant test for detecting abnormalities of the retinal pigment epithelium and is most frequently used for the specific detection of Best's disease.

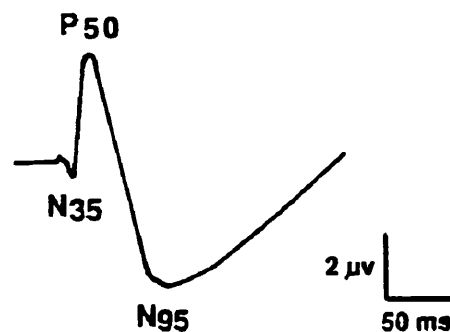
1.3.3 Pattern Evoked Electro-retinograms

The pattern electroretinogram (PERG) is elicited when a temporally modulated, patterned stimulus of constant total luminance is viewed. Such a stimulus appears as a checkerboard (Rimmer *et al* 1989). The subject is prepared in the same way as for an ERG with an active electrode positioned on the cornea, a ground electrode on the forehead and a reference electrode on the temple or earlobe. The usefulness of the PERG arises from the fact that the inner retinal layers, from where the PERG response is believed to be generated, do not contribute to the common flash ERG. It is thought that the PERG evokes responses from the macular and inner retinal layers giving information about the integrity of amacrine and ganglion cells, (Berninger *et al* 1988). Ganglion cells were initially considered to respond optimally to a particular

size of pattern element, i.e. to have spatial tuning. This was because the majority of them have concentric receptive fields in which centre and surround have opposite antagonistic effects. This spatial tuning effect has often been considered evidence to link the PERG to ganglion cell activity (Hess *et al* 1984), (Rimmer *et al* 1989). However, although the PERG may be derived from the ganglion cells it is now known that different ganglion cells may generate potentials for different check sizes (Bach *et al* 1988), (Bach *et al* 1989). It is more likely that multiple mechanisms generate the PERG (Sutter *et al* 1990).

The normal PERG response consists of at least three waves (Figure 1.15). The first small negative wave arises with a delay of $\simeq 35$ ms (N35). The second, a larger positive wave has a typical delay of $\simeq 50$ ms (P50) and the third is again a negative wave at $\simeq 95$ ms (N95). The P50 amplitude measurement is made between the trough of the N35 to the peak of the P50 waveforms and the N95 between the peak of the P50 and the trough of the N95. It is generally agreed that the amplitude of the PERG is often reduced in disease while changes in the latencies of these waves are found infrequently.

Figure 1.15 PERG waveform (negativity appears here as downward deflection)



As the PERG is very small in amplitude it is easily contaminated by artefacts, eye movements, blinking etc. Electrodes that do not interfere with the optics of the eye must be carefully positioned to minimise instability artefacts. It is important that the electrodes do not touch the skin of the cheek. A headrest is sometimes useful to minimise movement artefacts during the test. Clinical applications of the PERG centre around functional assessment of the ganglion cell layer. It is useful therefore in

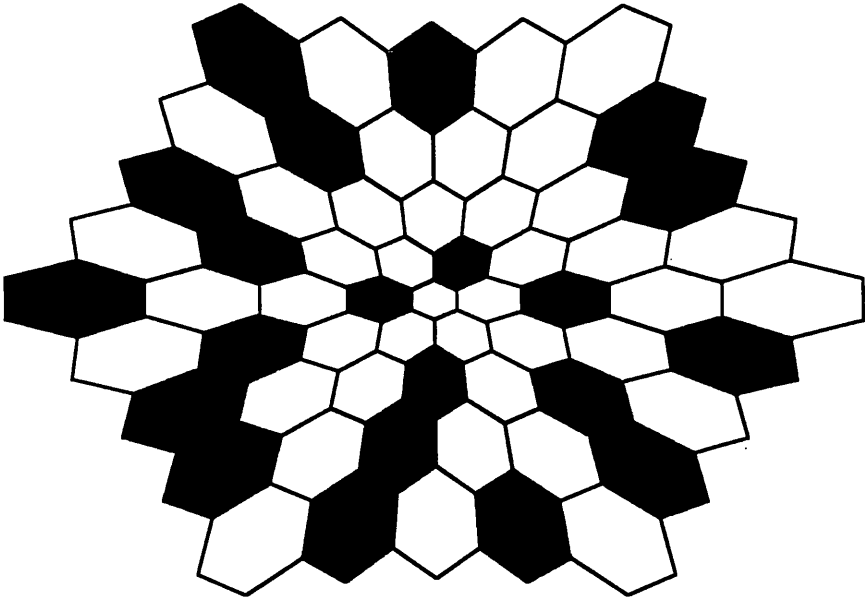
diagnosing optic nerve disease and also discriminating glaucoma from other cases of ocular hypertension. A severe reduction in PERG amplitude is highly diagnostic, though amplitudes a little smaller than normal may be more difficult to assess due to signal to noise problems. It is widely accepted that the amplitude of the PERG reduces with age. This is thought to be due to the loss of ganglion cells and other neurones that occurs naturally with age.

It must be remembered that any condition that affects macular function is highly likely to produce an abnormal PERG. The ganglion cells are the final common pathway from the retina to the brain. When visual loss is the presenting feature macular integrity must be assessed before proceeding with PERG testing.

1.3.4 The Multifocal Electroretinogram

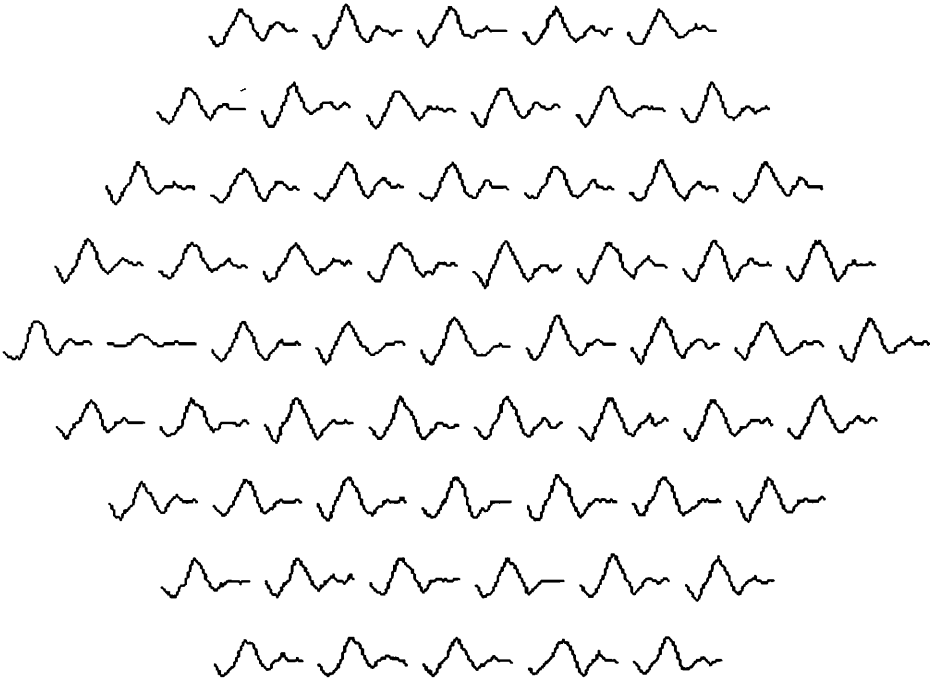
The multifocal electroretinogram (MFERG) has arisen out of a need to gain more information regarding the topographical nature of retina visual function. The full field Ganzfeld ERG has a number of limitations including the fact that it elicits a global retinal response. The macular area is used mainly for central, daylight vision. There are between 4 and 5 million cones in the human retina and most of these are close packed at the macula (Curcio *et al* 1990). However, there are also approximately 80 to 110 million rod photoreceptors, although none exist in the macular area. Diseases of the macular area are therefore difficult to diagnose due to its small size and the fact that over 90% of retinal photoreceptors (i.e. the rods) may be functioning normally. The macula is however most important for visual acuity. Development and modification of the ERG has resulted in the ability to concurrently focally stimulate multiple areas of the retina (Sutter *et al* 1992). The stimulus, which may be used to elicit such a response from a number of areas of retina simultaneously, is shown in (Figure 1.16).

Figure 1.16 The multifocal stimulus



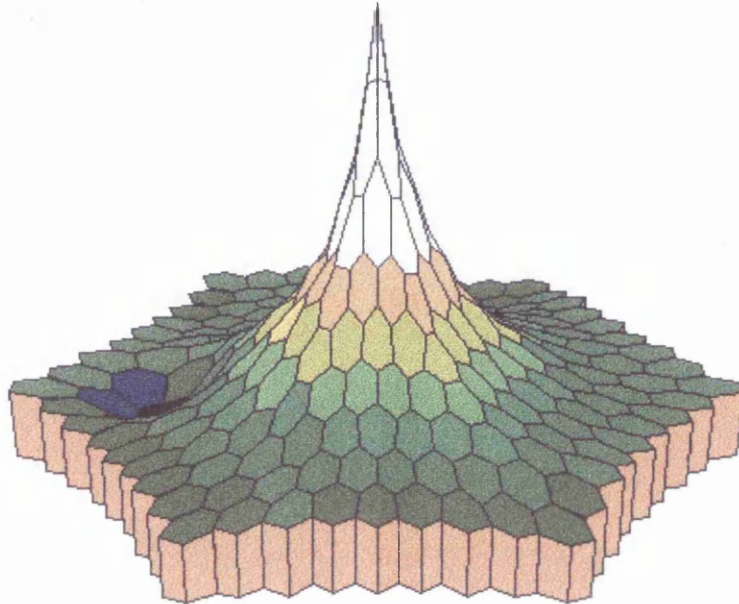
Individual focal responses (Figure 1.17) evoked by multiple stimulus elements are extracted from the composite retinal signal using a fast 'm transform' algorithm.

Figure 1.17 MFERG waveforms over the stimulus area



A topographical functional map of the retina over a central or wide field area may then be constructed (Figure 1.18)

Figure 1.18 MFERG Functional Plot



The luminance of each element of the multifocal electroretinogram is modulated independently using a pseudo random binary 'm sequence'. The contrast of the luminance modulation is around 100% and the mean luminance of the entire display remains nearly constant, as approximately half the stimulus elements are white and half black during each video frame. Fixation is aided using a cross in the centre of the screen. As signals from independent areas of the retina are small, (typically nV) artefacts and associated noise must be minimised. This is done using pre-amplifiers and the ability to record a large number of signal averages.

The large volume of data produced during each recording session is processed by reducing each waveform to a unique number that serves as a measure of either its response amplitude or latency. As with the global ERG waveform, the amplitudes are measured from peak to peak. The implicit time is measured from the time of stimulus onset to the peak of the 'b' wave amplitude. The local response estimated by this technique is generated by stimulus elements of different sizes. The results have no direct physiological meaning unless they are converted to response densities by

normalising to a unit retinal area. The resulting values are displayed in a 3D response density plot. An interpolation is employed to derive a pattern of finer resolution and this data may then be used in comparisons with other age matched data using previously calculated confidence plots. These illustrate any deviation from normative values.

1.4 Electrodes

There are many different types of electrode used in clinical ocular electrophysiology. Every electrode has its own inherent impedance and recording characteristics with unique associated artifacts. Most electrode related artefacts are due either to electrode polarisation, movement of the eye or a photo-voltaic effect. To avoid polarisation, care should be taken to ensure that both active and reference electrodes are of the same metallic type. Eye and hence electrode movement is potentially the largest source of artefact generation directly influencing the quality of ERG recordings. Subjects undertaking tests must exhibit a reasonable amount of co-operation when asked to fixate centrally. A fixation point is provided to facilitate this. The photovoltaic effect occurs when light strikes the electrode surface and generates a spike signal appearing early in the ERG recording. To eliminate this the electrode surface is shielded.

There is no universally accepted ocular electrode for general use though there are many to choose from (Barber 1994). The more common are contact lens electrodes, useful for long recording sessions and gold foil electrodes, useful for pattern ERG recordings as the optics of the eye remain unimpeded. Low mass conductive thread electrodes float on the cornea. The electrode of choice depends on the electrophysiological application (Robbins *et al* 1988). Considerations include ease of placement, subject comfort, electrode stability, and acceptable signal to noise ratio (SNR).

1.4.1 Contact Lens Electrodes

Contact lens electrodes were developed using a transparent non non-irritating lens that could be fitted onto the subject's eye for prolonged ERG recording sessions (Riggs, 1941). Contact lens electrodes are considered the 'gold standard' electrode by the International Society for Clinical Electrophysiology of Vision as they produce reliable

and reproducible results. The most common contact lens electrode is the 'Burian-Allen' electrode (Burian *et al* 1954) (Figure 1.19).

Figure 1.19 A Burian Allen Contact Lens Electrode



Like all corneal electrodes, topical anaesthesia is required before insertion. This particular type incorporates a speculum to hold the eyelids apart, while the active electrode, a circular silver wire around the circumference of the contact lens, makes contact with the cornea. Although this electrode has very good recording characteristics it has been found to be uncomfortable for routine use and in a small number of cases causes corneal abrasions (Vey E.K *et al* 1980).

1.4.2 Gold Foil Electrodes

The gold foil electrode, as its name suggests, is made from gold applied to the surface of a Mylar film making it flexible (Figure 1.20) (Border *et al* 1978, Arden *et al* 1979).

Figure 1.20 A Gold Foil Electrode



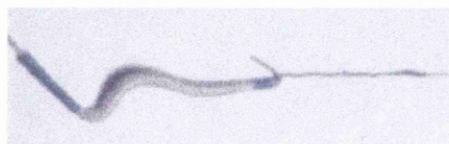
It is a flexible electrode and has been found to be more comfortable than standard contact lens electrodes. When inserted into the lower fornix of the eye it is bent to form a 'J' shape. In this position the electrode just touches the corneal margin while the connecting wire is taped against the cheek. This electrode has latterly been widely used in the UK and on the continent. It is found to record ERG's similar in shape, though reduced in amplitude, to those using a contact lens electrode.

These electrodes are prone to movement during recording and sometimes they fall out if excessive blinking occurs. However, with co-operative subjects this does not present a problem. As the optics of the subjects eye remain unimpeded throughout testing this electrode is particularly useful for recording pattern and multifocal ERG's.

1.4.3 DTL Fibre Electrodes

This electrode consists of a low-mass silver micro-fibre (Figure 1.21) that makes contact with the tear film meniscus of the eye and is electrically coupled to an insulated wire (Dawson *et al* 1979).

Figure 1.21 A DTL Fibre Electrode



The advantages of the DTL fibre include its comfort, and reduced electrode impedance. It is well tolerated by children and adults with keratitis. Like the gold foil electrode it does not obscure the optics of the eye and is therefore well designed for pattern ERG recordings. An added advantage of this electrode is its stability within the eye, it is quite difficult for it to fall out.

1.4.4 Skin Electrodes

It is possible to obtain ERG signals using skin electrodes (Tepas D.I *et al* 1962), (Adchi-Usami *et al* 1971). This is done without placing electrodes onto the eyes themselves. However the ERG signals recorded are of very much reduced amplitude, noisier, less reliable and more variable than those recovered when using corneal electrodes (Figure 1.22).

Figure 1.22 A Skin Electrode



These electrodes are tolerated well by infants, young children and patients who will not allow placement of a corneal or gold foil electrode. Due to the advantages of signal averaging in increasing the signal to noise ratio, skin electrodes have been used to detect oscillatory potentials and PERG waveforms. However, standardised placement of electrodes is difficult and they are only used in exceptional circumstances.

1.5 Summary and Conclusions

The eye is a complex structure, anatomically designed to focus light onto the highly sensitive photoreceptors of the retina. Physiologically the eye is a well-balanced system maintaining homeostasis of a wide variety of processes. Each structure within it contributes to the efficient conversion of light into electrical impulses resulting ultimately in electrical stimulation of the brain to initiate visual perception.

There are a variety of ways in which the processes within the eye may be studied. A typical non-invasive method of investigation is electroretinography. Measurement of the electromagnetic potentials produced by the retina is highly useful in the diagnosis and progression monitoring of a wide variety of retinal disorders. It is always anticipated that more accurate measurement and extraction of data from measurements made will ultimately improve clinical diagnoses. Electrodes of many different types, which may be used to make these measurements, have been described and their unique merits discussed. It is believed that an accurate model of the human eye will assist designers to overcome the current failures of clinical electrodes and enable their optimisation to measure, more accurately, electrical potentials on the accessible surface of the eye.

Chapter 2

Basic Theories and Current Practice

2.0 Introduction

Functional organisms may be investigated practically by constructing models to follow the operations of the organism as accurately as possible. The behaviour of the model should however follow the basic laws of science, (Malmivuo *et al* 1995). It may then be possible to perform experiments with the model that are simply not practical in the physical situation. The human eye can be modelled as a finite inhomogeneous structure. This means that the model takes into account the finite dimensions of the conductor and includes a consideration of the internal inhomogeneities. The basic requirement of a model of this kind is to accurately calculate the electromagnetic field that may be measured over the surface and within the human eye.

There have been many reports in the literature regarding the methods by which electromagnetic fields may be calculated in two and three dimensions (Trowbridge 1982), (Mur G *et al* 1985), (Plonsey *et al* 1987). Much of the initial work in this area has arisen from the requirements of the physics and engineering community to calculate magnetic fields and 'eddy' currents within and around various structures, (<http://www.mac-ndt.com/>). There are in some cases many solutions to these problems. However, more often than not, calculations centre on one of two distinct methods of solution namely the finite element method and the finite difference method.

Finite element analysis was first developed in 1943 (R Courant) and consists of a two or three dimensional computer model of a material that is stressed and analysed for specific results (<http://sog1.me.qub.ac.uk>). Within the model the programmer may insert numerous algorithms to make the system behave linearly or non-linearly. This method works using a complex system of points (nodes) which when joined together

make a grid called a mesh. The mesh itself is programmed to contain all the properties of the material to be modelled. Each area between the nodes is an element and the change of the dependent variable with regard to location is merely approximated within each element by an interpolation function. There has been some work in the literature that seeks to optimise this 'mesh generation' in order to increase calculation accuracy by developing realistically shaped models from magnetic resonance imaging (MRI) data sets (Ziółkowski M *et al* 1996). While two dimensional modelling simplifies the problem and allows the analysis to be run on a relatively 'normal' computer, three dimensional analysis of this kind will produce far more accurate results but may not run sufficiently well on all but the fastest computers.

The finite difference method is however less complex. In this case, the solution is approximated again using a grid of uniformly spaced nodes. However, this time the differential equation at each node itself is approximated by an algebraic expression that incorporates all adjacent nodes. A system of equations then is obtained by evaluating the previous algebraic approximations for each node. By either method calculations of the electromagnetic field existing within any volume or around any electromagnetic source may be made with varying degrees of accuracy.

2.1 Modelling Electromagnetic Events in the body

Modelling electrical phenomena of many different organs within the body has been attempted for decades. Early models of single nerve fibres in volume conductors showed analytically and then numerically how current flowed along axons in situ, (Clark J *et al*, 1968). Even these early models highlighted the importance of accurate conductivity values of structures close to the source of potential. The smooth muscle cells of the stomach, activated by spontaneous depolarisation and repolarisation have more recently been modelled. The electrical changes that occur are termed gastric electrical activity (GEA) and result in the creation of an electric field that may be measured and modelled. A computer model of such a system simulates depolarised smooth muscle cells as electrical dipoles in an annular band, (Mintchev MP *et al*, 1995). Results from this model have shown electrical coupling between different parts of the stomach as well as various effects observed when changing the measurement electrode configuration.

Modelling the electrical activity of the brain has in recent years become very popular with the increased development of MRI technology. In most cases in the literature the localisation of sources in the brain by calculating the electromagnetic field within the skull is undertaken by modelling the head as a homogeneous sphere, (Ary J.P *et al*, 1981), (Abboud S *et al* 1994), (Laarne P *et al* 1995). An initial set of source parameters is assumed and the potential distribution over the surface of the model head is subsequently calculated. This is then usually compared with the actual potentials measured over a real head. The theoretical parameters are then subsequently modified to minimise the differences between the two distributions. Such models are found to provide good approximations for sources close to the centre of the skull i.e. midbrain or brain stem sources (Sidman R.D *et al*, 1978). However, various corrections must be made for skull and scalp thicknesses if the sources are located at larger eccentricities (Ary J.P *et al*, 1981)

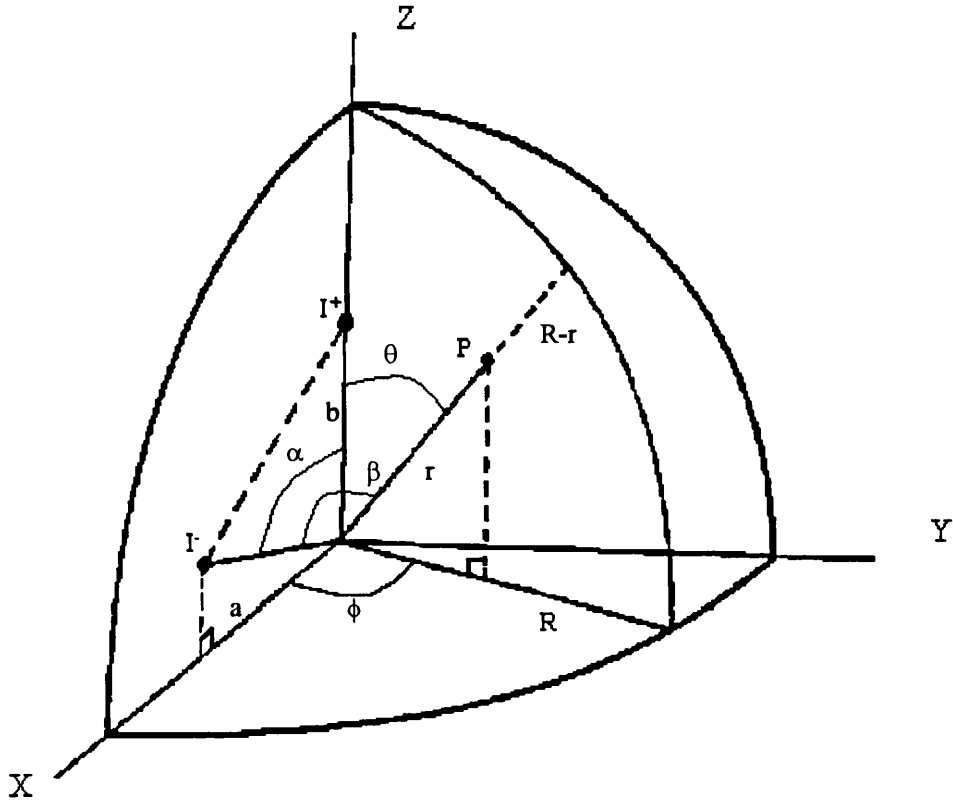
More recently the finite difference method has been used as the basis of computer models to calculate electromagnetic fields within the skull (Laarne P *et al* 1995). Most of these have been adapted from previously published work of other electromagnetic structures, (Doslak 1978). Models of this nature consist of either three or four conductive layers and a 'quasistatic' field is usually assumed, (Abboud S *et al*, 1994). In recent numerical model analyses of these physiological phenomena, calculated data is usually validated using analytical findings yet many numerical models remain sufficiently flexible to enable incorporation of the highly accurate conductivity values of discrete regions within the skull from recent MRI studies (Laarne P *et al*. 1995).

Models of the electrical nature of the heart have been widely published in the literature. Early models that investigated the origin of potentials found on the skin surface modelled the heart as two point current sources, I^+ and I^- (essentially a dipole) in a homogeneous conducting sphere, (Figure 2.1), (Frank, 1952). In an unbounded medium the potential at an arbitrary point is given by

$$V_{\infty} = \frac{I}{4\pi\gamma} \left(\frac{1}{r_b} - \frac{1}{r_a} \right)$$

Equation 2.1

Figure 2.1 Two point current sources in a homogeneous conducting sphere
 (adapted from Frank E, 'Electric Potential Produced by Two Point Sources in a Homogeneous Conducting Sphere' Journal of Applied Physics, 1952: 23(11); 1225 - 1228)



Where r_a and r_b are the distances of the sources to the arbitrary point $P(r, \theta, \phi)$.

When the current is confined to a sphere of radius R , Frank showed that the potential could be expressed as

$$V = \frac{I}{4\pi\gamma} \sum_{n=1}^{\infty} \left(\frac{n+1}{n} \frac{r^n}{R^{2n+1}} + \frac{1}{r^{n+1}} \right) \left[b^n P_n(\cos \theta) - a^n P_n(\cos \beta) \right]$$

For $r < b$

Equation 2.2

Where $P_n(\cos \theta)$ and $P_n(\cos \beta)$ are functions of the associated Legendre function.

Frank discusses several cases of special interest that may be derived from the general results. In particular, solutions with ϕ symmetry (when the orientation of the dipole passes through the origin of the sphere) are of interest.

When $a > 0$, $b > 0$ and $\alpha = 0$, the potential at the boundary of the sphere is

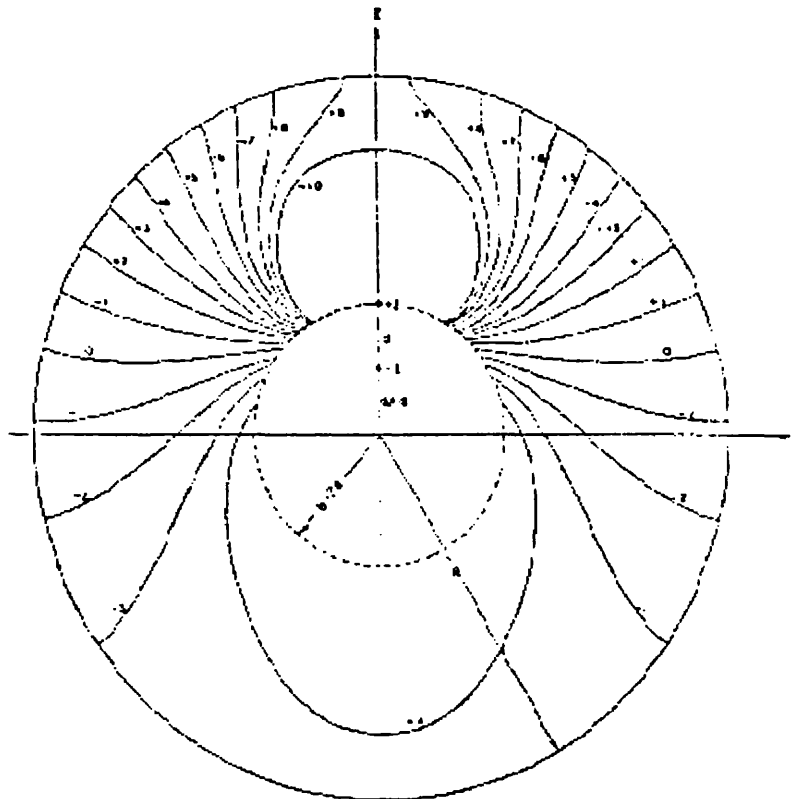
$$V_R = \frac{I}{4\pi\gamma} \sum_{n=1}^{\infty} \left(\frac{2n+1}{nR^{n+1}} \right) [b^n - a^n] P_n(\cos \theta)$$

Equation 2.3

Figure 2.2 shows the equipotential distribution in an equatorial plane. Such distributions have been confirmed experimentally in hemispherical water tanks.

Figure 2.2 Illustration equipotentials in an equatorial plane

(adapted from Frank E, 'Electric Potential Produced by Two Point Sources in a Homogeneous Conducting Sphere' Journal of Applied Physics, 1952: 23(11); 1225 - 1228).



One of the first computer models of a time varying dipolar heart source used an iterative technique to calculate surface potential maps for realistic thoracic geometries. (Barnard A.C.L *et al* (I and II) 1967). This work was unfortunately hampered by the lack of computing power available to perform the complex calculations required. On average only 49 iterations were possible. Analysis of the resulting potential field was found to be highly dependent on all modelling assumptions used, including the dielectric properties and internal inhomogeneities of the medium in which the source existed.

More recently, research in the USA has centred on developing computer models to study the origin of cardiac signals in an effort to predict myocardial fibre orientation and hence changes that occur in conduction during arrhythmias, (Henriquez C.S, 1993), (Muzikant A.L *et al.* 1997). These models use finite volume methods, (Harrild D.M. *et al* 1997) and adaptive mesh generation with optimised algorithms for supercomputers (Henriquez C.S. 1989). 'Parallel pipelining' techniques are also being developed to enable the solution of large-scale problems using parallel processing. Needless to say research centres of this nature have high speed direct links to state of the art computing resources such as CRAY T90 and IBM SP supercomputers. This work, though based primarily on cardiac function, is essentially the development of a more realistic numerical model of the heart to enable better interpretation of electrophysiological measurements. It is hoped that algorithms and computer visualization tools developed in this field to animate the conduction process in two and three dimensions may one day be used to simulate other sites of electrical conduction within the human body including the eye.

Calculations of the electroretinographic potential field produced by the eye or more precisely the retina have been described in the literature, (Holland *et al.* 1964). Early physiological investigations were undertaken to measure electroretinographic field parameters in the hope that the effects of retinal disease may be determined. This still remains the goal of present more advanced techniques. The use of differential electroretinography in live rabbits has enabled radially symmetric isopotential regions to be localised over the cornea and recent studies in humans also reach this conclusion. These early studies went further to state that the symmetry of the electroretinographic potential field was related to the spatial symmetry of the retinal

generators, (Holland *et al.* 1964). It was this early work that showed how the corneal potential field was indeed modified following localised retinal lesions. Investigations of this nature have provided essential building blocks for the more recent advances of multifocal electroretinography and the spatial localisation of retinal lesions in general.

Since these initial physiological experiments a number of theoretical models of the eye have been constructed. Initially the modelling of global retinal activity has been attempted as this may easily be compared with physiological recordings i.e. global ERG's. Theoretical modelling of a structure that produces an ERG signal is a non-trivial task as the ERG is known to be a complex waveform arising from the summed contributions of many different types of cells in the retina. The 'a' wave component of the ERG was thought to originate from the deepest 25% of the retina (i.e. photoreceptors). However, recent evidence suggests that off-bipolar cells are the major contributor, (Bush *et al* 1994, Bush *et al* 1996). Originally it was thought that the current source and sink generator for the 'b' wave of the electroretinogram was the Müller cell (Heyen *et al.* 1985), (Tomita *et al.* 1981), (Heyen *et al.* 1985). More recent evidence however points to the on-bipolar cells, (Karwoski *et al* 1996, Robson *et al* 1996, Hood *et al* 1996).

Problems associated with modelling the human eye (to a first approximation) include consideration of the physically inhomogeneous structures within the eye volume. Variable specific conductivities of these structures must be taken into account along with the site of origin of the electrical source, any light adaptation of the eye, the intensity of the light stimulus and the non-uniformity of the photoreceptors over the retina. A large number of assumptions make for an inherently inaccurate model. However, approximations based on accurate analysis of the physiological structure of the eye will ensure a good estimation of electroretinographic activity.

Before addressing the forward problem of these calculations it should be noted that a number of investigators have attempted the 'inverse' problem. This means that the electromagnetic field and conductor are known but the source is unknown (Malmivuo *et al* 1995). A theoretical paper in the literature describes this scenario and explains the fact that it does not have a unique solution, (Helmholtz 1853). However a number of investigators have attempted this problem for the eye, (Davey K.R *et al.* 1988),

(van Schijndel N.H *et al.* 1997). This work has been supported by earlier ground work in electromagnetic potential theory (Plonsey, 1984), (Doslak *et al.* 1980). However it is inherently more difficult than the forward problem due to limited number of skin electrodes usually used and the necessity of the accurate measurement of retinal potentials with which to compare the calculated results.

Early theoretical inverse models of this nature were of limited success, as they did not take into account any conductivity variations within the eyeball, (Davey K.R *et al.* 1988). However, experimentally acceptable results were found to detect disrupted retinal cell activity but with no real degree of spatial accuracy.

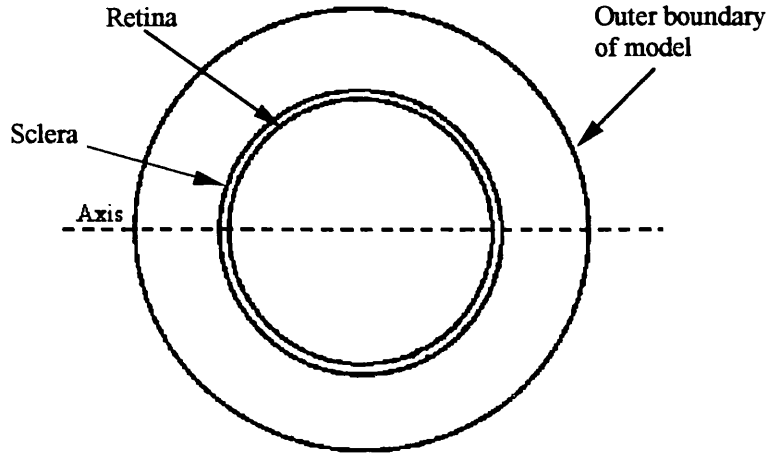
More recent work on the inverse problem has incorporated magnetic resonance imaging (MRI) data sets of conductivity values. The boundary element method (BEM) is used in these cases (van Schijndel *et al.* 1997). Here conductivity values of various regions within the skull and around the eye were taken into consideration. The BEM was found to be unsatisfactory at coping with extremely thin layers of tissue with largely contrasting conductivities. Hence the choroid, sclera, and retinal pigment epithelium were ignored in this model. As only eight skin electrodes were used to measure the potentials the inverse problem in this case was inherently 'underdetermined'. The information content from the electrodes was also thought to be of limited value and hence the authors describe the solution as 'ill-posed'.

The inverse technique in both of these cases was found to result in a 'spreading' of the estimated source distribution. Localisation of a region of activity is possible, however there remains no detail in the source distribution and large differences were found between the measured and predicted ERG's.

2.2 Analytical Modelling

In considering the forward problem, one theoretical model has previously been attempted (Doslak, 1978). Doslak's analytical model (Figure 2.3) consists of a uniform double layer (representing the retina) inside the orbit. This is represented by three concentric spheres.

Figure 2.3 Construction of the Analytical Model (adapted from ‘The Effects of Variations of the Conducting Media Inhomogeneities on the Electroretinogram’ PhD Thesis Case Western Reserve, M.J Doslak 1978).



In general the potential in each of these regions may be calculated using classical field theory (Plonsey & Collin 1961), (Panofsky & Phillips 1962) where

$$\Phi_1 = \frac{K}{\sigma_A} \sum_{n=0}^{\infty} A r^n P_n(\mu)$$

For $r < R_1$

Equation 2.4

$$\Phi_2 = \frac{K}{\sigma_B} \sum_{n=0}^{\infty} \left[B r^n + \frac{C}{r^{n+1}} \right] P_n(\mu)$$

For $R_1 < r \leq R_2$

Equation 2.5

$$\Phi_3 = \frac{K}{\sigma_c} \sum_{n=0}^{\infty} \left[D r^n + \frac{E}{r^{n+1}} \right] P_n(\mu)$$

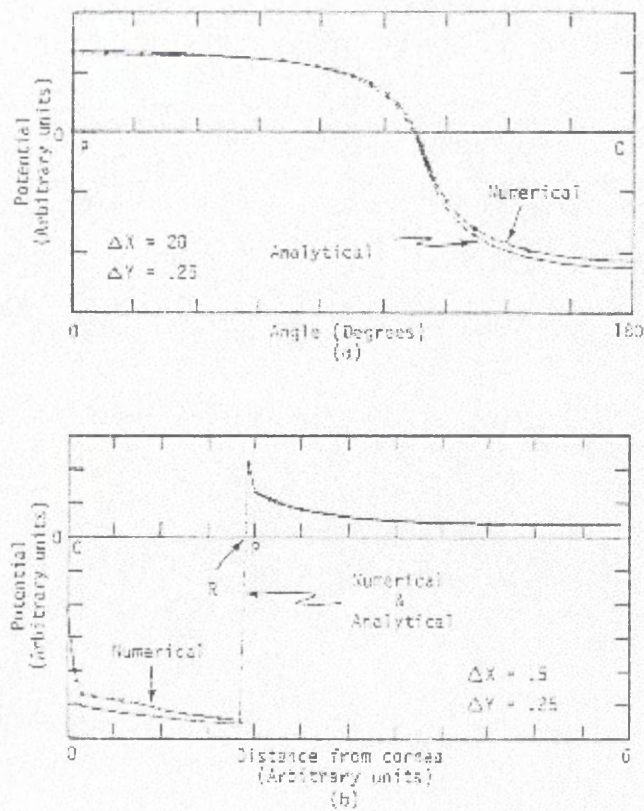
For $R_2 \leq r \leq R_3$

Equation 2.6

Where $\mu = \cos \theta$, $P_n(\mu)$ is the Legendre function and A, B, C, D, E and K are constants.

The boundary conditions are that the potential and the normal component of the current density are both continuous at passive interfaces. At the retina the normal component of current density is continuous but there is a potential discontinuity equal to the value of the double layer strength. By taking advantage of the orthogonal properties of the Legendre function, Doslak solved the above equations and was able to present results showing the distribution of potential along the circumference and midline of the model eye, (Figure 2.4). For completeness the original mathematical analytical development of this model (Doslak 1978) has been reproduced in Appendix A along with details of the associated supporting complex mathematics.

Figure 2.4 Numerical and analytical potentials along the circumference and midline of the eyeball (adapted from 'The Effects of Variations of the Conducting Media Inhomogeneities on the Electroretinogram' PhD Thesis Case Western Reserve, M.J Doslak 1978).

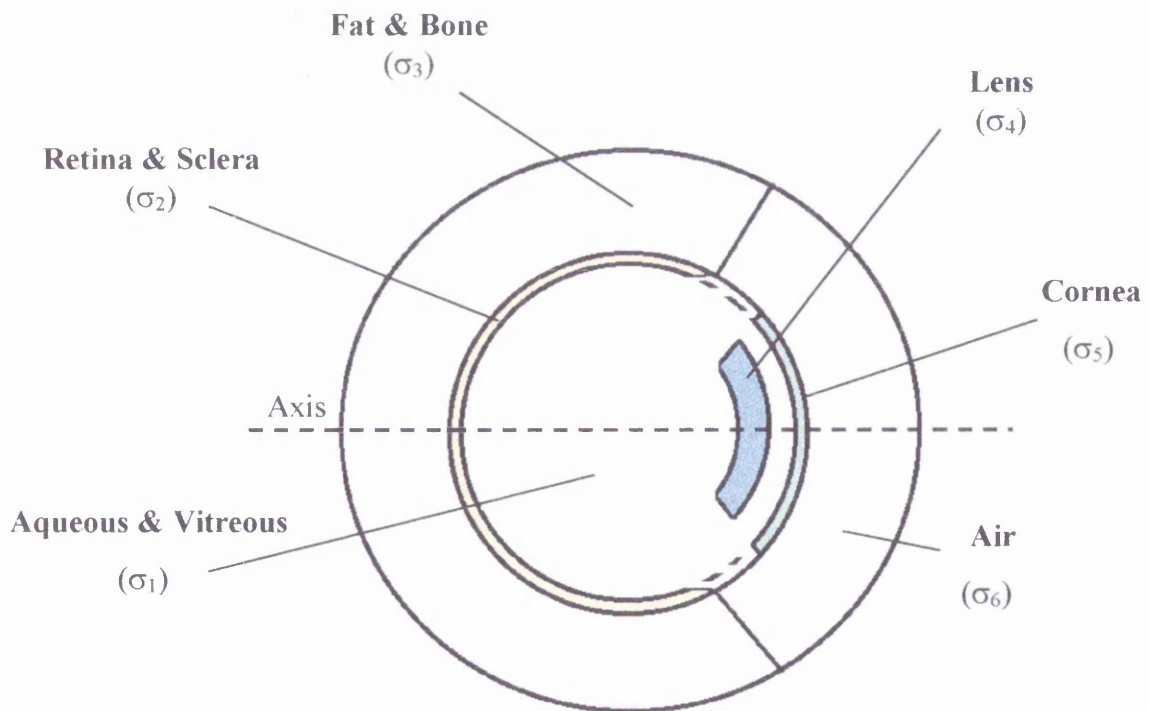


2.3 Numerical Modelling

In order to incorporate a more realistic representation of the physiology of the eye the analytical model may be further numerically modified. Each of the rings of the analytical model is now further divided to produce six different regions of the eye. The construction of the two-dimensional numerical model is shown in Figure 2.5.

These regions were designed to represent the aqueous and vitreous, the retina and sclera, fat and bone, the lens, cornea and air at the anterior surface of the eye. The retina in this case is modelled as an active, bioelectric, 'double layer', initially of uniform potential between the inner sphere (aqueous and vitreous) and the outer sphere (fat and bone).

Figure 2.5 Diagram showing the six different regions of the two dimensional model. (adapted from 'The Effects of Variations of the Conducting Media Inhomogeneities on the Electroretinogram' PhD Thesis Case Western Reserve, M.J Doslak 1978).



Current then flows throughout the surrounding volume conductor inducing an electromagnetic field within the structure. The volume conductor of the eye in this is constructed of a number of regions representing specific structures. Most of these

structures were considered to be electrically 'passive'. Three assumptions regarding these regions were made.

1. Each region within the volume conductor was considered to be linear (i.e. the electric field in the region was directly proportional to the current density).
2. Each region within the volume conductor was considered to be homogeneous (i.e. the electrical properties within each region did not vary within the volume).
3. Each region within the volume conductor was considered to be isotropic (i.e. the electrical properties within each region were the same in all directions).

It is known that the bioelectric nature of the retina varies with time and stimulus conditions. The field itself will become modified as it spreads out through the volume conductor (Doslak 1978). For initial calculations however, the electromagnetic field at a single point in time was calculated. While this was accepted to be an oversimplification of a model of the electric field within the eye it was considered to give a snapshot view of the field at a single instant in time.

Laplace's equation may then be applied throughout the model. At all the interfaces of the passive volume conductor continuity of potential and normal current were maintained. For frequencies less than 1kHz, propagation, capacitive and inductive effects in the volume conductor were considered to be negligible. However the capacitance of the active retinal membrane was not considered negligible and was therefore handled separately.

Each of the six regions represents a particular structure of the eye. The aqueous humor and vitreous body was considered a single volume having almost identical conductivities. The extra-ocular structures, (i.e. fat and bone) were also considered to be one conductivity region. The cornea was considered to be a single region however, the data used did not take into account the effects of the corneal epithelium as it lies between the corneal stroma and the air boundary. No anterior current flow has ever been found. Consequently the effect of the corneal epithelium on the potential field was considered to be negligible. The conductivity value for the air in front of the eye was set initially to zero. However a non-zero value was used in later experiments and

considered useful to compare the numerical with the analytical model.

The extent of the cornea was set to 67.5° . The thickness and extent of the lens were approximately that of the average human eye, however the posterior surface was made concave to facilitate the positioning of 'nodes'. The representation of the retina in the two dimensional numerical model extended halfway between the ora serrata and the region where the rods and cones cease. This was approximately 112.5° . The impedance of the retinal membrane was included implicitly in the calculations of potentials. Calculated potential values produced in the model were always dimensionless since the magnitude of the field was arbitrary and user defined. The outer diameter of the model eye was given a value of unity and used as a reference. All other linear dimensions were normalised to this reference value. A two-dimensional model represented in this way was considered to closely represent the gross structural nature of the human eye. Calculations using this model were considered to be uncompromised in making these simplifications.

To calculate the solution of the potential field within such a structure a network of 'nodes' was derived from previously published data, (Doslak, 1978). This was a non-uniform and variable arrangement and was designed to ensure a high degree of accuracy and rapid convergence to the solution. Table 2.1 shows the two dimensional co-ordinates of nodes used in this model.

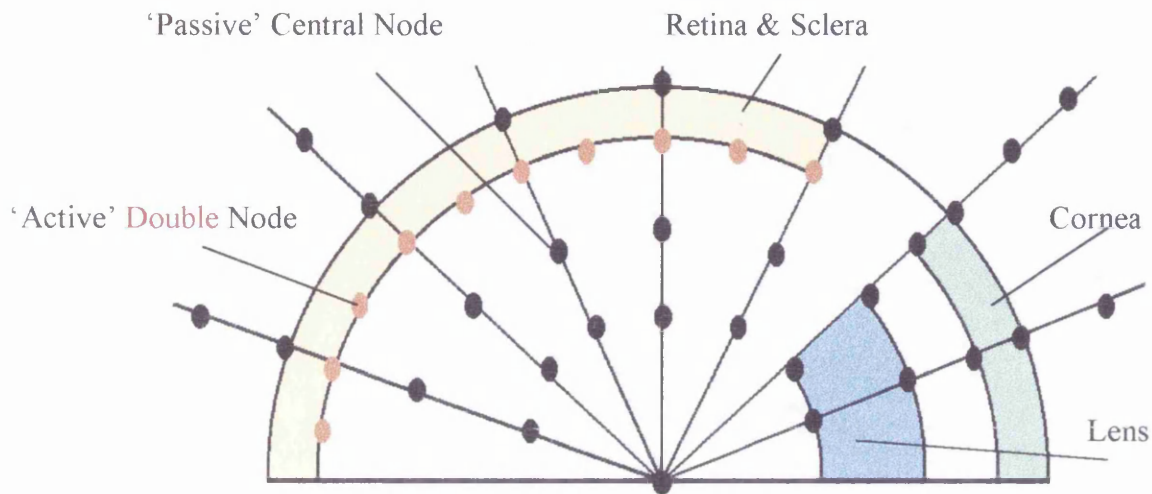
The set of nodes on the axis of symmetry and at the largest radius forms a closed boundary. This is important for the execution of the numerical solution. These nodes fill each region having variable spacing between them. The conductivity value associated with each node varies depending on in which region the node was positioned. As with the analytical model, the numerical model was considered to be axially symmetric. This has the effect of reducing the two-dimensional model to a simple 'segment' structure as shown (Figure 2.6).

Table 2.1**Table showing co-ordinates of nodes for Doslak's two-dimensional model**

Position	Radii	Angle (Degrees)	Angle (Radians)
1	0.000	0.00	0.000
2	0.080	11.10	0.196
3	0.140	22.50	0.393
4	0.200	33.70	0.589
5	0.250	45.00	0.785
6	0.300	56.30	0.982
7	0.360	67.50	1.178
8	0.420	78.70	1.374
9	0.430	85.00	1.483
10	0.440	90.00	1.571
11	0.510	96.00	1.675
12	0.610	101.25	1.767
13	0.710	104.00	1.815
14	0.720	107.00	1.867
15	0.730	108.50	1.894
16	0.800	110.00	1.920
17	0.840	110.50	1.929
18	0.890	111.00	1.937
19	0.895	111.50	1.946
20	0.900	111.75	1.950
21	0.902	112.00	1.955
22	0.905	112.50	1.963
23	0.910	113.00	1.972
24	0.915	113.40	1.979
25	0.925	113.80	1.986
26	0.960	114.20	1.993
27	0.990	114.60	2.000
28	1.000	115.00	2.007
29	1.001	116.00	2.025
30	1.040	117.00	2.042
31	1.080	120.00	2.094
32	1.150	123.75	2.160
33	1.220	126.00	2.199
34	1.290	128.40	2.241
35	1.370	129.00	2.251
36	1.500	129.60	2.261
37	1.750	135.00	2.356
38	2.100	141.00	2.461
39	2.500	145.50	2.539
40	2.950	146.25	2.552
41	3.500	147.00	2.566
42	4.150	157.50	2.749
43	4.900	168.75	2.945
44	5.000	180.00	3.142

Figure 2.6 Nodal arrangement for the two-dimensional numerical model.

(adapted from 'The Effects of Variations of the Conducting Media Inhomogeneities on the Electroretinogram' PhD Thesis Case Western Reserve, M.J Doslak 1978).



Nodes are also evident on the boundaries between as well as wholly within each region. The two dimensional numerical solution simply consists of solving for the potentials at each of the nodes within the 'nodal network'. Laplace's equation was satisfied at each of the nodes in the structure. The boundary conditions of continuity of normal current and potential were also satisfied at each interface between the boundaries of different conductivity.

Passive, central, nodes are contained anywhere within the volume conductor regions and are handled quite separately from active double nodes on the retinal membrane itself. For completeness, the original calculations required for 'passive central nodes' in this two-dimensional model has been reproduced in Appendix B. This appendix illustrates in detail how these equations have been developed. However, by way of summary, the solution for a central node within the volume conductor was found by consideration of the values of the potentials at each of the nearest surrounding nodes. The source strength of the retinal double layer was initially chosen to be spatially constant. While it was accepted that this was not an accurate representation of the actual physiological source distribution, it was useful for comparison and validation

with the two-dimensional analytical model (Doslak, 1978). The source strength distribution may be modified to more accurately represent photoreceptor density topography changes with eccentricity.

Original calculations of the potentials at a 'retinal double node' have been reproduced in Appendix C. In summary, the solution for nodes on the retina was handled separately as each was represented as a double node, (Klee & Plonsey 1972). Each double node consisted of two half nodes located just inside and just outside the membrane. They were however, mathematically considered to be at exactly the same radius. Difference equations for both the interior and exterior half node potentials in terms of the double layer strength, the retinal membrane impedance and the relevant conductivities and adjacent potentials are derived. The resulting retinal membrane impedance is analogous to the calculation of the generator internal impedance in circuit theory. Calculation of the nodal potential at the origin requires specific calculation and was therefore handled separately. Appendix D outlines the calculation required (Doslak, 1978). It should be noted that the algorithm for the potential at this central node does not depend on the conductivities of the nearest regions or the radial separation but only on the angular geometry of the adjacent nodes.

To calculate the final solution, each node in turn is considered by applying the appropriate final algorithm, dependent upon its position within the structure. This is done in an orderly sequential pattern examining all the nodes starting at the origin and progressing from 0 to 180 degrees in the next and subsequent radial layers of nodes. One traversal of the set of nodes constitutes a single 'iteration'. Subsequent iterations are performed until the convergence of each nodal potential is reached.

To achieve convergence as rapidly as possible, a successive over relaxation technique was employed, (Doslak, 1978) based on the equation

$$u^{n+1} = u^n + \omega (v^{n+1} - u^n)$$

Equation 2.7

where

u^{n+1} = new potential at the node for the current iteration

u^n = old potential from the previous iteration

v^{n+1} = an intermediate potential

ω = the over relaxation factor

Following each iteration a new potential is found at each node by extrapolation based on the estimated rate of convergence. The intermediate potential is found using the algorithms for either a passive node in the volume conductor or a double node on the retinal double layer as described. Some of the neighbouring nodes in the algorithm will have their old potentials and others a new updated potential depending on where they are located in the iteration pattern. As the specific algorithm is applied to each node its potential is updated to a new potential, ignoring the old potential afterwards. The over relaxation factor which determines the rate of convergence of the solution may be set to a value anywhere between 1 and 2. When equal to one, the successive over relaxation method reduces to a Gauss Seidel method (Doslak, 1978). When it is greater than 2, the solution does not converge, larger factors cause oscillation.

2.4 Delphi Programming in two dimensions

In order to obtain meaningful results it was initially necessary to replicate current findings (Doslak, 1978). This was achieved by constructing a two-dimensional computer program to calculate the required algorithms. The computer language used was Delphi 2.0. This is similar to 'Turbo-pascal' programming language and initially nine linked units were formed. In order to summarise the properties of the program the purpose of each of the units is summarised below. The full program listing of each unit for the two-dimensional numerical model may be found in Appendix E.

The program file is named 'Doslak' and describes the procedures and units that are used. The **main** unit accesses all the other units of the program. Arrays are constructed and procedures declared. The properties of each region of the model including the conductivity value are defined, as are the properties of the retinal membrane. Integer, double and complex parameters are used to define these variables. Radial and theta nodal positions are read into the program via arrays and the array into which the final values will be written is zeroed. All the other units of the program are accessed via this unit which uses the information provided by calculations completed in other units to calculate initially the nodal value at the centre of the model structure. The program then progresses by successively incrementing both the radial and theta values to calculate the potential at each of the nodal points. This procedure is then repeated until the number of iteration set has been achieved. Finally the resultant potential values from the calculations are written to an array which may be opened once the program has been terminated.

The **setup** unit contains variable declarations that the program requires. This includes the over relaxation factor ' ω ' and the frequency (initially set to zero). The radial and theta arrays of values are read into the **main** unit from the **setup** unit.

The **membrane** unit essentially calculates the potentials of the double nodes on the retinal membrane. The interior and exterior potentials UA and UB of each of the double nodes are then used in subsequent calculations of other nodal potentials.

The **radius** unit of the program calculates the radial component of each node by calculating the value of the radial component midway between each of the previous radial components and the present radial components. This is done in an effort to produce more accurate approximations to the calculated electromagnetic field.

The **angle** unit is used to calculate the angular component of each of the nodal potentials. In the same way as for the radial components, the angular component of the present node is found along with the angular components of the previous and following nodes. The absolute value of the difference between the present node and the previous node is calculated, as is the absolute value of the difference between the following value and the present value.

The **average** unit undertakes several averaging procedures of the calculated nodal potential at various places throughout the structure. There are a number of different procedures and many of them are programmed to occur near the retinal membrane structure.

The **voltage** unit again effectively averages values from nodes surrounding a particular region to enable an estimate of the potential at a particular node to be more accurately made. The potential at some nodes is calculated using mainly radial co-ordinates while for others it is calculated using mainly theta co-ordinates depending where they happen to be positioned in the nodal structure.

The **math** unit contains a number of preprogrammed functions and procedures to allow the program to compute the required algorithms using complex numbers.

Finally the **display** unit was constructed to enable the user to 'view' the nature of the electromagnetic field distribution within the eye. This unit was programmed to update repeatedly as the program is successively iterating. For this two-dimensional model the **display** unit produced a picture of a 'segment' of the eye constructed of coloured dots at each nodal position. The colour of the dots was modified with each iteration to simulate regions of high and low potential within the structure. A graph is also displayed which plots both the circumference and axial nodal potentials.

2.5 Summary and Conclusions

The advent of multifocal electroretinography has brought with it a desire to discover more accurately the processes taking place over small areas of the retina. Development of these findings will highlight how these processes affect the electromagnetic field within the eye ultimately influencing the potential measured on the anterior surface using an electrode. This current work will show how the electromagnetic distribution throughout the eye, in three-dimensions, may be calculated. Particular emphasis is placed on corneal potential distribution changes that may be predicted to occur as a consequence of a variety of stimulus conditions or simulated diseased states.

Chapter 3

Three Dimensional Modelling

3.0 Introduction

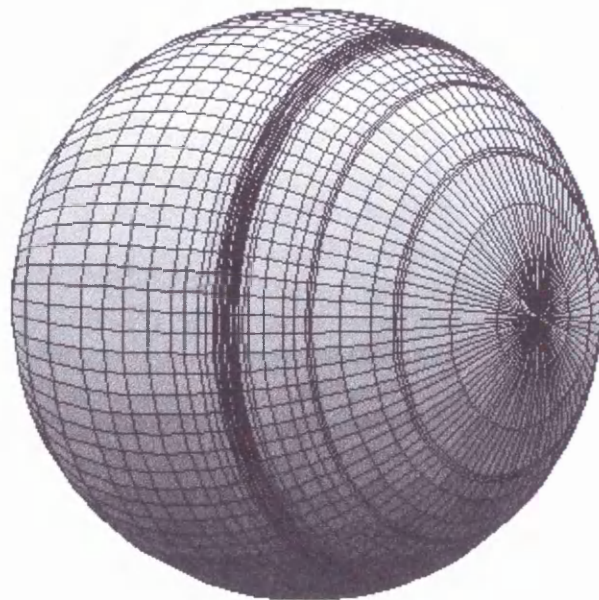
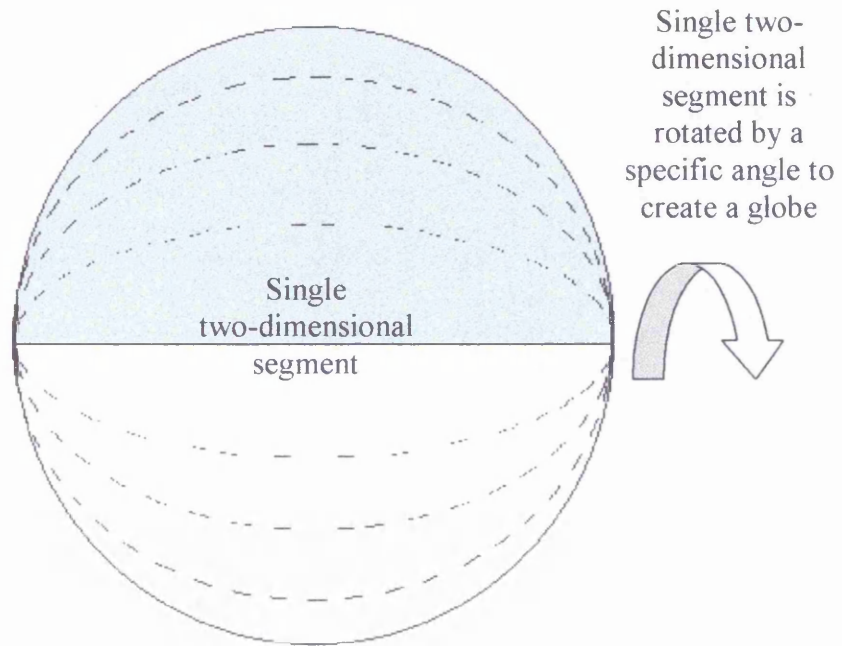
To date the three-dimensional spatial characteristics of the electromagnetic potential distributions produced by the human retina have been largely unexplored. There are very few references to the mechanism by which the electromagnetic field is induced throughout the globe. This work describes how the two-dimensional mathematical model may be further developed to encompass the third dimension. This development will, it is hoped, enable a more accurate representation of the corneal potential distribution to be calculated. The provision of topographical information may also help to optimise techniques for more accurate corneal potential measurement.

In the same way as for the two-dimensional case, the model essentially consists of a retinal double layer source inside an inhomogeneous volume conductor. The resulting electromagnetic distribution within and around the volume conductor is then calculated. The retinal bioelectric source is assumed to initiate a current flow throughout the surrounding passive volume conductor. This is known to set up an electric field within the volume. Solutions of the nature of this electric field are calculated in three-dimensional at specific instants in time, the field may be said to be 'quasi-static'.

The three-dimensional model is based directly on the structure of the two-dimensional model (Doslak 1978). This is achieved by reproducing the two-dimensional 'slice' a number of times rotating each subsequent slice by a specified angle. Repeating this procedure results in the construction of a three-dimensional symmetrical globe (Figure 3.1).

Figure 3.1

Three dimensional construction of model showing how two dimensional model is reproduced to make the three dimensional globe



As previously, the outer boundary of the eye was given a value of unity and used as a reference to which all other linear dimensions were normalised. The characteristics of each region of the model were identical to the regions for the two-dimensional case. This included the region outside the eye that was considered to be a thick, homogeneous layer of fat and bone beyond which the electrical potential was found to diminish rapidly. Conductivity values for all regions of the model identical to those used in the two-dimensional case and in the same way were considered dimensionless, as the magnitude of the electric field was arbitrary.

3.1 Theory

As the three-dimensional model is essentially constructed from the two-dimensional model, each of the unequally spaced nodes has a unique, individual conductivity. This is dependent on their position within the structure. The theoretical retina was modelled as an axially symmetric double layer of nodes. Initially these nodes were set to have spatially constant source strength. This value of strength represents the magnitude of the time varying source of potential at a particular instant in time. The solution for the potential at each of the nodes within the three-dimensional model was found by developing the finite difference equation used in the two-dimensional model. Essentially Laplace's equation was considered in three dimensions. Appendix F shows this mathematical progression in detail.

Summarising this technique we begin with Laplace's equation in three dimensions (Equation 3.1)

$$\sum_{\alpha=1}^8 \sigma_{\alpha} \left[\iint \frac{\partial U_{\alpha}}{\partial r} (r^2 \sin \theta) d\theta d\phi + \iint \frac{1}{r} \frac{\partial U_{\alpha}}{\partial \theta} (r \sin \theta) dr d\phi + \iint \frac{1}{r \sin \theta} \frac{\partial U_{\alpha}}{\partial \phi} r dr d\theta \right] = 0$$

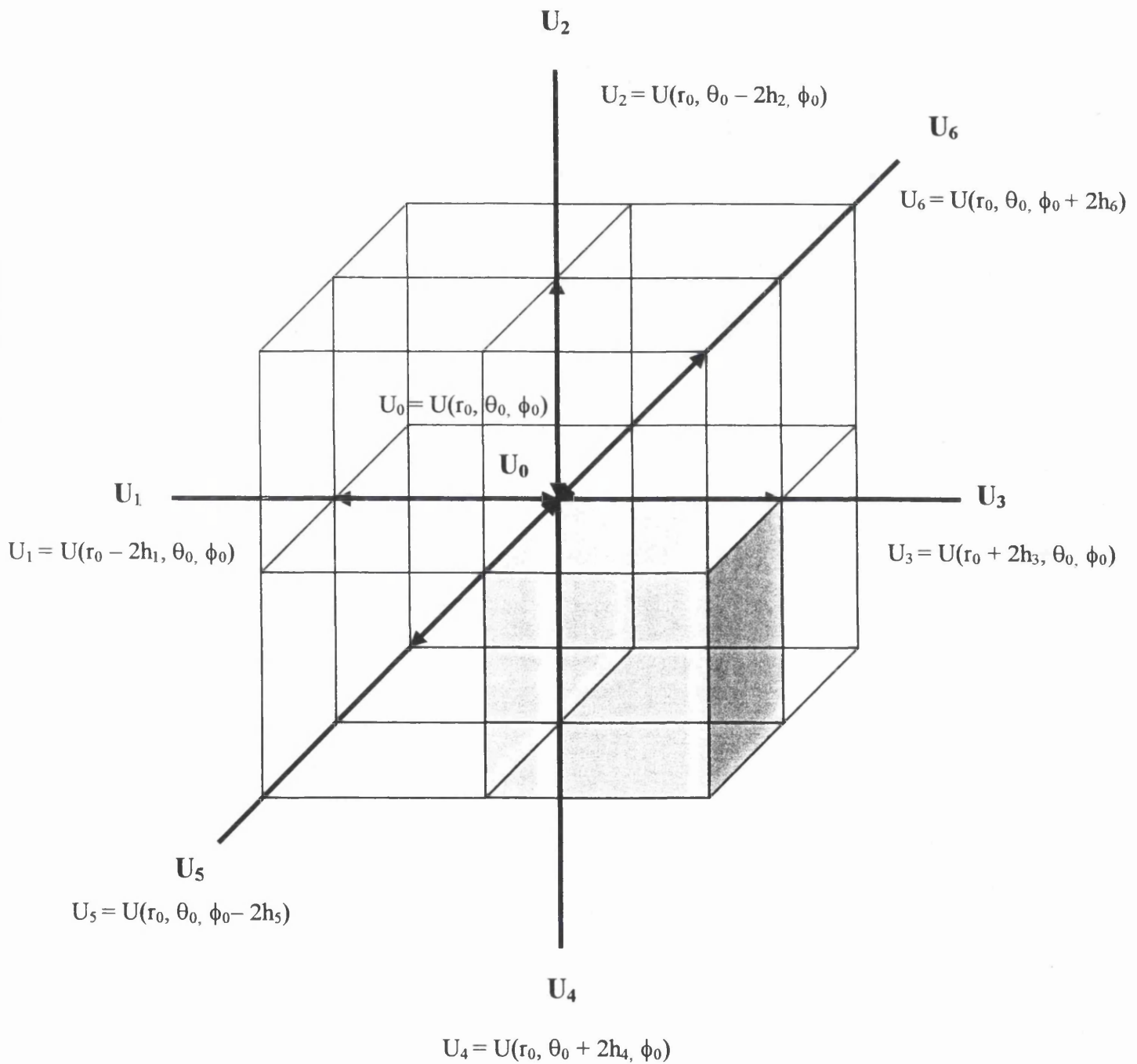
Equation 3.1

where U is the calculated potential at a specific point or 'node' within the model structure. This calculated potential is dependent on the potentials at the six nearest nodes and hence the conductivities of the eight surrounding regions. Figure 3.2 shows this in

more detail. In the two-dimensional model only four nearest nodes and hence, four conductivity regions were considered. In order to evaluate the first term the double integral is separated and integrated with respect to θ and ϕ respectively. The derivatives of the potential from the first term are considered at a constant radius. The integration process in each case effectively evaluates the magnitude of the potential over the surface of each of the nearest surrounding 'cubes', (Figure 3.2).

Figure 3.2

Nearest neighbour cubes over which the integral is evaluated



Having evaluated the first term of Equation 3.1, the other two terms are evaluated in a similar manner. For term two the potential is considered at a constant angle θ and for term three at a constant angle ϕ (see Appendix F for the full mathematical progression).

The final three-dimensional solution is then applied in succession at each of the three dimensional nodes within the 'passive' region of the volume conductor. The procedure begins at the origin and progresses sequentially to calculate all the nodes from 0° to 180° . The radius is then incremented and the procedure repeated in the next and subsequent 'layers' of nodes throughout the entire volume structure. In the same way as for the two-dimensional case, the final solution is again a system of linear equations, though there are many more in this three-dimensional case. The double layer nodes of the retina in the three-dimensional case are handled in an identical manner to the two dimensional case

A single traversal of each calculation for the entire set of nodes constitutes one 'iteration'. In order to achieve convergence of the potential at each node as rapidly as possible a Successive Over-relaxation (SOR) method was used. This incorporated the algorithms described and an over-relaxation factor ω that determined the rate of convergence. Repeated iterations ensured that convergence of each nodal potential was reached. Each iteration allows a new potential to be calculated at each node due to an extrapolation based on the estimated rate of convergence. As the appropriate algorithm is applied to each node in turn its potential is updated. The numerical value of the over relaxation factor, ω could have theoretically been anywhere between 1 and 2 although when $\omega \geq 2$ the solution was found not to converge. As the potential at a particular node is calculated using the potentials of the six nearest nodes it was found that an increased number of iterations were required to achieve convergence of the model. The source code for the three dimensional numerical model may be examined in Appendix G.

3.2 Validation of the model

Validation of the three-dimensional model was necessary with previous models to enable continued accurate predictions of the ocular electromagnetic field. This was achieved by comparing nodal calculations of potentials from the two-dimensional model (Doslak 1978) node by node to that of the three-dimensional model.

Previous studies (Doslak 1978) have shown extensive searches of the literature regarding the conductivity value for each of the model regions. Due to the small variation of recorded values, the actual values used spanned a small range. This range was determined from direct experimental recordings between 1906 and 1973 from human, (Schwan *et al* 1957), (Geddes *et al* 1967), bovine (Botazzi *et al* 1906), (Oskala *et al* 1959), (Pauly *et al* 1964), rabbit (Fischbarg 1973), frog (Brindley *et al* 1963), and dog (Rush *et al* 1963).

3.2.1 Comparisons with the Two Dimensional Model

Conductivity values used for the conductivity values are dimensionless, as the magnitude of the calculated field in the three-dimensional model is arbitrary. The conductivity value of each region was set to equal that previously used to ensure accurate comparisons between the two and three-dimensional models and the analytical model (Doslak 1978). Table 3.1 shows the conductivity values used. A comparison with previously published simpler models and independent microelectrode studies (Doslak 1978) was then undertaken. These experiments essentially simulated axially symmetrical uniform retinal stimulation in a spherical structure divided into three concentric volumes.

Method

In order to perform a node for node comparison between each of the models, the conductivity values of specific regions of the numerical models were made equal to similar regions of the analytical model. The lens was set to have the conductivity of the aqueous and vitreous regions. The sclera was set to have the conductivity of the cornea and air at the anterior surface of the eye was set to have the conductivity of fat and bone encasing the posterior surface of the eye. This effectively meant that for both the two and three-dimensional numerical models $\sigma_1 = \sigma_4$, $\sigma_2 = \sigma_5$ and $\sigma_3 = \sigma_6$. While it is accepted that this generalisation further simplifies a complex anatomical and physiological structure it does provide a means by which the accuracy both the two and three-dimensional numerical models may be to some degree quantified.

Table 3.1**Table of ranges of values used for each of the regions of the model**

(adapted from Doslak MJ (1978) 'The Effects of Variations of the Conducting Media Inhomogeneities on the Electroretinogram' PhD Dissertation, Case Western Reserve University.)

Region Name	Mathematical Descriptor	Values from Literature	Relative Conductivities	Values used in Model
Aqueous & Vitreous	σ_1	57 Ωcm	1×10^{-2} mho/cm	1
Sclera	σ_2	417-5265 Ωcm	$0.137-0.0109 \times 10^{-2}$ mho/cm	0.15-0.01
Fat, Muscle and Bone	σ_3	1500-5000 Ωcm	$0.0571-0.00571 \times 10^{-2}$ mho/cm	0.06-0.005
		150-2500 Ωcm		
		1800-16000 Ωcm		
Lens	σ_4	200-700 Ωcm	$0.286-0.0817 \times 10^{-2}$ mho/cm	0.3-0.08
Cornea	σ_5	67-1500 Ωcm	$0.853-0.0381 \times 10^{-2}$ mho/cm	0.86-0.03
Retinal Membrane Resistivity	RR or RMN	100-350 Ωcm^2	$0.571-0.163 \times 10^{-2}$ mho/cm ²	1.67-6.25
Retinal Membrane Capacitance	RC	50-100 $\mu\text{f} / \text{cm}^2$	$0.0179\text{f}-0.0359\text{f} \times 10^{-2}$ mho/cm ²	58.8/f-27.8/f

f = frequency (Hz)

Due to the range of conductivity values found in the literature, calculations were performed at both low and high conductivity values of each region. Table 3.2 shows these values for each 'conductivity set'.

Table 3.2
Conductivity Sets and their Values

Conductivity Set	Len / Aqueous / Vitreous $\sigma_1 = \sigma_4$	Sclera / Cornea $\sigma_2 = \sigma_5$	Air / Fat / Bone $\sigma_3 = \sigma_6$
A	1	0.01	0.005
B	1	0.01	0.06
C	1	0.15	0.06
D	1	0.15	0.005
E	1	0.01	1
F	1	0.15	1

In all the calculated solutions in this section the over relaxation value of the model was set to 1.80 and up to 15,000 iterations were performed to reach convergence. On completion, graphs were plotted of the calculated potentials along the central axis and around the circumference of each of the models in turn.

Results

Figures 3.3 to 3.8 show the two and three-dimensional numerical model axial potentials compared with calculated analytical values. Figures 3.9 to 3.14 show the two and three-dimensional model potentials plotted around the circumference of the model compared with calculated analytical values. The figures produced show good agreement of the three-dimensional numerical model with both the two-dimensional numerical and analytical models.

Figure 3.3

Graph showing axial plot of data from two and three-dimensional numerical data plotted against two-dimensional analytical data for Conductivity Set A.

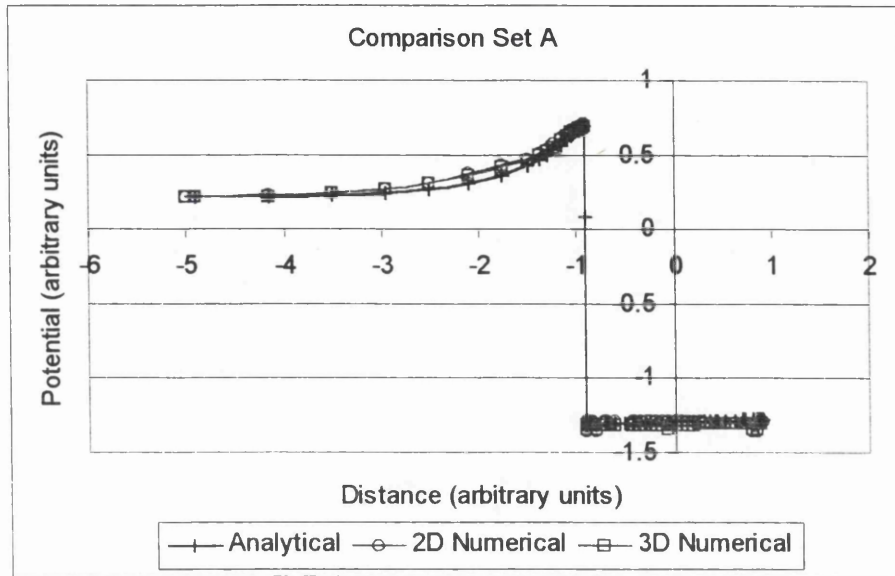


Figure 3.4

Graph showing axial plot of data from two and three-dimensional numerical data plotted against two-dimensional analytical data for Conductivity Set B.

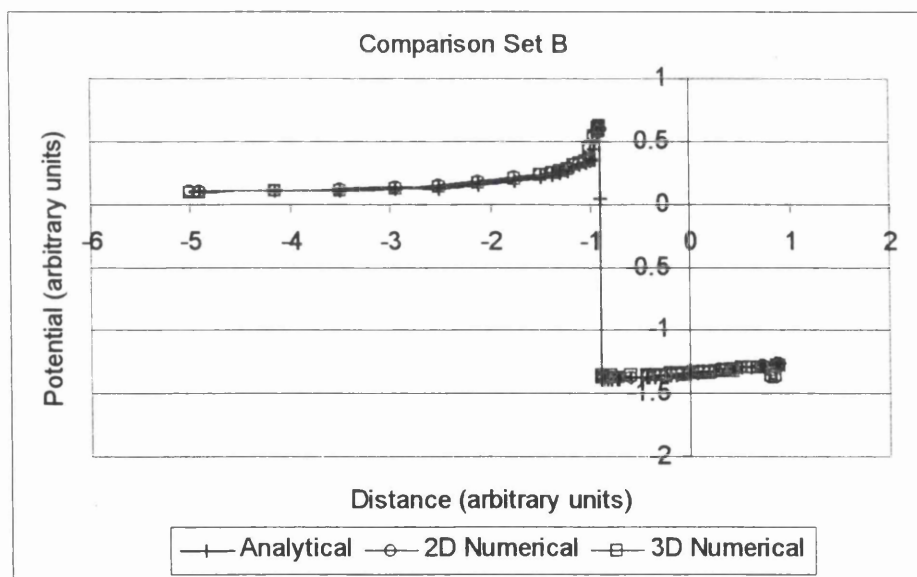


Figure 3.5

Graph showing axial plot of data from two and three-dimensional numerical data plotted against two-dimensional analytical data for Conductivity Set C.

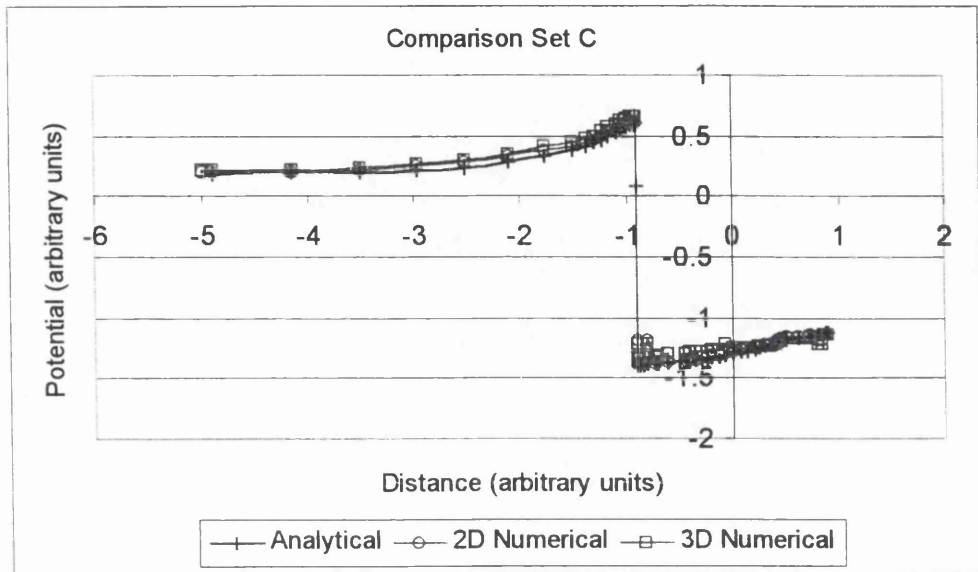


Figure 3.6

Graph showing axial plot of data from two and three-dimensional numerical data plotted against two-dimensional analytical data for Conductivity Set D.

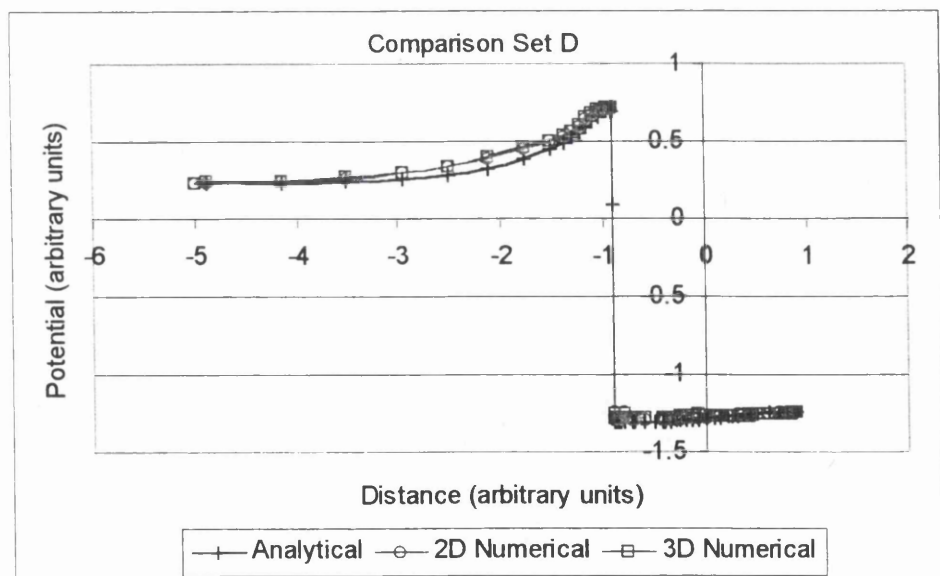


Figure 3.7

Graph showing axial plot of data from two and three-dimensional numerical data plotted against two-dimensional analytical data for Conductivity Set E.

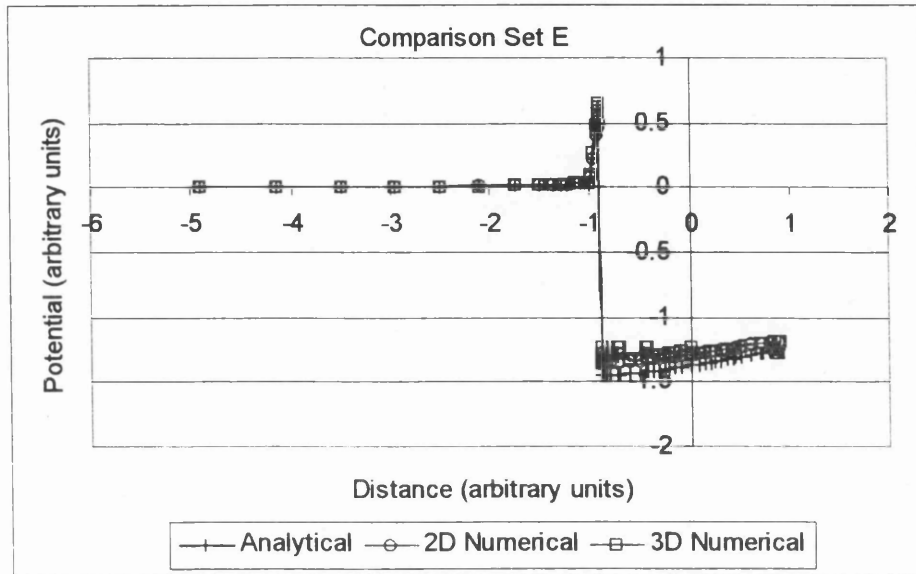


Figure 3.8

Graph showing axial plot of data from two and three-dimensional numerical data plotted against two-dimensional analytical data for Conductivity Set F.

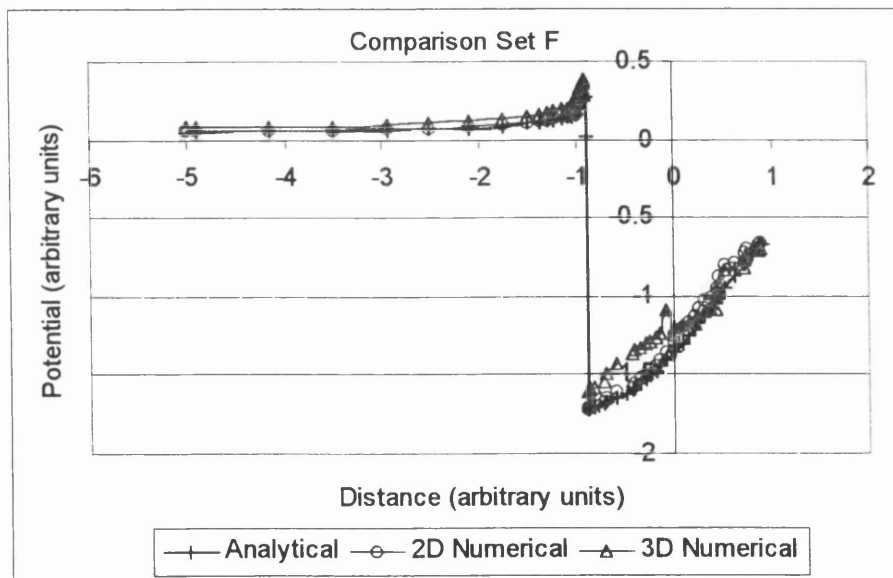


Figure 3.9

Graph showing circumference plot of data from two and three-dimensional numerical data against two-dimensional analytical data for Conductivity Set A.

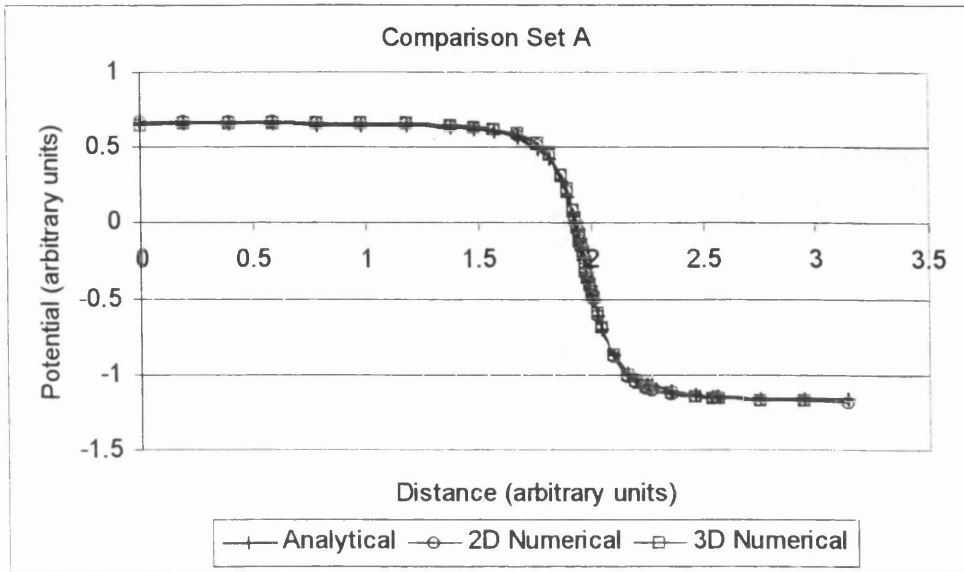


Figure 3.10

Graph showing circumference plot of data from two and three-dimensional numerical data against two-dimensional analytical data for Conductivity Set B.

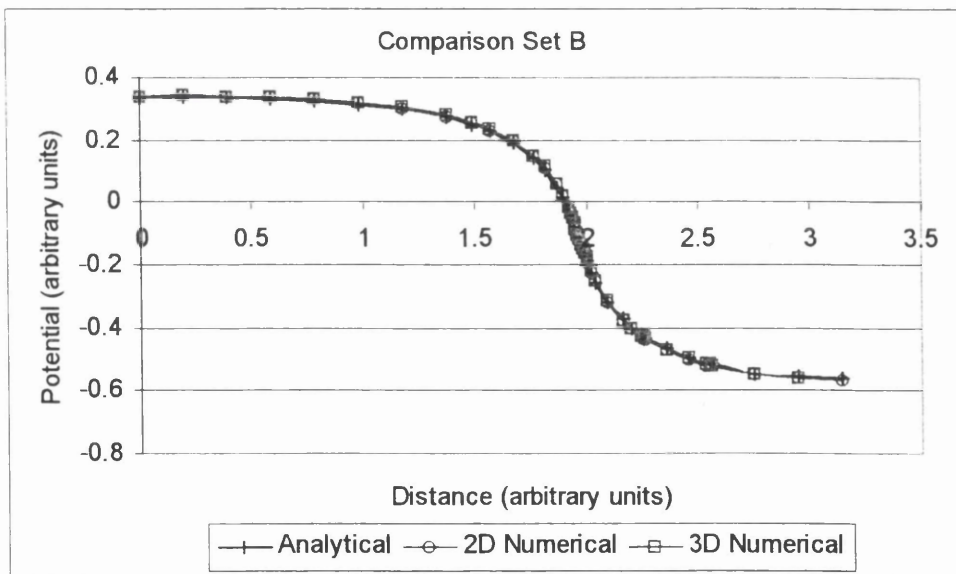


Figure 3.11

Graph showing circumference plot of data from two and three-dimensional numerical data against two-dimensional analytical data for Conductivity Set C.

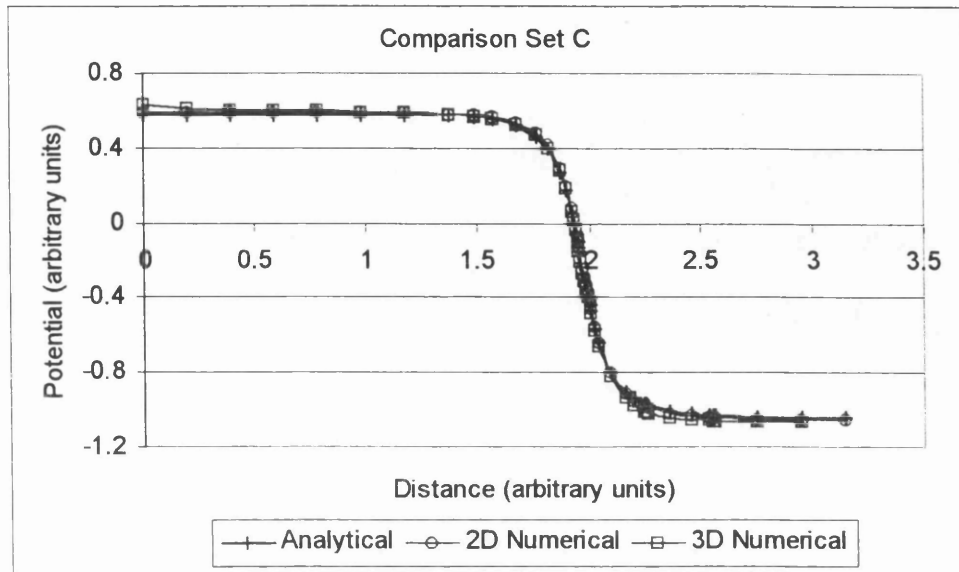


Figure 3.12

Graph showing circumference plot of data from two and three-dimensional numerical data against two-dimensional analytical data for Conductivity Set D.

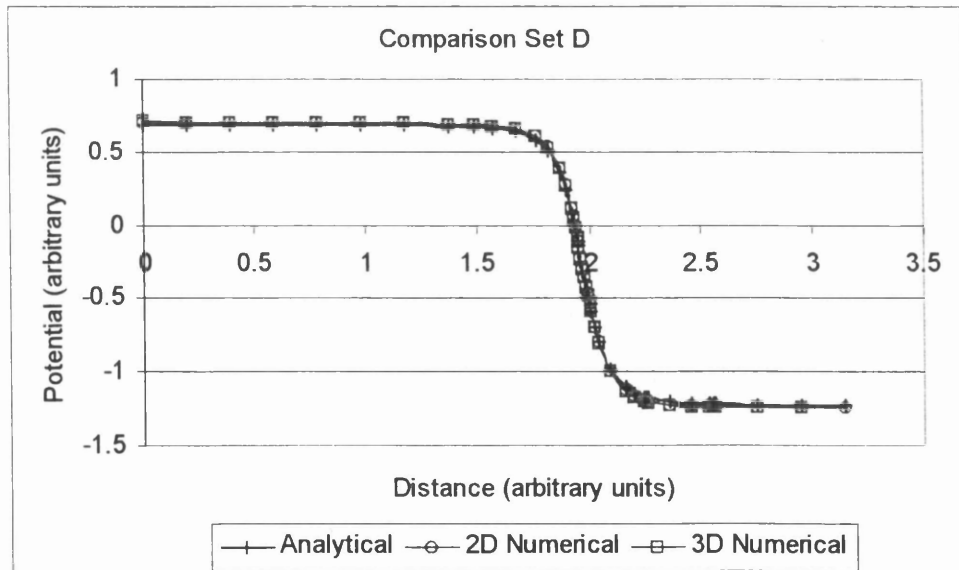


Figure 3.13

Graph showing circumference plot of data from two and three-dimensional numerical data against two-dimensional analytical data for Conductivity Set E.

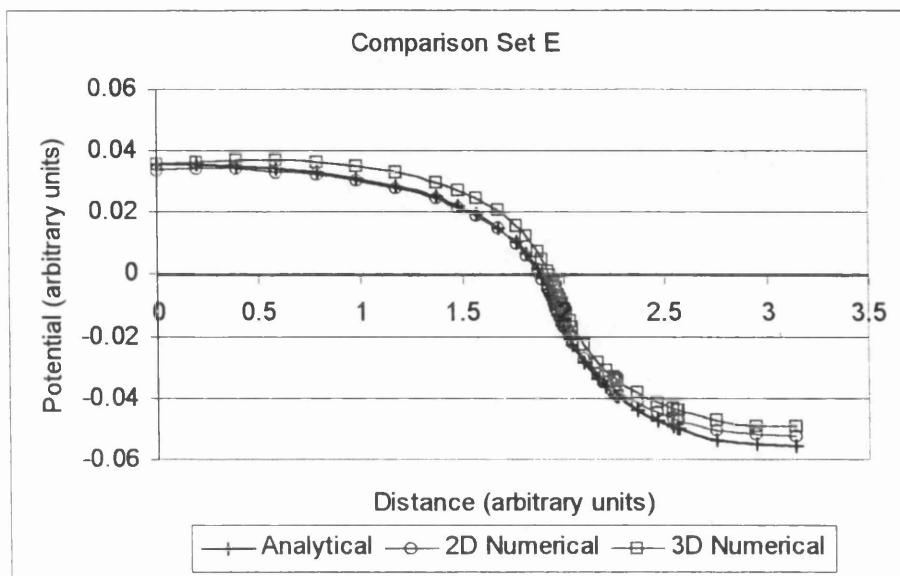


Figure 3.14

Graph showing circumference plot of data from two and three-dimensional numerical data against two-dimensional analytical data for Conductivity Set F.

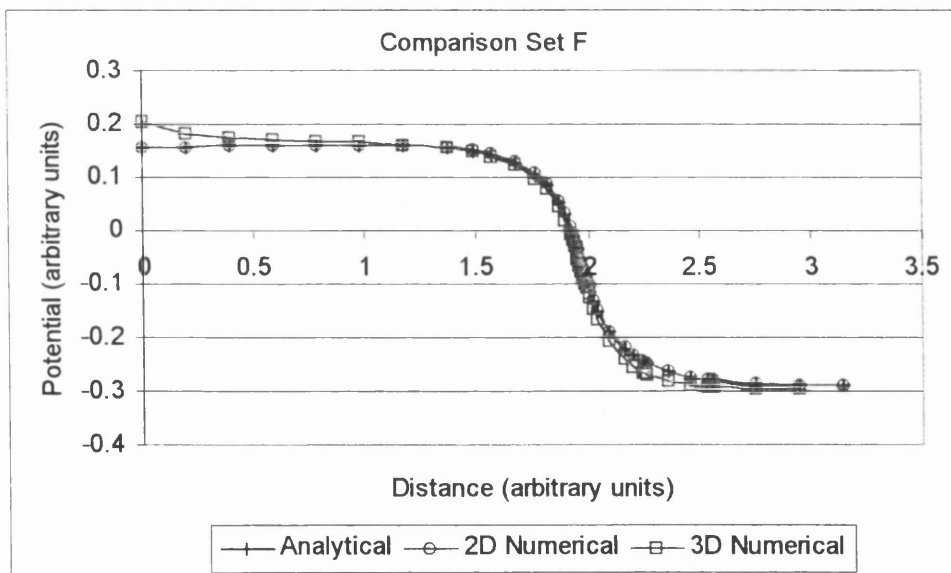


Table 3.3 shows the results of these comparisons represented as a percentage deviation in the two and three-dimensional numerical axial potential values from the calculated analytical axial potential values.

Table 3.3

The percentage deviation in two and three-dimensional numerical axial data from calculated analytical axial potential values.

Conductivity Conditions	2D Model %		3D Model %	
	Deviations		Deviations	
Conductivity Set A	Max.	0.9	Max.	2.1
	Min.	-2.4	Min.	-3.1
	Ave.	-0.5	Ave.	-0.2
Conductivity Set B	Max.	0.9	Max.	4.2
	Min.	-1.9	Min.	-1.8
	Ave.	-0.2	Ave.	0.6
Conductivity Set C	Max.	1.7	Max.	6.6
	Min.	-1.8	Min.	-10.6
	Ave.	0.1	Ave.	-1.6
Conductivity Set D	Max.	0.7	Max.	2.3
	Min.	-2.0	Min.	-4.0
	Ave.	0.3	Ave.	-0.6
Conductivity Set E	Max.	12.3	Max.	44.4
	Min.	2.7	Min.	-6.8
	Ave.	5.4	Ave.	3.5
Conductivity Set F	Max.	8.9	Max.	31.3
	Min.	-0.6	Min.	-22.7
	Ave.	2.0	Ave.	0.8

This table indicates that the average deviation of calculated two-dimensional axial potentials from analytical values is found to be approximately 1.0 %. The average deviation of calculated three-dimensional axial potentials from analytical values is found to be only 0.4 %.

A similar comparative analysis of these models may be made using the calculated potentials around the circumference of the eye. Table 3.4 shows the percentage deviation in the two and three-dimensional numerical circumference potentials from calculated analytical circumference potentials.

Table 3.4
The percentage deviation in two and three-dimensional numerical circumference data from calculated analytical circumference potential values.

Conductivity Conditions	2D Model %		3D Model %	
	Deviations		Deviations	
Conductivity Set A	Max.	-1.4	Max.	1.1
	Min.	-5.1	Min.	-6.1
	Ave.	-2.2	Ave.	-1.7
Conductivity Set B	Max.	0.4	Max.	0.8
	Min.	-4.8	Min.	-6.9
	Ave.	-1.5	Ave.	-1.4
Conductivity Set C	Max.	-0.8	Max.	-0.8
	Min.	-4.1	Min.	-7.7
	Ave.	-1.5	Ave.	-2.9
Conductivity Set D	Max.	-0.9	Max.	-1.3
	Min.	-4.3	Min.	-3.8
	Ave.	-1.7	Ave.	-2.1
Conductivity Set E	Max.	6.5	Max.	19.7
	Min.	2.3	Min.	-35.3
	Ave.	4.0	Ave.	0.7
Conductivity Set F	Max.	2.1	Max.	5.7
	Min.	-4.2	Min.	-9.1
	Ave.	-0.1	Ave.	-3.4

Here the average deviation in two-dimensional circumference potentials from calculated analytical potentials was found to be approximately -0.4% . The average deviation in three-dimensional circumference potentials from calculated analytical potentials was found to be greater at -1.5% . These data show a high degree of accuracy between

analytical and both two and three-dimensional numerical models following analysis of both axial and circumference potentials.

Conclusions

A three-dimensional numerical model has been developed from existing two-dimensional and analytical models (Doslak 1978). This model has been found to be accurate for specific, simplified inhomogeneity configurations. The average deviation of the two-dimensional model potentials from analytical values was found to be approximately 0.3%. The average deviation of the three-dimensional model potentials from analytical values was found to be -0.55%. It may be concluded therefore that a three dimensional model of this kind may be used, with care, to theoretically predict a resulting potential distribution within and around the eye following global stimulation.

3.2.2 Convergence of the Three Dimensional Model

Accurate convergence of the calculated potentials at each of the nodes within the three dimensional numerical model was required before the solution may be subsequently considered in any analysis. Convergence of these potentials model was largely governed by the relaxation factor (ω) used in the calculations. The calculated potentials were assumed to have converged when the ratio of the change in potential over the original potential was found to be less than 10^{-8} . In order to optimise the convergence criteria of the model, experiments to determine the rate of convergence were performed. This was repeated for each of the conductivity sets examined in '3.2.1 Comparisons with the Two Dimensional Model'.

Method

Experiments were undertaken using the three-dimensional numerical model to examine how quickly the solution converged for each set of parameter values. Using identical 'sets' of conductivity values as in the previous experiments (i.e. A, B, C, D, E and F), plots of axial and circumference potentials were produced. These graphs highlighted how quickly the calculated potentials from the three-dimensional converged to the analytical model values. Calculations were also performed to quantify the percentage deviation from analytical potential values for each of the conductivity sets examined.

Results

Figures 3.15 to 3.20 show how calculated axial potentials of the three dimensional model were found to converge to analytical axial potential values. These graphs show results following 2000, 5000, 10000 and 15000 iterations. Figures 3.21 to 3.26 show similar circumference convergence plots of calculated three-dimensional potential values.

Figure 3.15

Graph showing convergence of axial potentials to analytical solution for an increasing number of iterations with Conductivity Set A.

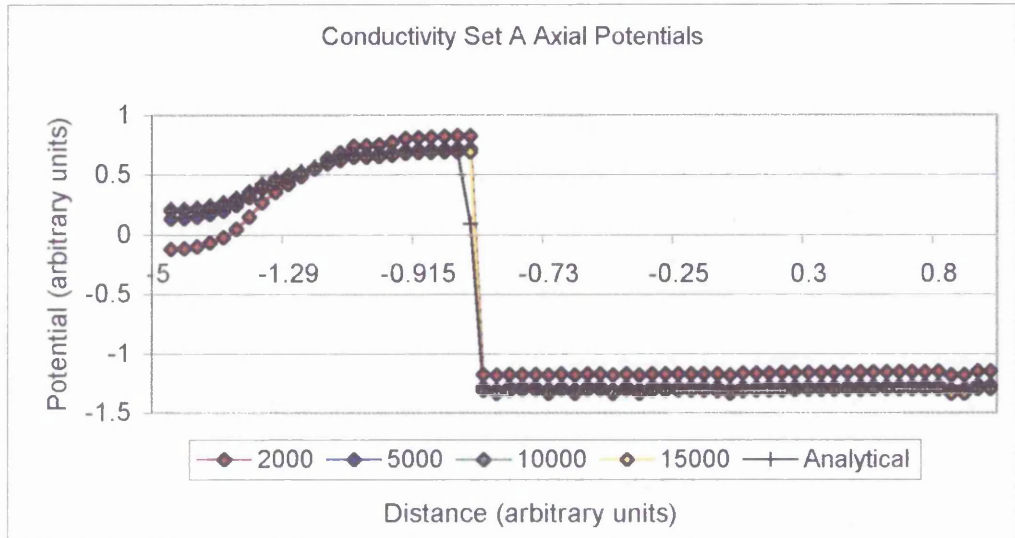


Figure 3.16

Graph showing convergence of axial potentials to analytical solution for an increasing number of iterations with Conductivity Set B

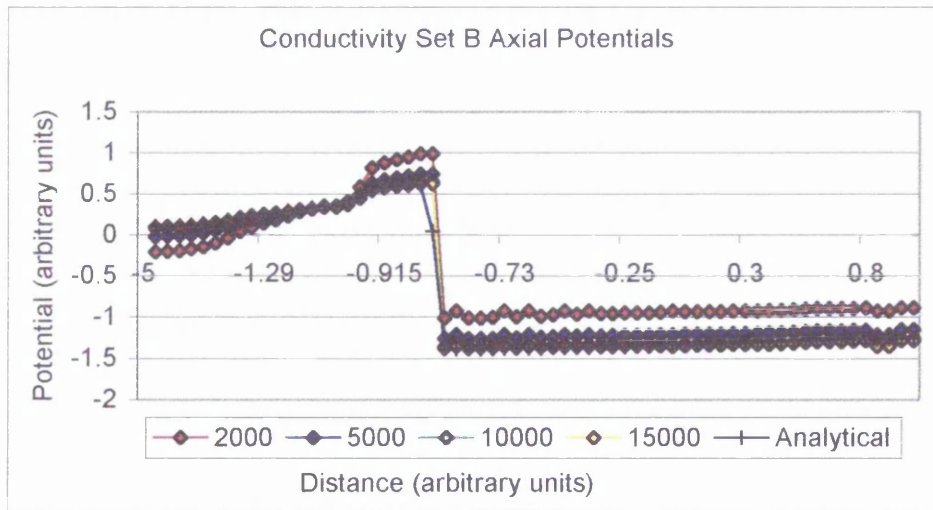


Figure 3.17

Graph showing convergence of axial potentials to analytical solution for an increasing number of iterations with Conductivity Set C

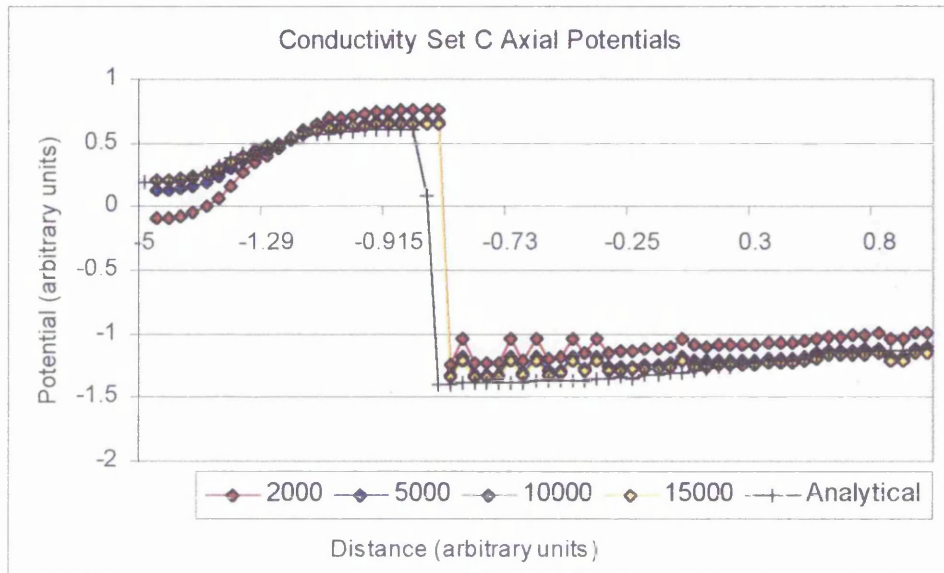


Figure 3.18

Graph showing convergence of axial potentials to analytical solution for an increasing number of iterations with Conductivity Set D

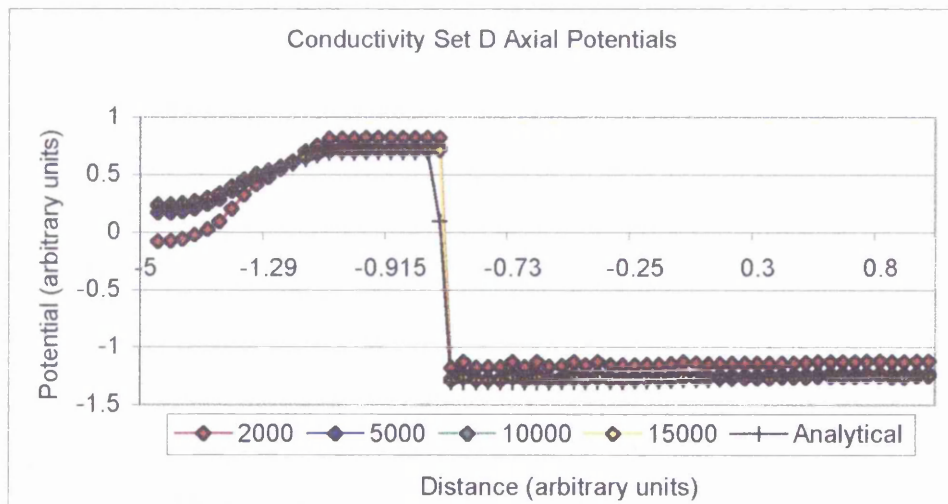


Figure 3.19

Graph showing convergence of axial potentials to analytical solution for an increasing number of iterations with Conductivity Set E

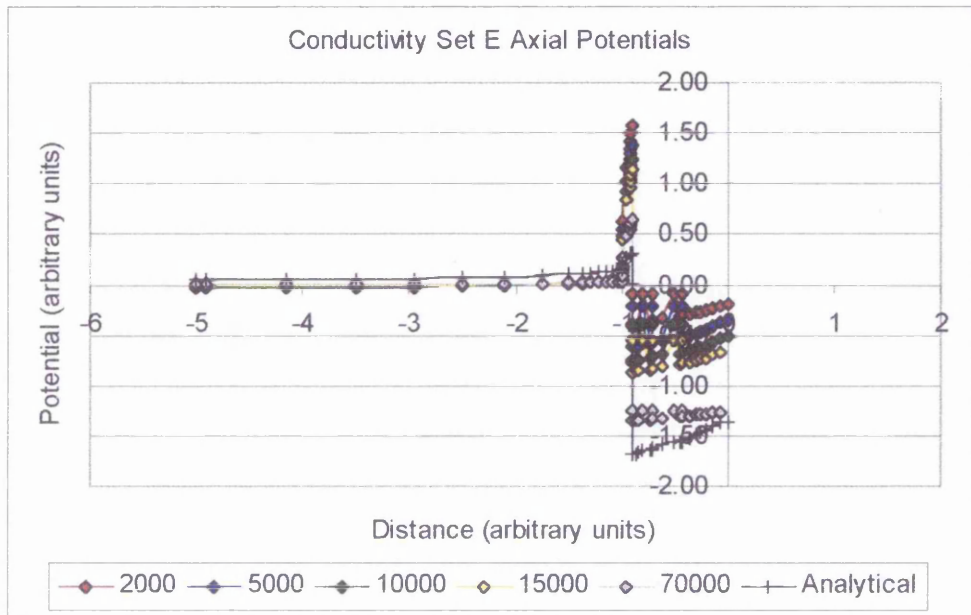


Figure 3.20

Graph showing convergence of axial potentials to analytical solution for an increasing number of iterations with Conductivity Set F

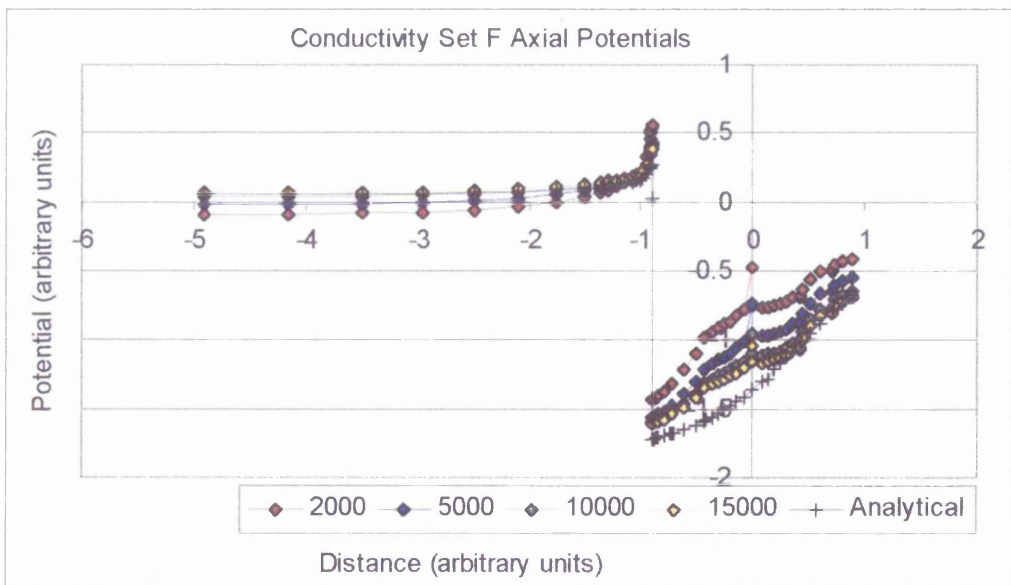


Figure 3.21

Graph showing convergence of circumference potentials to analytical solution for an increasing number of iterations with Conductivity Set A

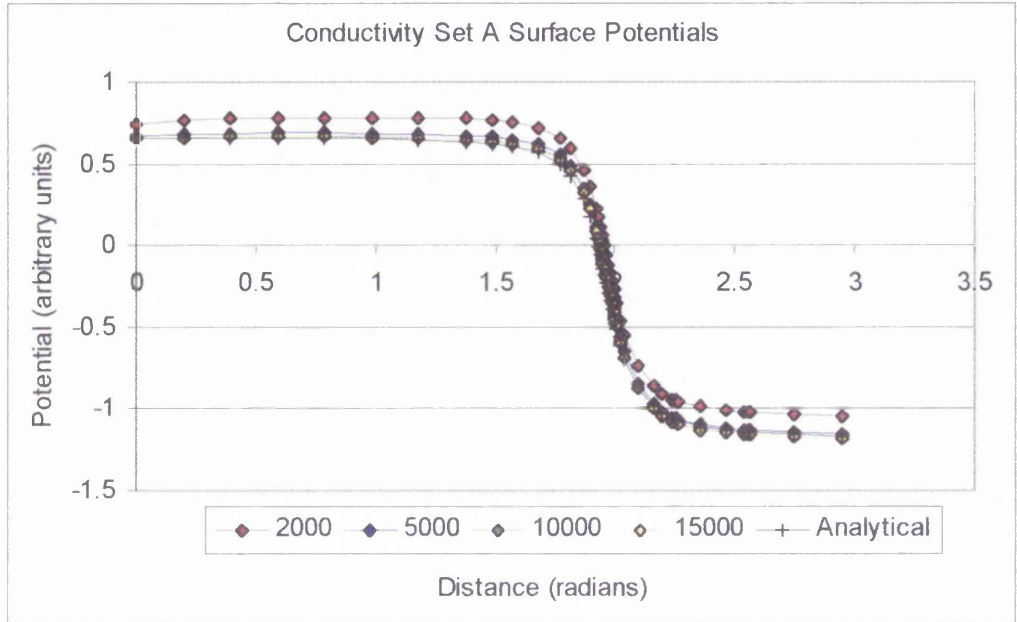


Figure 3.22

Graph showing convergence of circumference potentials to analytical solution for an increasing number of iterations with Conductivity Set B

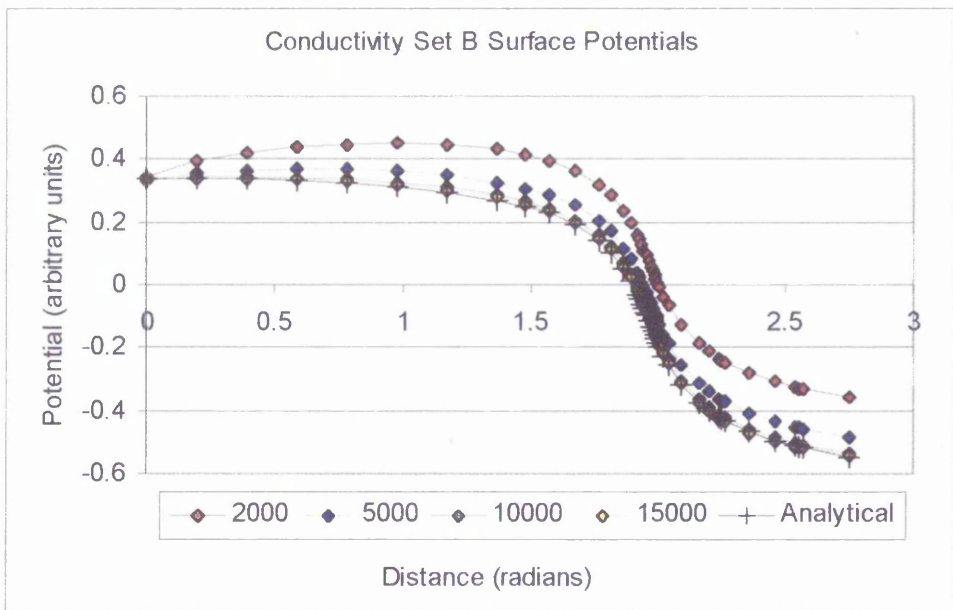


Figure 3.23

Graph showing convergence of circumference potentials to analytical solution for an increasing number of iterations with Conductivity Set C

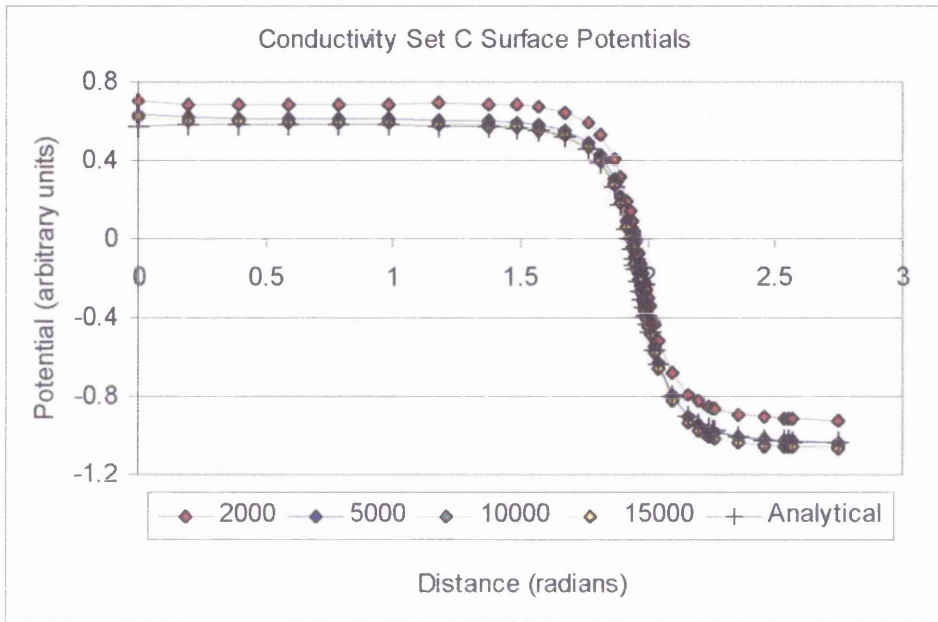


Figure 3.24

Graph showing convergence of circumference potentials to analytical solution for an increasing number of iterations with Conductivity Set D

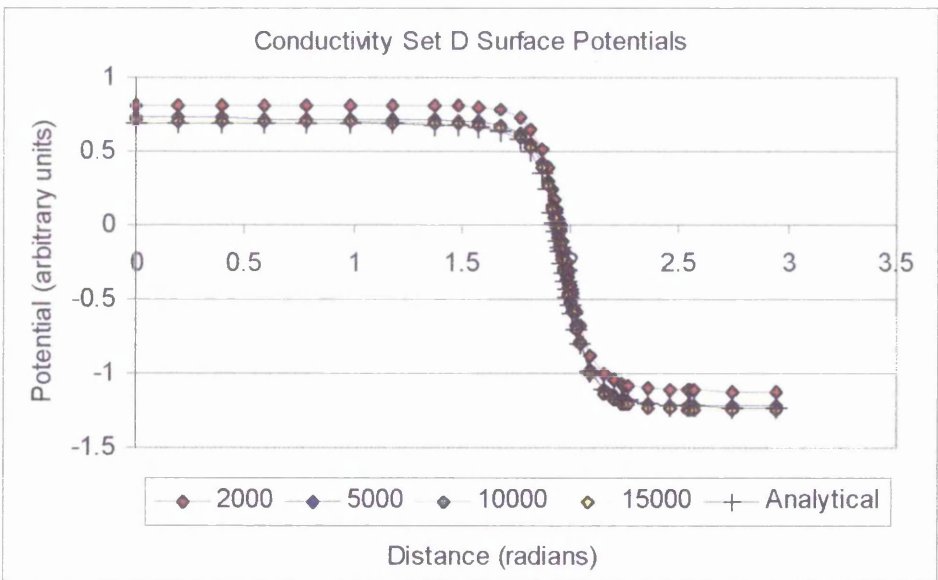


Figure 3.25

Graph showing convergence of circumference potentials to analytical solution for an increasing number of iterations with Conductivity Set E

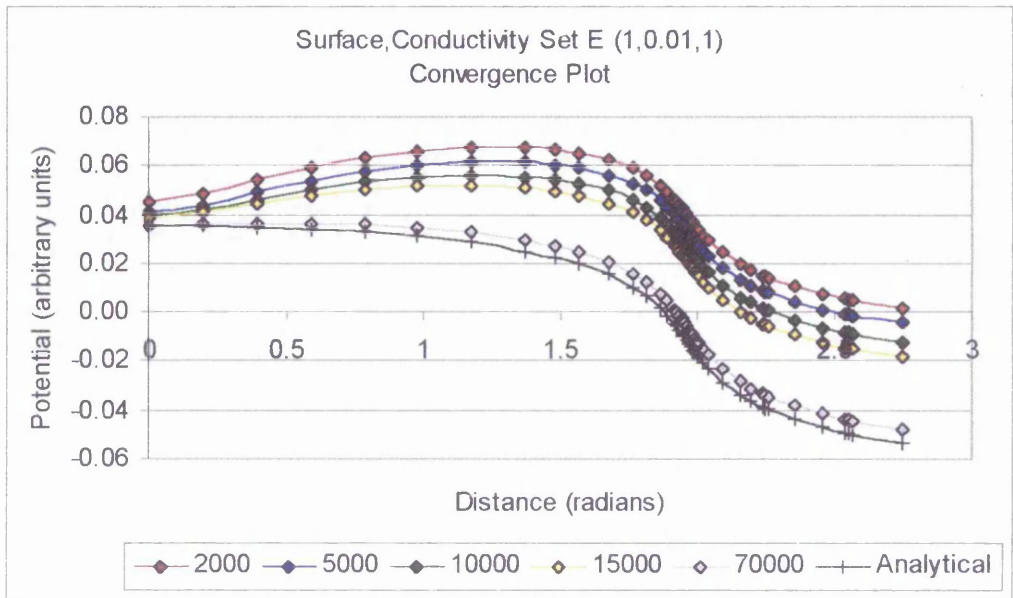
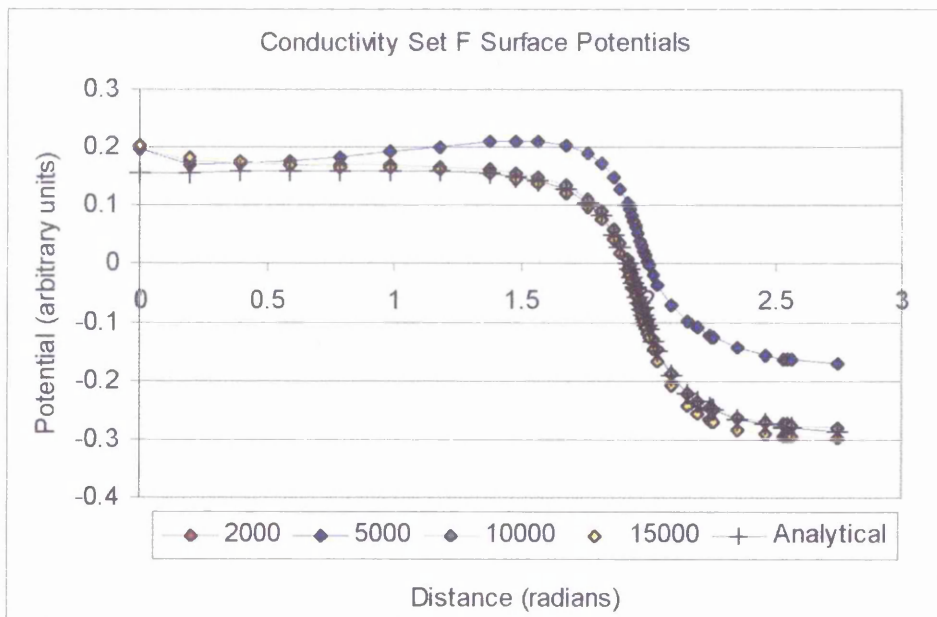


Figure 3.26

Graph showing convergence of circumference potentials to analytical solution for an increasing number of iterations with Conductivity Set F



The figures show how the calculated three-dimensional model potentials converge to the two-dimensional analytical potential values. Although the potentials calculated when conductivity sets A, B, C, D, and F converge reasonably well to the analytical values, it was found that for conductivity set E up to 70,000 iterations were needed before any convergence to the analytical model was found to be significant.

The differences in convergence 'rate' may, to some extent be quantified. Table 3.5 shows the how different the calculated three-dimensional potential values are to the analytical values at each of the iteration numbers studied (2000, 5000, 10000 and 15000). This table shows that when conductivity values from say set B were used, the solution converged to be most like the analytical potential values in the smallest number of iterations. On the other hand, using the conductivity values from say set E, a solution is produced that was least like the analytical potential values. Convergence of the model with these parameters was not significant until more than 70000 iterations had been performed (see Figure 3.19).

Table 3.5

Table showing convergence of the three dimensional model potentials to the analytical model potentials.

Conductivity Set		2,000		5,000		10,000		15,000	
		Iterations		Iterations		Iterations		Iterations	
		Axial	Surface	Axial	Surface	Axial	Surface	Axial	Surface
Set A % difference from analytical	Max.	155.4	-5.3	36.9	-2.4	4.5	0.9	2.1	1.1
	Min.	-6.2	-33.4	-0.9	-11.9	-3.1	-6.9	-3.3	-6.5
	Ave.	29.8	12.9	6.2	1.8	0.1	-1.8	-0.4	-1.7
Set B % difference from analytical	Max.	308.4	50.0	120.9	16.5	22.7	2.5	4.2	0.8
	Min.	3.9	-130.1	4.6	-47.9	-0.2	-13.8	-1.8	-7.4
	Ave.	65.5	-8.2	24.5	-3.5	4.4	-1.8	0.7	-1.5
Set C % difference from analytical	Max.	146.3	13.0	28.6	0.8	12.3	-3.0	12.0	-0.8
	Min.	-17.1	-29.4	-8.9	-10.2	-8.5	-8.4	-10.6	-8.3
	Ave.	29.0	-5.5	6.5	-3.3	-0.1	-1.2	-0.7	-2.9
Set D % difference from analytical	Max.	134.6	9.4	26.1	0.6	3.8	-1.2	3.7	-1.3
	Min.	-14.7	-25.1	-5.2	-7.9	-3.7	-4.2	-4.2	-3.9
	Ave.	24.7	-5.5	4.8	-2.7	0.0	-2.1	-0.3	-2.1
Set E % difference from analytical	Max.	8.5	-70.6	4.9	-247.9	1.5	-330.8	0.96	-340.8
	Min.	-53.93	-1563.2	-37.0	-1151.9	-23.2	-830.3	-17.1	-690.2
	Ave.	-19.54	-397.5	-11.6	-404.5	-6.5	-418.8	-4.3	-425.7
Set F % difference from analytical	Max.	271.7	56.1	137.8	56.1	29.9	3.0	23.9	5.7
	Min.	-17.8	-82.5	-12.1	-82.5	-23.6	-25.4	-29.4	-30.0
	Ave.	64.8	5.6	33.7	5.6	7.0	-3.7	-3.6	-5.8

Conclusions

The three-dimensional model has been examined to ascertain how quickly and to what extent the calculated potentials converge to the two-dimensional analytical solution previously described. It was found that convergence 'rate' and accuracy with analytical solutions was highly dependent on the conductivity values used for each of the regions examined. When the anterior air and posterior fat and bone regions were set to equal of either 0.005 or 0.6, the three-dimensional model produced calculated potentials that compared well with two-dimensional theoretical model predictions. However, in all cases the three-dimensional model is found to require a larger number of iterations to achieve the same degree of convergence. This is considered to be due to the sharp change in conductivity value between the regions. When the difference in conductivity value between regions is much less, it was found that a smaller number of iterations were needed.

On the whole the three-dimensional model was required to perform a larger number of iterations than current two-dimensional models to achieve similar potential values. This was believed to be due to the inherent nature of the calculation of three-dimensional nodal potentials. In the two-dimensional case each nodal potential is dependent only on the potential values of the four nearest neighbour nodes, while in the three-dimensional case this is increased to the six nearest neighbour nodes. This increases the variability of each nodal potential value and hence many more iterations are required before the same degree of accuracy is achieved in the converged calculations.

3.2.3 Parameter Variation

Previous experiments have over simplified the nature of the three-dimensional model in by setting distinctly different regions of the eye the same conductivity value. This was done initially to enable accurate comparisons with both two-dimensional analytical and numerical models. The three-dimensional model has been constructed in such a way that many minor modifications may be performed. In this way it is hoped that the three-dimensional model may be modified to more accurately represent the actual physiological situation. In this experiment each region of the model (lens, aqueous, vitreous, sclera, cornea, air and fat and bone) was given a different conductivity value

(i.e. no region had the same conductivity value as another region). As previously noted, Table 3.1 shows the range of possible conductivity values that may be associated with each region. Thorough analysis of the variation in conductivity parameters necessitates calculations to be performed following variation in the conductivity of each region.

Method

The three dimensional numerical model is made up of six regions. Each of these regions has an associated range of conductivity values. Calculations were performed following substitution of the smallest and largest conductivity values for each region in succession into the model. This highlighted any possible variations in the calculated electromagnetic field distribution due to conductivity value parameters. The membrane impedance was also believed to directly influence the potential field generated. Therefore it too was modified within a range of values from the literature. There were found to be 32 possible combinations of the conductivity value changes encompassing every region of the model. Table 3.6 shows the order in which these experiments were carried out and the values of the conductivity for each of the calculation combinations performed.

To examine the changes in the electromagnetic field distribution, the potential around the circumference and over the surface of the cornea, along with the potentials along the axis of the eye were examined. The difference between each of the electromagnetic field distributions was calculated and the data analysed. Regions that caused the largest and smallest changes in potential on the surface of the cornea were identified and compared with current physiological assumptions and knowledge of the human eye.

Table 3.6

Table showing the order in which conductivity values for each region were modified for the parameter variation experiments

σ_1	σ_2	σ_3	σ_4	σ_5	σ_6
1	0.15	0.06	0.3	0.86	0
1	0.01	0.06	0.3	0.86	0
1	0.01	0.06	0.3	0.03	0
1	0.01	0.06	0.08	0.03	0
1	0.15	0.005	0.08	0.03	0
1	0.01	0.005	0.3	0.03	0
1	0.01	0.005	0.08	0.86	0
1	0.15	0.06	0.08	0.03	0
1	0.15	0.005	0.3	0.03	0
1	0.15	0.005	0.08	0.86	0
1	0.15	0.06	0.3	0.03	0
1	0.15	0.005	0.3	0.86	0
1	0.01	0.005	0.08	0.03	0
1	0.15	0.06	0.08	0.86	0
1	0.01	0.005	0.3	0.86	0
1	0.01	0.06	0.08	0.86	0

Results

Three-dimensional model calculations were performed for each of the 32 possible combinations of the conductivity value changes expressed in Table 3.6. Analysis of these results was performed to enable the maximum, minimum and average change in potential to be expressed when the conductivity value of each region is varied from a low to a high value within the range specified (Table 3.1). In each case a relaxation factor of 1.80 was used in the calculations.

From this analysis, Tables 3.7 and 3.8 were produced. These show the effects of parameter variation along the axis of the model eye and on the potential field calculated over the entire surface of the eye respectively. Each value is shown as a percentage change. The largest potential percentage change over both the entire surface and along the axis of the three-dimensional model occurs due to the conductivity value change of the fat/muscle/bone region (σ_3). Next are the retinal membrane impedance (RMN) and the scleral region (σ_2). Almost no change in potential is found when the conductivity values of the lens or corneal regions (σ_4 and σ_5) are varied from high to low values.

Table 3.7

Table showing changes in potential along the axis of the eye

Parameter Varied	Changes in Potential		
	Minimum	Maximum	Mean
σ_2 (15 to 1)	0.0	75.0	17.9
σ_3 (12 to 1)	0.0	75.0	26.0
σ_4 (4 to 1)	0.0	1.4	0.0
σ_5 (30 to 1)	0.0	1.5	0.0
RMN(Low and High)	0.0	38.2	11.0

Table 3.8

Table showing changes in potential over the whole surface of the eye

Parameter Varied	Changes in Potential %		
	Minimum	Maximum	Mean
σ_2 (15 to 1)	0.4	46.6	25.2
σ_3 (12 to 1)	1.7	65.5	31.8
σ_4 (4 to 1)	0.0	0.3	0.0
σ_5 (30 to 1)	0.0	0.4	0.0
RMN (Low and High)	0.7	28.2	14.3

To compare these data with previously published work (Doslak 1978) the percentage changes in potential were calculated only over the surface of the cornea. Table 3.9 shows the results of this analysis. Previously published figures are shown in brackets in the table.

Table 3.9

Table showing changes in potential over the surface of the cornea

Parameter Varied	Changes in Potential		
	Minimum	Maximum	Mean
σ_2 (15 to 1)	(9.6) 7.8	(26.0) 24.1	(16.5) 16.0
σ_3 (12 to 1)	(8.0) 21.1	(17.1) 37.6	(11.2) 29.4
σ_4 (4 to 1)	(0.0) 0.0	(0.5) 0.6	(0.2) 0.2
σ_5 (30 to 1)	(0.0) 0.0	(1.9) 0.6	(0.8) 0.1
RMN (Low and High)	(3.4) 6.4	(23.6) 15.7	(12.2) 11.4
(Previously published figures (Doslak 1978))			

Conclusions

Calculations have been performed to quantify changes in the potential field following conductivity value modifications within specified ranges from the literature. From these data, analysis has revealed the potential difference changes along the axis and over the surface of the model eye. Essentially, these data show that large variations in σ_4 and σ_5 produce insignificant effects in resultant potential field. This shows that the effects of conductivity variations in the lens and cornea are small. This is believed to be because the electric field intensity and current density are small in these regions.

Variation of σ_3 produces the largest effect with σ_2 and RMN following. Current in the extra-ocular region, retinal membrane and sclera is therefore believed to be comparatively large especially near the double layer edge. Variations in the conductivity value of these regions will therefore have a greater effect on the resulting calculated potentials.

3.2.4 Frequency considerations

As the electroretinogram is a time varying signal it may be described using Fourier analysis. The dominant frequencies of the largest waveform of the ERG (the 'b' wave) are less than 20 Hz. Most of the structures within the three dimensional eye may be considered to have a negligible capacitive component. However the retinal membrane is believed to have large capacitive effects that cannot be ignored (Doslak 1978). In order to investigate this phenomenon, complex functions were introduced into the model. This allowed representation of both the parallel resistive and capacitive effects of the retinal membrane impedance. By varying the frequency of the bioelectric retinal source again the effects on corneal potential may be studied in more detail.

Method

In order to study frequency effects within the model the calculation of potential was slightly modified. The 'strength' (or magnitude) of the potential over the entire length of the source retinal double layer was considered to be in phase. However, associated currents on the retinal membrane may have phase lags. Complex number functions were introduced into the calculations in order to simulate the magnitude and phase component to each node.

The previous section, '3.2.3 Parameter variation', examined parameter variation for high and low values of conductivity. Only small changes in corneal potential were found for conductivity variations in the regions σ_4 (lens) and σ_5 (cornea). For the following analysis the conductivity values of these regions were set at constant values. σ_1 (aqueous/vitreous) was also held at a constant value of 1. Changes in corneal potential were then examined following systematic variation in the parameters σ_2 (sclera), σ_3 (fat/muscle/bone), retinal membrane resistance (RR), retinal membrane capacitance (RC) and frequency (f) which could be varied between 0Hz to 20Hz. Table 3.10 shows the values used for each of these regions.

Table 3.10

Table showing values of conductivity parameters used in frequency effects experiments.

(Adapted from Doslak M.J (1978) 'The Effects of Variations of the Conducting Media Inhomogeneities on the Electroretinogram' PhD Dissertation, Case Western Reserve University.)

Parameter	Low Value	Mean Value	High Value
σ_1	-	1.000	-
σ_2	0.010	-	0.150
σ_3	0.005	-	0.060
σ_4	-	0.190	-
σ_5	-	0.445	-
σ_6	-	0.000	-
RR	1.670	-	6.250
RC	27.8/f	-	58.8/f
Frequency (f)	0.000	-	20.000

Each parameter in turn was kept constant and the rest altered until all 24 permutations of these values had been examined. Table 3.11 shows the order in which the parameters were altered for the 0 Hz experiments and Table 3.12 shows the order in which the parameters were altered for the 20Hz experiments.

The optimum over-relaxation factor for each set of model parameter values is affected by the retinal capacitance and frequency values. In most of these experiments an over-relaxation factor of 1.88 was used but for some, values of 1.82 or 1.85 were needed to prevent divergence of the numerical solution.

Table 3.11**Table showing combinations for 0 Hz frequency experiments**

σ_1	σ_2	σ_3	σ_4	σ_5	σ_6	RR	RC
1	0.15	0.06	0.19	0.445	0	1.67	0
1	0.01	0.06	0.19	0.445	0	1.67	0
1	0.01	0.06	0.19	0.445	0	6.25	0
1	0.15	0.005	0.19	0.445	0	6.25	0
1	0.01	0.005	0.19	0.445	0	1.67	0
1	0.15	0.005	0.19	0.445	0	1.67	0
1	0.01	0.005	0.19	0.445	0	6.25	0
1	0.15	0.06	0.19	0.445	0	6.25	0

Table 3.12**Table showing combinations for 20 Hz frequency experiments**

σ_1	σ_2	σ_3	σ_4	σ_5	σ_6	RR	RC
1	0.15	0.06	0.19	0.445	0	1.67	58.8/f
1	0.01	0.06	0.19	0.445	0	1.67	58.8/f
1	0.01	0.06	0.19	0.445	0	1.67	27.8/f
1	0.01	0.06	0.19	0.445	0	6.25	27.8/f
1	0.15	0.005	0.19	0.445	0	6.25	27.8/f
1	0.01	0.005	0.19	0.445	0	1.67	27.8/f
1	0.01	0.005	0.19	0.445	0	6.25	58.8/f
1	0.15	0.06	0.19	0.445	0	6.25	27.8/f
1	0.15	0.005	0.19	0.445	0	1.67	27.8/f
1	0.15	0.005	0.19	0.445	0	6.25	58.8/f
1	0.15	0.06	0.19	0.445	0	1.67	27.8/f
1	0.15	0.005	0.19	0.445	0	1.67	58.8/f
1	0.01	0.005	0.19	0.445	0	6.25	27.8/f
1	0.15	0.06	0.19	0.445	0	6.25	58.8/f
1	0.01	0.005	0.19	0.445	0	1.67	58.8/f
1	0.01	0.06	0.19	0.445	0	6.25	58.8/f

Results

Following convergence of the potentials for each of these experiments, the changes in potential over the corneal surface were calculated for conductivity variations in each region of the model. Tables 3.13 and 3.14 show the changes in potential over the corneal surface for parameter variations at 0 Hz and 20 Hz respectively.

Table 3.13

Table showing changes in potential over the corneal surface for parameter variations for a frequency of 0 Hz.

Parameter Varied	Change in Potential		
	Minimum	Maximum	Mean
σ_2 (15 to 1)	(10.3) 8.7	(26.6) 9.1	(17.1) 8.9
σ_3 (12 to 1)	(7.8) 21.9	(17.0) 22.3	(11.1) 22.0
RR (4 to 1)	(3.6) 1.57	(23.6) 1.58	(12.3) 1.57
RC (2 to 1)	(0.0) 0.01	(0.0) 0.07	(0.0) 0.05

Table 3.14

Table showing changes in potential over the corneal surface for parameter variations for a frequency of 20 Hz.

Parameter Varied	Changes in Potential		
	Minimum	Maximum	Mean
σ_2 (15 to 1)	(4.1) 0.18	(10.7) 0.51	(7.9) 0.20
σ_3 (12 to 1)	(4.8) 0.34	(7.5) 0.35	(6.7) 0.35
RR (4 to 1)	(0.1) 0.21	(1.8) 0.22	(0.8) 0.22
RC (2 to 1)	(0.6) 0.00	(7.2) 0.00	(2.7) 0.00

The values obtained for the three-dimensional model have been compared with the data from the two-dimensional model (Doslak 1978) and are shown in brackets.

In order to examine more closely the electric field distribution within the three-dimensional model a single set of parameter values was chosen from these experiments and graphs of potential variation were plotted. These were $\sigma_1 = 1$, $\sigma_2 = 0.15$, $\sigma_3 = 0.005$, $\sigma_4 = 0.19$, $\sigma_5 = 0.44$, $\sigma_6 = 0$, $RR = 1.67$ and $RC = 58.8$. The frequency was set to 20 Hz. Figure 3.27 shows a plot of the potential magnitude and Figure 3.28 a plot of the phase along the axis of the eyeball.

Figure 3.27 Frequency Effects

Graph showing the potential magnitude along the axis of the eyeball when ($\sigma_1 = 1, \sigma_2 = 0.15, \sigma_3 = 0.005, \sigma_4 = 0.19, \sigma_5 = 0.44, \sigma_6 = 0, RR = 1.67, RC = 58.8$ and frequency = 20 Hz).

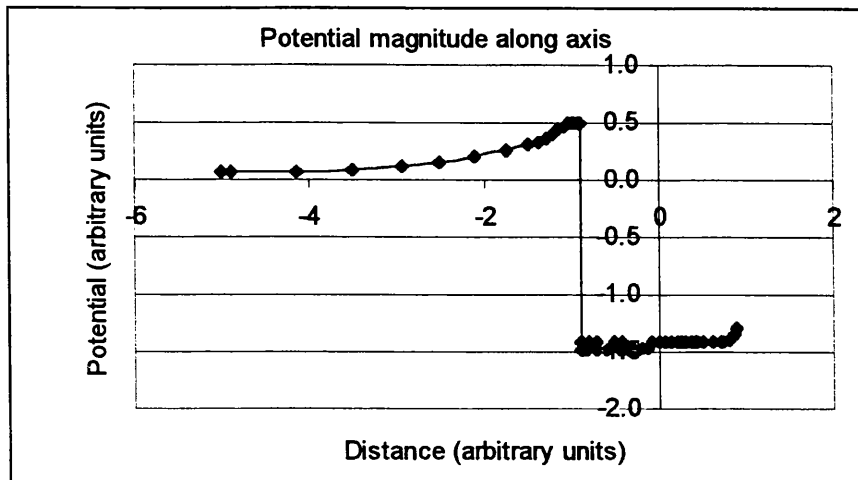
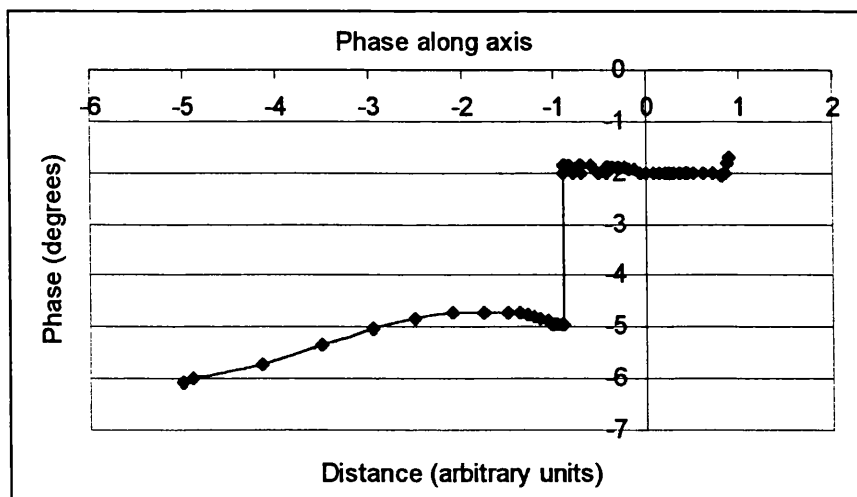


Figure 3.28 Frequency Effects

Graph showing the phase along the axis of the eyeball when ($\sigma_1 = 1, \sigma_2 = 0.15, \sigma_3 = 0.005, \sigma_4 = 0.19, \sigma_5 = 0.44, \sigma_6 = 0, RR = 1.67, RC = 58.8$ and frequency = 20 Hz).



As with previously published two-dimensional data (Doslak 1978), a small electric field is found to exist anteriorly along with a large field and phase lag near the double layer

edge. Figure 3.29 shows plot of the potential magnitude and Figure 3.30 a plot of the phase around the circumference of the eyeball.

Figure 3.29 Frequency Effects

Graph showing the potential magnitude around the circumference of the eyeball

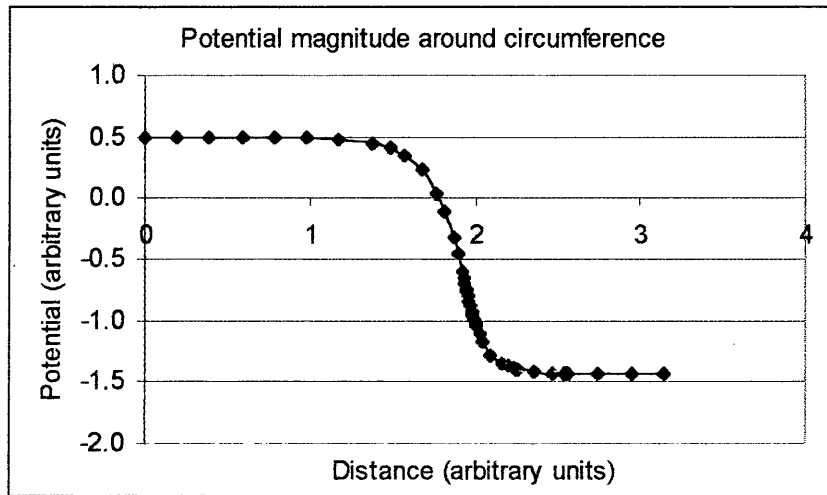
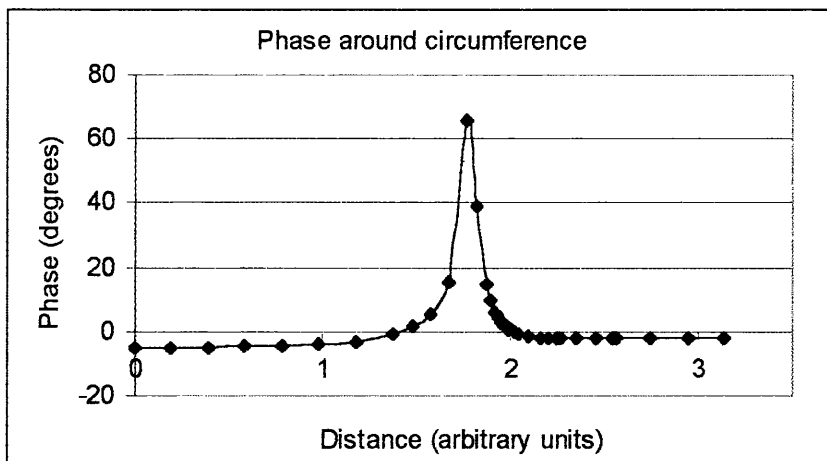


Figure 3.30 Frequency Considerations

Graph showing the phase around the circumference of the eyeball



Conclusions

The three dimensional model has been modified to incorporate a frequency component into the calculations. Corneal potential changes were examined at frequencies of both 0Hz and 20Hz. When the frequency is set to equal 0Hz, the model potential changes are found to be almost identical to previous parameter change experiments. This was because the only difference in these experiments was that mean values for σ_4 (lens) and σ_5 (cornea) were used. Changes in the parameters for σ_3 (fat/muscle/bone) and σ_2 (aqueous/vitreous) produced the largest changes in both the two and three-dimensional models at 0Hz. The retinal membrane capacitance value had the most insignificant effect on corneal potential values.

When the frequency was set to be 20Hz it was found that variations in each of the parameters did not produce changes in potential as large as for the 0Hz experiments. However it was again found that changing the conductivity values of the parameters σ_3 (fat/muscle/bone) and σ_2 (aqueous/vitreous) produced the largest changes in both the two and three-dimensional models at 20Hz.

3.2.5 Physiological Comparisons

In order to determine the ability of this three-dimensional model to simulate the physiological eye, comparisons may be made between calculated potentials and actual measurements made of the physiological system *in vivo*. Previous workers in this field have published data regarding electromagnetic potentials measured from both an isolated and an 'in situ' or *in vivo* eye. This section of work is essentially an abridged version of previous work (Doslak 1978) in which similar comparisons were made with a two-dimensional model. The parameters for each calculation may be modified to simulate a more accurate comparison with the physiological nature of the eye.

Method

The construction of the three-dimensional model may be modified to provide a more accurate comparison with data from physiological potential experiments. Comparisons were made between model and physiological results in two situations. Firstly when the eye is isolated, i.e. surrounded by air and secondly when the eye is *in vivo* i.e. almost totally surrounded by fat and bone. The literature regarding the *in vivo* experiments describes how measurements of 'b' wave potentials from the anterior circumference of an enucleated rabbit eye were made (Krakau 1958). The three-dimensional model was modified to simulate an isolated eye by setting the conductivity values of the various regions to mimic those of the physiological situation. The conductivity of the 'fat and bone' region at the posterior of the eye (σ_3) and the anterior 'air' region (σ_6) were set to zero. This simulated isolation of the whole eye from the boney cavity in which it normally 'sits'. The conductivity of the 'lens' region (σ_4) was set to be constant at 0.19. Likewise the conductivity of the 'cornea' region (σ_5) was set to be constant at 0.445. The conductivity of the 'aqueous / vitreous' region was set to 1. In these three latter cases the conductivity values remained constant as it had previously been shown that they produced insignificant effects on the potential magnitude distribution.

The retinal membrane capacitance was set at the mean of its predicted value, which was 43.3. Variation of the membrane capacitance had previously been shown to have minor effects on the potential distribution at low frequencies. The source frequency was set to 5 Hz and a common reference was used to limit any artefacts. For the isolated eye this was

at $\phi = 48^\circ$. The remaining two parameters, the conductivity of the 'retina/sclera' region (σ_2) and the retinal membrane impedance (RR) were then varied over their tabulated ranges to examine the effects of these parameter variations. Figures 3.31 to 3.34 plot the potential magnitude around the circumference of the eye for each combination of parameters.

For experiments regarding the eye in 'situ' or *in vivo* calculations were performed simulating the eye within the boney cavity of the orbit in the skull. Results from these calculations were then compared with measurements from an *in vivo* rabbit eye. In previous physiological experiments (Krakau 1958) an electrode was perforated through the anterior surface of the eye and advanced until it reached the optic nerve. The model parameters are therefore modified to simulate air at only the front surface of the eye. The posterior surface was simulated to have fat and bone surrounding it. To achieve this the conductivity of the 'lens' region (σ_4) was set to be constant at 0.19. Likewise the conductivity of the 'cornea' region (σ_5) was set to be constant at 0.445. The conductivity of the anterior 'air' region (σ_6) was set to zero and the 'aqueous / vitreous' (σ_1) region set to 1. This time the parameters σ_2 , σ_3 and RR were varied over their tabulated ranges (Table 3.1). The source frequency was set to 5 Hz and again to provide a meaningful comparison a common reference was used, this time $\phi = -0.021$. Figures 3.35 to 3.42 plot the potential magnitude from a point on the anterior surface, (R (29) = 1, T (35) = 129°) to a point at the posterior of the eye (R (32) = 1.08, T (4) = 33.75°) having penetrated the retina, for each combination of parameters.

Results

For the isolated eye, Figures 3.31 to 3.34 show how the calculated potential distribution using the three-dimensional model compares with measurements of potential made from an isolated eye. These data show a degree of uniformity over the cornea with a rapid decrease to smaller potential values near the posterior perimeter.

Figure 3.31

Physiological Comparisons (The isolated eye)

The potential magnitude around the circumference when $\sigma_1 = 1, \sigma_2 = 0.01, \sigma_3 = 0, \sigma_4 = 0.19, \sigma_5 = 0.445, \sigma_6 = 0, RR = 1.67, RC = 43.3$ and frequency = 5Hz.

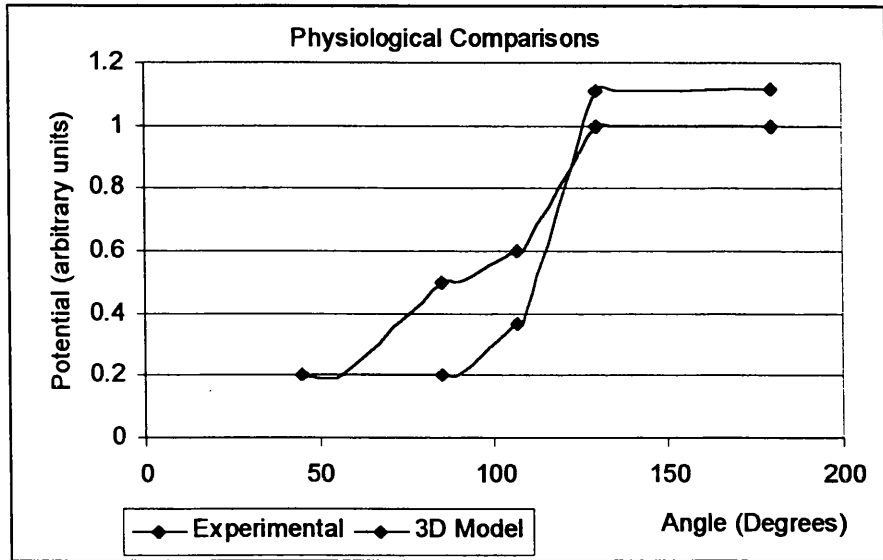


Figure 3.32

Physiological Comparisons (The isolated eye)

The potential magnitude around the circumference when $\sigma_1 = 1, \sigma_2 = 0.01, \sigma_3 = 0, \sigma_4 = 0.19, \sigma_5 = 0.445, \sigma_6 = 0, RR = 6.25, RC = 43.3$ and frequency = 5Hz.

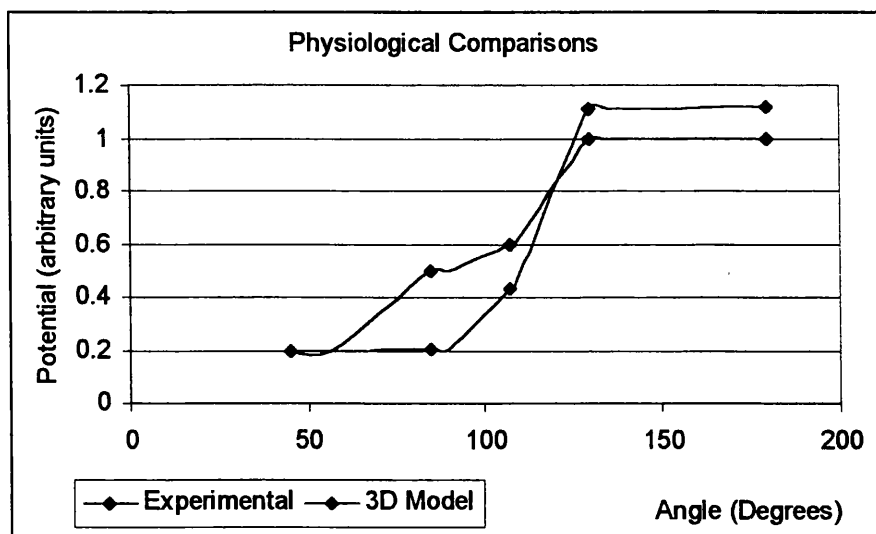


Figure 3.33

Physiological Comparisons (The isolated eye)

The potential magnitude around the circumference when $\sigma_1 = 1, \sigma_2 = 0.15, \sigma_3 = 0, \sigma_4 = 0.19, \sigma_5 = 0.445, \sigma_6 = 0, RR = 1.67, RC = 43.3$ and frequency = 5Hz.

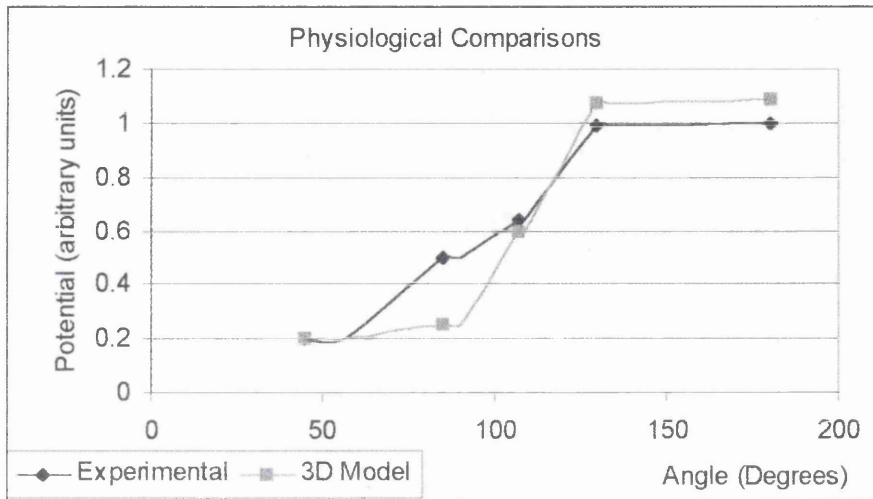
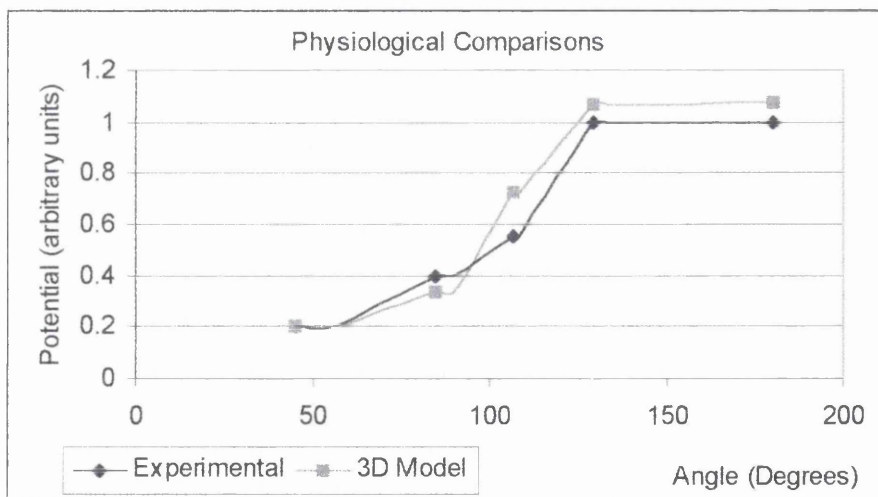


Figure 3.34

Physiological Comparisons (The isolated eye)

The potential magnitude around the circumference when $\sigma_1 = 1, \sigma_2 = 0.15, \sigma_3 = 0, \sigma_4 = 0.19, \sigma_5 = 0.445, \sigma_6 = 0, RR = 6.25, RC = 43.3$ and frequency = 5Hz.



For the eye in situ, Figures 3.35 to 3.42 show how the calculated potential distribution using the three-dimensional model compares with measurements of potential from an eye *in vivo*. Data of calculated potentials from the three-dimensional model was found to be in good agreement with previous experimental data (Krakau 1938). The graphs show increased potentials on the vitreous side of the retina. Once the retina is penetrated, the potential values are found to decrease rapidly.

Figure 3.35

Physiological Comparisons (The eye in situ)

Potential magnitude along the axis when $\sigma_1 = 1, \sigma_2 = 0.01, \sigma_3 = 0.005, \sigma_4 = 0.19, \sigma_5 = 0.445, \sigma_6 = 0, RR = 1.67, RC = 43.3$ and frequency = 5Hz.

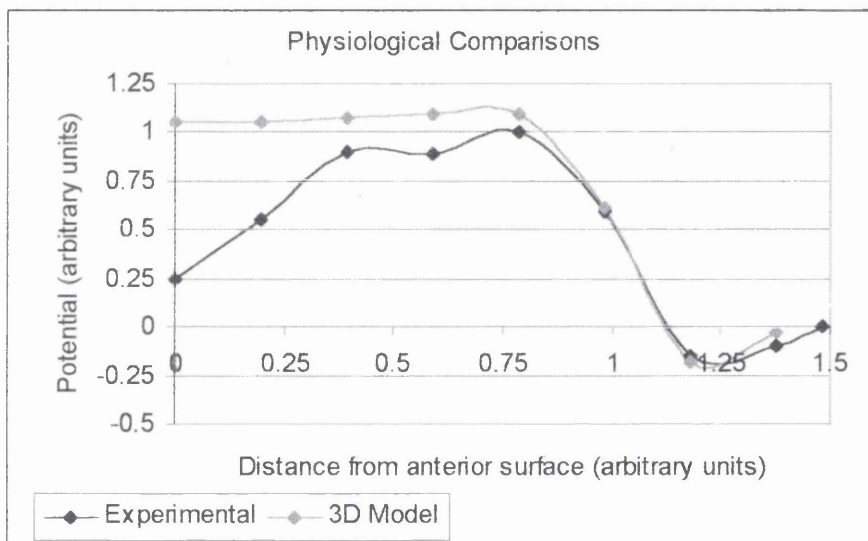


Figure 3.36

Physiological Comparisons (The eye in situ)

Potential magnitude along the axis when $\sigma_1 = 1, \sigma_2 = 0.01, \sigma_3 = 0.005, \sigma_4 = 0.19, \sigma_5 = 0.445, \sigma_6 = 0, RR = 6.25, RC = 43.3$ and frequency = 5Hz.

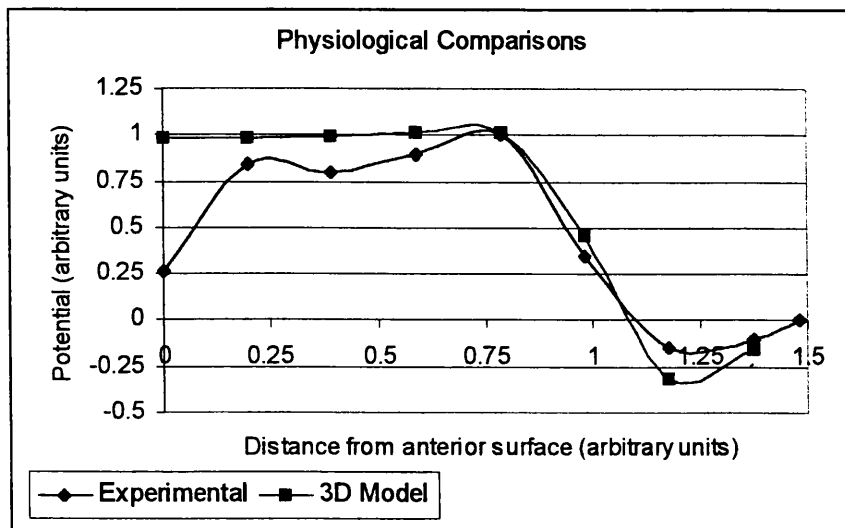


Figure 3.37

Physiological Comparisons (The eye in situ)

Potential magnitude along the axis when $\sigma_1 = 1, \sigma_2 = 0.01, \sigma_3 = 0.06, \sigma_4 = 0.19, \sigma_5 = 0.445, \sigma_6 = 0, RR = 1.67, RC = 43.3$ and frequency = 5Hz.

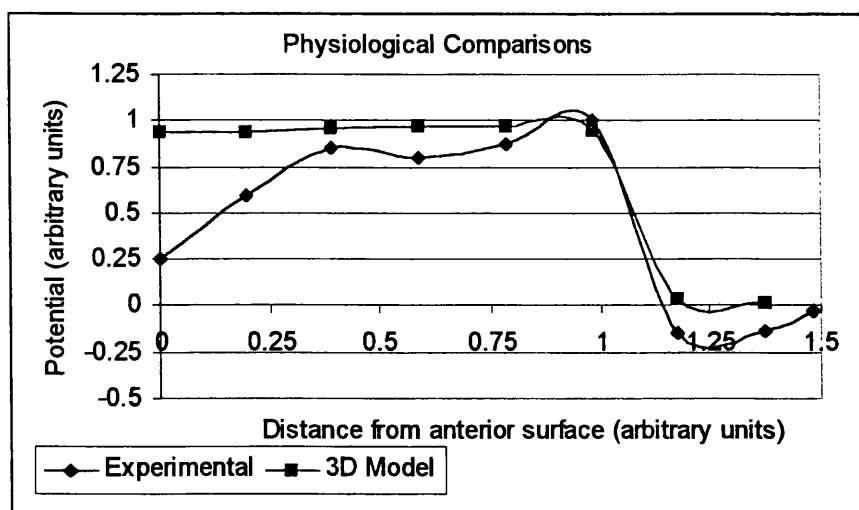


Figure 3.38

Physiological Comparisons (The eye in situ)

Potential magnitude along the axis when $\sigma_1 = 1$, $\sigma_2 = 0.01$, $\sigma_3 = 0.06$, $\sigma_4 = 0.19$, $\sigma_5 = 0.445$, $\sigma_6 = 0$, $RR = 6.25$, $RC = 43.3$ and frequency = 5Hz.

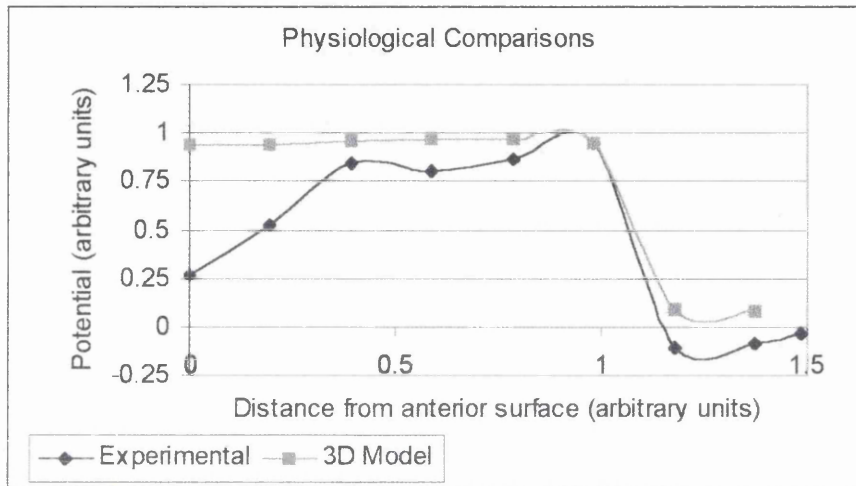


Figure 3.39

Physiological Comparisons (The eye in situ)

Potential magnitude along the axis when $\sigma_1 = 1$, $\sigma_2 = 0.15$, $\sigma_3 = 0.005$, $\sigma_4 = 0.19$, $\sigma_5 = 0.445$, $\sigma_6 = 0$, $RR = 1.67$, $RC = 43.3$ and frequency = 5Hz.

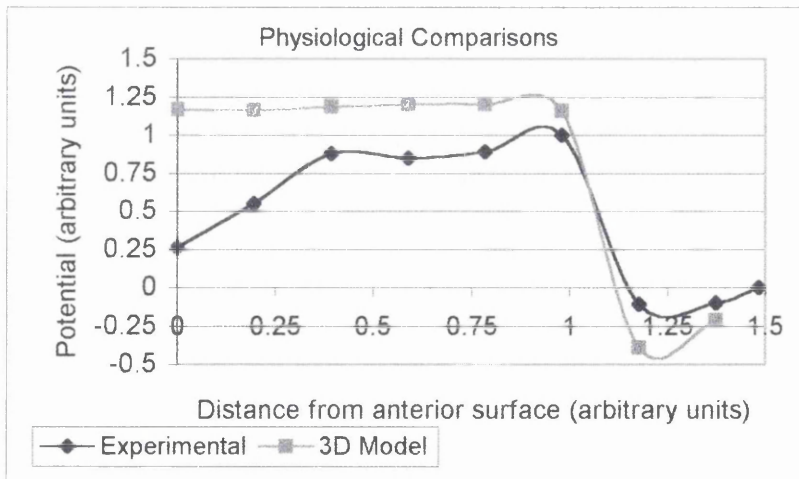


Figure 3.40

Physiological Comparisons (The eye in situ)

Potential magnitude along the axis when $\sigma_1 = 1, \sigma_2 = 0.15, \sigma_3 = 0.005, \sigma_4 = 0.19, \sigma_5 = 0.445, \sigma_6 = 0, RR = 6.25, RC = 43.3$ and frequency = 5Hz.

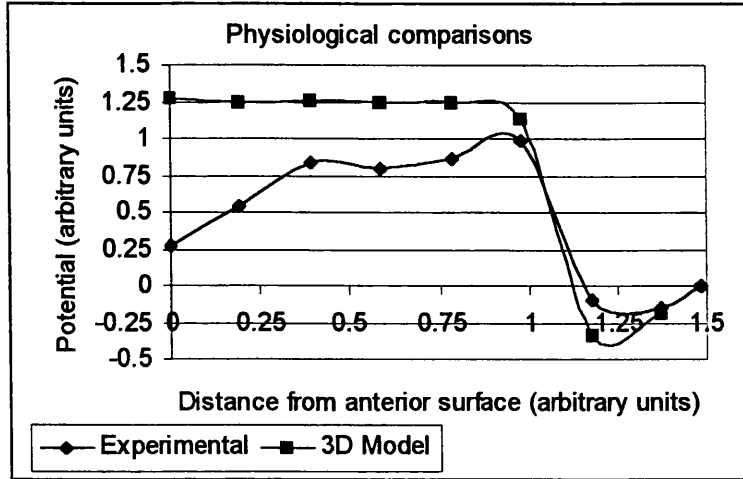


Figure 3.41

Physiological Comparisons (The eye in situ)

Potential magnitude along the axis when $\sigma_1 = 1, \sigma_2 = 0.15, \sigma_3 = 0.06, \sigma_4 = 0.19, \sigma_5 = 0.445, \sigma_6 = 0, RR = 1.67, RC = 43.3$ and frequency = 5Hz.

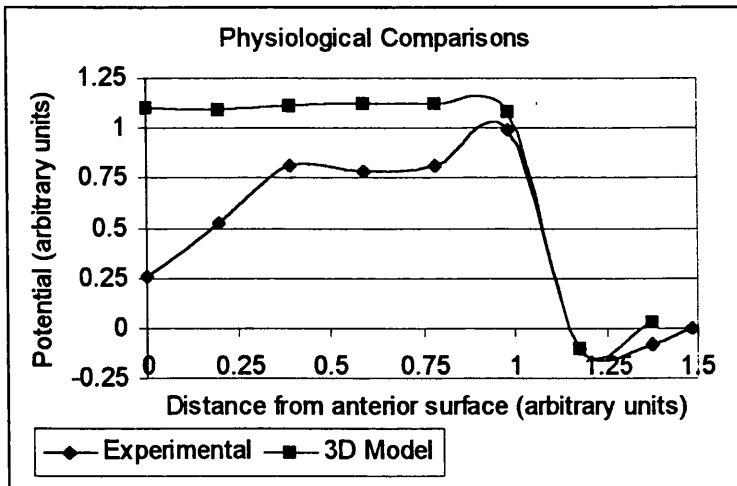
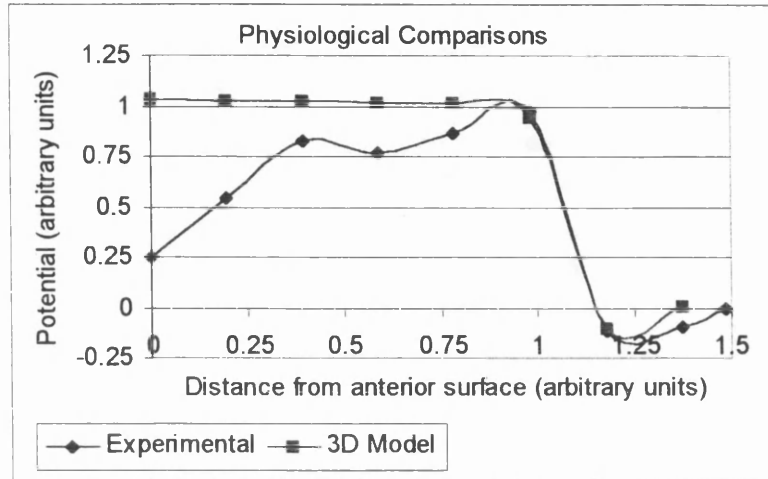


Figure 3.42

Physiological Comparisons (The eye in situ)

Potential magnitude along the axis when $\sigma_1 = 1$, $\sigma_2 = 0.15$, $\sigma_3 = 0.06$, $\sigma_4 = 0.19$, $\sigma_5 = 0.445$, $\sigma_6 = 0$, $RR = 6.25$, $RC = 43.3$ and frequency = 5Hz.



Conclusions

The three-dimensional model has been developed to facilitate the comparison of calculated potentials with actual experimental recordings from rabbit eye. Comparisons of the results from experimental and calculated potentials have revealed good agreement. The best agreement with documented experimental data for the isolated eye is found to occur when conductivity values of both the 'retina/sclera' region (σ_2) and the resistivity of the retinal membrane impedance 'RMN' are high, (Figure 3.34). The best agreement of the model potentials with experimental data of the eye *in situ* was found to occur when the conductivity of the 'retina/sclera' region (σ_2) was low and the conductivity of the 'fat / bone' region (σ_3) was high.

In previous work of this nature with a two-dimensional model (Doslak 1978) it was believed that the differences between the theoretical and physiological data sets might be due to a number of factors. These included the homogeneous representation of the retinal source strength in the model, inaccuracies in the conductivity values used for each region in the model and the use of a rabbit's eye rather than averaged values from a range of animals. There are almost certainly further physiological measurement inaccuracies.

3.3 Summary and Conclusions

A three-dimensional model has been constructed which may be used to accurately simulate the physiological eye. Validation of this model has been performed by comparison 'node by node' with an existing two-dimensional model (Doslak 1978). This comparison revealed an average magnitude change in the three-dimensional model of just 0.3%. It has been found throughout the course of the experimentation that the three-dimensional model requires a significant increase in the number of iterations to achieve the same degree of convergence. Sharp conductivity changes between the regions of the eye were believed to be the cause of 'slower' convergence.

The parameter variation experiments highlighted how even a large variation in the conductivity values of either the lens or cornea produced an insignificant effect on the corneal potential distribution. This is due to the electric field intensity and current density being small in these regions. When corneal potential changes were examined at 0Hz the model potential changes were found to be almost identical to previous parameter change experiments. The only differences of note here were that mean values for σ_4 (lens) and σ_5 (cornea) were used. At 20Hz variations in each of the parameters were not found to produce changes in potential as large as for the 0Hz experiments. However in both 0Hz and 20Hz cases, changing the conductivity values of the parameters σ_3 (fat/muscle/bone) and σ_2 (aqueous/vitreous) produced the largest changes in both the two and three-dimensional models. Finally, physiological comparisons of theoretically calculated potentials have been found to be in agreement with physiological measurements. The small differences found are believed to be due to a number of factors including the homogeneous representation of the retinal source strength in the model.

Having validated a three-dimensional theoretical model using current two-dimensional results, it may now be used experimentally to predict the corneal potential distribution produced by a variety of stimulus conditions. In this way corneal potential may theoretically be 'mapped'. Using this technique it may be then possible to optimise electrode placement and enhance corneal signal recovery.

Chapter 4

Model Variations

4.0 Introduction

A three-dimensional model has been constructed and validated to simulate to some extent the human eye *in vivo*. A series of experiments may now be conducted in which different stimulus conditions are provided to the theoretical model. The fairly recent advent of clinically used multifocal electroretinography allows the simultaneous stimulation of multiple single areas over the retina, (Bears M.A *et al* 1996). While it would require a vast amount of further work to accurately simulate this scenario, due to the capabilities of the model it is relatively simple to consider a single focal site or ring of stimulation or dysfunction on the theoretical retina. This chapter outlines how focal stimulation or scotoma simulation of the theoretical retina may be achieved and how calculated corneal potentials are found to be highly characteristic of retinal stimulus site.

4.1 Photoreceptor density scaling

It is initially important to ensure that the behaviour of the modelled retina mimics the physiological retina as far as possible. Previous experiments in preceding chapters of this work have described, in detail, a theoretical three-dimensional electromagnetic model with a constant, spatially uniform retinal source strength. This idealised representation is far from the physiological truth.

It is widely known that photoreceptor density is highly dependent on retinal eccentricity (Curcio C.A *et al* 1990). Although it is not known how the potential source strength of the retina varies with incident light intensity or any of a number of adaptive mechanisms, one crude possibility is that it may vary with photoreceptor density. The three-dimensional model has been constructed in such a way that the density of photoreceptors on the

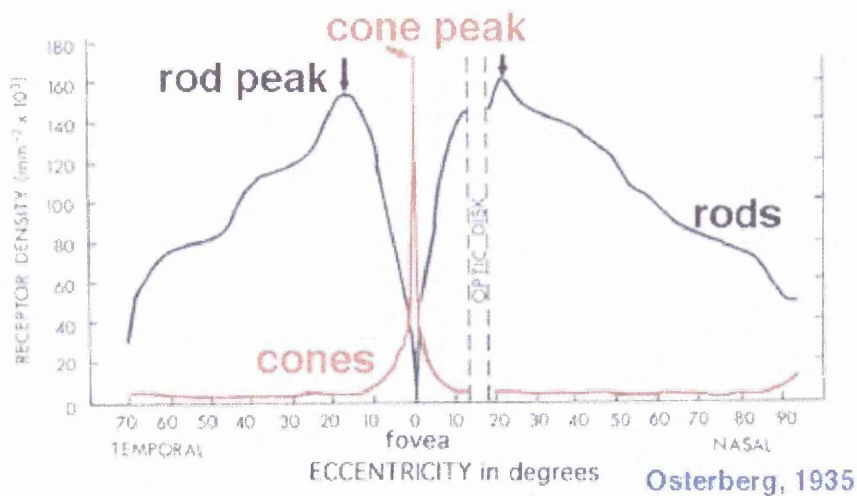
theoretical retina may be modified to more accurately represent the physiological condition. The density of both rods and cones are known to vary inferior, superiorly and naso-temporally (Curcio C.A *et al* 1990). Although cone density is always found to be highest in the foveal pit, falling off rapidly into the peripheral retina and rod density peaks in a ring around the fovea approximately 20 degrees from the foveal pit the actual densities found are known to be highly subject specific. The optic nerve (blind spot) is of course always photoreceptor free.

Average densities at specific eccentricities were therefore calculated and incorporated into the model. This was attempted using data from the literature (Osterberg (1935)), in order that results from the model may be accurately compared with those of previous model studies, (Doslak (1978)) (Figure 4.1).

Figure 4.1

Graph showing photoreceptor density variations with eccentricity, (Osterberg, 1935).

(Adapted from <http://webvision.med.utah.edu/photo2.html#densities>)



However, more recent studies of photoreceptor density, (Curcio C A *et al* 1987) would now allow more accurate model calculations and predictions of the changes in potential at the cornea. (Figure 4.2).

Figure 4.2

Graph showing photoreceptor density variations with eccentricity, (Curcio 1987)

(Adapted from <http://webvision.med.utah.edu/photo2.html#densities>)

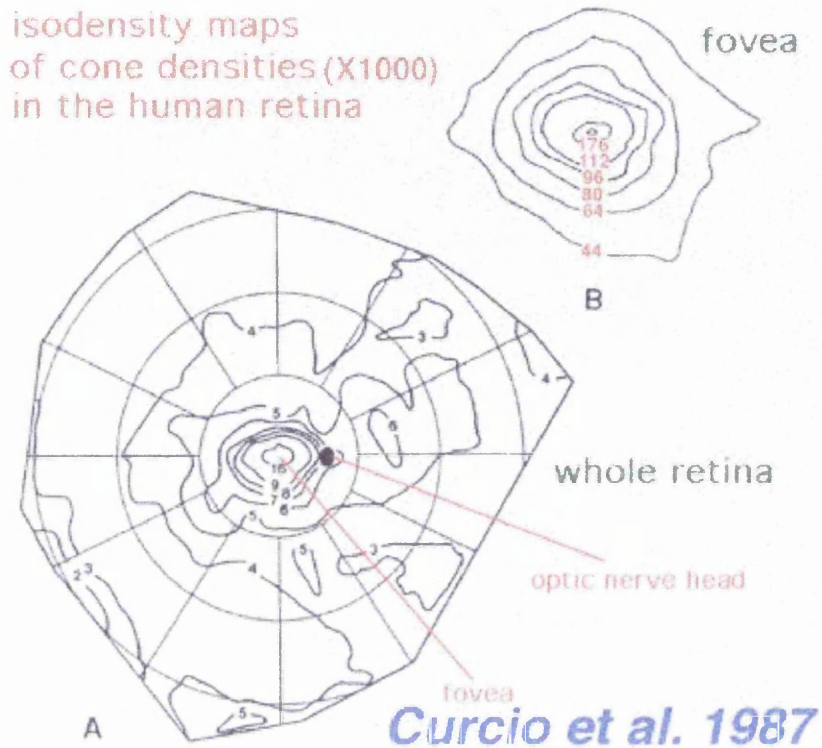


Table 4.1 shows the differences in calculated relative photoreceptor density from these data ((Osterberg 1935, Curcio *et al* 1987).

For eccentricities up to 70 degrees there is an average difference in the data of only – 0.23%. This is probably due to the high number of photoreceptors and hence statistically smaller variations in numbers of photoreceptors found in this region of the retina. At eccentricities greater than 70 degrees up to a maximum of 113 degrees the comparison becomes much less favourable with the average difference in the data rising to 59.3 %. The two data sets become increasingly divergent (Osterberg (1935), Curcio *et al* (1987)). The earlier data set (Osterberg (1935), is always found to claim a lower density of photoreceptors than that measured much more recently (Curcio *et al* (1987)). This could well have been due to advances in methods of fixing, counting and measurement techniques. However, the accuracy achieved by the earlier data set (Osterberg (1935)) is commendable.

Table 4.1

Table showing data comparison (Osterberg (1935), Curcio (1987)).

Retinal Location (degrees)	Measured Photoreceptor Density (x 1000 /mm²) <i>Curcio (1987)</i>	Calculated Relative Density <i>Curcio (1987)</i>	Measured Relative Density <i>Osterberg (1935)</i>	% Difference
0	92	1.13	-	-
11.1	124	1.52	1.54	-1.3
22.5	163	2.00	1.96	2.0
33.7	148	1.82	1.82	0.0
45.0	132	1.62	1.69	-4.3
56.3	117	1.44	1.42	1.4
67.5	102	1.25	1.24	0.8
78.7	87	1.07	0.96	10.3
85.0	78	0.96	0.84	12.5
90.0	71	0.87	0.70	19.5
96.0	63	0.77	0.62	19.5
101.25	56	0.69	0.42	39.1
104.0	53	0.65	0.32	50.1
107.0	48	0.59	0.21	64.4
108.5	46	0.56	0.15	73.2
110.0	44	0.54	0.094	82.6
110.5	44	0.54	0.075	86.1
111.0	43	0.53	0.056	89.4
111.5	42	0.52	0.037	92.9
111.75	42	0.52	0.028	94.6
112.5	41	0.50	0.018	96.4
113.4	40	0.49	-	-

Photoreceptor density values used in the three-dimensional model calculations were taken from the earlier data set (Osterberg (1935)). While it is accepted that these values may inherently be an underestimation of photoreceptor density, especially at large eccentricities, they are useful to enable accurate comparisons with previous two-dimensional model work (Doslak (1978)).

Methods

The three dimensional numerical model was modified in order to elicit purely photopic (cone) and subsequently, purely scotopic (rod) responses. This was achieved using photoreceptor density data from the literature (Osterberg, (1935)). Other model parameters were arbitrarily chosen within previously described ranges set out in Table 3.1.

The parameters chosen were $\sigma_1 = 1$, $\sigma_2 = 0.01$, $\sigma_3 = 0.005$, $\sigma_4 = 0.19$, $\sigma_5 = 0.445$, $\sigma_6 = 0$, $RR = 1.67$, $RC = 43.3$ and frequency = 5Hz. Following simulation of both photopic and scotopic responses, plots of axial and circumference potentials were produced. Data comparisons were then made with previous data (Doslak (1978)).

Results

Photopic axial and circumference potential plots were produced following cone photoreceptor density scaling, (Figure 4.3, Figure 4.4). Similarly scotopic axis and circumference potential plots were produced following rod photoreceptor density scaling, (Figure 4.5, Figure 4.6).

Figure 4.3

Cone response along axis of the three-dimensional model when $\sigma_1 = 1$, $\sigma_2 = 0.01$, $\sigma_3 = 0.005$, $\sigma_4 = 0.19$, $\sigma_5 = 0.445$, $\sigma_6 = 0$, $RR = 1.67$, $RC = 43.3$ and frequency = 5Hz.

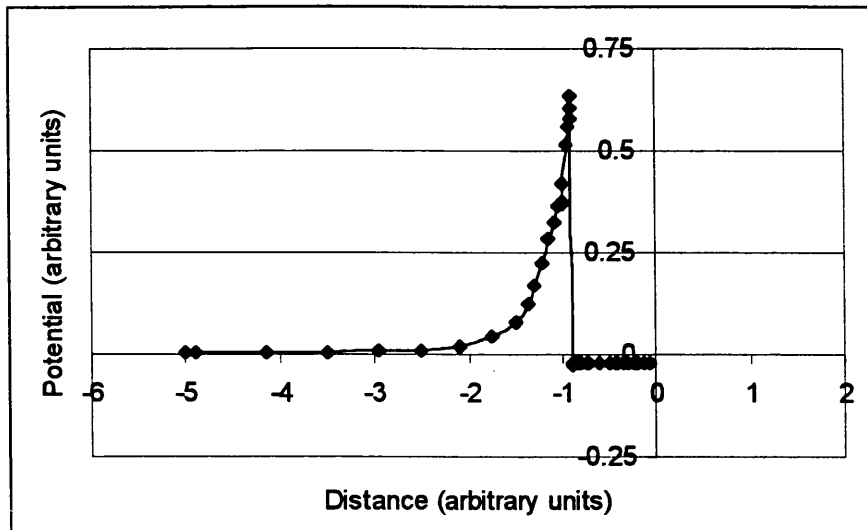


Figure 4.4

Cone response around circumference of the three-dimensional model when $\sigma_1 = 1$, $\sigma_2 = 0.01$, $\sigma_3 = 0.005$, $\sigma_4 = 0.19$, $\sigma_5 = 0.445$, $\sigma_6 = 0$, $RR = 1.67$, $RC = 43.3$ and frequency = 5Hz.

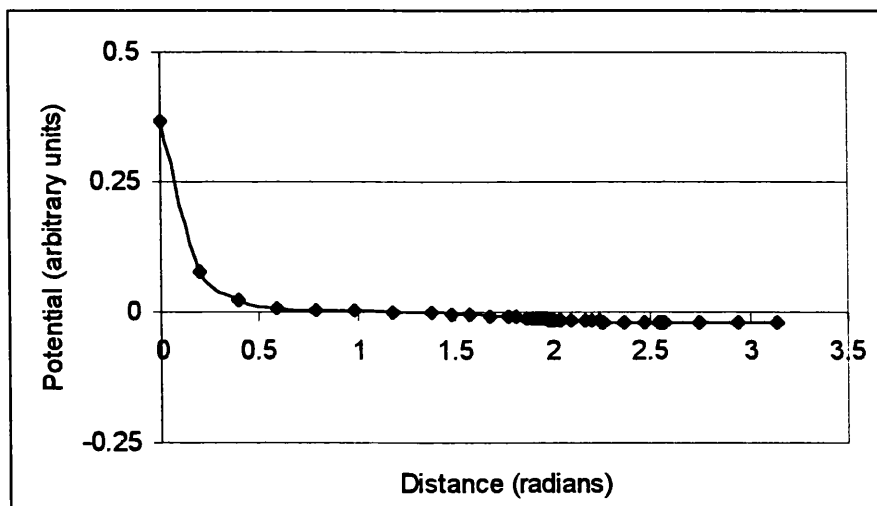


Figure 4.5

Rod response along axis of the three-dimensional model when $\sigma_1 = 1, \sigma_2 = 0.01, \sigma_3 = 0.005, \sigma_4 = 0.19, \sigma_5 = 0.445, \sigma_6 = 0, RR = 1.67, RC = 43.3$ and frequency = 5Hz.

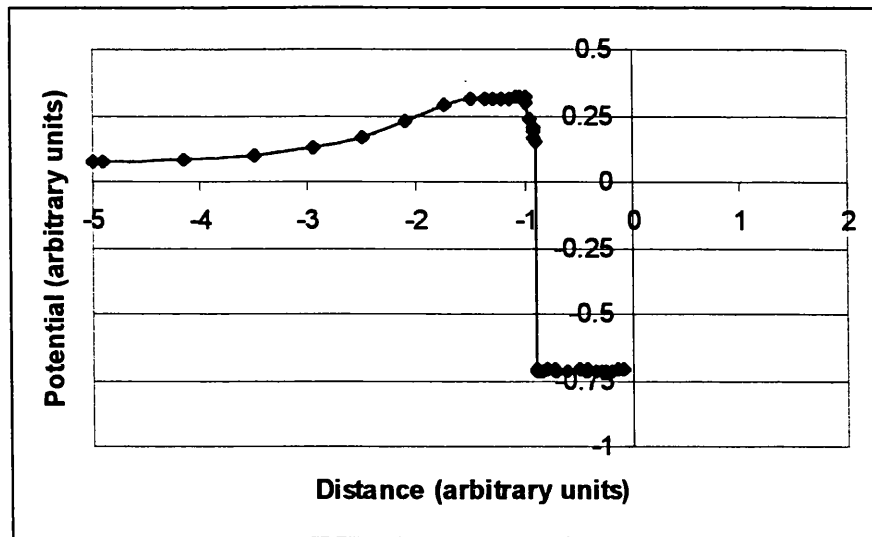
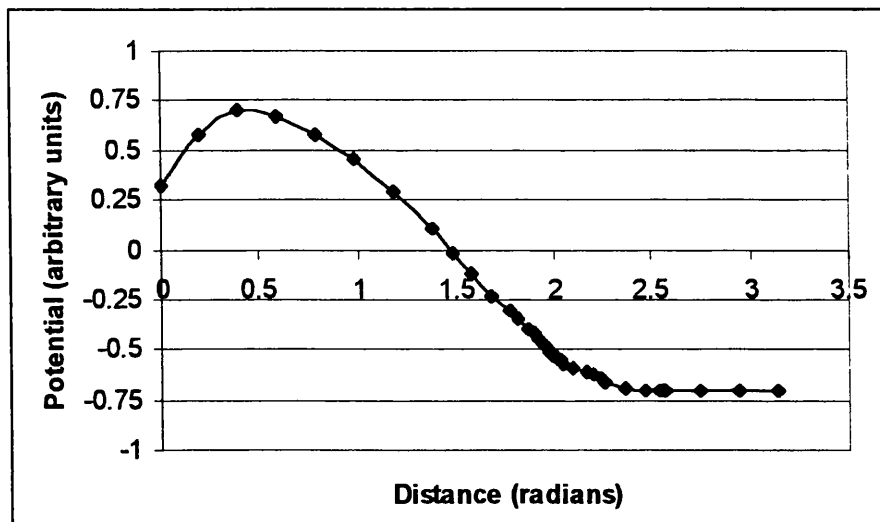


Figure 4.6

Rod response around circumference of the three-dimensional model when $\sigma_1 = 1, \sigma_2 = 0.01, \sigma_3 = 0.005, \sigma_4 = 0.19, \sigma_5 = 0.445, \sigma_6 = 0, RR = 1.67, RC = 43.3$ and frequency = 5Hz.



These figures show that the high density of cones on the axis of the eye gives rise to a sharply peaked potential, (Figure 4.3). The much more rounded axial potential (Figure 4.5) mimics rod density scaling. There are no rods found at 0 degrees on the retina and the potential instead peaks at approximately 20 degrees, the region of maximum rod density, (Figure 4.6).

Conclusions

It has been possible to modify the retinal source strength scaling of the three-dimensional model to more accurately represent the photoreceptor density changes of the physiological eye. Historical data (Osterberg 1935) has been used to enable comparison of the calculated results with that of other workers in the field (Doslak 1978). However, it is recognised that the use of more recent data (Curcio *et al* 1987) would allow more accurate three-dimensional model calculations of potentials. It has been shown that the magnitudes of the peaks for the uniquely cone and rod density scaled retina are clearly different due to the variation in the number of photoreceptors at specific eccentricities.

The absolute accuracy of these results maybe questionable however. It could be argued that there are insufficient nodes at which the potential is calculated to provide an accurate topographical analysis of the potential field. This is especially apparent within regions where the magnitude of the potential is known to vary rapidly. In the homogeneous retinal case the potential changes most sharply around the edges of the retinal membrane (the ora serrata) and so a larger density of nodes is positioned here. Following retinal source strength scaling, the potential is found to change more rapidly near the posterior of the eye and hence the nodal positioning could be further modified to contain a higher nodal density at the posterior rather than in the peripheral regions of the retina.

4.2 Focal and Ring Stimulation

The three dimensional model may be modified to simulate a variety of electrophysiological tests including both focal and ring stimulation of the retina. Stimulation of this nature has become of interest due to the increase in the use of multifocal electroretinographic techniques. Corneal potentials may be examined following focal stimuli along with other 'shaped' ring stimuli.

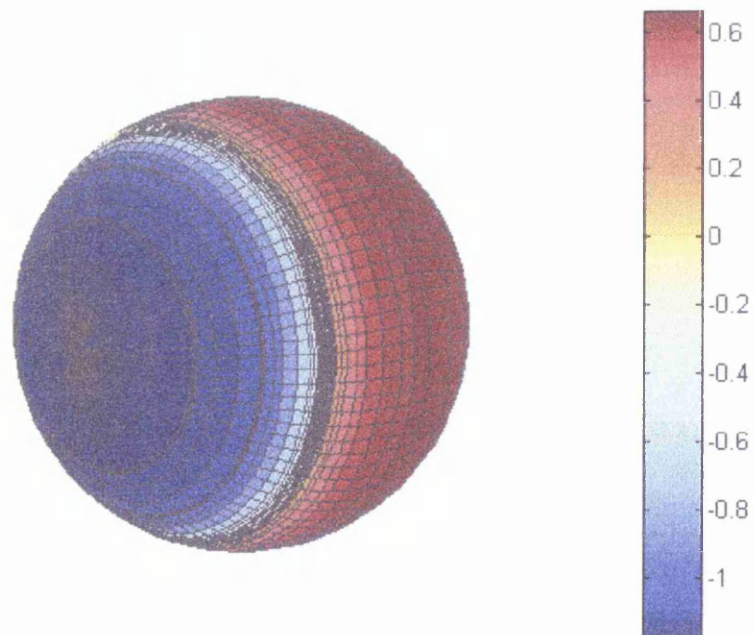
Of interest from these and subsequent experiments is the corneal potential distribution, since it is here that electroretinographic signal recordings are made. In order to examine and demonstrate corneal potential distributions from a wide variety of experimental stimulus conditions, corneal 'heat maps' have been produced. These effectively show regions of high and low potential over the three-dimensional corneal surface. A graphics tool 'Matlab 5.2' has been used to illustrate these potential plots in three-dimensions.

Method

In order to show how the graphics tool can be used to illustrate the three-dimensional potential plots, a 'heat map' was constructed following model calculations in which a uniform global stimulus was presented to a homogeneously scaled retina in three-dimensions. The calculated potential distribution over the entire surface of the model eye was then plotted, Figure 4.7.

Figure 4.7

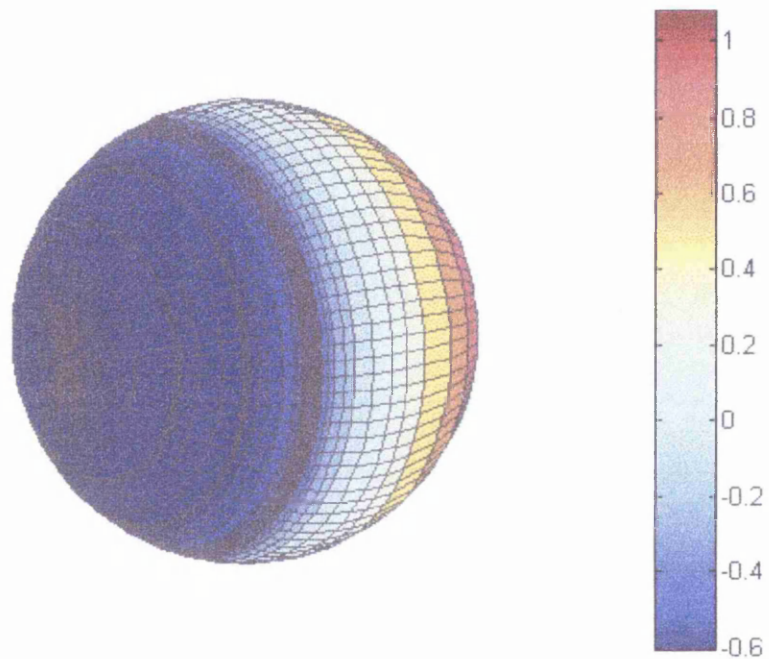
Three-dimensional heat map showing calculated surface potentials following homogeneous retinal global stimulation.



Photoreceptor density scaling corrections were then applied to the retina, as referred to above and again calculations were performed following a uniform global stimulus to the retina. The calculated potentials over the entire surface of the model eye were then plotted, Figure 4.8.

Figure 4.8

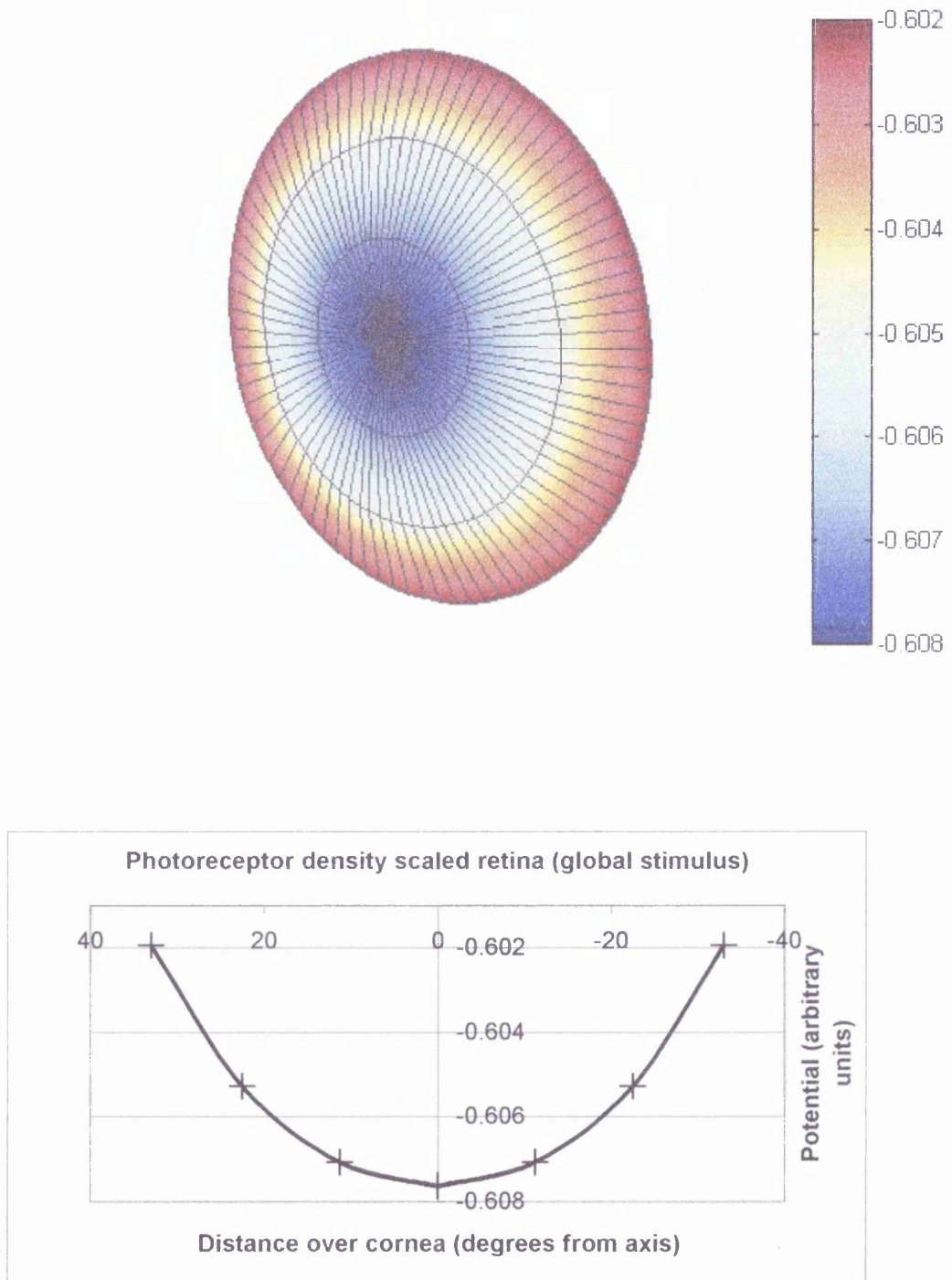
Three-dimensional heat map showing calculated surface potentials following photoreceptor density scaled retinal stimulation.



On initial examination (Figure 4.8), the surface distribution at the posterior of the eye shows the gradient distribution of potential due to photoreceptor density scaling corrections. The corneal surface may seem to be at a constant potential. However, variation in the corneal potential distribution is found to exist. As the potential changes over the posterior of the model eye are very large in comparison with the potential changes over the cornea these anterior potentials are effectively 'masked'. If the 'heat map' is modified to show only the corneal surface and rescaled to highlight any potential changes the corneal potential distribution is clearly seen. Figure 4.9 shows the potential distribution over the corneal surface only. All subsequent 'heat maps' show the corneal surface scaled optimally to represent the range of calculated potentials.

Figure 4.9

Heat map and graph showing electromagnetic potential variation over the cornea following photoreceptor density scaled global retinal stimulation.

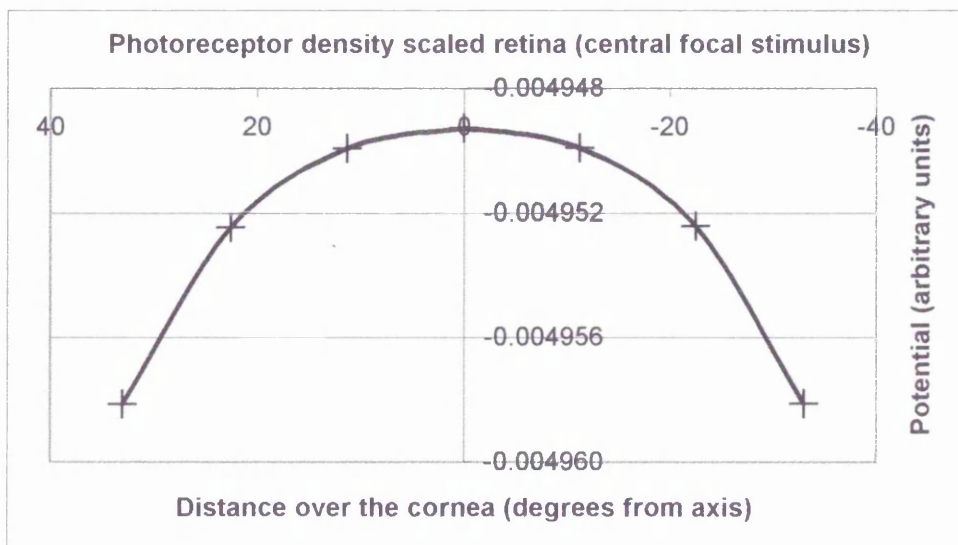
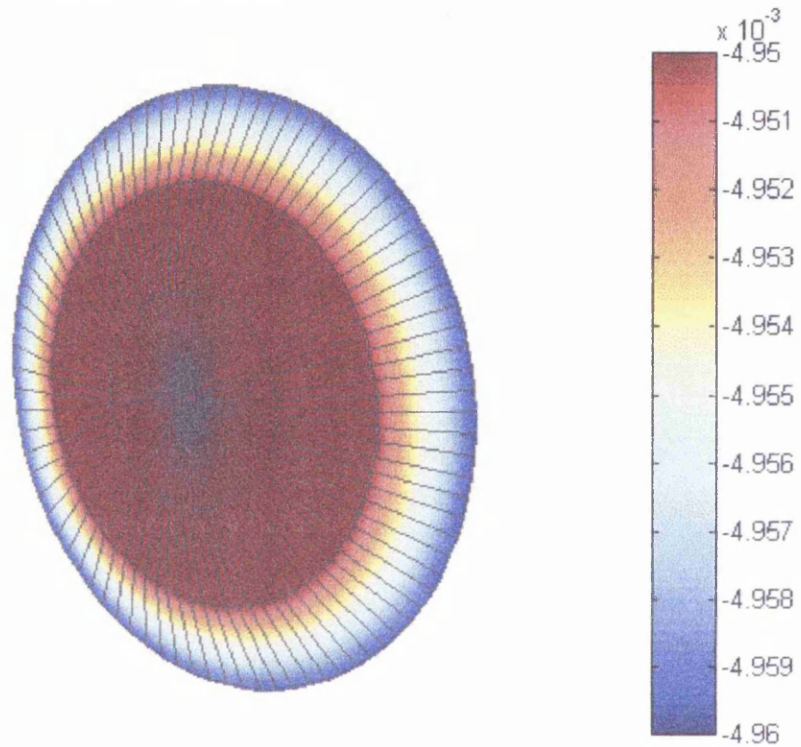


Changes in the corneal potential distribution were examined when a single focal stimulus of any reasonable size (in this case 10 degrees) was presented at specific places on the retina. This was achieved by setting all the nodes on the theoretical retina to equal zero

apart from the nodes that made up the stimulus. Figure 4.10 shows a heat map and graph of the corneal potential distribution following retinal stimulation with a central 10-degree focal spot.

Figure 4.10

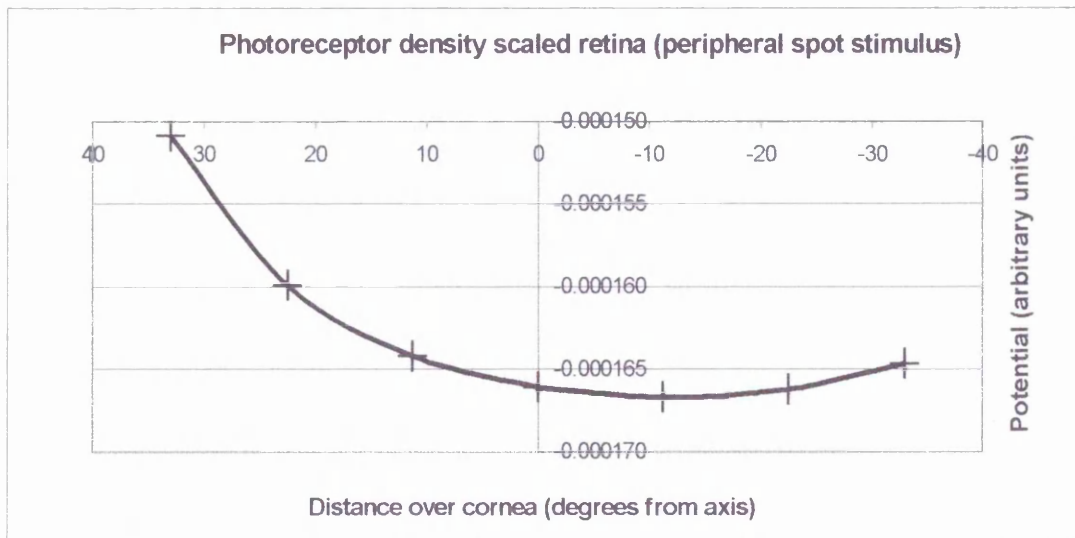
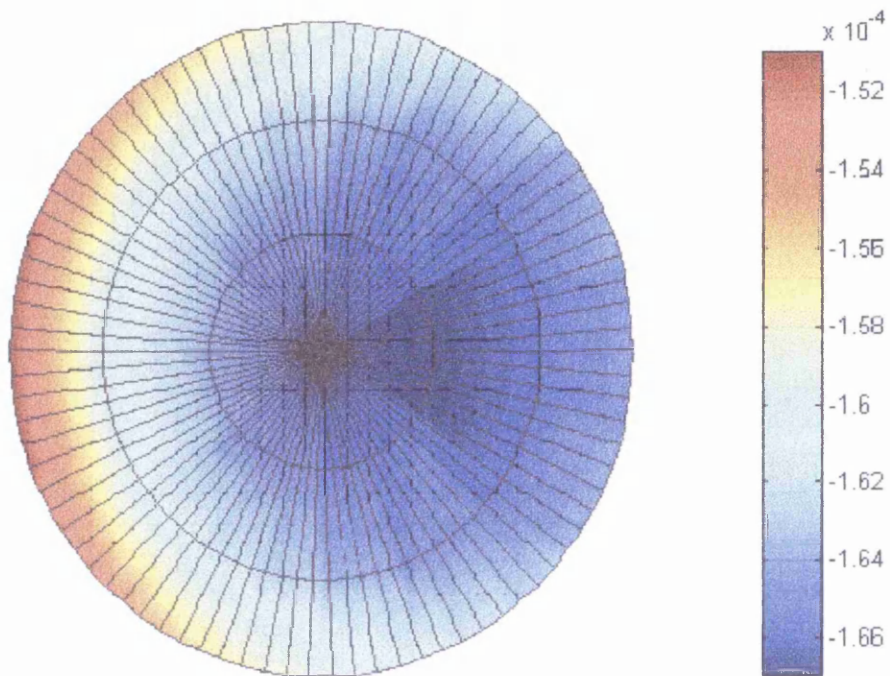
Heat map with graph showing electromagnetic potential variation over the cornea following central 10-degree focal stimulation.



Likewise Figure 4.11 shows a heat map and graph of the corneal potential distribution following peripheral focal stimulation of the same size.

Figure 4.11

Heat map with graph showing electromagnetic potential variation over the cornea following peripheral 10 degree focal stimulation.



Following minor modifications to the three-dimensional model, ring stimuli of 10-degree width may also be simulated. The corneal potential distribution was examined when ring stimulation simulations were performed both centrally (approximately 10 degrees from central axis) and peripherally. This was achieved by setting each node on the three-dimensional retina to equal zero apart from the nodes to allow focal ring stimulation. Figures 4.12 and 4.13 show heat maps and graphs of the corneal potential distribution following central and peripheral ring stimulation respectively.

From the data collected in this section, analysis of potential distribution changes following different types of stimulation may be performed. This will provide a theoretical insight into areas of high corneal potential which will allow some optimisation of recording positions for both full field and, more importantly in this case, multi-focal electroretinography.

Figure 4.12

Surface heat map with graph demonstrating corneal potential changed due to a central ring stimulus.

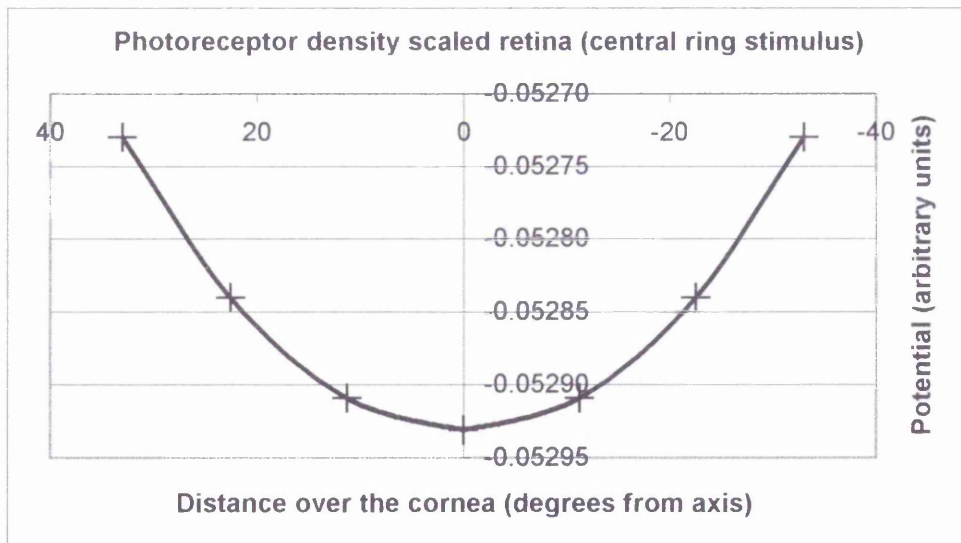
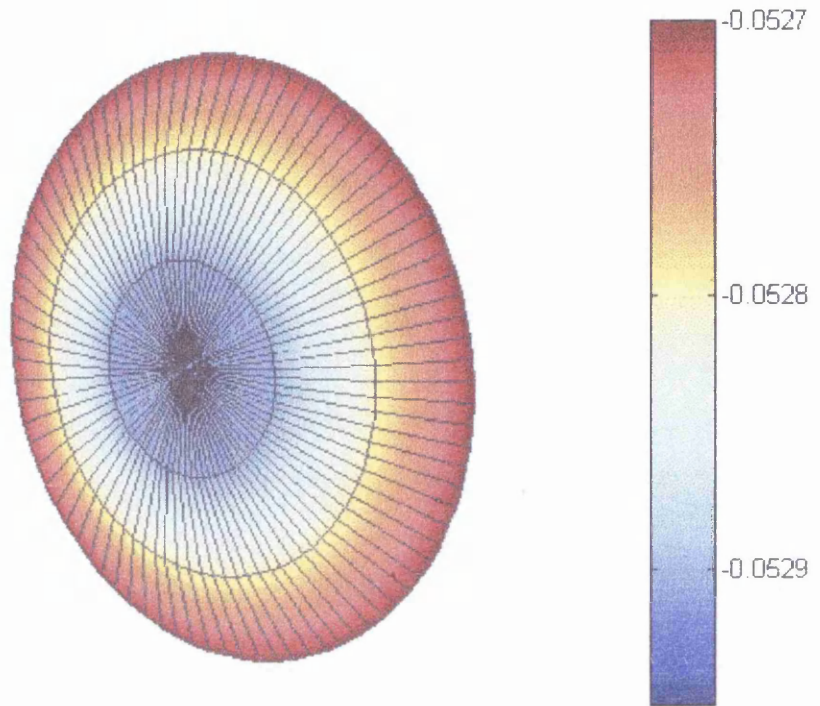
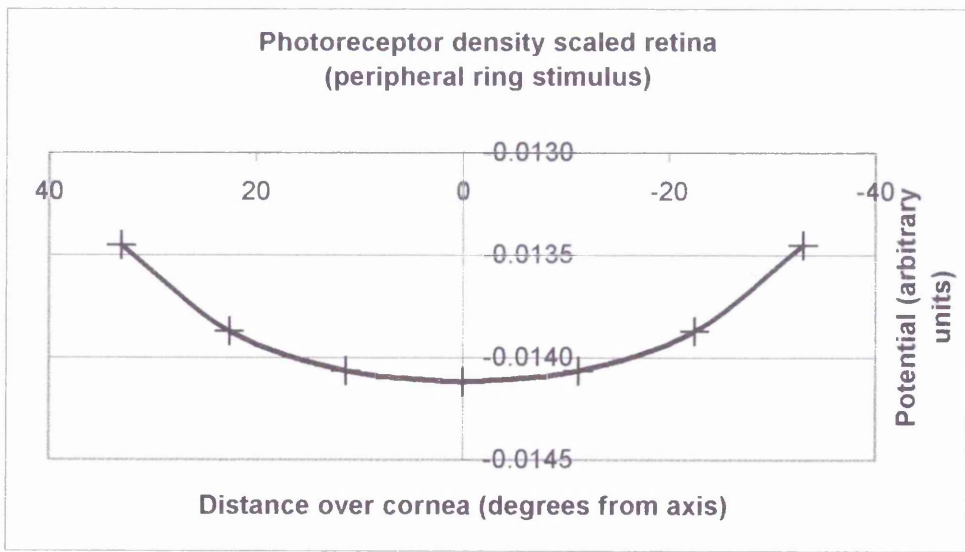
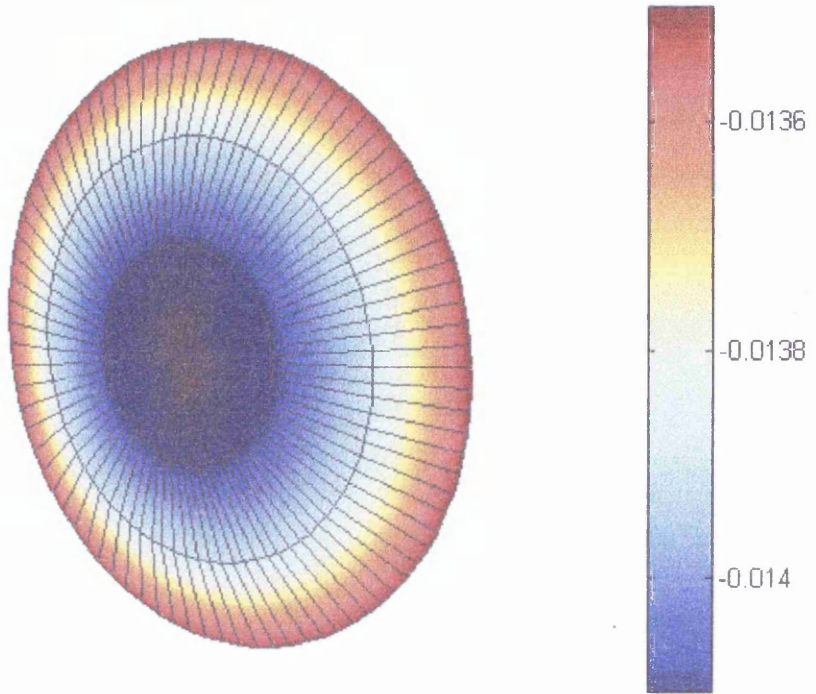


Figure 4.13

Surface heat map with graph demonstrating corneal potential changes due to a peripheral ring stimulus.



Results

The maximum variation in potential over the surface of the cornea for a full field global stimulus with both homogeneous and photoreceptor density scaled retina was found to be approximately 1%. As the stimulated retina in both cases is axially symmetrical, the potential distribution across the cornea is also found to be axially symmetric.

Calculations of the potential field following stimulation of the photoreceptor density scaled retina with a 10-degree central focal spot showed overall that corneal calculated potentials were approximately two orders of magnitude smaller than previous full field stimulus potentials. However, the change in potential over the corneal surface is found to be much smaller than 1% due to the small area of retina stimulated.

Calculations of the potential field following a peripheral 10-degree focal spot stimulation with a photoreceptor density scaled retina highlight the truly characteristic nature of the corneal potential field and its dependence on the retinal area stimulated. The calculated corneal potentials following a peripheral stimulation of this nature are approximately 3 orders of magnitude smaller than the initial photoreceptor density scaled global response. The change in potential over the corneal surface was calculated to be approximately 10%.

The potential field was calculated following both central (approximately 10 degrees off axis) and peripheral ring stimulation of approximately 10-degree width. Again the heat maps are found to be highly characteristic of the stimulus conditions. The calculated corneal potential variation following central ring stimulation was found to be less than 1%. However the calculated corneal potential variation following peripheral ring stimulation was found to be approximately 4%.

Conclusions

The symmetrical (1%) variation in corneal potential following both homogeneous and photoreceptor density scaled retina was considered very encouraging. Many centres currently practising electrophysiology in both the UK and Europe use single site electrodes, (eg. gold foil, HK loop, DTL fibre electrodes) in preference to Burian Allen contact lens electrodes, recording electromagnetic potentials from the lower fornix of the eye. This initial experiment predicts that for global stimulation of the eye, the optimal site

for signal recovery is a 'ring' around the cornea itself. Both single site and Burian Allen electrodes are therefore optimally positioned to record the maximum signal produced *in vivo*. However, to its advantage, the Burian Allen electrode is easily positioned while single site electrodes are often difficult to position, localise and reproduce.

Focal stimulation of central and peripheral areas is found to produce characteristic corneal plots that clearly indicate the site of retinal stimulus. Central focal stimulation produces much reduced potential amplitudes due to the size of the stimulus area. Peripheral focal stimulation of the same size highlights the effect of photoreceptor density scaling. The model predicts even smaller corneal potentials in this case due to retinal photoreceptor density scaling. As the magnitude or 'strength' of the retina is much less at the periphery the resulting corneal potentials are correspondingly smaller. The fact that the change in potential over the corneal surface may be calculated to be approximately 10 % poses some questions regarding the use of single site electrodes for focal and multifocal electroretinography. A difference in corneal potential of this size is considered of significance to future 'mono-electrode' multifocal electrophysiological recording techniques that involve peripheral focal stimulation.

Central and peripheral ring stimulation of the model was also found to significantly influence the corneal potential values calculated by the model. The central ring stimulus was found not to have as significant an influence (less than 1% variation over the cornea) as the peripheral ring stimulus (approximately 4% variation over the cornea). This is believed to be due to the closer proximity of the peripheral stimulus site than the central stimulus site to the cornea.

4.3 Focal and Ring Scotoma Simulation

In the same way as for focal and ring stimulation, it is possible to modify the three-dimensional model to simulate focal and ring scotomas (areas not stimulated). This approach may prove to be useful in examining how the corneal potential distribution may be modified for specific disease processes. Two disease processes are described that relate to loss of function (i.e. lack of electrical stimulation) of specific photoreceptors of the retina.

Cone dystrophy is an inherited disorder, (autosomal dominant, autosomal recessive and X-linked recessive mechanisms). The patient usually presents earlier in the disease process than with rod dystrophies as central vision is affected. It produces a loss in visual acuity and a central scotoma region. Colour vision is also affected. Electrophysiology of these patients reveals absent cone ERG's. However, rod ERG's may be completely unaffected in the early stages of the disease. The three-dimensional model may be used to simulate cone dystrophy over an area of central localised dysfunction, a central spot scotoma (<http://www.lkc.com/retinal.html>).

Retinitis pigmentosa (RP) is the most common type of retinal degeneration and may in some cases progress from tunnelling of vision to complete blindness. This again is an inherited disorder, (autosomal dominant, autosomal recessive and X-linked recessive mechanisms) and it affects mainly rod photoreceptor function. As the disease progresses some cone function may still be recorded after the rod response is extinguished. The three-dimensional model is capable of simulating to some extent the early stages of this disease process as the peripheral retina is dominated with rod photoreceptors. Simulating a peripheral ring of localised dysfunction therefore 'mimics' the disease, (<http://www.lkc.com/retinal.html>).

Methods

In order to evaluate the possible corneal potential variations likely to occur in cone dystrophy, the three-dimensional model was modified to simulate a central area of localised dysfunction. In this case, the nodes of the retina that made up the central 10-degrees were set to equal zero and all others set to their photoreceptor density scaled value. Following convergence of the three-dimensional model a heat map and graph of the potential distribution over the retina were produced, Figure 4.14.

Corneal potential variations likely in retinitis pigmentosa were examined by setting a ring of nodes on the peripheral retina to equal zero. In this way an attempt to mimick localised rod dysfunction is made. Following convergence of the three-dimensional model a heat map and graph of the potential distribution over the retina were again produced, Figure 4.15.

Figure 4.14

Surface heat map with graph illustrating the change in corneal potential distribution following central focal scotoma simulation

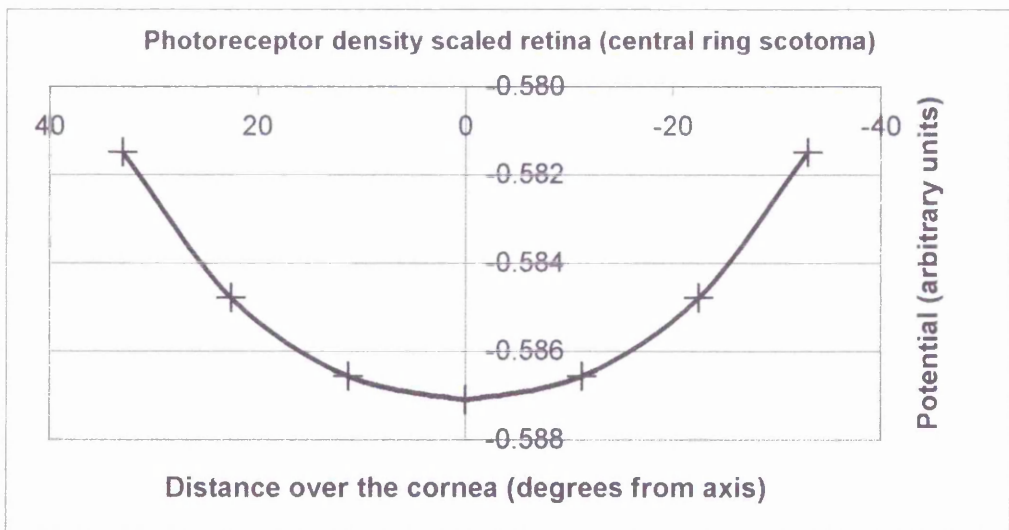
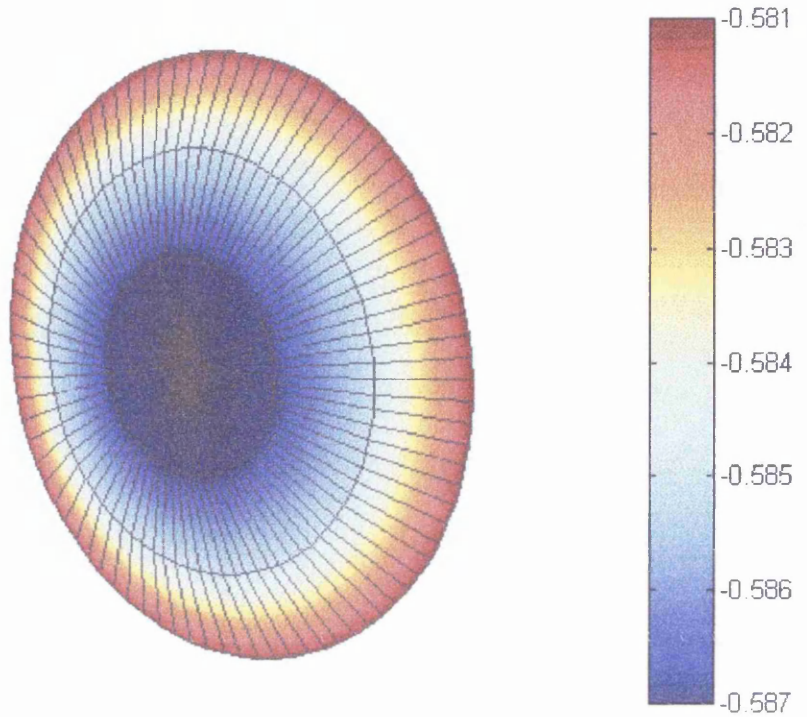
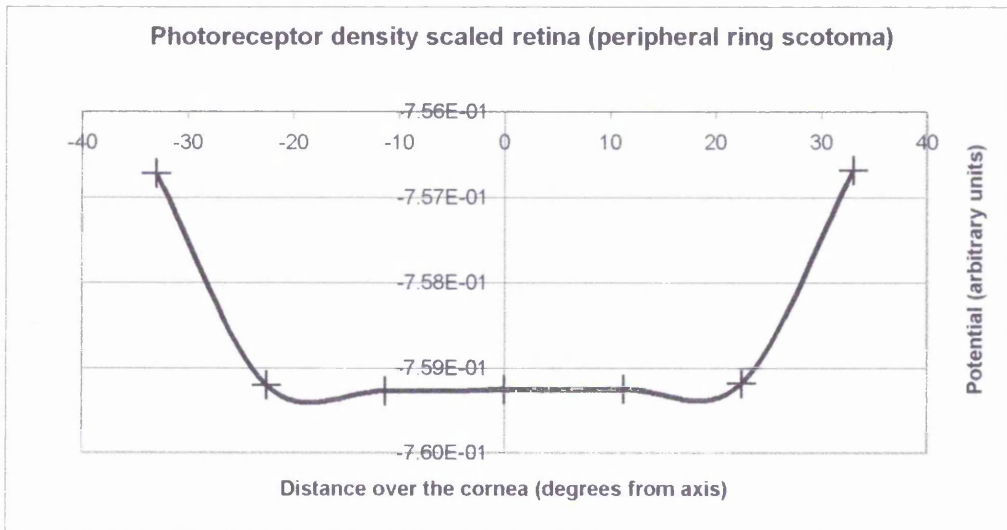
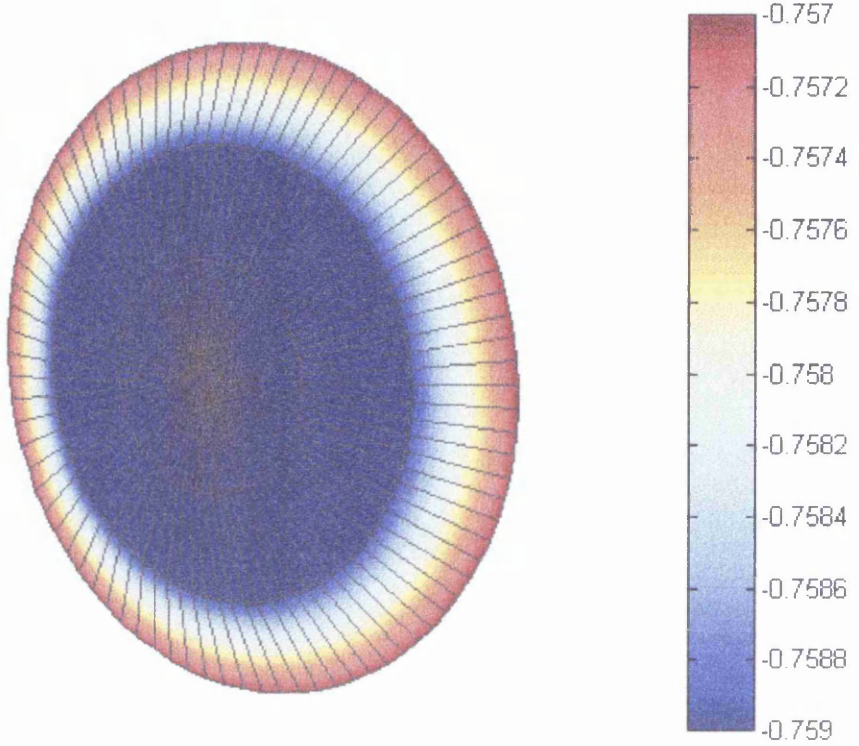


Figure 4.15

Surface heat map with graph illustrating the change in corneal potential distribution following peripheral ring scotoma simulation.



Results

Figure 4.14 shows the corneal potential distribution following simulation of a central localised area of retinal dysfunction. These data show a 1% variation in corneal potential from central to peripheral corneal regions and only a 3% reduction in overall corneal potentials from previous global values.

Figure 4.15 shows the corneal potential distribution following simulation of a peripheral localised ring scotoma. These data again show approximately 1% difference in corneal potential from central to peripheral corneal regions. Of interest in this case is the 25% difference in corneal potential from previous global values.

Conclusions

The three-dimensional model has again been modified to simulate localised scotoma conditions occurring at the retina. These conditions have been chosen to mimic specific disease processes. Results from experiments simulating a central area of localised dysfunction have found only a 3% reduction in maximum corneal potential from those recorded using a 'normal retina'. This figure is assumed to be highly dependent on the size of the central scotoma as in the model (and presumably in the eye) it directly affects the retinal source strength.

Results from experiments simulating a peripheral ring of localised dysfunction have also found a characteristic potential distribution. The 'shape' of the potential distribution in this case is 'slightly flatter' than for the central scotoma. This is believed to be due to the close proximity of the dysfunction to the corneal site. The 25% difference between global stimulation potentials and those calculated following peripheral ring scotoma simulation is believed to be due to the large number of dysfunctioning photoreceptors necessary to simulate a 10-degree width stimulus throughout the full 360 degrees of the globe.

These findings to some extent confirm the experience of many ocular electrophysiologists who agree that fairly gross dystrophy of the retina must occur before significant reduction in the amplitudes of recorded global electroretinograms are found.

4.4 Summary and Conclusions

The flexibility of the three dimensional model has enabled theoretical predictions of both intra-ocular and corneal potential distribution fields for a wide variety of parameters. For a full field retinal stimulus a difference in potential of 1% is found between the central and peripheral regions of the cornea. This is considered encouraging as electromagnetic potentials are presently recorded following global stimulation from a single corneal or scleral electrode often difficult to position or localise. It is reassuring that a calculated maximum difference of only 1 % exists over the entire corneal area of measurement.

Characteristic changes in corneal topography are observed when the location of focal stimuli is varied. Experiments have been performed using both focal spot and ring stimuli and scotomas. These data have given an insight into optimal electrode positioning and confirmed the frequent findings of full field global responses from many ocular electrophysiology centres.

It is now considered necessary to further quantify potential changes experienced at the corneal surface. This may be undertaken practically for a wide variety of retinal stimulus types to enable future, more accurate assessment of the optimal electrode placement for a variety of electroretinographic recordings. Theoretical calculations of this sort may be found to have a direct influence on the electrode of choice for a number of applications by identifying areas of the cornea with increased signal recovery. Optimisation of the localisation of recording sites will be useful for improving signal to noise ratios in current multi-focal applications, which involve concurrent focal stimulation of a large number of discrete areas of the retina.

Chapter 5

Topographical Potential Measurements

5.0 Introduction

The preceding chapters have described in detail the construction, validation and use of a three-dimensional theoretical electromagnetic model of the human eye. In the previous chapter, simulations were undertaken to calculate the theoretical topographical potential changes, induced by the retina. These potentials may be measured physiologically over the anterior surface of the eye. The following work outlines how anterior surface potentials may actually be measured and compared with previously calculated theoretical results.

5.1 Anterior Surface Potential Measurement

The measurement of anterior surface potentials is routinely made using standard, documented techniques (Marmor *et al* 1989, Marmor *et al* 1994, Marmor *et al* 1996). These have been developed to ensure the recording of accurate, reproducible results from centres worldwide allowing legitimate intercomparisons between centres to be made. Although the 'gold standard' electrode of choice is accepted worldwide to be the Burian Allen type contact lens electrode (Marmor *et al* 1989), it is known that a large variety of other 'less invasive' electrodes may be used for this purpose. The characteristics of the most common types have already been described in Chapter 1, Introduction. These include common artefact problems, impedance and specific recording characteristics (Barber, 1994). For this reason, the electrode chosen should therefore always be selected carefully to ensure its suitability for the application required.

When an electroretinographic signal of any kind is measured, the 'active' electrode detects the electrical impulse produced at the retina. This electrode is positioned at the anterior surface of the eye and is compared to a 'reference' signal simultaneously recorded from a reference point on the patient. It is very important that both the

'active' and 'reference' electrodes are of the same type (i.e. made of the same metal) as any differences will cause an 'offset' in the electrical potential between the signal and reference detection. Significant potential differences are found between metals and in some cases can be very large compared with the magnitude of the recording itself.

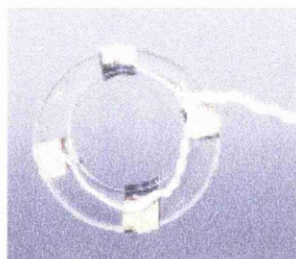
Movement of the eyeball or uneven fitting of the 'active' or 'reference' electrode will also produce artefacts in the recordings. An additional source of noise will occur when photic stimulation strikes the electrode surface and generates a photovoltaic signal appearing as a spike early in the recording. If the electrode surface is shielded from the light source this artefact is effectively removed.

5.2 Examination of the Anterior Surface Potential Distribution

In order to examine electromagnetic potential distribution changes, *in vivo*, 'standard' gold foil electrodes were used in various 'non-standard' positions. Four electrodes were applied to a post-operative haptic shell using an ophthalmic adhesive 'Hystoacryl'. This adhesive is often used in ophthalmic surgery to bind together sections of sclera when sutures are considered impractical to seal the wound. The electrodes were applied to the posterior surface of the shell around the perimeter in a sector arrangement (Figure 5.1). The shell was made to specific measurements of the subjects' right eye and the central 10mm diameter was removed to ensure unimpeded optics. Post-operative haptic shells are used routinely to aid conjunctival healing following eye surgery.

Figure 5.1

Four gold foil electrodes positioned on a 'post operative haptic' shell producing a quadrupolar scleral electrode



Connecting wires from each electrode surface were twisted together to make the assembly easier to manage. A topical anaesthetic (1.0% Benoxinate) was administered and the scleral electrode was then placed on the eye such that the electrodes were

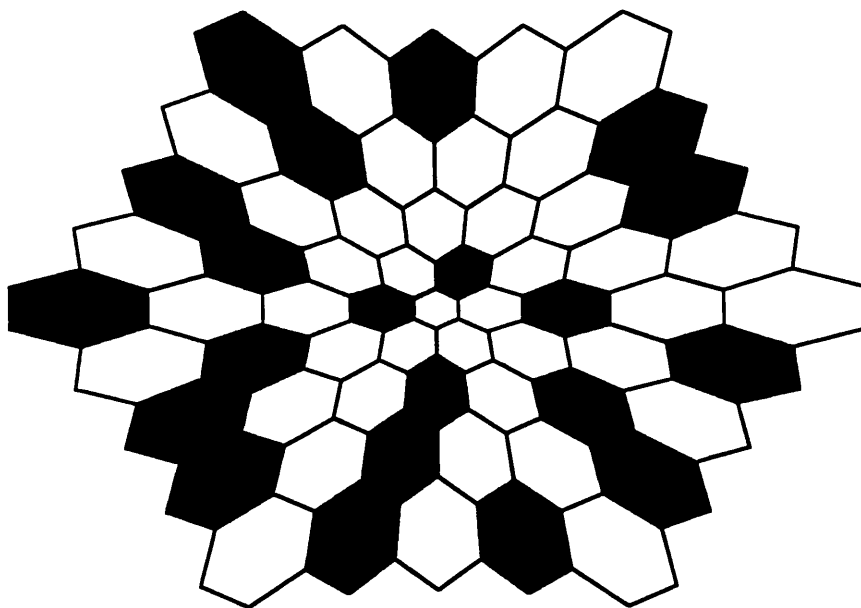
positioned superiorly, inferiorly, temporally and nasally on the orbit. To ensure stability of the scleral shell in this position, the twisted connecting wires were taped to the subjects' cheek. In this arrangement, with the electrodes in contact with the sclera, measurements of retinal electrical signals may be made simultaneously from four independent sites during any type of retinal focal or global stimulation.

5.3 Multi-focal Stimulation of the Eye

Multi-focal electroretinography is a means by which individual focal responses evoked by a number of discrete stimulus elements on the retina may be extracted from the composite retinal signal using a fast 'm transform' algorithm (Sutter E.E 1991). This technique enables topographical maps of retinal function to be constructed from a single electrode site. This is possible as the multi-focal electroretinogram is designed to stimulate a large number of retinal locations. The luminance of each element within the densely packed stimulus array is modulated independently using a pseudo random binary 'm sequence'. The contrast of the luminance modulation is close to 100% and the mean luminance of the entire display remains nearly constant, as approximately half the stimulus elements are white and half black during each video frame, (Figure 5.2).

Figure 5.2

The Multifocal Stimulus



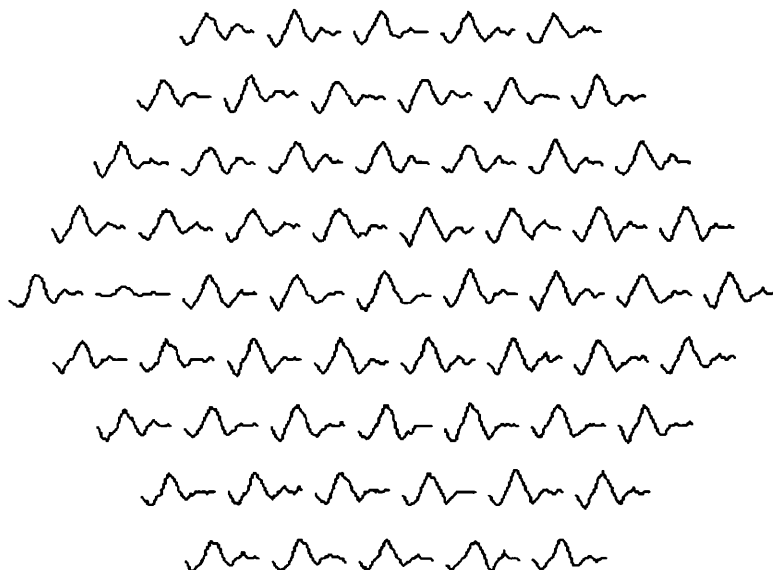
As the signals from each of the independent areas of the retina are small (typically nV), artefacts and associated noise should be minimised as much as possible. The

recording quality of any evoked response is determined primarily by the electrode subject interface, i.e. the electrode impedance. To achieve as low impedance as possible, care should be taken to clean the site of electrode placement. A good connection to ground is essential and all unused channels in the amplifiers (including the pre-amplifier) should be shorted out. The length of the electrode leads should also be kept to a minimum and not looped or positioned in close proximity to other power lines.

Following multi-focal stimulation and data collection of impulses from the retina, the system display shows each local ERG signal displayed in a hexagonal array similar in topography to the stimulus array (Figure 5.3). The large volume of data produced during each recording session is then processed to allow the user to visualise the electrophysiological signals on a topographical basis. To achieve this each waveform may be reduced to a unique number that serves as a measure of either the retinal response amplitude or latency. As with the ERG waveform, the amplitudes are measured from peak to peak values for both 'a' and 'b' waves. Implicit time is measured from the time of stimulus onset to the peak of the 'b' wave amplitude.

Figure 5.3

System display showing localised ERG signals one from each area stimulated.



If the amplitude (A) of the waveform (r) is the true signal (s) with added or subtracted noise (n) then an assessment of the amplitude of a waveform is achieved. One of note is the Root Mean Square (RMS)

$$A = \sqrt{r \bullet r}$$

Equation 5.1

This may also be expressed as

$$A = \frac{(s^2 - 2 \cdot sn + n^2)}{\sqrt{r \bullet r}}$$

Equation 5.2

It can be seen from this equation that there is an added noise component of n^2 .

A variation of this method of amplitude measurement is the Scalar Product of a template t and the waveform to be measured.

$$A_s = \sqrt{t \bullet r}$$

Equation 5.3

If the template is set to be the normalised average of the measured waveform and we express this in the same manner as equation 5.2 we have.

$$A_s = \sqrt{s(s+n)} = \sqrt{s^2 + sn}$$

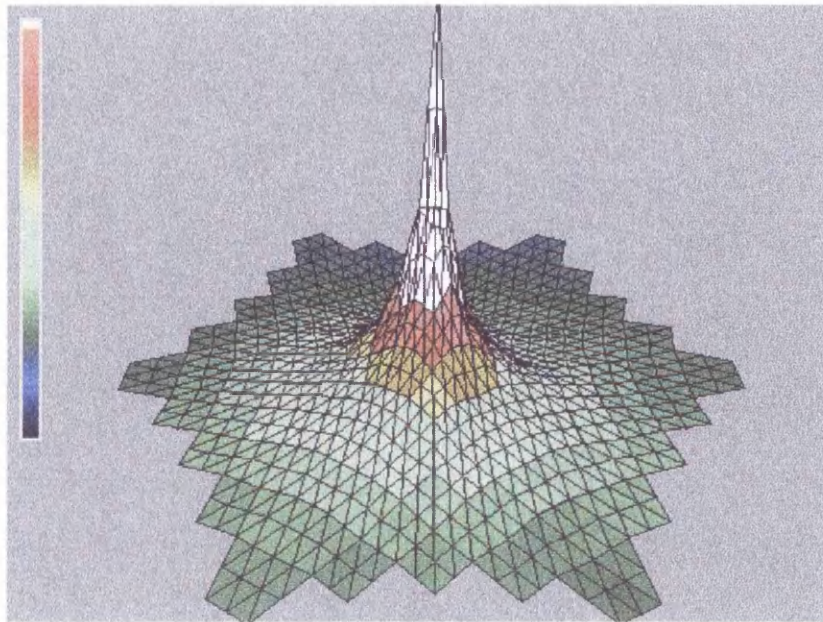
Equation 5.4

This equation does not have an extra added noise component, and if data from an adequate number of controls is available then a more accurate template may be used. This new template is therefore a direct measure of the median normalised values from the control data and may consist of say 61 separate waveform templates (Parks 1998).

The local response estimated by this technique is generated by stimulus elements of different sizes in an attempt to stimulate equal numbers of photoreceptors. They have no direct physiological meaning unless they are converted to response densities by normalising to a unit retinal area. This is achieved by dividing each scalar product value by the area subtended and then by the stimulus element that generated it. The resulting values may be displayed (Figure 5.4) in a three-dimensional response density plot.

Figure 5.4

Three dimensional response density plot



An interpolation procedure (by subdividing stimulus elements and taking the mean) is employed to derive a pattern of finer resolution. This data may then be used in comparisons with other age matched data using confidence plots previously calculated in the assessment of age grouped controls. These illustrate any deviation in the recorded signals from normative values.

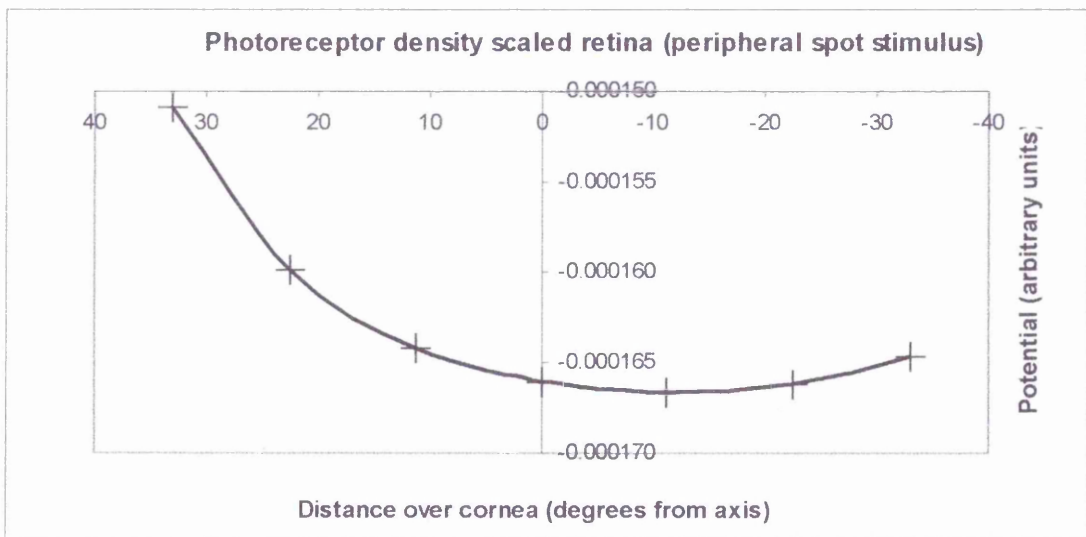
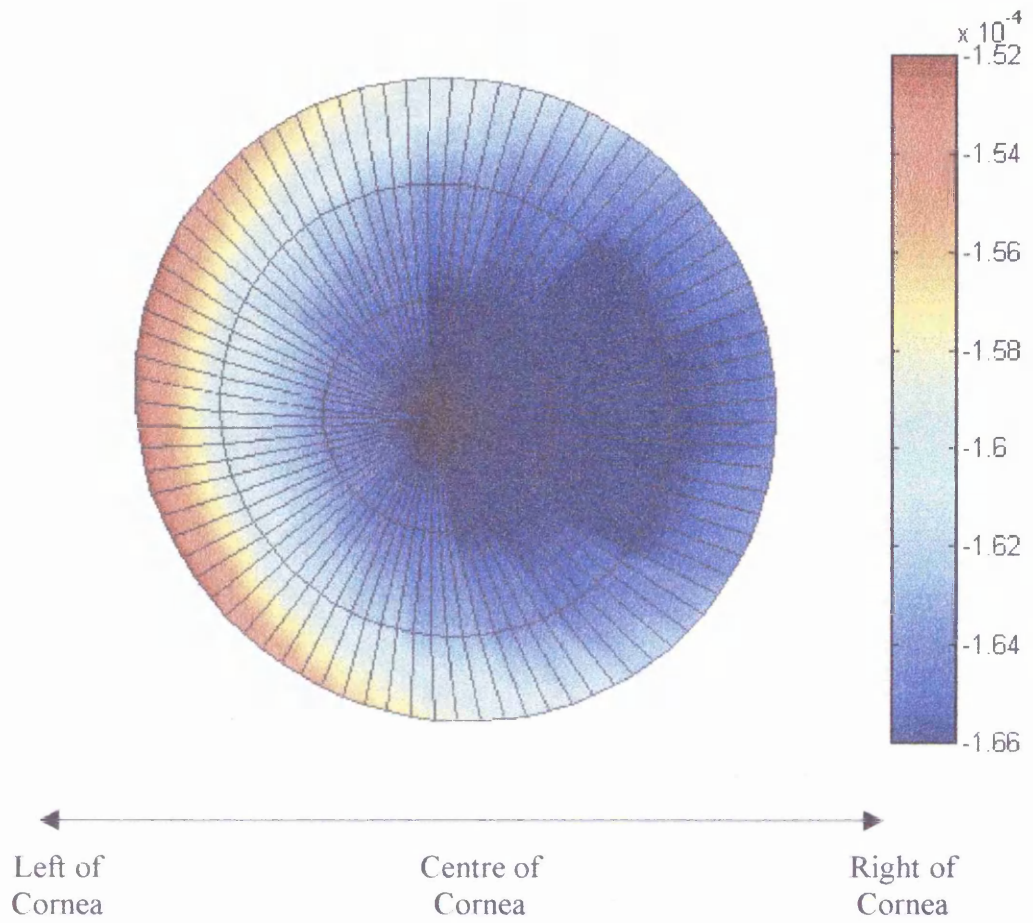
5.4 Comparison of recordings using multifocal stimulation

In order to compare the previously constructed three-dimensional mathematical model calculations and the recordings from the post operative haptic shell electrodes, the model was modified to calculate the corneal potential topography following stimulation of a similar type.

Method

The model was modified to simulate a peripheral focal stimulation of approximately 10 degrees in size at 60 degrees from the horizontal axis. A surface heat plot and graph showing how the potential distribution varies across the cornea were then constructed (Figure 5.5).

Figure 5.5 Surface heat plot and graph showing electrical topography changes following single 10 degree peripheral stimulation.



When wide-field stimulation is used, the accurate measurement of peripheral responses makes severe demands on all aspects of signal acquisition. It may be possible to maximise these small signals by selecting the optimum position of the recording electrodes over the cornea. In order to attempt this comparisons were made between calculated theoretical potential topography changes and *in vivo* measurements over the surface of the eye using the quadrupolar scleral electrode

Scleral Electrode Measurements

Following maximal dilation of the subject's pupil using 1.0% tropicamide, topical application of 1.0% benoxinate was also administered. The post operative haptic shell electrode was then placed in position as described previously with the four gold foil electrodes superiorly, inferiorly, temporally and nasally. To ensure stability during the recording procedure it was secured in position by taping the twisted connecting wires to the subject's cheek. A reference (Ag/AgCl) skin electrode was positioned on the subject's outer canthus and secured in position.

For all electrode measurements, the stimulus was an in house designed multi-focal electroretinography system (MFERG) and was set to stimulate 100 degrees of the visual field in order to maximise peripheral visual field recordings. The system uses a digital polysilicon projection system with a maximum screen intensity of 1500 candelas per metre square and a refresh rate of 75Hz. A series of eight minute (15 bit), wide field multi-focal stimulus sequences were acquired. Recovered waveforms were amplified using a custom made four-channel amplifier system with the filter bandwidth set at 1 Hz to 300 Hz to ensure preservation of true waveform shape (Keating *et al* 1997).

Results

Theoretical Calculations

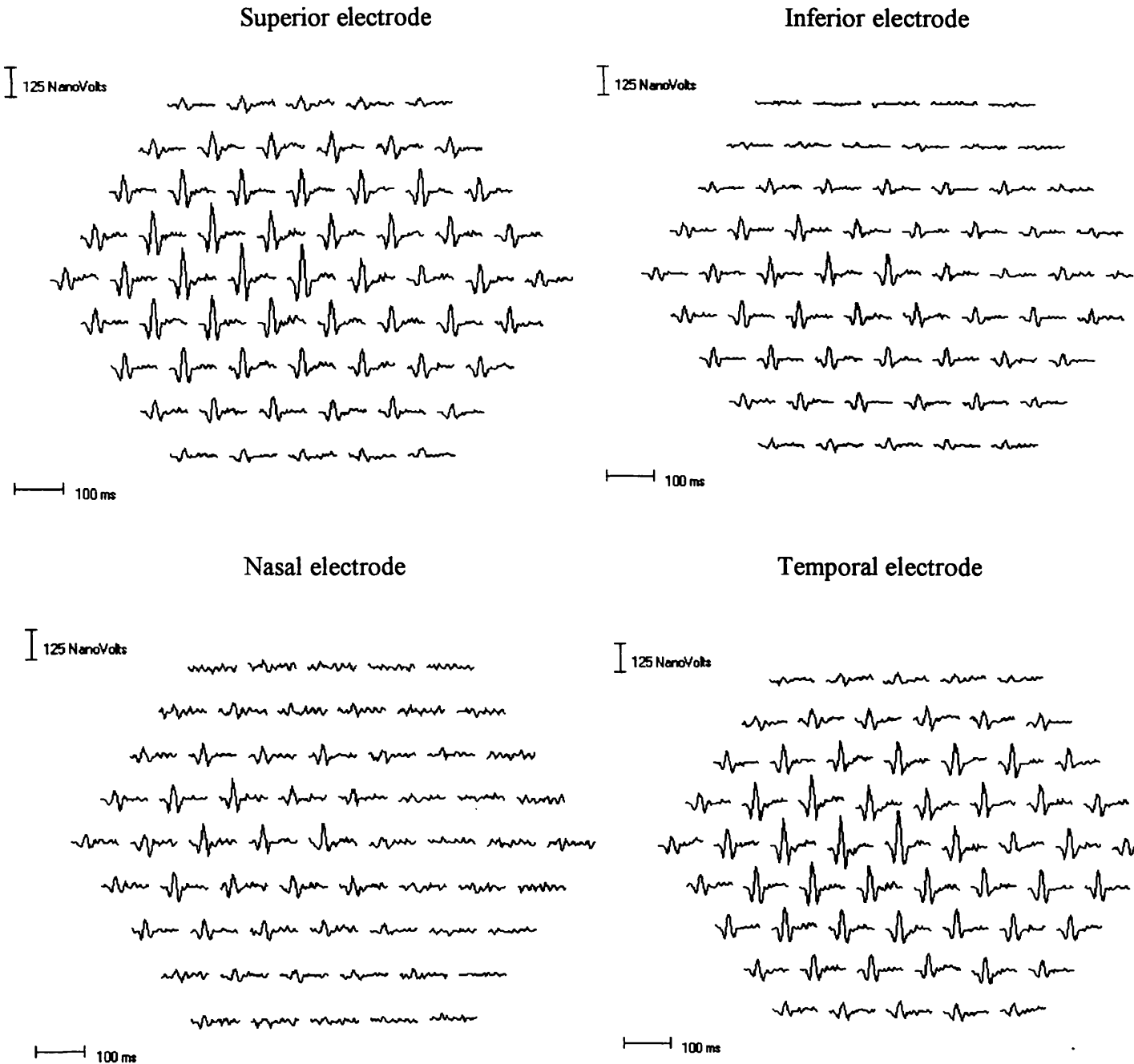
A three dimensional model was used to simulate the action of light producing a retinally activated electromagnetic field within the human eye. Simulation of a theoretical focal spot of 10-degrees in size at a peripheral site 60 degrees from the horizontal axis of the model eye revealed a change in corneal potential from the site nearest stimulation to the site furthest from it of approximately 9 %. The heat plot (Figure 5.5) has been scaled to highlight the topographical potential distribution changes.

The impetus for validating this theoretical result against *in vivo* results from the quadrupolar scleral electrode is increasing evidence that measurement of peripheral retinal function may give a valuable insight into the the pathogenesis of a number of retinal disorders. Latency shifts have been reported in the peripheral retina in areas of normal visual field in patients with Retinitis Pigmentosa (Hood *et al* 1998, Parks *et al* 1998) and in patients with Age Related Macular Degeneration (Parks *et al* 2000). Variation in anterior surface potential due to the site of stimulation will be even more critical when wide field stimulation is used, eg. peripheral retinal loss in patients with Vigabatrin toxicity (McDonagh *et al* 2000).

Results from in vivo Scleral Electrode Measurements

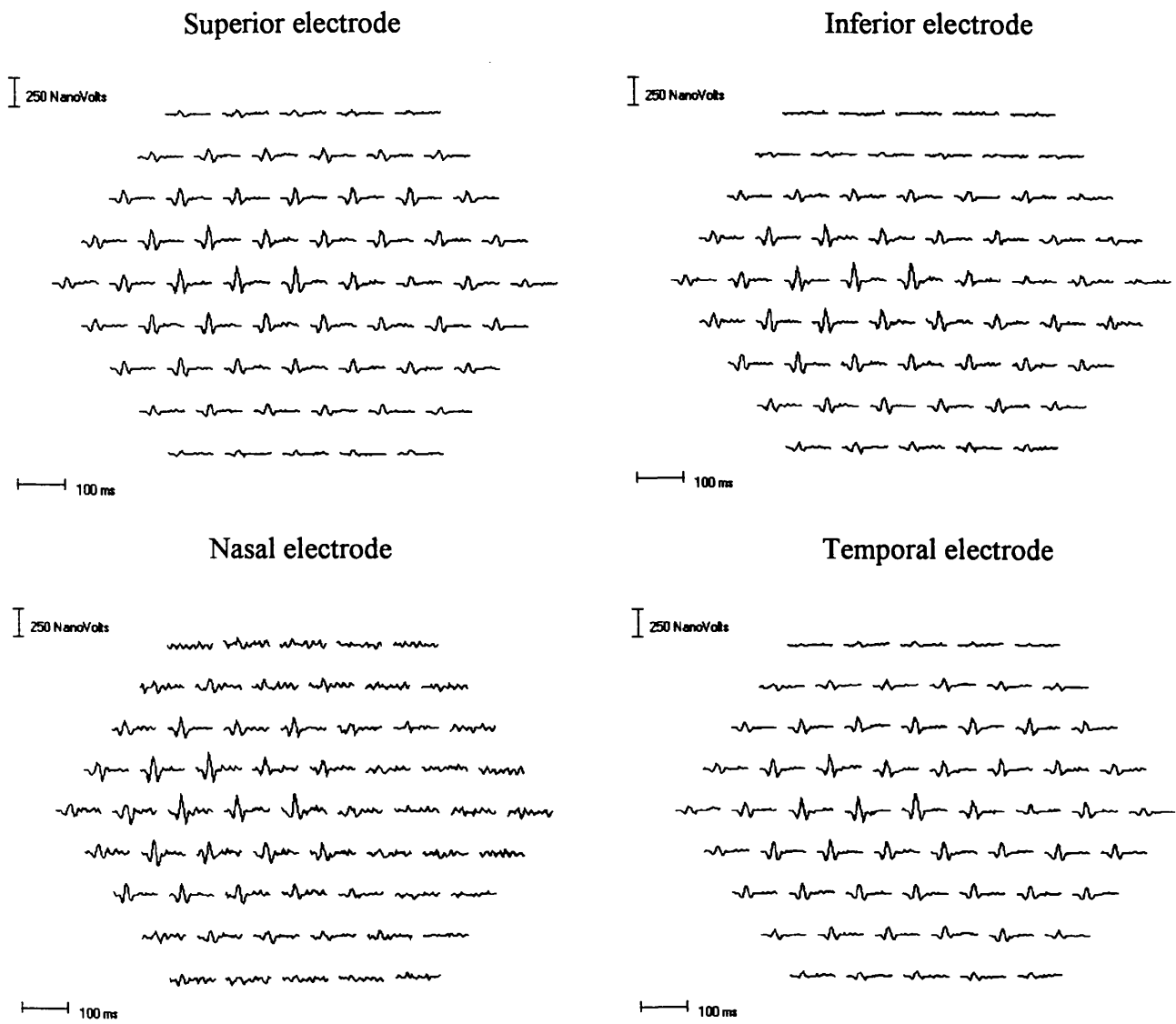
In this case four multifocal data sets were simultaneously acquired from each of the four electrodes on the post-operative haptic shell (Figure 5.6). In all of these data sets the signals recorded were referenced to the outer canthus skin electrode. It is immediately apparent that signals from the nasal field are larger than those from other quadrants for each electrode site. This may be due to the greater photoreceptor density in that part of the retina; Curcio *et al.* (1990) state that cone density is 40-45% higher in nasal compared to temporal retina at equivalent eccentricities.

Figure 5.6 Raw data traces from the four electrode sites



Since there is no gross angular asymmetry about the axis inside the eye, consideration of the geometrical relationships between the four electrode positions on the cornea and a stimulus area at the fovea suggests that the central trace should be of the same amplitude in each electrode. Since the central traces are not the same in the raw data, it is assumed that the differences are a function of the signal processing procedures and the trace arrays have therefore been normalised (Figure 5.7).

Figure 5.7 Normalised trace arrays giving equal amplitudes at the central element



As is common in multifocal experiments, different areas of each trace array were summed in order to simplify the analysis. The results of these summed responses are shown in Table 5.1. A visual inspection of the peripheral responses (Figure 5.7) shows dramatic differences in the signal amplitudes of the peripheral responses depending on the location of the recording electrode used. The superior and inferior electrode sites show similar traces for the temporal and nasal fields yet significant differences are apparent for superior/inferior field measurements. The superior field signals are four times larger when measured with the superior electrode than with the inferior electrode. Although the inferior field is larger when measured with the inferior electrode, the difference is not so apparent as with the superior field.

Table 5.1 Amplitude values for summed traces for superior, inferior, nasal and temporal fields for the four electrode sites.

Average Values	Superior field <i>NV/degree²</i>	Inferior field <i>nV/degree²</i>	Nasal field <i>nV/degree²</i>	Temporal field <i>nV/degree²</i>
Inferior electrode	19	98	128	75
Superior electrode	79	69	129	99
Nasal electrode	51	65	148	27
Temporal electrode	68	89	109	112

A similar picture is observed for the nasal and temporal electrodes. The superior and inferior fields are similar in both electrode positions (except that the nasal electrode tracings are noisier). However the temporal field is four times larger when measured with the temporal electrode than with the nasal electrode. Similarly, the nasal field is larger when measured with the nasal electrode.

Conclusions

A mathematical model has been used to accurately predict the change in corneal / scleral potentials following focal peripheral retinal stimulation. The model predicts that a 9 % difference in corneal potential would be found between the site nearest and the site furthest away from a peripheral focal stimulation site of 10 degrees at an angle of 60 degrees from the horizontal axis. Following a practical investigation using a new scleral electrode, it was found that a difference of up to 75% may exist over the corneal / scleral surface when the retina is peripherally focally stimulated.

5.5 Summary and Conclusions

The theoretical model predicted changes in corneal/scleral potentials following focal stimulation. For a peripheral focal stimulus of 10 degrees diameter placed at 60 degrees from the centre of the retina, an amplitude difference of 9 % between the site nearest to the location of focal stimulation and the site furthest away is predicted. The large discrepancies found between the predicted and physiologically measured variation in corneal/scleral potentials are partly due to model inadequacies. Although the retina is scaled for variations in photoreceptor density with eccentricity, it does not as yet take into account nasal/temporal and superior/ inferior variations.

The practical measurements showed that these differences can be as much as 75% across the cornea. Several variables could contribute towards the practical findings of this study. The position of the reference electrode, in the standard location on the subject's outer canthus, may not be sufficiently remote from the location of the active electrodes. However, the inferior and superior electrodes were equidistant from the reference whereas the results show a clear difference in the inferior and superior fields for these electrodes. There is a physiological variation in peripheral photoreceptor density over the quadrants of the retina, the density being higher in the nasal field (Curcio et al., 1990). Although that study of cone density found no significant superior/inferior differences, threshold values in perimetry are some 10% lower in the peripheral superior field (Katz *et al*, 1986). However, the variation in signal amplitude observed with different positions of the active electrode are too large to be explained by reference electrode position and cone density distribution alone.

Multi-focal electroretinography is most often undertaken using gold foil, HK-loop or DTL electrodes, measurements of the potential distribution being made from a single measurement site. It has been found that three dimensional scalar product plots of these measurements frequently contain reduced amplitude signals superiorly. Until now this was considered to be due to the effect of the upper eyelid on the retinal field causing inhibition of the signal from the superior field. However this paper demonstrates that this may not be the case. A large proportion of the reduction in amplitude of these signals may be due to the fact that an inferior electrode is used to record them.

Modification of the three dimensional electromagnetic model may provide a more accurate insight into the induction of the electromagnetic field throughout the eye. However, in order to gain a more accurate analysis of retinal function it may be necessary to modify current electrode techniques. While it is acknowledged that this problem will not occur when measuring potentials using a Burian Allen electrode as yet it is not the electrode of choice in many European clinics. It may therefore be necessary to apply correction factors to the superior part of the field when using a single inferior electrode to measure the potential topography of the whole retina. This may not be necessary, if data is compared with large control groups using the same electrode configurations. The effect is also more pronounced for wide field multifocal measurements as opposed to the more standard 30 – 60 degree measurements.

Chapter 6

Discussion & Further Work

6.0 Introduction

This work has exposed the complexity and detailed structure of the human eye, which of course is inherent in a structure designed to perform such a broad range of functions in order to produce accurate visual perception. Anatomically the eye is designed to focus light onto photoreceptors positioned on its posterior surface, which elicit electrical impulses that travel to the brain to generate vision. At present many different electrophysiological techniques are used in attempts to gain an insight into the normal and abnormal electrical responses of the eye. By these methods, it is hoped that accurate diagnosis of a wide variety of retinal disorders may be made. Although many of these tests involve complex signal recovery and data processing techniques the advantage of all electrophysiological investigations is that they provide a fairly non invasive, objective measurement of visual function. They are therefore considered by some as more reliable than other more subjective measurements of visual function.

Electrophysiology of the visual system is currently a rapidly expanding area of research. New electrodes designed to overcome inherent limitations are constantly being developed. New techniques in topographical 'mapping' of visual function using multifocal electroretinography are being developed to investigate the adaptive mechanisms of the retina. For all these advancements the primary goal of the researcher is to optimise the signal recovery mechanism enabling small changes in retinal function to be detected. This research has attempted to optimise electrophysiological techniques by providing a valuable insight into variations that may exist in the electromagnetic potential over the corneal / scleral measurement site. It is hoped that further development of these ideas will enable clinical electrophysiologists to more accurately, and with greater confidence, determine the cause, location and likely progression of retinal dysfunction.

6.1 Discussion

Modelling the eye is not a new concept. Many researchers have attempted this rather difficult task developing their ideas from previous models of the heart. The advent of computers sporting faster data processing capabilities has enabled much more complex (and therefore in most cases more accurate) models to be designed. The purpose of designing such a complex model is to enable calculation of the expected changes in potential over the surface of the cornea / sclera. Confident prediction of the variations of corneal potentials in diseased states would provide valuable information for clinical diagnosis.

The limitations of a two-dimensional model of the eye are many, though it may be stated that even a very simple model is better than no model at all. Yet what is to be gained by adding the third dimension? Recently multifocal electroretinography has become more widely used in routine clinics. This means that topographical field plots of retinal function are routinely being requested by clinicians in order to be confident of disease diagnosis. An accurate functional representation of the retina provides the clinician with a clear view of the outcome of surgery or the extent of a particular disease and in some cases its likely progression. It is clear therefore that ocular electrophysiologists are now being asked to provide more detailed 'three-dimensional' retinal potential information.

The three-dimensional model adapted from two-dimensional algorithms extends the limits of our knowledge regarding the behaviour of an electromagnetic field inside the human eye. This work has shown how various calculation experiments may be used to assess the accuracy and usefulness of such a model. Validation experiments comparing the three-dimensional (node by node) calculated numerical potentials with previous two-dimensional analytical potentials have revealed very minor differences between the two. This was an expected conclusion as the three-dimensional model itself is based initially on the two-dimensional numerical model but more fundamentally on the two-dimensional analytical model. In order to achieve the same degree of accuracy however, calculation of the potentials at each node of the three-dimensional model required a far greater number of iterations. This was believed to be due to the increased number of 'nearest neighbour node' potentials utilised by each individual node in the three-dimensional model at which the potential was calculated.

The ever-spiralling increase in computer processing speed has enabled an increased number of iterations to be performed in a very short time. The calculation of a three dimensional potential field is therefore not as time consuming as earlier previous attempts were to discover. Where former two-dimensional models were made simpler to enable shorter calculation times, the three-dimensional model may be made more realistic, hence more complex as computation times are decreasing. It is anticipated that this phenomenon will continue to be a major advantage to complex models of this type.

If the three-dimensional model potential values (and very similar two-dimensional potential values) are compared to micro-electrode data from the literature reasonable agreement is found. However the slight differences are believed to be due to a number of contributory factors. The most obvious is the inaccurate representation of the retina. Both the two-dimensional and the initial three-dimensional models calculate corneal potentials with a completely uniform retinal source representation. This is far from the physiological truth.

Attempts have been made in this work to rescale the retinal source strength to reflect photoreceptor density changes. The absolute accuracy of this development may be concluded to be questionable due to insufficient nodes in regions where the potential is believed to vary rapidly, near the ora serrata. Density corrections in this model were only implemented based on absolute eccentricity. This is inherently a gross over simplification, as it is widely known that photoreceptor density varies naso/temporally as well as superior/inferiorly (Curcio *et al* 1990). Further work in this area with the most recent data would improve the model parameters to enable a more accurate representation of the physiological eye.

The model due to its very simplistic dimensions and geometry introduces further inaccuracies. The physiological eye is not a homogeneous sphere and the representation of the internal structures especially the lens (modelled with a concave posterior surface to facilitate the placement of nodes) all influence the calculation of the theoretical potentials. Comparisons of these calculated potentials therefore are unlikely to be exactly equal to those found physiologically. The model could be substantially improved by ensuring that each structure within the eye was more 'life-like'. The three-dimensional model described in this work is capable of being

modified to represent an oval or, for that matter, any other shape of eye. Calculations to discover the influence of eye shape on potential distribution should be undertaken as this may give a further insight into the variation of corneal potentials between different eyes and different subjects.

The conductivity values of each of the regions within the model have been examined. Large variations in the conductivity values of the lens and cornea were found to produce insignificant effects on the calculated potential distribution. This is believed to be due to the small current density within these structures. However, large variations in the fat/bone, sclera and retinal membrane impedance were found to produce large changes in the global potential distribution. This is most likely to be due to the sharp change in conductivity values between nearest neighbour regions. A thorough literature search was conducted to ascertain a full range of conductivity values for each structure. The actual conductivity value for the human eye may lie outwith this range. A more in depth study is required involving *in vitro* experimental research into the conductivity values of each of the eye structures of the human eye.

The three-dimensional model has been used to simulate peripheral focal stimulation, and corneal potential plots were found to be highly characteristic of the stimulus site. Although a peripheral stimulus has been found to have a greater effect on the percentage difference of the potential distribution over the cornea than a global stimulus, the magnitude of these differences is at least one if not two or three orders of magnitude smaller. A further study examining the effects of peripheral stimulation should be undertaken once further development of the retinal source strength scaling has been undertaken.

In the ring scotoma experiments where a 10-degree ring scotoma is simulated at approximately 60 degrees, only 1% difference in corneal potential is found to exist from central to peripheral corneal regions. However, a 25% difference is found between these and the corneal potentials from previous global values. Initially this difference appears large. However as the nodes on the model retina are unequally spaced, approximately 25% of them are required to be zeroed to simulate a ring scotoma of this type. More equal spacing of the retinal nodes, involving an overall increase in the number of nodes may highlight further the corneal potential changes due to ring scotomas.

The new type of electrode constructed using four gold foil electrodes applied to a post-operative haptic shell was used with an in-house designed polysilicon, wide field multi-focal system to make measurements from the cornea *in vivo*. These experiments were initially very difficult, as insertion of the electrode was 'tricky' and often painful. Consequently only one subject was examined and repeatability and reproducibility studies were therefore not undertaken. It was considered that the geometrical relationships between the four electrode positions on the cornea and a stimulus area at the fovea suggested that the central traces from each of the electrodes should be of the same amplitude. By inspection alone they are quite obviously not ! It is assumed in the text that these differences are a function of the signal processing procedures used to record the signals. However there may be further explanations for this phenomenon including the mechanism of construction of the scleral electrode that is by design, inherently unstable.

Each of the gold foil electrodes used to measure the potential at the corneal surface is essentially 'bent' around the outside edge of the post-operative haptic shell. Complete confidence in an electrical contact with the scleral / tear film boundary therefore cannot be relied upon. During the acquisition of a large number of signals on which to perform averaging procedures, electrical contact may be broken and hence the amplitude of the final signal reduced. The scleral electrode does show however that a detectable difference in potential over the surface of the cornea is apparent and therefore electrode recordings may be concluded to be position dependent. Further experimentation is needed in this area to assess the repeatability and reproducibility of these recordings on an increased number of subjects.

The three dimensional model, predicted approximately 10% variation in scleral/corneal potential when a focal stimulus of 10 degrees in size is used at 60 degrees eccentricity. Although the multifocal recordings were of similar size and eccentricity much larger variations (up to and above 75%) were found to exist physiologically. This large difference is believed to be due to a number of contributory factors, some of which have been mentioned previously. Initially, inadequacies of the model, especially the inaccurate retinal source representation are major factors in such a large discrepancy. Further experimentation must also be undertaken regarding reference electrode placement. Initially the reference electrode

was placed on the outer canthus of the eye tested. Further investigations should show how the reference electrode location influences the amplitude of the signals recorded. A study examining the potentials produced from a multifocal recording referenced to the ipsilateral and contralateral eyes as well as the fore-head should be undertaken.

The variations in signal amplitude observed using the quadrupolar scleral electrode system are too large to be explained by reference electrode position and cone density distribution alone. Active electrode position itself may be equally, if not more important than both these factors. In order to compensate for electrode position it may in future be possible to introduce correction factors for each electrode type and position to enable a more accurate assessment of retinal function.

6.2 Further work

The three-dimensional model is still, it seems, a crude analysis of a biological, functional system. Many more developments are required to extend our understanding of the properties and characteristics of the electromagnetic field within the human eye. The model so constructed is capable of a large degree of flexibility in terms of size and shape of the eye as well as retinal source representation and reference electrode position. Hence future developments are possible and relatively simple to perform.

At present, although each node of the model is referenced to a single node outside the model itself no technique is currently employed to incorporate the more or less influence it has over an 'active' electrode positioned closer or further away from it. Modification of the model along with further experimentation on a larger number of subjects will show the importance of reference electrode position.

Development of the theoretical retina in the naso/temporal as well as the superior inferior dimensions would produce more accurate physiological predictions of the characteristic corneal / scleral potential distribution. The inclusion of more up to data photoreceptor topographic data would instantly facilitate this (Curcio *et al*, 1990).

Although this work has shown how current multi-focal techniques may be used to stimulate the peripheral retina in order to compare physiological recordings with theoretically predicted values, it may be easier to simply focally stimulate the retina

over a number of single areas, (Miyake Y, 1998) one at a time. By this method each component may be evaluated independently and a simpler, legitimate evaluation may be compared with calculated theoretical values.

Scotopic and photopic electroretinographic stimulation is carried out in electrophysiology clinics all over the world to describe a variety of different systemic disease processes, (Papakostopoulos *et al* 1996). The model is capable of being modified to simulate such experimentation. Retinal source scaling to simulate simply rods or cones may be easily inserted into the three-dimensional model parameters to predict the variation in recorded potentials found physiologically.

A model of this kind is essential if we are to understand further the function of the retina and the corneal potential distribution by which we measure this. Though the result of this work is a very simplistic three-dimensional model, variations have been found in the electromagnetic potential over the accessible measurement site (i.e. sclera and cornea). This fact alone provokes the need for more thorough investigation of measurement techniques currently used to facilitate optimal signal recovery.

References

- Abboud S, Eshel Y, Levy S, Rosenfeld M, 'Numerical calculation of the potential distribution due to dipole sources in a spherical model of the head', *Comput. Biomed. Research*, 1994: 27(6); 441 – 455.
- Adachi-Usami E, Chiba Y, 'The clinical ERG detected with skin electrodes', *Acta Soc. Ophthalmol. Jap.*, 1971: 75; 1056-1061.
- Arden G.B, 'Three components of the photocurrent generated in the receptor layer of the rat retina', In *Vertebrate Photoreception*, (edited by Barlow and Fatt), 1977: 141 – 158. Academic Press, New York.
- Arden G.B, Carter R.M, Hogg C, Siegel I.M, Margolis S, 'A gold foil electrode: Extending the horizons for clinical electroretinography', *Investigative Ophthalmology & Visual Science*, 1979: 18; 421 – 426.
- Ary J.P, Klein S.A, Fender D.H, 'Location of Sources of Evoked Scalp Potentials : Corrections for Skull and Scalp Thicknesses', *Biomedical Engineering*, 1981: 28(6); 447 – 452.
- Bach M, Hiss P, Röver J, 'Check-size specific changes of pattern electroretinogram in patients with early open-angle glaucoma', *Documenta Ophthalmologica*, 1988: 69; 315 – 322.
- Bach M, Speidel-Fiaux A, ' Pattern electroretinogram in glaucoma and ocular hypertension', *Documenta Ophthalmologica*, 1989: 73; 173 – 181.
- Barber C, 'Electrodes and the recording of the human electroretinogram (ERG)', *International Journal of Psychophysiology*, 1994: 16; 131-136.
- Barnard A.C.L, Duck I.M, Lynn M.S, 'The application of electromagnetic theory to electrocardiology : I Derivation of the Integral Equations', *Biophysical Journal* 1967: 7; 443 – 462.
- Barnard A.C.L, Duck I.M, Lynn M.S, Timlake W.P, 'The application of electromagnetic theory to electrocardiology : II Numerical Solution of the Integral Equations', *Biophysical Journal* 1967: 7; 463 – 491.
- Bearse M.A, Sutter EE, 'Imaging localized retinal dysfunction with the multifocal electroretinogram,' *J. Opt. Soc* 1996: 13(3); 634 – 640.
- Berninger T.A, Arden G.B, 'The pattern electroretinogram', *Eye*, 1988: 2 Suppl.; S257 – S283.
- Borda R.P, Gilliam R.M, Coats A.C, 'Gold coated mylar electrode for electroretinography', *Documenta Ophthalmologica*, 1978: 15; 339 – 343.

Botazzi, Sturchio, (cited by Oskala A, Lehtinin A), 'Comparative Studies on the Electrical Conductivity of Aqueous Humour, Vitreous Body, Cornea and Sclera', *Acta Ophth.*, 1959: 37; 388 – 394.

Brindley G.S, Hamasaki D.I, 'The Properties and Nature of the R Membrane of the Frog's Eye', *J. Physiol.*, 1963: 167; 599 – 606.

Burian H.M, Allen L, 'A speculum contact lens electrode for electroretinography' *Electroencephalogr. Clin. Neurophysiol.*, 1954: 6; 509 – 511.

Burnes J.E, Kaelber D.C, Taccardi B, Lux RL, Ershler P.R, Rudy Y, 'A field-compatible method for interpolating biopotentials', *Ann. Biomed. Eng.*, 1998: 26(1); 37 – 47.

Bush R.A, Sieving P.A, 'A proximal retinal component in the primate photopic ERG a-wave', *Invest. Ophthalmol. Vis. Sci.*, 1994: 35; 635 – 645.

Bush R.A, Sieving P.A, 'Inner retinal contributions to the primate photopic fast flicker electroretinogram', *J. Opt. Soc. Am.*, 1996: 13; 557 – 565.

Carr R.E, Siegel I.M, 'Electrodiagnostic Testing of the Visual System : A Clinical Guide', New York University Medical Centre, F.A Davis Company, Philadelphia, 1990.

Clark J, Plonsey R, 'The extracellular potential field of the single active nerve fiber in a volume conductor', *Biophysical Journal*, 1968: 8; 842 – 864.

Curcio, C. A., Sloan, K. R., Packer, O., Hendrickson, A. E. and Kalina, R. E, 'Distribution of cones in human and monkey retina: individual variability and radial asymmetry', *Science*, 1987: 236; 579-582.

Curcio C.A, Sloan K.R, Meyers D, 'Computer methods for sampling, reconstruction, display and analysis of retinal whole mounts', *Vision Research*, 1989: 29; 529 – 540.

Curcio C.A, Sloan K.R, Kalina R.E, Hendrickson A.E, 'Human Photoreceptor Topography', *J. Comp. Neurology*, 1990: 292: 497 – 523.

Davey K.R, Thompson B, Wang S, Koblasz A, Nation B, 'Predicting Distributed Retinal Source Activity from ERG data – Part I: Field Theoretic Approach', *IEEE Transactions on Biomedical Engineering*, 1988: 35(11); 942 – 947.

Davey K.R, Thompson B, Wang S, Koblasz A, Nation B, 'Predicting Distributed Retinal Source Activity from ERG data – Part II: Multiple Stimulus Approach', *IEEE Transactions on Biomedical Engineering*, 1988: 35(11); 948 – 952.

Davson H, 'Physiology of the Eye', Fifth Edition, Churchill Livingstone, 1990.

Dawson W.W, Tricke G.L, Litzkow C.A, 'Improved electrode for electroretinography', *Investigative Ophthalmology & Visual Science*, 1979: 18; 998 – 991.

Dewar J, 'The physiological action of light', *Nature*, 1877: 15; 433 – 435.

Doslak M.J, 'The Effects of Variations of the Conducting Media Inhomogeneities on the Electroretinogram', PhD Dissertation, Case Western Reserve University, 1978.

Doslak M.J, Plonsey R, Thomas C.W, 'The effects of variations of the conducting media inhomogeneities on the electroretinogram', *IEEE Transactions on Biomedical Engineering*, 1980: 27(2); 88 – 94.

Dowling J.E, 'The Retina an Approachable Part of the Brain', The Belknap Press of Harvard University Press, 1987.

Fischbarg J, 'Active and Passive Properties of the Rabbit Corneal Endothelium', *Exp. Eye Research*, 1973: 15; 615 – 638.

Frank E, 'Electric Potential Produced by Two Point Current Sources in a Homogeneous Conducting Sphere', *Journal of Applied Physics*, 1952: 23(11); 1225 – 1228.

Geddes L.A, Baker L.E, 'The Specific Resistance of Biological Material – A Compendium of Data for the Biomedical Engineer and Physiologist', *Med and Biol. Eng.*, 1967: 5; 271 – 293.

Gouras P, 'Color Vision', *Prog. Ret. Research*, 1984: 3: 227 – 261.

Gray H, 'Gray's Anatomy', Parragon Book Service Ltd, 1995.

Harrild D.M, Henriquez C.S. 'A Finite Volume Model of Cardiac Propagation', *Ann. Biomed. Eng.*, 1997: 25 ; 337 – 356.

Heckenlively J.R, Arden G.B, 'Principles and Practice of Clinical Electrophysiology of Vision', Mosby-Year Book Inc. USA, 1991.

Helmholtz HLF, 'Ueber einige Gesetze der Vertheilung elektrischer Ströme in körperlichen Leitern mit Anwendung auf die thierisch-elektrischen Versuche', *Ann. Physik und Chemie*, 1853: 89; 211 – 233, 354 – 377.

Hess R.F, Baker C.L, 'Human Pattern-Evoked Electroretinogram', *Journal of Neurophysiology*, 1984: 51(5); 939 – 951.

Heynen H, van Norren D, 'Origin of the electroretinogram in the intact macaque eye II – current source density analysis', *Vision Research*, 1985: 25(5); 709-715.

Henriquez C.S, 'An examination of a computationally efficient algorithm for modeling propagation in cardiac tissue', *Innov Technol Biol Med*, 1989: 10; 23 – 35.

Henriquez C.S, 'Simulating the electrical behaviour of cardiac tissue using the bidomain model', *Crit Rev Biomed Engr*, 1993: 21; 1 – 77.

Hodson S, Wigham C, 'The permeability of rabbit and human corneal endothelium', *Journal of Physiology*, 1983: 342; 409-419.

Holland M.G, Herr N, 'The electroretinographic potential field. I. Differential and vector electroretinography', *Am. J. Ophthalmol.* 1964: 57; 466 – 475.

Holland M.G, Herr N, 'The electroretinographic potential field. Localization of retinal lesions', *Am. J. Ophthalmol.* 1964: 57; 639 – 645.

Hood D.C, Birch D.G, 'B-wave of the scotopic (rod) electroretinogram as a measure of the activity of human on-bipolar cells', *J. Opt. Soc. Am.*, 1996: 13; 623 – 633.

Hood D.C, Holopigian K, Greenstein V, Seiple W, Li J, Sutter E.E, Carr R.E, 'Assessment of local retinal function in patients with retinitis pigmentosa using the multi-focal ERG technique', *Vision Research*, 1998: 38(1); 163 – 179.

Hood D.C, Greenstein V, Frishman L, Holopigian K, Viswanathan S, Seiple W, Ahmed J, Robson J.G, 'Identifying inner retinal contributions to the human multifocal ERG', *Vision Research*, 1999: 39; 2285 – 2291.

Job H.M, Keating D, Evans A.L, Parks S, 'A Three Dimensional Electromagnetic Model of the Human Eye: Advances Towards the Optimisation of Electroretinographic Signal Detection', *Medical & Biological Engineering & Computing*, 1999: 37(6); 710-719.

Kanski J.J, 'Clinical Ophthalmology: A Systematic Approach', Second Edition, Butterworths, 1988.

Karwoski C.J, Xu X, Yu H, 'Current-source density analysis of the electroretinogram of the frog : methodological issues and origin of components', *J. Opt. Soc. Am.*, 1996: 13; 549 – 556.

Katz J, Sommer A, 'Asymmetry and variation in the normal hill of vision', *Arch. Ophthalmol.*, 1986: 104; 65 – 68.

Kauppinen P, Hyttinen J, Laarne P, Malmivuo J, 'A software implementation for detailed volume conductor modelling in electrophysiology using finite difference method', *Comput Methods Programs Biomed.*, 1999: 58(2); 191 – 203.

Keating D, Parks S, Evans A.L, Williamson T.H, Elliott A.T and Jay J.L, 'The effect of filter bandwidth on the multifocal electroretinogram', *Documenta Ophthalmologica*, 1997: 92; 291 – 300.

Klyce S.D, 'Electrical profiles in the corneal epithelium', *Journal of Physiology*, 1972: 226; 407-429.

Klee M, Plonsey R, 'Finite difference solution for biopotentials of single cells', *Biophys J*, 1972: 12(12); 1661 – 1675.

Kolb H, 'The neural organisation of the human retina', Chapter 5 in 'Principles and Practices of Clinical Electrophysiology of Vision' (Ed, Heckenlively J.R, & Arden G.B), Mosby Year Book Inc. St Louis, 1991: 25 – 52.

Krakau C.E.T, 'On the Potential Field of the Rabbit Electroretinogram', Acta Ophth. 1958: 36; 183 – 207.

Laarne P, Eskola H, Hyttinen J, Suihko V, Malmivuo J, 'Validation of a detailed computer model for the electric fields in the brain', J. Med. Eng. Technol. 1995: 19(2-3); 84 – 87.

Levett J, 'Dipole Studies : Intraretinal *b* and *d* wave potential fields' Letter to the Editors, Vision Research, 1974: 14; 895 – 897.

Mackenna B.R, Callander R, 'Illustrated Physiology', Fifth Edition, Churchill Livingstone, 1990.

Malmivuo J, Plonsey R, 'Bioelectromagnetism' Oxford University Press, 1995; 113 – 158.

Marmor M.F, Arden G.B, Nilsson S.E.G, Zrenner E, 'Standard for Clinical Electroretinography', Arch Ophthalmol. 1989: 107; 816 – 819.

Marmor M.F, Zrenner E, 'Standard for Clinical Electro-oculography', Arch Ophthalmol. 1993: 111; 601-604.

Marmor M.F, Zrenner E, 'Standard for clinical electrophysiology (1994 update)', Documenta Ophthalmologica, 1995: 89; 199-210.

Marmor M.F, Holder G.E, Porciatti V, Trick G.L, Zrenner E, 'Guidelines for basic pattern electroretinography', Documenta Ophthalmologica, 1996 : 91; 291 – 298.

Maurice D.M, 'Epithelial potential of the cornea', Exp Eye Res., 1967: 6(2); 138 – 40.

McDonagh J, Grierson D.J, Keating D, Parks S, 'The Wide Field Multifocal ERG reveals a retinal defect caused by Vigabatrin toxicity ? – A Case Report' Brit. J. Ophthalmology, 2000 (in press).

Michels R.G, Wilkinson C.P, Rice T.A, 'Retinal Detachment', The C.V Mosby Company, 1990.

Mintchev M.P, Bowes K.L, 'Conoidal dipole model of electrical field produced by the human stomach', Med. Biol. Eng. Comput., 1995: 33(2); 179 – 184.

Miyake Y, 'Focal macular electroretinography', Nagoya J Med Sci, 1998: 61(3-4); 79 – 84.

Modrell R.W, Potts A.M, ' The influence of medium composition, pH and temperature on the transcorneal potential', American Journal of Ophthalmology, 1959: 48; 834 – 842.

Mur G, de Hoop A.T, 'A finite-element method for computing three-dimensional electromagnetic fields in inhomogeneous media', *IEEE Transactions on Magnetics*, 1985: 21(6); 2188 – 2191.

Muzikant A.L, Henriquez C.S, 'Paced activation mapping reveals organization of myocardial fibers: A simulation study', *J Cardiovasc Electrophysiol*, 1997: 8; 281 – 294.

Oksala A, Lehtinen A, 'Comparative Studies on the Electrical Conductivity of Aqueous Humour, Vitreous Body, Cornea and Sclera', *Acta Ophth.* 1959: 37; 388 – 394.

Østerberg, 'Topography of the layer of rods and cones in the human retina', *Acta. Ophth. Suppl.* 1935: 6; 1-103.

Panofsky W.K.H, Phillips M, 'Classical Electricity and Magnetism', Addison-Wesley Publishing Co. Inc. 2nd Edition, 1962: 81 – 82.

Papakostopoulos D, Hart JC, Corral RJ, Harney B, 'The scotopic electroretinogram to blue flashes and pattern reversal visual evoked potentials in insulin dependent diabetes.', *Int J Psychophysiol.* 1996: 21(1); 33 – 43.

Parks S, Keating D, Evans A.L, Williamson T.H, Jay J.L and Elliott A.T, 'Comparison of repeatability of the multifocal electroretinogram and Humphrey perimeter', *Documenta Ophthalmologica*, 1997: 92; 281 – 289.

Parks S, Keating D, Evans A.L, Elliott A.T, Jay J.L, 'A change in delay of multifocal ERGs found in Retinitis Pigmentosa, *Invest. Ophthalmol. Vis. Sci.* 1998: 39 (Suppl.), 891 (Abstract).

Parks S, Keating D, Evans A.L, 'Peripheral retinal dysfunction in age related macular degeneration', *Invest. Ophthalmol. Vis. Sci.* 2000: 41 (Suppl.), 496 (Abstract).

Parks S W, 'Electroretinographic mapping of retinal function : Evaluation and Clinical Application' PhD Thesis 1998, University of Glasgow.

Pauly H, Schwan H.P, 'The Dielectric Properties of the Bovine Eye Lens', *IEEE Trans. on BME*, 1964: Jul; 103 – 109.

Plonsey R, Collin R, 'Principles and Applications of Electromagnetic Fields', New York, McGraw-Hill Book Company Inc. 1961.

Plonsey R, 'Quantitative formulations of electrophysiological sources of potential fields in volume conductors', *IEEE Trans BME* 1984: 31; 868 – 872.

Plonsey R, Barr RC, 'Mathematical modeling of electrical activity of the heart', *J. Electrocardiol.* 1987: 20(3); 219 – 226.

Polyak S.L, 'The Retina', University of Chicago Press, Chicago, 1941.

Riggs L.A, 'Continuous and reproducible records of the electrical activity of the human retina', *Proc. Soc. Exp. Biol.*, 1941: 48; 204 – 207.

Rimmer S, Katz B, 'The Pattern Electroretinogram : Technical Aspects and Clinical Significance', *Journal of Clinical Neurophysiology*, 1989: 6(1); 85-99.

Robbins J, Turner J, 'Assessment of various types of electrode in clinical ERG', *Impulse*, 1988: 5; 2-5.

Robson J.G, Frishman L.J, 'Photoreceptor and bipolar cell contributions to the cat electroretinogram : a kinetic model for the early part of the flash response', *J/ Opt. Soc. Am.*, 1996: 13; 613 – 622.

Rodieck R.W, Ford R.W, 'The cat local electroretinogram to incremental stimuli', *Vision Research*, 1969: 9(1); 1-24.

Rosen E, Rosen W, 'Ophthalmology', *Medico-Legal Practitioner Series*, Cavendish Publishing Ltd, 1997.

Rush S, Abildskov J.A, McFee R, 'Resistivity of Body Tissues at Low Frequencies', *Cir. Res.*, 1963: 12; 40 – 50.

Schwan H.P, Kay C.F, 'The Conductivity of Living Tissues', *Ann. N.Y. Acad. Sci.*, 1957: 65; 1007 – 1013.

Sidman R.D, Giambalvo V, Allison T, Bergey P, 'A method for localization of sources in human cerebral potentials evoked by sensory stimuli', *Sensory Processes*, 1978: 2; 116 – 129.

Spalton D.J, Hitchings R.A, Hunter P.A, 'Atlas of Clinical Ophthalmology', Second Edition, Wolfe Publishing, 1994.

Steinberg R.H, Linsenmeier R.A, Griff E.R, 'Three light evoked responses of the retinal pigment epithelium', *Vision Research*, 1983: 23(11); 1315 – 1323.

Straatsma B.R, Hall M.O, Allen R.A and Crescitelli F (Eds.) 'The Retina', Los Angeles: University of California Press 1969.

Sutter E.E, Vaegan, 'Lateral interaction component and local luminance nonlinearities in the human pattern reversal ERG', *Vision Research*, 1990: 30(5); 659 – 671.

Sutter E.E, 'The fast m-transform : A fast computation of cross-correlations with binary m-sequences', *Siam J. Comput.* 1991: 20; 686 – 694.

Sutter E.E, Bearse M.A. Jr, 'The optic nerve head component of the human ERG', *Vision Research*, 1999: 39; 419 – 436.

Sutter E.E, Tran D, 'The field topography of ERG components in man – I. The photopic luminance response', *Vision Research*, 1992: 32(3); 433-46.

Tepas D.I, Armington J.C, 'Electroretinograms from non-corneal electrodes', *Investigative Ophthalmology & Visual Science*, 1962: 1: 784 – 786.

Tomita T, Yanagida T, 'Origins of the ERG waves', *Vision Research*, 1981: 21; 1703-1707.

Tortora G.J, Grabowski S.R, 'Principles of Anatomy and Physiology', Seventh Edition, Harper Collins College Publishers, 1992.

Trowbridge C.W, 'Three-dimensional field computation', *IEEE Transactions on Magnetics*, 1982: 18(1); 293 – 297.

Van Buren J.M, 'The retinal ganglion cell layer', Charles C. Thomas, Springfield, Illinois, 1963.

van Schijndel N.H, Thijssen J.M, Oostendorp T.F, Cuypers M.H.M, Huiskamp G.J.M, 'The Inverse Problem in Electroretinography : A Study Based on Skin Potentials an a Realistic Geometry Model', *IEEE Transactions on Biomedical Engineering*, 1997: 44(2); 209 – 211.

Vey E.K, Kozak W.M, Danowski T.S, 'Electroretinographic testing in diabetics : a comparison study of the Burian-Allen and the Henkes corneal electrodes', 1980: 48(2); 337 – 344.

Witnall S.E, 'Anatomy of the Human orbit and accessory organs of vision', Robert E Kreiger Publishing Co, 1979.

Wolff E 'Anatomy of the Eye and Orbit' rev. Warwick R. Philadelphia : W.B Saunders, 1976.

Ziólkowski M, Brauer H, 'Methods of Mesh Generation for Biomagnetic Problems', *IEEE Transactions on Magnetics* 1996: 32(3); 1345 – 1348.

Web site addresses

<http://alpha.ipfw.edu/histo-embryo/histeye.html>

<http://sog1.me.qub.ac.uk>

<http://webvision.med.utah.edu/anatomy.html>

<http://webvision.med.utah.edu/GC1.html>

<http://webvision.med.utah.edu/IPL.html>

<http://webvision.med.utah.edu/sretina/html>

<http://webvision.med.utah.edu/OPL1.html>

<http://webvision.med.utah.edu/photo1.html>

<http://webvision.med.utah.edu/photo2.html>

<http://webvision.med.utah.edu/photo2.html#densities>

<http://www.lkc.com/retinal.html>

<http://www.mac-ndt.com/>

Appendix A

Original development of a two-dimensional analytical model along with the associated complex mathematics (from 'The Effects of Variations of the Conducting Media Inhomogeneities on the Electroretinogram' PhD Thesis Case Western Reserve, M.J Doslak, 1978)

Three equations are developed to describe the generalised potentials in each of the regions shown in Figure 2.2 using classical field theory (Panofsky & Phillips 1962). They may be written as equations A1, A2 and A3.

$$\Phi_1 = \frac{K}{\sigma_A} \sum_{n=0}^{\infty} A r^n P_n(\mu)$$

For $r < R_1$

Equation A.1

$$\Phi_2 = \frac{K}{\sigma_B} \sum_{n=0}^{\infty} \left[B r^n + \frac{C}{r^{n+1}} \right] P_n(\mu)$$

For $R_1 < r \leq R_2$

Equation A.2

$$\Phi_3 = \frac{K}{\sigma_C} \sum_{n=0}^{\infty} \left[D r^n + \frac{E}{r^{n+1}} \right] P_n(\mu)$$

For $R_2 \leq r \leq R_3$

Equation A.3

where

$$\mu = \cos \theta$$

$P_n(\mu)$ = Legendre Function

K = arbitrary constant

A,B,C,D,E = constants to be evaluated

The boundary conditions are set such that

$$\sigma_A \frac{\partial \Phi_1}{\partial r} = \sigma_B \frac{\partial \Phi_2}{\partial r}$$

when $r = R_1$

Equation A.4

$$\Phi_2 - \Phi_1 = T$$

when $r = R_1$ and $0 \leq \theta \leq \theta_0$

Equation A.5

$$\Phi_2 - \Phi_1 = 0$$

when $r = R_1$ and $\theta_0 < \theta$

Equation A.6

$$\sigma_B \frac{\partial \Phi_2}{\partial r} = \sigma_C \frac{\partial \Phi_3}{\partial r}$$

when $r = R_2$

Equation A.7

$$\Phi_3 - \Phi_2 = 0$$

when $r = R_2$

Equation A.8

$$\sigma_C \frac{\partial \Phi_3}{\partial r} = 0$$

when $r = R_3$

Equation A.9

If Equations A.1 and A.2 are substituted into the first boundary condition (Equation A.4) we have

$$\sum_{n=0}^{\infty} nAr^{n-1}P_n(\mu) = \sum_{n=0}^{\infty} \left[nBr^{n-1} - \frac{(n+1)C}{r^{n+2}} \right] P_n(\mu)$$

at $r = R_1$

Equation A.10

This is simplified to give

$$A = B - \left(\frac{n+1}{n} \right) \frac{C}{R_1^{2n+1}}$$

Equation A.11

If Equations A.1 and A.2 are substituted into the second boundary condition (Equation A.5) then

$$\frac{K}{\sigma_B} \sum_{n=0}^{\infty} \left[Br^n + \frac{C}{r_1^{n+1}} \right] P_n(\mu) - \frac{K}{\sigma_A} \sum_{n=0}^{\infty} Ar^n P_n(\mu) = T$$

at $r = R_1$

Equation A.12

The orthogonality property of Legendre functions is then used and following some simplification we have

$$\frac{\sigma_A}{\sigma_B} \sum_{n=0}^{\infty} \left[BR_1^n + \frac{C}{R_1^{n+1}} \right] P_n(\mu) P_m(\mu) - \sum_{n=0}^{\infty} AR_1^n P_n(\mu) P_m(\mu) = \frac{T\sigma_A}{K} P_m(\mu)$$

Equation A.13

Both sides are then integrated from $\mu = -1$ to 1 and remembering that

$$\int_{-1}^1 P_n(\mu)P_m(\mu)d\mu = 0$$

For $m \neq n$

$$\int_{-1}^1 P_n(\mu)P_m(\mu)d\mu = \frac{2}{2n+1}$$

For $m = n$

we have

$$\frac{\sigma_A}{\sigma_B} \left(BR_1^n + \frac{C}{R_1^{n+1}} \right) \left(\frac{2}{2n+1} \right) - AR_1^n \left(\frac{2}{2n+1} \right) = \int_{\cos\theta_0}^1 \frac{T\sigma_A}{K} P_n(\mu) d\mu$$

Equation A.14

Now solving for A

$$A = \left(\frac{\sigma_A}{\sigma_B} \right) B + \left(\frac{\sigma_A}{\sigma_B} \right) \frac{C}{R_1^{2n+1}} - \left(\frac{2n+1}{2} \right) \left(\frac{\alpha}{R_1^n} \right) \int_{\cos\theta_0}^1 P_n(\mu) d\mu$$

Equation A.15

where

$$\alpha = \frac{T\sigma_A}{K}$$

and K is an arbitrary constant.

Substituting Equations A.2 and A.3 into the third boundary condition (Equation A.6) gives

$$\sum_{n=0}^{\infty} \left[nBr^{n-1} - \frac{(n+1)C}{r^{n+2}} \right] P_n(\mu) = \sum_{n=0}^{\infty} \left[nDr^{n-1} - \frac{(n+1)E}{r^{n+2}} \right] P_n(\mu)$$

For $r = R_2$

Equation A.16

This was then simplified to show that

$$B = \left(\frac{n+1}{n} \right) \frac{C}{R_2^{2n+1}} + D - \left(\frac{n+1}{n} \right) \frac{E}{R_2^{2n+1}}$$

Equation A.17

Equations A.2 and A.3 were substituted into the fourth boundary condition (Equation A.7) and

$$\sum_{n=0}^{\infty} \left[Dr^n + \frac{E}{r^{n+1}} \right] P_n(\mu) = \sum_{n=0}^{\infty} \left[Br^n + \frac{C}{r^{n+1}} \right] P_n(\mu)$$

For $r = R_2$

Equation A.18

This was further simplified, giving

$$B = \frac{-C}{R_2^{2n+1}} + \left(\frac{\sigma_B}{\sigma_C} \right) D + \left(\frac{\sigma_B}{\sigma_C} \right) \frac{E}{R_2^{2n+1}}$$

Equation A.19

Equation A.3 was then substituted into the fifth boundary condition (Equation A.9)

$$\sum_{n=0}^{\infty} \left[nDr^{n-1} - (n+1) \frac{E}{r^{n+2}} \right] P_n(\mu) = 0$$

For $r = R_3$

Equation A.20

following simplification this gives

$$D = \left(\frac{n+1}{n} \right) \frac{E}{R_3^{2n+1}}$$

Equation A.21

Equations A.11, A.15, A.17, A.19, A.21 are five equations with five unknowns which are solved using algebraic manipulation. The solution to these equations is as follows.

$$A = - \left[\frac{a_2}{a_1} k_{43} + 1 \right] \left[\frac{b}{DEN} \right]$$

$$B = - \left(\frac{R_1}{R_2} \right)^{2n+1} k_{43} \left[\frac{b}{DEN} \right]$$

$$C = \frac{1}{a_1 a_4} \left[\frac{b}{DEN} \right]$$

$$D = \left(\frac{a_3}{a_1 \left[1 - \frac{a_3}{a_2} \right]} \right) \left(\frac{\left(\frac{k_1}{k_2 a_4} \right) - 1}{1 + \left(\frac{k_1}{k_2} \right)} + 1 \right) \left[\frac{b}{DEN} \right]$$

$$E = \left(\frac{1}{a_1 a_4 \left[1 - \frac{a_3}{a_2} \right]} \right) \left[k_{43} + 1 \right] \left[\frac{b}{DEN} \right]$$

Equation A.22

Where the following substitutions have been made

$$a_1 = \frac{1}{R_1^{2n+1}}$$

$$a_2 = \frac{1}{R_2^{2n+1}}$$

$$a_3 = \frac{1}{R_3^{2n+1}}$$

$$a_4 = \frac{(n+1)}{n}$$

$$a_5 = \frac{\sigma_A}{\sigma_B}$$

$$a_6 = \frac{\sigma_B}{\sigma_C}$$

$$k_1 = a_2 a_4 - a_3 a_4$$

$$k_2 = a_2 a_6 + a_3 a_4 a_6$$

$$k_3 = 1 + \left(\frac{k_1}{k_2} \right)$$

$$DEN = \left(\frac{a_2}{a_1} \right) k_{43} (1 - a_5) + 1 + \left(\frac{a_5}{a_4} \right)$$

$$k_{43} = \frac{\left\{ \left(\frac{k_1}{a_4 k_2} \right) - 1 \right\}}{1 + \left(\frac{k_1}{k_2} \right)}$$

$$k_4 = \left(\frac{k_1}{k_2} \right) - a_4$$

$$b = \left(\frac{2n+1}{2} \right) \left(\frac{\alpha}{R_1^n} \right) \int_{\cos\theta_0}^1 P_n(\mu) d\mu$$

$$\alpha = T \frac{\sigma_A}{K}$$

These expressions were then inserted into the original generalised potential equations (Equations A.1, A.2 and A.3). By summing with respect to the index n in each of these equations the values of the potentials Φ_1 , Φ_2 and Φ_3 in each of the regions at every point with (r, θ) co-ordinates can be found. This is the analytical solution using this method (Doslak, 1978).

Appendix B

Original development of two-dimensional 'passive node' algorithms

(adapted from 'The Effects of Variations of the Conducting Media Inhomogeneities on the Electroretinogram' PhD Thesis Case Western Reserve, M.J Doslak 1978)

For each node located within the 'passive' region of the volume conductor where there are no sources of current we have

$$\nabla \cdot \sigma \nabla U = 0$$

Equation B.1

Where U is the potential at the node and σ' is the electrical conductivity of the region in which the node exists. As the conductivity was considered to be constant within each block and there were eight regions surrounding each node which may each have had a different conductivity value. Equation B.1 may therefore be written as

$$\sum_{\alpha=1}^8 \sigma'_{\alpha} (\nabla \cdot \nabla U_{\alpha}) = 0$$

Equation B.2

This equation was then evaluated over the whole volume surrounding the node using integration.

$$\sum_{\alpha=1}^8 \sigma'_{\alpha} \int_V (\nabla \cdot \nabla U_{\alpha}) dV = 0$$

Equation B.3

Using Gauss' Divergence theorem this was rearranged and expressed as

$$\sum_{\alpha=1}^8 \sigma'_{\alpha} \oint_S \nabla U_{\alpha} \cdot d\vec{S} = 0$$

Equation B.4

In spherical co-ordinates Laplace's equation was then written as

$$\sum_{\alpha=1}^8 \sigma_{\alpha} \left[\iint \frac{\partial U_{\alpha}}{\partial r} (r^2 \sin \theta) d\theta d\phi + \iint \frac{1}{r} \frac{\partial U_{\alpha}}{\partial \theta} (r \sin \theta) dr d\phi + \iint \frac{1}{r \sin \theta} \frac{\partial U_{\alpha}}{\partial \phi} r dr d\theta \right] = 0$$

Radial Term Theta Term Phi Term

Equation B.5

Where U was the calculated potential at a specific point depending on the potentials and conductivities of the eight surrounding regions. Equation B.5 was the three dimensional form of Laplace's equation and consisted of radial, theta and phi terms. For the two dimensional case this algorithm was simplified. Firstly Doslak considered that the model was symmetric about the axis. Therefore

$$(U_{\alpha}(\phi) = U_{\alpha}(-\phi))$$

Equation B.6

This means that the phi term of Equation B.5 was considered equal to zero. Re-writing and reducing the remaining two terms to two dimensions therefore

$$\sum_{\alpha=1}^4 \sigma_{\alpha} \left[\iint \frac{\partial U_{\alpha}}{\partial r} (r^2 \sin \theta) d\theta d\phi + \iint \frac{1}{r} \frac{\partial U_{\alpha}}{\partial \theta} (r \sin \theta) dr d\phi \right] = 0$$

Equation B.7

Equation B.7 is then rearranged and divided by $\int d\phi = 2\pi$ we are left with

$$\sum_{\alpha=1}^4 \sigma_{\alpha} \left[\int \frac{\partial U_{\alpha}}{\partial r} (r^2 \sin \theta) d\theta + \int \frac{\partial U_{\alpha}}{\partial \theta} (\sin \theta) dr \right] = 0$$

Equation B.8

This equation forms the basis of Doslak's solution to estimate the value of the potential at each node within the passive region of the model. The first four terms of the two dimensional solution were then derived from the first term of Equation B.8

$$\sum_{\alpha=1}^4 \sigma_{\alpha} \int \frac{\partial U_{\alpha}}{\partial r} (r^2 \sin \theta) d\theta$$

Equation B.9

The co-ordinates of the central node are given by (r_0, θ_0) and u_r is set to be the derivative of the potential at a constant r . Therefore the integral in Equation B.9 can be expanded. Effectively the potential is integrated over the surface of each of the four 'cubes'.

$$\begin{aligned} & \sigma_1 \int_{\theta_0-h_2}^{\theta_0} (r_0 - h_1)^2 [-u_r(r_0 - h_1)] \sin \theta d\theta + \\ & \sigma_2 \int_{\theta_0-h_2}^{\theta_0} (r_0 + h_3)^2 [u_r(r_0 + h_3)] \sin \theta d\theta + \\ & \sigma_3 \int_{\theta_0}^{\theta_0+h_4} (r_0 + h_3)^2 [u_r(r_0 + h_3)] \sin \theta d\theta + \\ & \sigma_4 \int_{\theta_0}^{\theta_0+h_4} (r_0 - h_1)^2 [-u_r(r_0 - h_1)] \sin \theta d\theta + \end{aligned}$$

Equation B.10

To simplify the equation manipulation Doslak allows

$$-u_r(r_0 - h_1) = \frac{U_1 - U_0}{2h_1}$$

Equation B.11

and

$$u_r(r_0 - h_3) = \frac{U_3 - U_0}{2h_3}$$

Equation B.12

Equations B.11 and B.12 are substituted into Equation B.10 and further simplified then

$$\begin{aligned}
& U_1 \left[\frac{\sigma_1}{2h_1} (r_0 - h_1)^2 (-\cos(\theta_0) + \cos(\theta_0 - h_2)) + \frac{\sigma_4}{2h_1} (r_0 - h_1)^2 (-\cos(\theta_0 + h_4) + \cos(\theta_0)) \right] + \\
& U_3 \left[\frac{\sigma_2}{2h_3} (r_0 + h_3)^2 (-\cos(\theta_0) + \cos(\theta_0 - h_2)) + \frac{\sigma_3}{2h_3} (r_0 + h_3)^2 (-\cos(\theta_0 + h_4) + \cos(\theta_0)) \right] - \\
& U_0 \left[\frac{\sigma_1}{2h_1} (r_0 - h_1)^2 (-\cos(\theta_0) + \cos(\theta_0 - h_2)) + \frac{\sigma_2}{2h_3} (r_0 + h_3)^2 (-\cos(\theta_0) + \cos(\theta_0 - h_2)) \right] + \\
& \left[\frac{\sigma_3}{2h_3} (r_0 + h_3)^2 (-\cos(\theta_0 + h_4) + \cos(\theta_0)) + \frac{\sigma_4}{2h_1} (r_0 - h_1)^2 (-\cos(\theta_0 + h_4) + \cos(\theta_0)) \right] +
\end{aligned}$$

Equation B.13

This equation shows the development of the four equations that result from the first term of Equation B.8. The second term of Equation B.8 was developed in the same way to reveal

$$\begin{aligned}
& U_2 \left[\frac{\sigma_1}{2h_2} (\sin(\theta_0 - h_2))(-2h_1) + \frac{\sigma_2}{2h_2} (\sin(\theta_0 - h_2))(-2h_3) \right] + \\
& U_4 \left[\frac{\sigma_3}{2h_4} (\sin(\theta_0 + h_4))(-2h_3) + \frac{\sigma_4}{2h_4} (\sin(\theta_0 + h_4))(-2h_1) \right] - \\
& U_0 \left[\frac{\sigma_1}{2h_2} (\sin(\theta_0 - h_2))(-2h_1) + \frac{\sigma_2}{2h_2} (\sin(\theta_0 - h_2))(-2h_3) \right] + \\
& \left[\frac{\sigma_3}{2h_4} (\sin(\theta_0 + h_4))(-2h_3) + \frac{\sigma_4}{2h_4} (\sin(\theta_0 + h_4))(-2h_1) \right]
\end{aligned}$$

Equation B.14

If Equations B.13 and B.14 are now added together we find that the resulting final difference equation is given by

$$U(I, J, K) = \frac{(FR_1 * U(I-1, J, K) + FR_2 * U(I, J-1) + FR_3 * U(I+1, J, K) + FR_4 * U(I, J+1))}{(FR_1 + FR_2 + FR_3 + FR_4)}$$

Equation B.15

where

$$FR_1 = \frac{(r_0 - h_1)^2}{-2h_1} [\sigma_1 (\cos(\theta_0 - h_2) - \cos(\theta_0)) + \sigma_4 (\cos(\theta_0) - \cos(\theta_0 + h_4))]$$

$$FR_2 = \frac{(\sin(\theta_0 - h_2))}{2h_2} [\sigma_1 (-2h_1) + \sigma_2 (-2h_3)]$$

$$FR_3 = \frac{(r_0 - h_3)^2}{-2h_3} [\sigma_2 (\cos(\theta_0 - h_2) - \cos(\theta_0)) + \sigma_3 (\cos(\theta_0) - \cos(\theta_0 + h_4))]$$

$$FR_4 = \frac{(\sin(\theta_0 + h_4))}{2h_4} [\sigma_3 (-2h_3) + \sigma_4 (-2h_1)]$$

Equation B.15 takes into account all variable conductivities and inter-nodal spacing. The conductivity values required for each region are represented by $\sigma_1, \sigma_2, \sigma_3, \sigma_4$ and relate to the surrounding nearest regions for that node. FR_1, FR_2, FR_3, FR_4 are specific weighting factors depending on the location of the node within the volume conductor, the distance between the nearest nodes the derivatives on each side and the surrounding conductivities. If it is assumed that U_0 is the required potential of the node and U_1, U_2, U_3, U_4 are the potentials at the surrounding nodes then

$$U_0 = \frac{FR_1 \cdot U_1 + FR_2 \cdot U_2 + FR_3 \cdot U_3 + FR_4 \cdot U_4}{FR_1 + FR_2 + FR_3 + FR_4}$$

Equation B.16

Appendix C

Original development of two-dimensional 'active node' algorithms

(adapted from 'The Effects of Variations of the Conducting Media Inhomogeneities on the Electroretinogram' PhD Thesis Case Western Reserve, M.J Doslak 1978)

Each node on the retina was represented as a double node (Klee and Plonsey 1972). Every node was made up of two half nodes located just inside and just outside the retinal membrane. Mathematically however, they were considered to lie at exactly the same radius. The boundary conditions for these nodes are such that

$$\sigma_i \frac{\partial \Phi_i}{\partial n} = \sigma_e \frac{\partial \Phi_e}{\partial n}$$

Equation C.1

where

$$\Phi_e - \Phi_i = T - Z_R (\bar{J}_e \cdot \bar{n})$$

Equation C.2

Φ_i = interior half node potential

Φ_e = exterior half node potential

σ_i = interior region conductivity

σ_e = exterior region conductivity

T = double layer strength

Z_R = Retinal membrane impedance

J_e = exterior normal current density

Now as

$$\bar{J}_e = -\sigma_e \frac{\partial \Phi_e}{\partial n}$$

Equation C.3

Equation C.2 may be re-written as

$$\Phi_e - \Phi_i = T + Z_R \left(\sigma_e \frac{\partial \Phi_e}{\partial n} \right)$$

Equation C.4

From Equation C.4 it was shown that

$$\frac{\partial \Phi_i}{\partial n} = C_A \Phi_i - C_B \Phi_1 + C_C \Phi_2$$

$$\frac{\partial \Phi_e}{\partial n} = -C_D \Phi_e + C_E \Phi_3 - C_F \Phi_4$$

Equation C.5

where

$$C_A = \frac{2d_1 + d_2}{d_1(d_1 + d_2)}$$

$$C_B = \frac{d_1 + d_2}{d_1 d_2}$$

$$C_C = \frac{d_1}{d_2(d_1 + d_2)}$$

$$C_D = \frac{2d_3 + d_4}{d_3(d_3 + d_4)}$$

$$C_E = \frac{d_3 + d_4}{d_3 d_4}$$

$$C_F = \frac{d_3}{d_4(d_3 + d_4)}$$

Equation C.6

Using these equations it may be shown that

$$\sigma_i (C_A \Phi_i - C_B \Phi_1 + C_C \Phi_2) = \sigma_e (-C_D \Phi_e + C_E \Phi_3 - C_F \Phi_4)$$

Equation C.7

and

$$\Phi_e = \Phi_i + T + Z_R \sigma_e (-C_D \Phi_e + C_E \Phi_3 - C_F \Phi_4)$$

Equation C.8

then

$$\Phi_e = \frac{[\Phi_i + T + Z_R \sigma_e (C_E \Phi_3 - C_F \Phi_4)]}{(1 + Z_R \sigma_e C_D)}$$

Equation C.9

and

$$\sigma_i C_A \Phi_i + \sigma_i (-C_B \Phi_1 + C_C \Phi_2) = -\sigma_e C_D \left\{ \left[\frac{\Phi_i + T + Z_R \sigma_e (C_E \Phi_3 - C_F \Phi_4)}{1 + Z_R \sigma_e C_D} \right] \right\} + \sigma_e (C_E \Phi_3 - C_F \Phi_4)$$

Equation C.10

Using these equations to solve for Φ_i we arrive at the difference equation for the interior half node potential in terms of the exterior half node potential, the double layer strength, the retinal membrane impedance and the relevant conductivities and adjacent potentials both interior and exterior.

$$\Phi_i = \frac{\left[-\sigma_e C_D \left\{ \frac{[T + Z_R \sigma_e (C_E \Phi_3 - C_F \Phi_4)]}{(1 + Z_R \sigma_e C_D)} \right\} + \sigma_i (C_B \Phi_1 - C_C \Phi_2) + \sigma_e (C_E \Phi_3 - C_F \Phi_4) \right]}{\left[\sigma_i C_A + \left\{ \frac{\sigma_e C_D}{1 + Z_R \sigma_e C_D} \right\} \right]}$$

Equation C.11

The difference equation for the exterior half node potential is derived in a similar manner.

For the exterior half node potential therefore

$$\Phi_i = \Phi_e (1 + Z_R \sigma_e C_D) - T + Z_R \sigma_e (C_F \Phi_4 - C_E \Phi_3)$$

Equation C.12

and

$$\begin{aligned} \sigma_i C_A [\Phi_e (1 + Z_R \sigma_e C_D) - T + Z_R \sigma_e (C_F \Phi_4 - C_E \Phi_3)] + \sigma_i (-C_B \Phi_1 + C_C \Phi_2) = \\ -\sigma_e C_D \Phi_e + \sigma_e (C_E \Phi_3 - C_F \Phi_4) \end{aligned}$$

Equation C.13

Solving for Φ_e the exterior half node potential we have

$$\Phi_e = \frac{\{\sigma_i C_A [T + Z_R \sigma_e (C_E \Phi_3 - C_F \Phi_4)] + \sigma_e (C_E \Phi_3 - C_F \Phi_4) + \sigma_i (C_B \Phi_1 - C_C \Phi_2)\}}{[\sigma_i C_A (1 + Z_R \sigma_e C_D) + \sigma_e C_D]}$$

Equation C.14

This is the difference equation for the exterior half node potential in terms of the interior half node potential, the double layer strength, the retinal membrane impedance and the relevant conductivities and adjacent potentials both interior and exterior. Equation C.11 and C.14 are therefore used to calculate the potentials on the retinal membrane itself.

Appendix D

Original development of the two dimensional algorithms to calculate the potential at the origin

(adapted from 'The Effects of Variations of the Conducting Media Inhomogeneities on the Electroretinogram' PhD Thesis Case Western Reserve, M.J Doslak 1978)

For a node at the origin Doslak derived the difference equation as follows. Starting with Equation D.1 and integrating over the whole volume V we have

$$\int_V \nabla \cdot \nabla U dv = 0$$

Equation D.1

Gauss' divergence theorem was then applied

$$\oint_S \nabla U \cdot d\vec{s}$$

Equation D.2

As he had a symmetrical model, so

$$\frac{\partial U}{\partial \phi} = 0$$

and therefore

$$\iint \frac{\partial U}{\partial r} (r^2 \sin \theta) d\theta d\phi + \iint \frac{1}{r} \frac{\partial U}{\partial \theta} (r \sin \theta) dr d\phi = 0$$
$$\iint \frac{\partial U}{\partial r} (r^2 \sin \theta) d\theta d\phi + \iint \frac{1}{r} \frac{\partial U}{\partial \theta} (r \sin \theta) dr d\phi = 0$$

Equation D.3

The integrals were then rearranged and the constants divided out

$$\int (r^2 \sin \theta) \frac{\partial U}{\partial r} d\theta + \int (\sin \theta) \frac{\partial U}{\partial \theta} dr = 0$$

Equation D.4

Each of these line integrals were then evaluated around the perimeter of each area. The second integral becomes zero since $\theta = 0$ and 180 degrees.

The first integral was re-written as

$$\int_0^{\frac{\pi}{4}} h^2 [u_1(h)] \sin \theta d\theta + \int_{\frac{\pi}{4}}^{\frac{\pi}{2}} h^2 [u_2(h)] \sin \theta d\theta + \int_{\frac{\pi}{2}}^{\frac{3\pi}{4}} h^2 [u_3(h)] \sin \theta d\theta + \int_{\frac{3\pi}{4}}^{\pi} h^2 [u_4(h)] \sin \theta d\theta = 0$$

Equation D.5

If

$$u_1 = \frac{U_1 + U_2 - 2U_0}{h}$$

$$u_2 = \frac{U_2 + U_3 - 2U_0}{h}$$

$$u_3 = \frac{U_3 + U_4 - 2U_0}{h}$$

$$u_4 = \frac{U_4 + U_5 - 2U_0}{h}$$

Then following substitution and rearrangement of Equation D.5 we have

$$U_0 = \frac{[(0.29289)U_1 + U_2 + (1.41422)U_3 + U_4 + (0.29289)U_5]}{4}$$

Equation D.6

This is the difference equation for the single node at the origin. Doslak noted that it depended only on the angular geometry of the adjacent nodes and not on the conductivity or radial separation.

Appendix E Source code for two-dimensional numerical model

```
program Doslak;
```

```
uses
```

```
  Forms,  
  Main in 'Main.pas',  
  Display in 'Display.pas',  
  Angle in 'Angle.pas',  
  Voltage in 'Voltage.pas',  
  Membrane in 'Membrane.pas',  
  Setup in 'Setup.pas',  
  Radius in 'Radius.pas',  
  Mathunit in 'helen\Mathunit.pas',  
  Average in 'Average.pas';
```

```
begin
```

```
  Application.Initialize;  
  Application.CreateForm(TForm1, Form1);  
  Application.Run;  
end.
```

```
unit Main;
```

```
interface
```

```
uses
```

```
  WinProcs, Wintypes, Messages, SysUtils, Classes, Graphics, Controls, Forms, Dialogs,  
  StdCtrls, Setup, Display, Radius, Angle, Mathunit, ExtCtrls, Membrane, Voltage,  
  Average ;
```

```
type
```

```
  TForm1 = class(TForm)
```

```
  {Button Declarations}
```

```
    Button1: TButton;  
    Button2: TButton;
```

```
  {Label declarations}
```

```
    Label1: TLabel;  
    Label2: TLabel;  
    Label3: TLabel;  
    Label4: TLabel;  
    Label5: TLabel;  
    Label6: TLabel;  
    Label7: TLabel;  
    Label8: TLabel;  
    Label9: TLabel;
```

```
  {Edit Box declarations}
```

```
    Edit1: TEdit;
```

```
  {Procedure declarations in this unit}
```

```
procedure FormActivate(Sender: TObject);
procedure Button1Click(Sender: TObject);
procedure Button2Click(Sender: TObject);
procedure Save_to_file(Sender: Tobject);
```

```
private
  { Private declarations }
public
  { Public declarations }
```

```
{Conductivity values for the various regions of the model}
```

```
SigmaAqVit: double;
SigmaSclera: double;
SigmaExtraoc: double;
SigmaLens: double;
SigmaCornea: double;
SigmaAir: double;
```

```
{Internal and External retinal double node conductivity values}
```

```
SigmaInt: double;
SigmaExt: double;
```

```
{Declarations for the retinal membrane}
```

```
RMembraneResistance: double;
RMembraneCapacitance: double;
CapacitiveReactance: double;
InverseRMembraneResistance: double;
InverseRMembraneCapacitance: double;
RMembraneImpedance: complex;
```

```
{Array of the magnitude of the calculated potentials}
```

```
inputUMag: array[1..45,1..44] of real;
```

```
{Real part of the input array}
```

```
inputRU: array[1..45,1..44] of double;
```

```
{Radial co-ordinate array}
```

```
inputR: array[1..45] of double;
```

```
{Theta co-ordinate array}
```

```
inputT: array[1..44] of double;
```

```
{Photoreceptor scaled array}
```

```
retina: array[1..22] of double;
```

```
{Control array}
```

```
control: array[1..10000] of integer;
```

```
{Zeroed potential input array}
```

```
inputU: array[1..45,1..44] of complex;
```

```
{Display array}
```

```
Display: array[1..45,1..44] of integer;
```

```
{Two arrays of double node retinal potentials}
```

```
UA: array[1..22] of complex;
```

```
UB: array[1..22] of complex;
```

```
{Array containing conductivity values}
```

```
SIG: array[1..7] of real;
```

```
fname: string;
```

```

binvalue:array[0..9] of double;

{Integer variables}
No_of_loops,Voltage_Flag,Theta_Flag,Toggle,Iterations,ZoomFlag,RunFlag,RunFlag2: Integer;
N1,N2,N3,N4,NA1,NA2,NA3,NA4,NB1,NB2,NB3,NB4: Integer;
I,IMinus,IP,J,JM,JP,P: Integer;

{Double variables}
TAU,Frequency:Double;
W: Double;
HIM,HIP,RM,RP,TJ,TJP,TJM,HJM,HJP,TM,TP,COM,COP: Double;
D1,D2,D3,D4,CA,CB,CC,CD,CE,CF: Double;
SIGA,SIGB,SIGC,SIGD: Real;
SIG1,SIG2,SIG3,SIG4,SIG5,SIG6: Double;
RI,RIM,RIP: Double;
A,B,C,D: Double;
binlevel,binincrement: Double;

{Complex variables}
tempc,tempc2,tempc3,tempc4,tempc5,tempc6,tempc7,tempc8,tempc9,tempc10: Complex;
tempc11,tempc12,tempc13,tempc14,tempc15,tempc16,tempc17,tempc18,tempc19,tempc20: complex;
Ref_value: Complex;
CAC,CBC,CCC,CDC,CEC,CFC: Complex;
FR1,FR2,FR3,FR4,FR5,RY: Complex;
ANA,ANB,AD,BNA,BNB,BD: Complex;
V,V1,V2,V3,V4,WC: Complex;
maxval,minval: double;
SigmaExtC,SigmaExtCMinus,SigmaIntC,TauC,OneC: Complex;

{Text variables to write values to file}
E,F: Textfile;
end;

var
Form1: TForm1;

implementation

procedure TForm1.Button1Click(Sender: TObject);

var
I,J,K,L,P,Pointer: Integer;

begin
Iterations:=0;

{Initial paramters read in}
Start(Sender);

{Input potential array set to zero}
For J:=1 to 44 do
begin
For I:=1 to 45 do
begin
Cmake(0,0,Form1.inputU[I,J]);

```

```

        end;
    end;

    {Retinal double node arrays set to zero}
    For I:=1 to 22 do
        begin
            Cmake(0,0,Form1.UA[I]);
            Cmake(0,0,Form1.UB[I]);
        end;

    {Assign filenames to output files}
    Form1.fname:='SegAxis.txt';
    AssignFile(Form1.E,Form1.fname);
    Rewrite(Form1.E);

    Form1.fname:='SegCirc.txt';
    AssignFile(Form1.F,Form1.fname);
    Rewrite(Form1.F);

    Repeat

    {Iteration number}
    Form1.Refresh;
    Form1.Edit1.Text:=IntToStr(Form1.Iterations);
    Runflag:=0;

    {Display Routine}
    Eye(Sender);

    Pointer:=1;
    Runflag:=1;
    Form1.I:=1;
    Form1.J:=1;

    {Initial conductivity values set}
    Form1.SIGA:=Form1.SIG[1];
    Form1.SIGB:=Form1.SIG[1];
    Form1.SIGC:=Form1.SIG[1];
    Form1.SIGD:=Form1.SIG[1];

    {First nodal value at 1,1 calculated}
    CMake(0.29289,0,tempc);
    CMake(1.41422,0,tempc2);
    CMake(4,0,tempc3);

    Cmult(tempc,Form1.inputU[2,1],tempc4);
    Cmult(tempc,Form1.inputU[2,44],tempc6);
    Cmult(tempc2,Form1.inputU[2,10],tempc5);

    Cadd(tempc4,Form1.inputU[2,5],tempc7);
    Cadd(tempc5,Form1.inputU[2,37],tempc8);
    Cadd(tempc7,tempc8,tempc9);
    Cadd(tempc9,tempc6,tempc10);

    Cdiv(tempc10,tempc3,Form1.V);

```

```

{New potential found from old one using  $U[I,J]=(W*V)+((1-W)*U[I,J]);$ }
Cmake(Form1.W,0,Form1.WC);
Cmult(Form1.WC,Form1.V,tempc);
Cmake(1,0,tempc2);
Csub(tempc2,Form1.WC,tempc3);
Cmult(tempc3,Form1.inputU[Form1.I,Form1.J],tempc4);
Cadd(tempc,tempc4,Form1.inputU[Form1.I,Form1.J]);
K:=0;
  Repeat
    K:=K+1;
    Form1.I:=Form1.control[Pointer];
    If Form1.I<>99 then    {Membrane routine initiated if I = 99}
      begin
        Form1.IMinus:=Form1.control[Pointer+1];    {IM value}
        Form1.IP:=Form1.control[Pointer+2];        {IP value}

{Radial component of potential calculated}
        Radial(Sender);

        No_of_loops:=control[Pointer+3];
        Pointer:=Pointer+5;

        For L:=1 to Form1.No_of_loops do
          begin
            Form1.J:=Form1.control[Pointer];          {J value}
            Form1.JM:=Form1.control[Pointer+1];      {JM value}
            Form1.JP:=Form1.control[Pointer+2];      {JP value}

{Voltage flag routines if node averaged}
            Form1.Voltage_Flag:=Form1.control[Pointer+3];

{Theta component of potential calculated}
            Form1.Theta_Flag:=Form1.control[Pointer+4];

{Conductivity value changes if necessary}
            if Form1.control[Pointer+2] > 100 then
              begin
                Form1.SIGA:=Form1.SIG[Form1.Control[Pointer+5]];
                Form1.SIGB:=Form1.SIG[Form1.control[Pointer+6]];
                Form1.SIGC:=Form1.SIG[Form1.control[Pointer+7]];
                Form1.SIGD:=Form1.SIG[Form1.control[Pointer+8]];
                Form1.JP:=Form1.control[Pointer+2]-100;
                Pointer:=Pointer+9;
              end
            else
              begin
                Pointer:=Pointer+5;
              end;

        If Form1.Voltage_Flag >0 then Average.Calculate_Average(Sender);

        If Form1.Theta_Flag > 0 then Angle.Theta(Sender);
          end;
        end

```

```

        else
            begin
{Double node potentials calculated}
            Membrane.Retina(Sender);
            Pointer:=Pointer+1;
            end;

        until K=75;

        For P:=1 to 22 Do
            begin
                Form1.inputU[20,P]:=Form1.UA[P];
                Form1.inputU[22,P]:=Form1.UB[P];
            end;

{Graphical display of the calculated potentials}
            Eye(Sender);

{Reference values subtracted from each nodal potential}
            Ref_value:=Form1.inputU[44,35];
            For I:=1 to 45 do
                begin
                    For J:=1 to 44 do
                        begin
                            CSub(Form1.inputU[I,J],Ref_value,Form1.inputU[I,J]);
                        end;
                    end;
                end;

            For J:=1 to 22 do
                begin
                    CSub(Form1.UA[J],Ref_value,Form1.UA[J]);
                end;
                Form1.iterations:=Form1.iterations+1;

{Number of iterations}
            until Form1.Iterations=10000;

            Save_to_file(sender);
            CloseFile(Form1.E);
            CloseFile(Form1.F);
            end;

{Potentials along axis saved to file}
            procedure TForm1.Save_to_file(Sender: Tobject);
            var
                I,J: integer;
            begin
                For I:=Rmax downto 1 do
                    begin
                        write(Form1.E,' ',Form1.inputU[I,1].Re);
                    end;
                For I:=2 to RMax do
                    begin
                        write(Form1.E,' ',Form1.inputU[I,44].Re);
                    end;
                end;
            end;

```

```

end;

For J:= 1 to 44 do
begin
write(Form1.F,' ',Form1.inputU[29,J].Re);
end;
end;

procedure TForm1.FormActivate(Sender: TObject);
begin
Form1.Button2.Caption:='Zoom OFF';
Start(Sender);
runflag:=0;
runflag2:=0;
Eye(Sender);
end;

{Zoom Control}
procedure TForm1.Button2Click(Sender: TObject);
begin
ZoomFlag:=1-ZoomFlag;
If ZoomFlag=1 Then Form1.Button2.Caption:='Zoom ON';
If ZoomFlag=0 Then Form1.Button2.Caption:='Zoom OFF';
Form1.Activate;
end;

end.

```

```

unit Setup;

```

```

interface

```

```

uses

```

```

Windows, Messages, SysUtils, Classes, Graphics, Controls, Forms, Dialogs,
StdCtrls;

```

```

procedure Start(Sender: TObject);

```

```

implementation

```

```

uses Main, Mathunit;

```

```

procedure Start(Sender: TObject);

```

```

var

```

```

I,J,K:Integer;

```

```

tempc2: complex;

```

```

begin

```

```

Form1.Label1.visible:=False;

```

```

Form1.Label2.visible:=False;

```

```

Form1.Label3.visible:=False;

```

```

Form1.Label4.visible:=False;

```

```
Form1.Label5.visible:=False;
Form1.Label6.visible:=False;
Form1.Label7.visible:=False;
Form1.Label8.visible:=False;
Form1.toggle:=0;
```

```
{Over Relaxation Factor}
```

```
Form1.W:=1.88;
```

```
{Conductivity regions}
```

```
Form1.SigmaAqVit:=1;
Form1.SigmaSclera:=0.01;
Form1.SigmaExtraoc:=1.0;
Form1.SigmaLens:=1.0;
Form1.SigmaCornea:=0.01;
Form1.SigmaAir:=1.0;
Form1.RMembraneResistance:=1.67;
Form1.RMembraneCapacitance:=43.3;
```

```
Form1.SIG[1]:=1;
```

```
Form1.SIG[2]:=0.01;
```

```
Form1.SIG[3]:=1;
```

```
Form1.SIG[4]:=1;
```

```
Form1.SIG[5]:=0.01;
```

```
Form1.SIG[6]:=1;
```

```
Form1.SIG[7]:=0;
```

```
{Calculation of retinal membrane impedance}
```

```
Form1.Frequency:=0;
```

```
If Form1.Frequency>0.01 then
```

```
Form1.CapacitiveReactance:=Form1.RMembraneCapacitance/Form1.Frequency;
```

```
Form1.InverseRMembraneResistance:=1/Form1.RMembraneResistance;
```

```
If Form1.Frequency<0.01 then Form1.InverseRMembraneCapacitance:=0;
```

```
If Form1.Frequency>0.01 then Form1.InverseRMembraneCapacitance:=1/Form1.CapacitiveReactance;
```

```
CMake(Form1.InverseRMembraneResistance,Form1.InverseRMembraneCapacitance,Form1.tempc);
```

```
CMake(1,0,tempc2);
```

```
Cdiv(tempc2,Form1.tempc,Form1.RMembraneImpedance);
```

```
Form1.SigmaInt:=Form1.SigmaAqVit;
```

```
Form1.SigmaExt:=Form1.SigmaSclera;
```

```
{Retinal Weighting Factors}
```

```
Form1.NA1:=18;
```

```
Form1.NA2:=17;
```

```
Form1.NA3:=24;
```

```
Form1.NA4:=25;
```

```
Form1.NB1:=19;
```

```
Form1.NB2:=18;
```

```
Form1.NB3:=23;
```

```
Form1.NB4:=24;
```

```
{Radial array}
```

```
Form1.fname:='inputR.txt';
```

```
AssignFile(Form1.E,Form1.fname);
```

```
Reset(Form1.E);
```

```

For I:=1 to 45 do
  begin
    readln(Form1.E,Form1.inputR[I]);
  end;
CloseFile(Form1.E);

```

```
{Theta array}
```

```
Form1.inputT[1]:=0;
```

```
For J:=2 to 9 do
```

```
begin
```

```
  Form1.inputT[J]:=Form1.inputT[J-1]+(Pi/16);
```

```
end;
```

```
Form1.inputT[9]:=85*(Pi/180);
```

```
Form1.inputT[10]:=90*(Pi/180);
```

```
Form1.inputT[11]:=96*(Pi/180);
```

```
Form1.inputT[12]:=101.25*(Pi/180);
```

```
Form1.inputT[13]:=104*(Pi/180);
```

```
Form1.inputT[14]:=107*(Pi/180);
```

```
Form1.inputT[15]:=108.5*(Pi/180);
```

```
Form1.inputT[16]:=110*(Pi/180);
```

```
Form1.inputT[17]:=110.5*(Pi/180);
```

```
Form1.inputT[18]:=111*(Pi/180);
```

```
Form1.inputT[19]:=111.5*(Pi/180);
```

```
Form1.inputT[20]:=111.75*(Pi/180);
```

```
Form1.inputT[21]:=112*(Pi/180);
```

```
Form1.inputT[22]:=112.5*(Pi/180);
```

```
Form1.inputT[23]:=113*(Pi/180);
```

```
Form1.inputT[24]:=113.4*(Pi/180);
```

```
Form1.inputT[25]:=113.8*(Pi/180);
```

```
Form1.inputT[26]:=114.2*(Pi/180);
```

```
Form1.inputT[27]:=114.6*(Pi/180);
```

```
Form1.inputT[28]:=115*(Pi/180);
```

```
Form1.inputT[29]:=116*(Pi/180);
```

```
Form1.inputT[30]:=117*(Pi/180);
```

```
Form1.inputT[31]:=120*(Pi/180);
```

```
Form1.inputT[32]:=123.75*(Pi/180);
```

```
Form1.inputT[33]:=126*(Pi/180);
```

```
Form1.inputT[35]:=129*(Pi/180);
```

```
Form1.inputT[34]:=Form1.inputT[35]-(0.01/Form1.inputR[29]);
```

```
Form1.inputT[36]:=Form1.inputT[35]+(0.01/Form1.inputR[29]);
```

```
Form1.inputT[37]:=135*(Pi/180);
```

```
Form1.inputT[38]:=141*(Pi/180);
```

```
Form1.inputT[40]:=146.25*(Pi/180);
```

```
Form1.inputT[39]:=Form1.inputT[40]-(0.01/Form1.inputR[14]);
```

```
Form1.inputT[41]:=Form1.inputT[40]+(0.01/Form1.inputR[14]);
```

```
Form1.inputT[42]:=157.5*(Pi/180);
```

```
Form1.inputT[43]:=168.75*(Pi/180);
```

```
Form1.inputT[44]:=Pi;
```

```
{Retinal array}
```

```
Form1.fname:='retina2.txt';
```

```
AssignFile(Form1.E,Form1.fname);
```

```
Reset(Form1.E);
```

```
For I:=1 to 22 do
```

```
  begin
```

```

    readln(Form1.E,Form1.retina[I]);
    end;
    CloseFile(Form1.E);

{Control array}
    Form1.fname:='control3.txt';
    AssignFile(Form1.E,Form1.fname);
    Reset(Form1.E);
    For K:= 1 to 6223 do
        begin
            read(Form1.E,Form1.control[K]);
            end;
        CloseFile(Form1.E);

{Display area}
    For I:=1 to 45 do
        begin
            For J:=1 to 44 do
                begin
                    Form1.Display[I,J]:=0;
                    end;
                end;

{Used nodes}
    Form1.fname:='usednodes.txt';
    AssignFile(Form1.E,Form1.fname);
    Reset(Form1.E);
    For K:= 1 to 2358 do
        begin
            read(Form1.E,I);
            read(Form1.E,J);
            Form1.Display[I,J]:=1;
            end;
        CloseFile(Form1.E);
    end;

end.

```

```

unit Membrane;

```

```

interface

```

```

uses

```

```

    Windows, Messages, SysUtils, Classes, Graphics, Controls, Forms, Dialogs,
    StdCtrls,Mathunit;

```

```

    procedure Retina(Sender: TObject);

```

```

implementation

```

```

uses Main;

```

```

procedure Retina(Sender: TObject);

```

```
var J: integer;  
begin
```

```
{Retinal Weighting Factors}
```

```
Form1.N1:=Form1.NA1;  
Form1.N2:=Form1.NA2;  
Form1.N3:=Form1.NA3;  
Form1.N4:=Form1.NA4;
```

```
J:=0;
```

```
REPEAT
```

```
J:=J+1;
```

```
Form1.J:=J;
```

```
{Variable Weighting Factors}
```

```
IF Form1.J>=13 then Form1.N1:=Form1.NB1;  
IF Form1.J>=13 then Form1.N2:=Form1.NB2;  
IF Form1.J>=13 then Form1.N3:=Form1.NB3;  
IF Form1.J>=13 then Form1.N4:=Form1.NB4;
```

```
Form1.TAU:=Form1.retina[Form1.J];
```

```
{Parameter calculation for double node potentials}
```

```
Form1.D1:= Form1.inputR[21]-Form1.inputR[Form1.N1];  
Form1.D2:= Form1.inputR[Form1.N1]-Form1.inputR[Form1.N2];  
Form1.D3:= Form1.inputR[Form1.N3]-Form1.inputR[21];  
Form1.D4:= Form1.inputR[Form1.N4]-Form1.inputR[Form1.N3];  
Form1.CA:=(2*Form1.D1+Form1.D2)/(Form1.D1*(Form1.D1+Form1.D2));  
Form1.CB:=(Form1.D1+Form1.D2)/(Form1.D1*Form1.D2);  
Form1.CC:=Form1.D1/(Form1.D2*(Form1.D1+Form1.D2));  
Form1.CD:=(2*Form1.D3+Form1.D4)/(Form1.D3*(Form1.D3+Form1.D4));  
Form1.CE:=(Form1.D3+Form1.D4)/(Form1.D3*Form1.D4);  
Form1.CF:=Form1.D3/(Form1.D4*(Form1.D3+Form1.D4));
```

```
{Conversion to complex numbers}
```

```
CMake(Form1.SigmaExt,0,Form1.SigmaExtC);  
CMake(-Form1.SigmaExt,0,Form1.SigmaExtCMinus);  
CMake(Form1.SigmaInt,0,Form1.SigmaIntC);  
CMake(Form1.CA,0,Form1.CAC);  
CMake(Form1.CB,0,Form1.CBC);  
CMake(Form1.CC,0,Form1.CCC);  
CMake(Form1.CD,0,Form1.CDC);  
CMake(Form1.CE,0,Form1.CEC);  
CMake(Form1.CF,0,Form1.CFC);  
CMake(Form1.Tau,0,Form1.TauC);  
CMake(1,0,Form1.oneC);
```

```
{ANA:=-SIGE*CD*(TAU+(RMN*SIGE*(CE*U(N3,J)-CF*(N4,J)))/(1+RMN*SIGE*CD))}
```

```
CMult(Form1.CEC,Form1.inputU[Form1.N3,Form1.J],Form1.tempc);  
CMult(Form1.CFC,Form1.inputU[Form1.N4,Form1.J],Form1.tempc2);  
CSub(Form1.tempc,Form1.tempc2,Form1.tempc3);  
Cmult(Form1.RMembraneImpedance,Form1.SigmaExtC,Form1.tempc4);  
CMult(Form1.Tempc3,Form1.tempc4,Form1.tempc5);  
CAdd(Form1.TauC,Form1.tempc5,Form1.tempc6);
```

```

CMult(Form1.tempc4,Form1.CDC,Form1.tempc7);
CAdd(Form1.onec,Form1.tempc7,Form1.tempc8);

CDiv(Form1.tempc6,Form1.tempc8,Form1.tempc9);

CMult(Form1.SigmaExtCMinus,Form1.CDC,Form1.tempc10);
CMult(Form1.tempc10,Form1.tempc9,Form1.ANA);

{ANB:=SIGI*(CB*U[N1,J]-CC*U[N2,J])+SIGE*(CE*U[N3,J]-CF*U[N4,J])}
CMult(Form1.CBC,Form1.inputU[Form1.N1,Form1.J],Form1.tempc11);
CMult(Form1.CCC,Form1.inputU[Form1.N2,Form1.J],Form1.tempc12);
CSub(Form1.Tempc11,Form1.tempc12,Form1.tempc13);
CMult(Form1.tempc13,Form1.SigmaIntC,Form1.tempc14);
CMult(Form1.SigmaExtC,Form1.tempc3,Form1.tempc15);
CAdd(Form1.tempc14,Form1.tempc15,Form1.ANB);

{AD:=SIGI*CA+(SIGE*CD)/(1+RMN*SIGE*CD)}
CMult(Form1.SigmaExtC,Form1.CDC,Form1.tempc16);
CDiv(Form1.tempc16,Form1.tempc8,Form1.tempc17);
CMult(Form1.SigmaIntC,Form1.CAC,Form1.tempc18);
CAdd(Form1.tempc18,Form1.tempc17,Form1.AD);

{BNA:=SIGI*CA*(TAU+(RMN*SIGE*(CE*U[N3,J]-CF*U[N4,J])));}
CMult(Form1.SigmaIntC,Form1.CAC,Form1.Tempc19);
CMult(Form1.Tempc19,Form1.tempc6,Form1.BNA);

{BNB:=SIGE*(CE*U[N3,J]-CF*U[N4,J])+ SIGI*(CB*U[N1,J]-CC*U[N2,J])}
Form1.BNB:=Form1.ANB;

{BD:=SIGI*CA*(1+RMN*SIGE*CD)+SIGE*CD}
CMult(Form1.tempc18,Form1.tempc8,Form1.tempc20);
CAdd(Form1.tempc20,Form1.tempc16,Form1.BD);

{PotA:=ANA+ANB/AD}
Cadd(Form1.ANA,Form1.ANB,Form1.tempc);
Cdiv(Form1.tempc,Form1.AD,Form1.UA[Form1.J]);

{PotB:=BNA+BNB/BD}
Cadd(Form1.BNA,Form1.BNB,Form1.tempc2);
Cdiv(Form1.tempc2,Form1.BD,Form1.UB[Form1.J]);

UNTIL J=22;

end;

end.
-----

unit Radius;

interface

uses

```

SysUtils, WinTypes, WinProcs, Messages, Classes, Graphics, Controls,
Forms, Dialogs, StdCtrls;

procedure Radial(Sender: TObject);

implementation

uses Main, Mathunit;

procedure Radial(Sender: TObject);

begin

{R(I)}

Form1.RI:=Form1.inputR[Form1.I] ;

{RIM}

Form1.RIM:=Form1.inputR[Form1.IMinus];

{RIP}

Form1.RIP:=Form1.inputR[Form1.IP];

{HIM}

Form1.HIM:=Form1.RI-Form1.RIM;

{HIP}

Form1.HIP:=Form1.RIP-Form1.RI;

{RM}

Form1.RM:=(Form1.RIM+ Form1.RI) /2 ;

{RP}

Form1.RP:=(Form1.RI+ Form1.RIP) /2 ;

end;

end.

unit Angle;

interface

uses

SysUtils, WinTypes, WinProcs, Messages, Classes, Graphics, Controls,
Forms, Dialogs, StdCtrls, MathUnit;

procedure Theta(Sender: TObject);

implementation

uses Main;

procedure Theta(Sender: TObject);

var

```
temp:double;
tempc,tempc2,tempc3,tempc4: complex;
```

```
begin
```

```
{T(J)}
```

```
Form1.TJ:=Form1.inputT[Form1.J];
```

```
{T(JM)}
```

```
Form1.TJM:=Form1.inputT[Form1.JM];
```

```
{T(JP)}
```

```
Form1.TJP:=Form1.inputT[Form1.JP];
```

```
{HJM}
```

```
Form1.HJM:=Form1.TJ - Form1.TJM;
```

```
Form1.HJM:=Abs(Form1.HJM);
```

```
{HJP}
```

```
Form1.HJP:= Form1.TJP - Form1.TJ;
```

```
Form1.HJP:=Abs(Form1.HJP);
```

```
{TM}
```

```
Form1.TM:=(Form1.TJM + Form1.TJ)/ 2;
```

```
{TP}
```

```
Form1.TP:=(Form1.TJ+ Form1.TJP)/ 2;
```

```
{COM}
```

```
Form1.COM:=Abs(Cos(Form1.TM) - Cos(Form1.TJ));
```

```
{COP}
```

```
Form1.COP:=Abs(Cos(Form1.TJ) - Cos(Form1.TP));
```

```
{FR1}
```

```
temp:=((Form1.RM*Form1.RM)/Form1.HIM)*((Form1.SIGA*Form1.COM)+(Form1.SIGD*Form1.COP));  
Cmake(temp,0,Form1.FR1);
```

```
{FR2}
```

```
temp:=((Sin(Form1.TM))/(2*Form1.HJM))*((Form1.SIGA*Form1.HIM)+(Form1.SIGB*Form1.HIP));
```

```
Cmake(temp,0,Form1.FR2);
```

```
{FR3}
```

```
temp:=((Form1.RP*Form1.RP)/Form1.HIP)*((Form1.SIGB*Form1.COM)+(Form1.SIGC*Form1.COP));
```

```
Cmake(temp,0,Form1.FR3);
```

```
{FR4}
```

```
temp:=((Sin(Form1.TP))/(2*Form1.HJP))*((Form1.SIGC*Form1.HIP)+(Form1.SIGD*Form1.HIM));
```

```
Cmake(temp,0,Form1.FR4);
```

```
{FR1+FR2+FR3+FR4}
```

```
Cadd(Form1.FR1,Form1.FR2,Form1.FR5);
```

```
Cadd(Form1.FR5,Form1.FR3,Form1.FR5);
```

```
Cadd(Form1.FR5,Form1.FR4,Form1.FR5);
```

```

{V1}
  Cmult(Form1.FR1,Form1.inputU[Form1.IMinus,Form1.J],Form1.V1);

{V2}
  Cmult(Form1.FR2,Form1.inputU[Form1.I,Form1.JM],Form1.V2);

{V3}
  Cmult(Form1.FR3,Form1.inputU[Form1.IP,Form1.J],Form1.V3);

{V4}
  Cmult(Form1.FR4,Form1.inputU[Form1.I,Form1.JP],Form1.V4);

{V}
  Cadd(Form1.V1,Form1.V2,tempc);
  Cadd(tempc,Form1.V3,tempc);
  Cadd(tempc,Form1.V4,tempc);
  Cdiv(tempc,Form1.FR5,Form1.V);

{U[I,J]}
  Cmake(Form1.W,0,Form1.WC);
  Cmult(Form1.WC,Form1.V,tempc);
  Cmake(1,0,tempc2);
  Csub(tempc2,Form1.WC,tempc3);
  Cmult(tempc3,Form1.inputU[Form1.I,Form1.J],tempc4);
  Cadd(tempc,tempc4,Form1.inputU[Form1.I,Form1.J]);
end;

end.

```

unit Average;

interface

uses

Windows, Messages, SysUtils, Classes, Graphics, Controls, Forms, Dialogs,
StdCtrls;

procedure Calculate_Average(Sender: TObject);

implementation

uses Main, Setup, Mathunit;

{Averaging procedure}

procedure Calculate_Average(Sender: TObject);

var

tempc,tempc2,tempc3,tempc4: complex;

A,B,C,D: complex;

begin

{Integer = 1}

If Form1.Voltage_Flag=1 then

begin

Form1.inputU[1,Form1.J]:=Form1.inputU[1,1];

```

end;

{Integer = 2}
If Form1.Voltage_Flag=2 then
begin
Cmake(2,0,tempc2);
Cadd(Form1.inputU[Form1.IMinus,Form1.JM],Form1.inputU[Form1.IMinus,Form1.JP],tempc);
Cdiv(tempc,tempc2,Form1.inputU[Form1.IMinus,Form1.J]);
end;

{Integer = 3}
If Form1.Voltage_Flag=3 then
begin
Form1.A:=Form1.inputT[Form1.JP]-Form1.inputT[Form1.J];
Cmake(Form1.A,0,A);
Form1.B:=Form1.inputT[Form1.J]-Form1.inputT[Form1.JM];
Cmake(Form1.B,0,B);

Cmult(A,Form1.inputU[Form1.IMinus,Form1.JM],tempc);
Cmult(B,Form1.inputU[Form1.IMinus,Form1.JP],tempc2);
Cadd(A,B,tempc3);
Cadd(tempc,tempc2,tempc4);
Cdiv(tempc4,tempc3,Form1.inputU[Form1.IMinus,Form1.J]);
end;

{Integer = 4}
If Form1.Voltage_Flag=4 then
begin
Form1.C:=Form1.inputR[Form1.IP]-Form1.inputR[Form1.I];
Cmake(Form1.C,0,C);
Form1.D:=Form1.inputR[Form1.I]-Form1.inputR[Form1.IMinus];
Cmake(Form1.D,0,D);

Cmult(C,Form1.inputU[Form1.IMinus,Form1.JM],tempc);
Cmult(D,Form1.inputU[Form1.IP,Form1.JM],tempc2);
Cadd(C,D,tempc3);
Cadd(tempc,tempc2,tempc4);
Cdiv(tempc4,tempc3,Form1.inputU[Form1.I,Form1.JM]);
end;

{Integer = 5}
If Form1.Voltage_Flag=5 then
begin
Form1.inputU[21,Form1.J]:=Form1.UA[Form1.J];
end;

{Integer = 6}
If Form1.Voltage_Flag=6 then
begin
Form1.inputU[21,Form1.J]:=Form1.UB[Form1.J];
end;

{Integer = 7}
If Form1.Voltage_Flag=7 then
begin

```

```
Form1.C:=Form1.inputR[21]-Form1.inputR[19];
Cmake(Form1.C,0,C);
Form1.D:=Form1.inputR[19]-Form1.inputR[18];
Cmake(Form1.D,0,D);
```

```
Cmult(C,Form1.inputU[18,12],tempc);
Cmult(D,Form1.UA[12],tempc2);
Cadd(C,D,tempc3);
Cadd(tempc,tempc2,tempc4);
Cdiv(tempc4,tempc3,Form1.inputU[19,12]);
end;
```

```
{Integer = 8}
```

```
If Form1.Voltage_Flag=8 then
begin
Form1.C:=Form1.inputR[23]-Form1.inputR[22];
Cmake(Form1.C,0,C);
Form1.D:=Form1.inputR[22]-Form1.inputR[21];
Cmake(Form1.D,0,D);
```

```
Cmult(C,Form1.UB[22],tempc);
Cmult(D,Form1.inputU[23,22],tempc2);
Cadd(C,D,tempc3);
Cadd(tempc,tempc2,tempc4);
Cdiv(tempc4,tempc3,Form1.inputU[22,22]);
end;
```

```
{Integer = 9}
```

```
If Form1.Voltage_Flag=9 then
begin
Cmake(2,0,tempc2);
Cadd(Form1.UA[22],Form1.UB[22],tempc);
Cdiv(tempc,tempc2,Form1.inputU[21,22]);
end;
```

```
{Integer = 10}
```

```
If Form1.Voltage_Flag=10 then
begin
Form1.C:=Form1.inputR[21]-Form1.inputR[20];
Cmake(Form1.C,0,C);
Form1.D:=Form1.inputR[20]-Form1.inputR[19];
Cmake(Form1.D,0,D);
```

```
Cmult(D,Form1.UA[22],tempc);
Cmult(C,Form1.inputU[19,22],tempc2);
Cadd(C,D,tempc3);
Cadd(tempc,tempc2,tempc4);
Cdiv(tempc4,tempc3,Form1.inputU[20,22]);
end;
```

```
end;
end.
```

unit Voltage;

interface

uses

Windows, Messages, SysUtils, Classes, Graphics, Controls, Forms, Dialogs,
StdCtrls;

procedure Calculate_Voltage(Sender: TObject);

implementation

uses Main, Setup, Mathunit;

{Averaging procedure}

procedure Calculate_Voltage(Sender: TObject);

var

tempc,tempc2,tempc3,tempc4: complex;

A,B,C,D: complex;

begin

{Integer = 1}

If Form1.Voltage_Flag=1 then

begin

Form1.inputU[1,Form1.J]:=Form1.inputU[1,1];

end;

{Integer = 2}

If Form1.Voltage_Flag=2 then

begin

Cmake(2,0,tempc2);

Cadd(Form1.inputU[Form1.IMinus,Form1.JM],Form1.inputU[Form1.IMinus,Form1.JP],tempc);

Cdiv(tempc,tempc2,Form1.inputU[Form1.IMinus,Form1.J]);

end;

{Integer = 3}

If Form1.Voltage_Flag=3 then

begin

Form1.A:=Form1.inputT[Form1.JP]-Form1.inputT[Form1.J];

Cmake(Form1.A,0,A);

Form1.B:=Form1.inputT[Form1.J]-Form1.inputT[Form1.JM];

Cmake(Form1.B,0,B);

Cmult(A,Form1.inputU[Form1.IMinus,Form1.JM],tempc);

Cmult(B,Form1.inputU[Form1.IMinus,Form1.JP],tempc2);

Cadd(A,B,tempc3);

Cadd(tempc,tempc2,tempc4);

Cdiv(tempc4,tempc3,Form1.inputU[Form1.IMinus,Form1.J]);

end;

{Integer = 4}

If Form1.Voltage_Flag=4 then

begin

Form1.C:=Form1.inputR[Form1.IP]-Form1.inputR[Form1.I];

Cmake(Form1.C,0,C);

Form1.D:=Form1.inputR[Form1.I]-Form1.inputR[Form1.IMinus];

```

Cmake(Form1.D,0,D);

Cmult(C,Form1.inputU[Form1.IMinus,Form1.JM],tempc);
Cmult(D,Form1.inputU[Form1.IP,Form1.JM],tempc2);
Cadd(C,D,tempc3);
Cadd(tempc,tempc2,tempc4);
Cdiv(tempc4,tempc3,Form1.inputU[Form1.I,Form1.JM]);
end;

{Integer = 5}
If Form1.Voltage_Flag=5 then
begin
Form1.inputU[21,Form1.J]:=Form1.UA[Form1.J];
end;

{Integer = 6}
If Form1.Voltage_Flag=6 then
begin
Form1.inputU[21,Form1.J]:=Form1.UB[Form1.J];
end;

{Integer = 7}
If Form1.Voltage_Flag=7 then
begin
Form1.C:=Form1.inputR[21]-Form1.inputR[19];
Cmake(Form1.C,0,C);
Form1.D:=Form1.inputR[19]-Form1.inputR[18];
Cmake(Form1.D,0,D);

Cmult(C,Form1.inputU[18,12],tempc);
Cmult(D,Form1.UA[12],tempc2);
Cadd(C,D,tempc3);
Cadd(tempc,tempc2,tempc4);
Cdiv(tempc4,tempc3,Form1.inputU[19,12]);
end;

{Integer = 8}
If Form1.Voltage_Flag=8 then
begin
Form1.C:=Form1.inputR[23]-Form1.inputR[22];
Cmake(Form1.C,0,C);
Form1.D:=Form1.inputR[22]-Form1.inputR[21];
Cmake(Form1.D,0,D);

Cmult(C,Form1.UB[22],tempc);
Cmult(D,Form1.inputU[23,22],tempc2);
Cadd(C,D,tempc3);
Cadd(tempc,tempc2,tempc4);
Cdiv(tempc4,tempc3,Form1.inputU[22,22]);
end;

{Integer = 9}
If Form1.Voltage_Flag=9 then
begin
Cmake(2,0,tempc2);

```

```
Cadd(Form1.UA[22],Form1.UB[22],tempc);
Cdiv(tempc,tempc2,Form1.inputU[21,22]);
end;
```

```
{Integer = 10}
```

```
If Form1.Voltage_Flag=10 then
begin
```

```
Form1.A:=Form1.inputT[17]-Form1.inputT[16];
Cmake(Form1.A,0,A);
Form1.B:=Form1.inputT[16]-Form1.inputT[15];
Cmake(Form1.B,0,B);
Cmult(A,Form1.inputU[31,15],tempc);
Cmult(B,Form1.inputU[31,17],tempc2);
Cadd(A,B,tempc3);
Cadd(tempc,tempc2,tempc4);
Cdiv(tempc4,tempc3,Form1.inputU[31,16]);
```

```
Form1.A:=Form1.inputT[19]-Form1.inputT[18];
Cmake(Form1.A,0,A);
Form1.B:=Form1.inputT[18]-Form1.inputT[17];
Cmake(Form1.B,0,B);
Cmult(A,Form1.inputU[31,17],tempc);
Cmult(B,Form1.inputU[31,19],tempc2);
Cadd(A,B,tempc3);
Cadd(tempc,tempc2,tempc4);
Cdiv(tempc4,tempc3,Form1.inputU[31,18]);
```

```
Form1.A:=Form1.inputT[22]-Form1.inputT[20];
Cmake(Form1.A,0,A);
Form1.B:=Form1.inputT[20]-Form1.inputT[19];
Cmake(Form1.B,0,B);
Cmult(A,Form1.inputU[31,19],tempc);
Cmult(B,Form1.inputU[31,22],tempc2);
Cadd(A,B,tempc3);
Cadd(tempc,tempc2,tempc4);
Cdiv(tempc4,tempc3,Form1.inputU[31,20]);
```

```
Form1.A:=Form1.inputT[25]-Form1.inputT[24];
Cmake(Form1.A,0,A);
Form1.B:=Form1.inputT[24]-Form1.inputT[22];
Cmake(Form1.B,0,B);
Cmult(A,Form1.inputU[31,22],tempc);
Cmult(B,Form1.inputU[31,25],tempc2);
Cadd(A,B,tempc3);
Cadd(tempc,tempc2,tempc4);
Cdiv(tempc4,tempc3,Form1.inputU[31,24]);
```

```
Form1.A:=Form1.inputT[27]-Form1.inputT[26];
Cmake(Form1.A,0,A);
Form1.B:=Form1.inputT[26]-Form1.inputT[25];
Cmake(Form1.B,0,B);
Cmult(A,Form1.inputU[31,25],tempc);
Cmult(B,Form1.inputU[31,27],tempc2);
Cadd(A,B,tempc3);
Cadd(tempc,tempc2,tempc4);
```

```
Cdiv(tempc4,tempc3,Form1.inputU[31,26]);
```

```
Form1.A:=Form1.inputT[29]-Form1.inputT[28];  
Cmake(Form1.A,0,A);  
Form1.B:=Form1.inputT[28]-Form1.inputT[27];  
Cmake(Form1.B,0,B);  
Cmult(A,Form1.inputU[31,27],tempc);  
Cmult(B,Form1.inputU[31,29],tempc2);  
Cadd(A,B,tempc3);  
Cadd(tempc,tempc2,tempc4);  
Cdiv(tempc4,tempc3,Form1.inputU[31,28]);  
end;
```

```
{Integer = 11}
```

```
If Form1.Voltage_Flag=11 then  
begin
```

```
Form1.A:=Form1.inputT[40]-Form1.inputT[39];  
Cmake(Form1.A,0,A);  
Form1.B:=Form1.inputT[39]-Form1.inputT[38];  
Cmake(Form1.B,0,B);
```

```
Cmult(A,Form1.inputU[7,38],tempc);  
Cmult(B,Form1.inputU[7,40],tempc2);  
Cadd(A,B,tempc3);  
Cadd(tempc,tempc2,tempc4);  
Cdiv(tempc4,tempc3,Form1.inputU[7,39]);
```

```
Form1.C:=Form1.inputR[9]-Form1.inputR[8];  
Cmake(Form1.C,0,C);  
Form1.D:=Form1.inputR[8]-Form1.inputR[7];  
Cmake(Form1.D,0,D);
```

```
Cmult(C,Form1.inputU[7,38],tempc);  
Cmult(D,Form1.inputU[9,38],tempc2);  
Cadd(C,D,tempc3);  
Cadd(tempc,tempc2,tempc4);  
Cdiv(tempc4,tempc3,Form1.inputU[8,38]);  
end;
```

```
{Integer = 12}
```

```
If Form1.Voltage_Flag=12 then  
begin
```

```
Form1.A:=Form1.inputT[35]-Form1.inputT[33];  
Cmake(Form1.A,0,A);  
Form1.B:=Form1.inputT[33]-Form1.inputT[32];  
Cmake(Form1.B,0,B);
```

```
Cmult(A,Form1.inputU[17,32],tempc);  
Cmult(B,Form1.inputU[17,35],tempc2);  
Cadd(A,B,tempc3);  
Cadd(tempc,tempc2,tempc4);  
Cdiv(tempc4,tempc3,Form1.inputU[17,33]);
```

```
Form1.C:=Form1.inputR[20]-Form1.inputR[18];  
Cmake(Form1.C,0,C);
```

```
Form1.D:=Form1.inputR[18]-Form1.inputR[17];  
Cmake(Form1.D,0,D);
```

```
Cmult(C,Form1.inputU[17,33],tempc);  
Cmult(D,Form1.inputU[20,33],tempc2);  
Cadd(C,D,tempc3);  
Cadd(tempc,tempc2,tempc4);  
Cdiv(tempc4,tempc3,Form1.inputU[18,33]);  
end;
```

```
{Integer = 13}
```

```
If Form1.Voltage_Flag=13 then  
begin
```

```
Form1.A:=Form1.inputT[22]-Form1.inputT[21];  
Cmake(Form1.A,0,A);  
Form1.B:=Form1.inputT[21]-Form1.inputT[20];  
Cmake(Form1.B,0,B);
```

```
Cmult(A,Form1.inputU[29,20],tempc);  
Cmult(B,Form1.inputU[29,22],tempc2);  
Cadd(A,B,tempc3);  
Cadd(tempc,tempc2,tempc4);  
Cdiv(tempc4,tempc3,Form1.inputU[29,21]);
```

```
Form1.A:=Form1.inputT[24]-Form1.inputT[23];  
Cmake(Form1.A,0,A);  
Form1.B:=Form1.inputT[23]-Form1.inputT[22];  
Cmake(Form1.B,0,B);
```

```
Cmult(A,Form1.inputU[29,22],tempc);  
Cmult(B,Form1.inputU[29,24],tempc2);  
Cadd(A,B,tempc3);  
Cadd(tempc,tempc2,tempc4);  
Cdiv(tempc4,tempc3,Form1.inputU[29,23]);  
end;
```

```
{Integer = 14}
```

```
If Form1.Voltage_Flag=14 then  
begin
```

```
Form1.C:=Form1.inputR[26]-Form1.inputR[23];  
Cmake(Form1.C,0,C);  
Form1.D:=Form1.inputR[23]-Form1.inputR[22];  
Cmake(Form1.D,0,D);
```

```
Cmult(C,Form1.inputU[22,31],tempc);  
Cmult(D,Form1.inputU[26,31],tempc2);  
Cadd(C,D,tempc3);  
Cadd(tempc,tempc2,tempc4);  
Cdiv(tempc4,tempc3,Form1.inputU[23,31]);  
end;
```

```
{Integer = 15}
```

```
If Form1.Voltage_Flag=15 then  
begin
```

```
Form1.C:=Form1.inputR[26]-Form1.inputR[24];
```

```
Cmake(Form1.C,0,C);
Form1.D:=Form1.inputR[24]-Form1.inputR[22];
Cmake(Form1.D,0,D);
```

```
Cmult(C,Form1.inputU[22,31],tempc);
Cmult(D,Form1.inputU[26,31],tempc2);
Cadd(C,D,tempc3);
Cadd(tempc,tempc2,tempc4);
Cdiv(tempc4,tempc3,Form1.inputU[24,31]);
end;
```

```
{Integer = 16}
```

```
If Form1.Voltage_Flag=16 then
begin
Form1.C:=Form1.inputR[26]-Form1.inputR[25];
Cmake(Form1.C,0,C);
Form1.D:=Form1.inputR[25]-Form1.inputR[22];
Cmake(Form1.D,0,D);
```

```
Cmult(C,Form1.inputU[22,31],tempc);
Cmult(D,Form1.inputU[26,31],tempc2);
Cadd(C,D,tempc3);
Cadd(tempc,tempc2,tempc4);
Cdiv(tempc4,tempc3,Form1.inputU[25,31]);
end;
```

```
{Integer = 17}
```

```
If Form1.Voltage_Flag=17 then
begin
Form1.A:=Form1.inputT[22]-Form1.inputT[Form1.J];
Cmake(Form1.A,0,A);
Form1.B:=Form1.inputT[Form1.J]-Form1.inputT[16];
Cmake(Form1.B,0,B);
```

```
Cmult(A,Form1.inputU[17,16],tempc);
Cmult(B,Form1.inputU[17,22],tempc2);
Cadd(A,B,tempc3);
Cadd(tempc,tempc2,tempc4);
Cdiv(tempc4,tempc3,Form1.inputU[17,Form1.J]);
end;
```

```
{Integer = 18}
```

```
If Form1.Voltage_Flag=18 then
begin
Form1.A:=Form1.inputT[30]-Form1.inputT[Form1.J];
Cmake(Form1.A,0,A);
Form1.B:=Form1.inputT[Form1.J]-Form1.inputT[22];
Cmake(Form1.B,0,B);
```

```
Cmult(A,Form1.inputU[17,22],tempc);
Cmult(B,Form1.inputU[17,30],tempc2);
Cadd(A,B,tempc3);
Cadd(tempc,tempc2,tempc4);
Cdiv(tempc4,tempc3,Form1.inputU[17,Form1.J]);
end;
```

```

{Integer = 19}
  If Form1.Voltage_Flag=19 then
  begin
  Form1.C:=Form1.inputR[20]-Form1.inputR[19];
  Cmake(Form1.C,0,C);
  Form1.D:=Form1.inputR[19]-Form1.inputR[18];
  Cmake(Form1.D,0,D);

  Cmult(C,Form1.inputU[18,32],tempc);
  Cmult(D,Form1.inputU[20,32],tempc2);
  Cadd(C,D,tempc3);
  Cadd(tempc,tempc2,tempc4);
  Cdiv(tempc4,tempc3,Form1.inputU[19,32]);
  end;

{Integer = 20}
  If Form1.Voltage_Flag=20 then
  begin
  Form1.C:=Form1.inputR[21]-Form1.inputR[20];
  Cmake(Form1.C,0,C);
  Form1.D:=Form1.inputR[20]-Form1.inputR[19];
  Cmake(Form1.D,0,D);

  Cmult(D,Form1.UA[22],tempc);
  Cmult(C,Form1.inputU[19,22],tempc2);
  Cadd(C,D,tempc3);
  Cadd(tempc,tempc2,tempc4);
  Cdiv(tempc4,tempc3,Form1.inputU[20,22]);
  end;

{Integer = 21}
  If Form1.Voltage_Flag=21 then
  begin
  Form1.A:=Form1.inputT[35]-Form1.inputT[33];
  Cmake(Form1.A,0,A);
  Form1.B:=Form1.inputT[33]-Form1.inputT[32];
  Cmake(Form1.B,0,B);

  Cmult(A,Form1.inputU[17,32],tempc);
  Cmult(B,Form1.inputU[17,35],tempc2);
  Cadd(A,B,tempc3);
  Cadd(tempc,tempc2,tempc4);
  Cdiv(tempc4,tempc3,Form1.inputU[17,33]);
  end;

{Integer = 22}
  If Form1.Voltage_Flag=22 then
  begin
  Form1.A:=Form1.inputT[15]-Form1.inputT[13];
  Cmake(Form1.A,0,A);
  Form1.B:=Form1.inputT[13]-Form1.inputT[12];
  Cmake(Form1.B,0,B);

  Cmult(A,Form1.inputU[35,12],tempc);

```

```
Cmult(B,Form1.inputU[35,15],tempc2);
Cadd(A,B,tempc3);
Cadd(tempc,tempc2,tempc4);
Cdiv(tempc4,tempc3,Form1.inputU[35,13]);
```

```
Form1.A:=Form1.inputT[40]-Form1.inputT[38];
Cmake(Form1.A,0,A);
Form1.B:=Form1.inputT[38]-Form1.inputT[37];
Cmake(Form1.B,0,B);
```

```
Cmult(A,Form1.inputU[33,37],tempc);
Cmult(B,Form1.inputU[33,40],tempc2);
Cadd(A,B,tempc3);
Cadd(tempc,tempc2,tempc4);
Cdiv(tempc4,tempc3,Form1.inputU[33,38]);
end;
```

```
{Integer = 24}
```

```
If Form1.Voltage_Flag=24 then
begin
Form1.A:=Form1.inputT[35]-Form1.inputT[34];
Cmake(Form1.A,0,A);
Form1.B:=Form1.inputT[34]-Form1.inputT[32];
Cmake(Form1.B,0,B);
```

```
Cmult(A,Form1.inputU[17,32],tempc);
Cmult(B,Form1.inputU[17,35],tempc2);
Cadd(A,B,tempc3);
Cadd(tempc,tempc2,tempc4);
Cdiv(tempc4,tempc3,Form1.inputU[17,34]);
end;
```

```
{Integer = 25}
```

```
If Form1.Voltage_Flag=25 then
begin
Form1.A:=Form1.inputT[35]-Form1.inputT[35];
Cmake(Form1.A,0,A);
Form1.B:=Form1.inputT[35]-Form1.inputT[32];
Cmake(Form1.B,0,B);
```

```
Cmult(A,Form1.inputU[17,32],tempc);
Cmult(B,Form1.inputU[17,35],tempc2);
Cadd(A,B,tempc3);
Cadd(tempc,tempc2,tempc4);
Cdiv(tempc4,tempc3,Form1.inputU[17,35]);
end;
```

```
{Integer = 26}
```

```
If Form1.Voltage_Flag=26 then
begin
Form1.A:=Form1.inputT[15]-Form1.inputT[14];
Cmake(Form1.A,0,A);
Form1.B:=Form1.inputT[14]-Form1.inputT[12];
Cmake(Form1.B,0,B);
Cmult(A,Form1.inputU[32,12],tempc);
```

```
Cmult(B,Form1.inputU[32,15],tempc2);
Cadd(A,B,tempc3);
Cadd(tempc,tempc2,tempc4);
Cdiv(tempc4,tempc3,Form1.inputU[32,14]);
```

```
Form1.A:=Form1.inputT[22]-Form1.inputT[17];
Cmake(Form1.A,0,A);
Form1.B:=Form1.inputT[17]-Form1.inputT[15];
Cmake(Form1.B,0,B);
Cmult(A,Form1.inputU[32,15],tempc);
Cmult(B,Form1.inputU[32,22],tempc2);
Cadd(A,B,tempc3);
Cadd(tempc,tempc2,tempc4);
Cdiv(tempc4,tempc3,Form1.inputU[32,17]);
```

```
Form1.A:=Form1.inputT[22]-Form1.inputT[19];
Cmake(Form1.A,0,A);
Form1.B:=Form1.inputT[19]-Form1.inputT[15];
Cmake(Form1.B,0,B);
Cmult(A,Form1.inputU[32,15],tempc);
Cmult(B,Form1.inputU[32,22],tempc2);
Cadd(A,B,tempc3);
Cadd(tempc,tempc2,tempc4);
Cdiv(tempc4,tempc3,Form1.inputU[32,19]);
```

```
Form1.A:=Form1.inputT[30]-Form1.inputT[25];
Cmake(Form1.A,0,A);
Form1.B:=Form1.inputT[25]-Form1.inputT[22];
Cmake(Form1.B,0,B);
Cmult(A,Form1.inputU[32,22],tempc);
Cmult(B,Form1.inputU[32,30],tempc2);
Cadd(A,B,tempc3);
Cadd(tempc,tempc2,tempc4);
Cdiv(tempc4,tempc3,Form1.inputU[32,25]);
```

```
Form1.A:=Form1.inputT[30]-Form1.inputT[27];
Cmake(Form1.A,0,A);
Form1.B:=Form1.inputT[27]-Form1.inputT[22];
Cmake(Form1.B,0,B);
Cmult(A,Form1.inputU[32,22],tempc);
Cmult(B,Form1.inputU[32,30],tempc2);
Cadd(A,B,tempc3);
Cadd(tempc,tempc2,tempc4);
Cdiv(tempc4,tempc3,Form1.inputU[32,27]);
```

```
Form1.A:=Form1.inputT[30]-Form1.inputT[29];
Cmake(Form1.A,0,A);
Form1.B:=Form1.inputT[29]-Form1.inputT[22];
Cmake(Form1.B,0,B);
Cmult(A,Form1.inputU[32,22],tempc);
Cmult(B,Form1.inputU[32,30],tempc2);
Cadd(A,B,tempc3);
Cadd(tempc,tempc2,tempc4);
Cdiv(tempc4,tempc3,Form1.inputU[32,29]);
end;
```

```

{Integer = 27}
  If Form1.Voltage_Flag=27 then
  begin
  Form1.A:=Form1.inputT[10]-Form1.inputT[9];
  Cmake(Form1.A,0,A);
  Form1.B:=Form1.inputT[9]-Form1.inputT[8];
  Cmake(Form1.B,0,B);
  Cmult(A,Form1.inputU[36,8],tempc);
  Cmult(B,Form1.inputU[36,10],tempc2);
  Cadd(A,B,tempc3);
  Cadd(tempc,tempc2,tempc4);
  Cdiv(tempc4,tempc3,Form1.inputU[36,9]);

  Form1.A:=Form1.inputT[12]-Form1.inputT[11];
  Cmake(Form1.A,0,A);
  Form1.B:=Form1.inputT[11]-Form1.inputT[10];
  Cmake(Form1.B,0,B);
  Cmult(A,Form1.inputU[36,10],tempc);
  Cmult(B,Form1.inputU[36,12],tempc2);
  Cadd(A,B,tempc3);
  Cadd(tempc,tempc2,tempc4);
  Cdiv(tempc4,tempc3,Form1.inputU[36,11]);

  Form1.A:=Form1.inputT[32]-Form1.inputT[31];
  Cmake(Form1.A,0,A);
  Form1.B:=Form1.inputT[31]-Form1.inputT[30];
  Cmake(Form1.B,0,B);
  Cmult(A,Form1.inputU[36,30],tempc);
  Cmult(B,Form1.inputU[36,32],tempc2);
  Cadd(A,B,tempc3);
  Cadd(tempc,tempc2,tempc4);
  Cdiv(tempc4,tempc3,Form1.inputU[36,31]);
  end;
end;

end.

```

```

unit Display;

```

```

interface

```

```

uses

```

```

  WinProcs, Wintypes, Messages, SysUtils, Classes, Graphics, Controls, Forms, Dialogs,
  StdCtrls, Mathunit, Setup;

```

```

procedure Eye(Sender: TObject);

```

```

var

```

```

  Rmax: integer;

```

```

  x,y:array[1..45,1..44] of integer;

```

```

  yval:array[1..90] of integer;

```

```

  xval:array[1..90] of integer;

```

implementation

uses Main;

{Node potentials displayed as a heat plot}

procedure Eye(Sender: TObject);

var

R,T: integer;

I,J,K,zctr,pctr,x1,x2: integer;

gridline,gridinc: integer;

xr,yr,temp1,temp2: Real;

Pixelvalue:array[1..45,1..44] of longint;

Lenscolor,nodecolor,retinacolor,comeacolor,Aircolor,ExtraOcColor:integer;

AcVitColor:integer;

clOrange: longint;

begin

If Form1.runflag2=0 then

begin

Form1.Refresh;

{First work out x and y coordinates}

If Form1.ZoomFlag=1 then RMax:=35;

If Form1.ZoomFlag=0 then RMax:=44;

{Draw black background for line graph}

For R := 1 to RMax do

begin

For T:= 1 to 44 do

begin

xr:=Form1.InputR[R]*(cos(Form1.InputT[T]));

yr:=Form1.InputR[R]*(sin(Form1.InputT[T]));

x[r,t]:= 400-(Round(xr*72)*(1+Form1.ZoomFlag*3));

y[r,t]:= 375-(Round(yr*72)*(1+Form1.ZoomFlag*3));

end;

end;

{Region labels}

Form1.Label1.visible:=True;

Form1.Label2.visible:=True;

Form1.Label3.visible:=True;

Form1.Label4.visible:=True;

Form1.Label5.visible:=True;

Form1.Label6.visible:=True;

Form1.Label7.visible:=True;

Form1.Label8.visible:=True;

{Region colours}

If Form1.Runflag=0 then

begin

nodecolor:=clWhite;

Lenscolor:=clGray;

retinacolor:=clRed;

Form1.canvas.pen.color:=Lenscolor;

```
Form1.Canvas.Brush.Color:=Lenscolor;  
CorneaColor:=clGray;  
AirColor:=ClSilver;  
AcVitColor:=clolive;  
ExtraocColor:=clTeal;  
end
```

```
else
```

```
{Black background}
```

```
begin  
nodecolor:=clBlack;  
Lenscolor:=clBlack;  
retinacolor:=clBlack;  
Form1.canvas.pen.color:=clBlack;  
Form1.Canvas.Brush.Color:=clBlack;  
CorneaColor:=clBlack;  
AirColor:=ClBlack;  
AcVitColor:=clBlack;  
ExtraocColor:=clBlack;  
end;
```

```
{Co-ordinates of regional areas}
```

```
Form1.Canvas.Brush.Color:=Corneacolor;  
Form1.Canvas.Polygon([Point(x[21,40],y[21,40]),Point(x[29,40],y[29,40]),  
Point(x[29,41],y[29,41]),Point(x[29,42],y[29,42]),Point(x[29,43],y[29,43]),  
Point(x[29,44],y[29,44]),Point(x[21,44],y[21,44]),  
Point(x[21,44],y[21,44]),Point(x[21,44],y[21,44]),Point(x[21,43],y[21,43]),  
Point(x[21,42],y[21,42]),Point(x[21,41],y[21,41]),Point(x[21,40],y[21,40])]);
```

```
Form1.Canvas.pen.color:=Aircolor;
```

```
Form1.Canvas.Brush.Color:=Aircolor;
```

```
Form1.Canvas.Polygon([Point(x[29,35],y[29,35]),Point(x[RMax,35],y[RMax,35]),  
Point(x[RMax,36],y[RMax,36]),Point(x[RMax,37],y[RMax,37]),Point(x[RMax,38],  
y[RMax,38]),Point(x[RMax,39],y[RMax,39]),Point(x[RMax,40],y[RMax,40]),  
Point(x[Rmax,41],y[RMax,41]),Point(x[RMax,42],y[RMax,42]),Point(x[RMax,43],  
y[RMax,43]),Point(x[RMax,44],y[RMax,44]),Point(x[29,44],y[29,44]),Point(x[29,43],  
y[29,43]),Point(x[29,42],y[29,42]),Point(x[29,41],y[29,41]),Point(x[29,40],y[29,40]),  
Point(x[29,39],y[29,39]),Point(x[29,38],y[29,38]),Point(x[29,37],y[29,37]),  
Point(x[29,36],y[29,36]),Point(x[29,35],y[29,35])]);
```

```
Form1.Canvas.pen.color:=ExtraOcColor;
```

```
Form1.Canvas.Brush.Color:=ExtraOcColor;
```

```
Form1.Canvas.Polygon([Point(x[29,35],y[29,35]),Point(x[29,34],y[29,34]),  
Point(x[29,33],y[29,33]),Point(x[29,32],y[29,32]),Point(x[29,31],y[29,31]),  
Point(x[29,30],y[29,30]),Point(x[29,29],y[29,29]),  
Point(x[29,28],y[29,28]),Point(x[29,27],y[29,27]),Point(x[29,26],y[29,26]),  
Point(x[29,25],y[29,25]),  
Point(x[RMax,25],y[RMax,25]),Point(x[RMax,26],y[RMax,26]),Point(x[RMax,27],  
y[RMax,27]),Point(x[RMax,28],y[RMax,28]),Point(x[RMax,29],y[RMax,29]),Point(x[RMax,30],  
y[RMax,30]),Point(x[RMax,31],y[RMax,31]),Point(x[RMax,32],y[RMax,32]),Point(x[RMax,33],  
y[RMax,33]),Point(x[RMax,34],y[RMax,34]),Point(x[RMax,35],y[RMax,35])]);
```

```
Form1.Canvas.Polygon([Point(x[29,25],y[29,25]),Point(x[29,24],y[29,24]),  
Point(x[29,23],y[29,23]),Point(x[29,22],y[29,22]),Point(x[29,21],y[29,21]),  
Point(x[29,20],y[29,20]),  
Point(x[RMax,20],y[RMax,20]),Point(x[RMax,21],y[RMax,21]),Point(x[RMax,22],  
y[RMax,22]),Point(x[RMax,23],y[RMax,23]),Point(x[RMax,24],y[RMax,24]),Point(x[RMax,25],
```

y[RMax,25]),Point(x[29,25],y[29,25]));

Form1.Canvas.Polygon([Point(x[29,20],y[29,20]),Point(x[29,19],y[29,19]),
Point(x[29,18],y[29,18]),Point(x[29,17],y[29,17]),Point(x[29,16],y[29,16]),
Point(x[29,15],y[29,15]),
Point(x[29,14],y[29,14]),Point(x[29,13],y[29,13]),Point(x[RMax,13],y[RMax,13]),
Point(x[RMax,14],y[RMax,14]),Point(x[RMax,15],y[RMax,15]),Point(x[RMax,16],
y[RMax,16]),Point(x[RMax,17],y[RMax,17]),Point(x[RMax,18],y[RMax,18]),Point(x[RMax,19],
y[RMax,19]),Point(x[RMax,20],y[RMax,20]),Point(x[29,20],y[29,20]));
Form1.Canvas.Polygon([Point(x[29,13],y[29,13]),Point(x[29,12],y[29,12]),
Point(x[29,11],y[29,11]),Point(x[29,10],y[29,10]),Point(x[29,9],y[29,9]),
Point(x[29,8],y[29,8]),Point(x[29,7],y[29,7]),Point(x[RMax,7],y[RMax,7]),
Point(x[RMax,8],y[RMax,8]),Point(x[RMax,9],y[RMax,9]),Point(x[RMax,10],y[RMax,10]),
Point(x[RMax,11],y[RMax,11]),Point(x[RMax,12],y[RMax,12]),Point(x[RMax,13],y[RMax,13]),
Point(x[29,13],y[29,13]));

Form1.Canvas.Polygon([Point(x[29,7],y[29,7]),Point(x[29,6],y[29,6]),Point(x[29,5],
y[29,5]),Point(x[29,4],y[29,4]),Point(x[29,3],y[29,3]),
Point(x[29,2],y[29,2]),Point(x[29,1],y[29,1]),Point(x[RMax,1],y[RMax,1]),
Point(x[RMax,2],y[RMax,2]),Point(x[RMax,3],y[RMax,3]),Point(x[RMax,4],y[RMax,4]),
Point(x[RMax,5],y[RMax,5]),Point(x[RMax,6],y[RMax,6]),Point(x[RMax,7],y[RMax,7]),
Point(x[29,7],y[29,7]));

Form1.Canvas.pen.Color:=retinacolor;

Form1.Canvas.Brush.Color:=retinacolor;

For J:=2 to 44 do

begin

Form1.Canvas.MoveTo(x[22,j-1],y[22,j-1]);

Form1.Canvas.LineTo(x[22,j],y[22,j]);

Form1.Canvas.MoveTo(x[20,j-1],y[20,j-1]);

Form1.Canvas.LineTo(x[20,j],y[20,j]);

end;

Form1.Canvas.MoveTo(x[22,1],y[22,1]);

Form1.Canvas.LineTo(x[22,44],y[22,44]);

Form1.Canvas.FloodFill(x[11,10],y[11,10],retinacolor,fsborder);

Form1.Canvas.FloodFill(x[11,30],y[11,30],retinacolor,fsborder);

Form1.Canvas.pen.color:=LensColor;

Form1.Canvas.Brush.Color:=Lenscolor;

Form1.Canvas.Polygon([Point(x[9,39],y[9,39]),Point(x[9,40],y[9,40]),Point(x[9,41],

y[9,41]),Point(x[9,42],y[9,42]),Point(x[9,43],y[9,43]),Point(x[9,44],y[9,44]),

Point(x[10,44],y[10,44]),

Point(x[11,44],y[11,44]),Point(x[12,44],y[12,44]),Point(x[12,43],y[12,43]),

Point(x[12,42],y[12,42]),Point(x[12,41],y[12,41]),Point(x[12,40],y[12,40]),

Point(x[12,39],y[12,39]),Point(x[9,39],y[9,39]));

Form1.Canvas.pen.color:=Comeacolor;

{Nodes displayed in white}

For R := 1 to RMax do

begin

For T:= 1 to 44 do

begin

if Form1.Display[R,T]= 1 then

begin

Form1.Canvas.Pixels[x[r,t],y[r,t]]:=nodecolor;

```

Form1.Canvas.Pixels[x[r,t]+1,y[r,t]]:=clWhite ;
Form1.Canvas.Pixels[x[r,t]-1,y[r,t]]:=clWhite ;
Form1.Canvas.Pixels[x[r,t],y[r,t]+1]:=clWhite ;
Form1.Canvas.Pixels[x[r,t],y[r,t]-1]:=clWhite ;
end;

```

```
end;
```

```

Form1.canvas.pen.color:=Form1.Color;
Form1.Canvas.Brush.Color:=Form1.Color;
Form1.Canvas.MoveTo(x[1,1],y[1,1]);
Form1.Canvas.LineTo(x[Rmax,22],y[Rmax,22]);
Form1.canvas.pen.color:=clBlack;
  Form1.Canvas.Brush.Color:=clBlack;
  x1:=400-(Round(RMax*72)*(1+Form1.ZoomFlag*3));
  x2:=400+(Round(RMax*72)*(1+Form1.ZoomFlag*3));
  Form1.Canvas.Rectangle(x[Rmax,1],420,x[Rmax,44],700);

```

```

If Form1.Runflag=1 then
  Form1.RunFlag2:=1;

```

```
end;
```

```
end
else
```

```

begin
  clorange:=2651391;
  zctr:=0;
  Form1.minval:=100000;
  Form1.maxval:=-100000;

```

```
{Nodes displayed as 'heat' plot}
```

```

For I:= 1 to RMax do
  begin
    For J:=1 to 44 do
      begin
        If Form1.Display[I,J]= 1 then
          begin
            If Form1.minval>Form1.inputU[I,J].Re then
              Form1.minval:=Form1.inputU[I,J].Re;

            If Form1.maxval<Form1.inputU[I,J].Re then
              Form1.maxval:=Form1.inputU[I,J].Re;
          end;
        end;
      end;
    end;
  end;
end;

```

```
{Graph shows range from -2.5 to +2.5 volts}
```

```

Form1.maxval:=2.5;
Form1.minval:=-2.5;

```

```

Form1.binincrement:=(Form1.maxval-Form1.minval)/10;
Form1.binlevel:=Form1.minval-Form1.binincrement;
For k:=0 to 9 do

```

```

begin
  Form1.binlevel:=Form1.binlevel+Form1.binincrement;
  Form1.binvalue[k]:=Form1.binlevel;
end;

For I:= 1 to RMax do
  begin
    For J:=1 to 44 do
      begin
        For k:=0 to 8 do
          begin
            If ((Form1.inputU[I,J].Re < Form1.binvalue[k+1]) and
              (Form1.inputU[I,J].Re> Form1.binvalue[k])) then
              begin
                pixelvalue[I,J]:=k;
              end;
            end;
          If (Form1.inputU[I,J].Re< Form1.maxval) and
            (Form1.inputU[I,J].Re>(Form1.binvalue[9]))then
            pixelvalue[I,J]:=9;
          end;
        end;
      end;
    end;

  For R := 1 to RMax do
    begin
      For T:= 1 to 44 do
        begin
          If Form1.Display[R,T] = 1 then
            begin
              If pixelvalue[R,T]=0 then Pixelvalue[R,T]:=cLBlue;
              If pixelvalue[R,T]=1 then Pixelvalue[R,T]:=cLPurple;
              If pixelvalue[R,T]=2 then Pixelvalue[R,T]:=cLTeal;
              If pixelvalue[R,T]=3 then Pixelvalue[R,T]:=cLOlive ;
              If pixelvalue[R,T]=4 then Pixelvalue[R,T]:=cLGreen ;
              If pixelvalue[R,T]=5 then Pixelvalue[R,T]:=cLLime ;
              If pixelvalue[R,T]=6 then Pixelvalue[R,T]:=cLYellow ;
              If pixelvalue[R,T]=7 then Pixelvalue[R,T]:=cLOrange;
              If pixelvalue[R,T]=8 then Pixelvalue[R,T]:=cLRed ;
              If pixelvalue[R,T]=9 then Pixelvalue[R,T]:=cLWhite ;

              Form1.Canvas.Pixels[x[r,t],y[r,t]]:=Pixelvalue[R,T];
              Form1.Canvas.Pixels[x[r,t]+1,y[r,t]]:=Pixelvalue[R,T] ;
              Form1.Canvas.Pixels[x[r,t]-1,y[r,t]]:=Pixelvalue[R,T] ;
              Form1.Canvas.Pixels[x[r,t],y[r,t]+1]:=Pixelvalue[R,T] ;
              Form1.Canvas.Pixels[x[r,t],y[r,t]-1]:=Pixelvalue[R,T] ;

            end;
          end;
        end;
      end;

      zctr:=0;
      pctr:=0;

      {Draw set of graph guide lines}
      xval[1]:=x[Rmax,1];

```

```
xval[2]:=x[RMax,44];  
Form1.canvas.pen.color:=clGreen;
```

```
For gridinc:=0 to 10 do  
begin  
Form1.canvas.pen.color:=clGreen;  
If gridinc=5 then Form1.canvas.pen.color:=clAqua;  
Form1.canvas.MoveTo(xval[1],700-Round(gridinc*28));  
Form1.canvas.LineTo(xval[2],700-Round(gridinc*28));  
end;
```

```
xval[1]:=x[21,1];  
Form1.canvas.MoveTo(xval[1],700);  
Form1.canvas.LineTo(xval[1],420);
```

```
xval[1]:=x[21,44];  
Form1.canvas.MoveTo(xval[1],700);  
Form1.canvas.LineTo(xval[1],420);
```

```
{Graph plotted}
```

```
For I:= RMax downto 1 do  
begin  
If (Form1.minval>Form1.inputU[I,1].Re) and  
(Form1.Display[I,1]=1) then Form1.minval:=Form1.inputU[I,1].Re;  
If (Form1.maxval<Form1.inputU[I,1].Re) and  
(Form1.Display[I,1]=1) then Form1.maxval:=Form1.inputU[I,1].Re;  
end;
```

```
For I:= 2 to RMax do  
begin  
If (Form1.minval>Form1.inputU[I,44].Re) and  
(Form1.Display[I,44]=1) then Form1.minval:=Form1.inputU[I,44].Re;  
If (Form1.maxval<Form1.inputU[I,44].Re) and  
(Form1.Display[I,44]=1) then Form1.maxval:=Form1.inputU[I,44].Re;  
end;
```

```
For I:= RMax downto 1 do  
begin  
zctr:=zctr+1;  
If Form1.Display[I,1]=1 then  
begin  
pctr:=pctr+1;  
yval[pctr]:=ROUND(((Form1.inputU[I,1].Re-Form1.minval)*280)/  
(Form1.maxval-Form1.minval));  
xval[pctr]:=x[I,1];  
end;  
end;
```

```
For I:= 2 to RMax do  
begin  
zctr:=zctr+1;  
If Form1.Display[I,44]=1 then  
begin  
pctr:=pctr+1;  
xval[pctr]:=x[I,44];
```

```
yval[pctr]:=ROUND(((Form1.inputU[I,44].Re-Form1.minval)*280)/
(Form1.maxval-Form1.minval));
end;
end;
```

```
Form1.Canvas.pen.color:=clWhite;
zctr:=0;
For zctr:=2 to pctr do
begin
Form1.canvas.MoveTo(xval[zctr-1],700-yval[zctr-1]);
Form1.canvas.LineTo(xval[zctr],700-yval[zctr]);
end;
```

```
zctr:=0;
pctr:=0;
For J:= 1 to 44 do
begin
zctr:=zctr+1;
If Form1.Display[29,J]=1 then
begin
pctr:=pctr+1;
yval[pctr]:=ROUND(((Form1.inputU[29,J].Re-Form1.minval)*280)/
(Form1.maxval-Form1.minval));
xval[pctr]:=x[29,J];
end;
end;
```

```
Form1.Canvas.pen.color:=clRed;
```

```
For zctr:=2 to pctr do
begin
Form1.canvas.MoveTo(xval[zctr-1],700-yval[zctr-1]);
Form1.canvas.LineTo(xval[zctr],700-yval[zctr]);
end;
```

{Key for graph}

```
Form1.Canvas.Brush.Color:=clBlack;
```

```
If Form1.iterations>1 then
```

```
begin
```

```
For k:=0 to 8 do
```

```
begin
```

```
If K=0 then Form1.Canvas.Brush.Color:=clBlue;
```

```
If K=1 then Form1.Canvas.Brush.Color:=clPurple;
```

```
If K=2 then Form1.Canvas.Brush.Color:=clTeal;
```

```
If K=3 then Form1.Canvas.Brush.Color:=clOlive;
```

```
If K=4 then Form1.Canvas.Brush.Color:=clGreen;
```

```
If K=5 then Form1.Canvas.Brush.Color:=clLime;
```

```
If K=6 then Form1.Canvas.Brush.Color:=clYellow;
```

```
If K=7 then Form1.Canvas.Brush.Color:=clOrange;
```

```
If K=8 then Form1.Canvas.Brush.Color:=clRed;
```

```
If K=9 then Form1.Canvas.Brush.Color:=clWhite;
```

```
tempr:=((Form1.binvalue[k]-Form1.minval)*280)/(Form1.maxval-Form1.minval);
```

```
tempr2:=((Form1.binvalue[k+1]-Form1.minval)*280)/(Form1.maxval-Form1.minval);
```

```
If (tempr<32000) and (tempr2<32000) then
```

```
begin
  yval[1]:=round(tempr);
  yval[2]:=round(tempr2);
  Form1.Canvas.Rectangle(x[Rmax,44]+20,700-yval[1],x[Rmax,44]+50,700-yval[2]);
  end;
end;
tempr:=((Form1.binvalue[9]-Form1.minval)*280)/(Form1.maxval-Form1.minval);
yval[1]:=Round(tempr);
Form1.Canvas.Brush.Color:=clWhite;
Form1.Canvas.Rectangle(x[Rmax,44]+20,700-yval[1],x[Rmax,44]+50,420);
end;
end;
end;
end.
```

Appendix F

Full mathematical progression of the 'passive node' algorithms for the three dimensional numerical model

The three dimensional model involves Laplace's equation in three dimensions. This may be expressed as

$$\sum_{\alpha=1}^8 \sigma_{\alpha} \left[\iint \frac{\partial U_{\alpha}}{\partial r} (r^2 \sin \theta) d\theta d\phi + \iint \frac{1}{r} \frac{\partial U_{\alpha}}{\partial \theta} (r \sin \theta) dr d\phi + \iint \frac{1}{r \sin \theta} \frac{\partial U_{\alpha}}{\partial \phi} r dr d\theta \right] = 0$$

Equation F.1

where U is the calculated potential at a specific point depending on the potentials at the six nearest nodes and the conductivities of the eight surrounding regions. If the first term only is considered then we have

$$\sum_{N=1}^8 \sigma_N \iint \frac{\partial U_N}{\partial r} (r^2 \sin \theta) d\theta d\phi$$

Equation F.2

This double integral may be separated in order to integrate over the θ and ϕ dimensions independently

$$\sum_{N=1}^8 \sigma_N \int \frac{\partial U_N}{\partial r} (r^2 \sin \theta) d\theta \int d\phi$$

Equation F.3

If u_r is set to be the derivative of the potential at a constant r the integral can be expanded to form Equation F.4

$$\begin{aligned}
& \sigma_1 \int_{\theta_0-h_2}^{\theta_0} (r_0-h_1)^2 [-u_r(r_0-h_1)] \sin\theta d\theta \int_{\phi_0-h_5}^{\phi_0} d\phi + \\
& \sigma_2 \int_{\theta_0-h_2}^{\theta_0} (r_0+h_3)^2 [u_r(r_0+h_3)] \sin\theta d\theta \int_{\phi_0-h_5}^{\phi_0} d\phi + \\
& \sigma_3 \int_{\theta_0}^{\theta_0+h_4} (r_0+h_3)^2 [u_r(r_0+h_3)] \sin\theta d\theta \int_{\phi_0-h_5}^{\phi_0} d\phi + \\
& \sigma_4 \int_{\theta_0}^{\theta_0+h_4} (r_0-h_1)^2 [-u_r(r_0-h_1)] \sin\theta d\theta \int_{\phi_0-h_5}^{\phi_0} d\phi + \\
& \sigma_5 \int_{\theta_0-h_2}^{\theta_0} (r_0-h_1)^2 [-u_r(r_0-h_1)] \sin\theta d\theta \int_{\phi_0}^{\phi_0+h_6} d\phi + \\
& \sigma_6 \int_{\theta_0-h_2}^{\theta_0} (r_0+h_3)^2 [u_r(r_0+h_3)] \sin\theta d\theta \int_{\phi_0}^{\phi_0+h_6} d\phi + \\
& \sigma_7 \int_{\theta_0}^{\theta_0+h_4} (r_0+h_3)^2 [u_r(r_0+h_3)] \sin\theta d\theta \int_{\phi_0}^{\phi_0+h_6} d\phi + \\
& \sigma_8 \int_{\theta_0}^{\theta_0+h_4} (r_0-h_1)^2 [-u_r(r_0-h_1)] \sin\theta d\theta \int_{\phi_0}^{\phi_0+h_6} d\phi
\end{aligned}$$

Equation F.4

To simplify the equation manipulation a little, we allow

$$-u_r(r_0-h_1) = \frac{U_1 - U_0}{2h_1}$$

Equation F.5

and

$$\int_{\phi_0}^{\phi_0+h_6} d\phi = (\phi_0 + h_6) - \phi_0 = h_6$$

Equation F.6

The integrals at the end of each term in Equation F.4 are evaluated like this

$$\int_{\phi_0 - h_5}^{\phi_0} d\phi = \phi_0 - (\phi_0 - h_5) = h_5$$

$$\int_{\phi_0}^{\phi_0 + h_6} d\phi = (\phi_0 + h_6) - \phi_0 = h_6$$

Equation F.7

Substituting these equations back into the original first term we now have

$$\begin{aligned} & \sigma_1 \int_{\theta_0 - h_2}^{\theta_0} (r_0 - h_1)^2 \left[\frac{U_1 - U_0}{2h_1} \right] \text{Sin } \theta d\theta (h_5) + \\ & \sigma_2 \int_{\theta_0 - h_2}^{\theta_0} (r_0 + h_3)^2 \left[\frac{U_3 - U_0}{2h_3} \right] \text{Sin } \theta d\theta (h_5) + \\ & \sigma_3 \int_{\theta_0}^{\theta_0 + h_4} (r_0 + h_3)^2 \left[\frac{U_3 - U_0}{2h_3} \right] \text{Sin } \theta d\theta (h_5) + \\ & \sigma_4 \int_{\theta_0}^{\theta_0 + h_4} (r_0 - h_1)^2 \left[\frac{U_1 - U_0}{2h_1} \right] \text{Sin } \theta d\theta (h_5) + \\ & \sigma_5 \int_{\theta_0 - h_2}^{\theta_0} (r_0 - h_1)^2 \left[\frac{U_1 - U_0}{2h_1} \right] \text{Sin } \theta d\theta (h_6) + \\ & \sigma_6 \int_{\theta_0 - h_2}^{\theta_0} (r_0 + h_3)^2 \left[\frac{U_3 - U_0}{2h_3} \right] \text{Sin } \theta d\theta (h_6) + \\ & \sigma_7 \int_{\theta_0}^{\theta_0 + h_4} (r_0 + h_3)^2 \left[\frac{U_3 - U_0}{2h_3} \right] \text{Sin } \theta d\theta (h_6) + \\ & \sigma_8 \int_{\theta_0}^{\theta_0 + h_4} (r_0 - h_1)^2 \left[\frac{U_1 - U_0}{2h_1} \right] \text{Sin } \theta d\theta (h_6) \end{aligned}$$

Equation F.8

And now the integral is evaluated to reveal Equation F.9

$$\begin{aligned}
 & U_1 \left[\frac{\sigma_1}{2h_1} (h_5)(r_0 - h_1)^2 (-\cos(\theta_0) + \cos(\theta_0 - h_2)) + \frac{\sigma_4}{2h_1} (h_5)(r_0 - h_1)^2 (-\cos(\theta_0 + h_4) + \cos(\theta_0)) + \right. \\
 & \left. \frac{\sigma_5}{2h_1} (h_6)(r_0 - h_1)^2 (-\cos(\theta_0) + \cos(\theta_0 - h_2)) + \frac{\sigma_8}{2h_1} (h_6)(r_0 - h_1)^2 (-\cos(\theta_0 + h_4) + \cos(\theta_0)) \right] + \\
 & U_3 \left[\frac{\sigma_2}{2h_3} (h_5)(r_0 + h_3)^2 (-\cos(\theta_0) + \cos(\theta_0 - h_2)) + \frac{\sigma_3}{2h_3} (h_5)(r_0 + h_3)^2 (-\cos(\theta_0 + h_4) + \cos(\theta_0)) + \right. \\
 & \left. \frac{\sigma_6}{2h_3} (h_6)(r_0 + h_3)^2 (-\cos(\theta_0) + \cos(\theta_0 - h_2)) + \frac{\sigma_7}{2h_3} (h_6)(r_0 + h_3)^2 (-\cos(\theta_0 + h_4) + \cos(\theta_0)) \right] - \\
 & U_0 \left[\frac{\sigma_1}{2h_1} (h_5)(r_0 - h_1)^2 (-\cos(\theta_0) + \cos(\theta_0 - h_2)) + \frac{\sigma_2}{2h_3} (h_5)(r_0 + h_3)^2 (-\cos(\theta_0) + \cos(\theta_0 - h_2)) + \right. \\
 & \frac{\sigma_3}{2h_3} (h_5)(r_0 + h_3)^2 (-\cos(\theta_0 + h_4) + \cos(\theta_0)) + \frac{\sigma_4}{2h_1} (h_5)(r_0 - h_1)^2 (-\cos(\theta_0 + h_4) + \cos(\theta_0)) + \\
 & \frac{\sigma_5}{2h_1} (h_6)(r_0 - h_1)^2 (-\cos(\theta_0) + \cos(\theta_0 - h_2)) + \frac{\sigma_6}{2h_3} (h_6)(r_0 + h_3)^2 (-\cos(\theta_0) + \cos(\theta_0 - h_2)) + \\
 & \left. \frac{\sigma_7}{2h_3} (h_6)(r_0 + h_3)^2 (-\cos(\theta_0 + h_4) + \cos(\theta_0)) + \frac{\sigma_8}{2h_1} (h_6)(r_0 - h_1)^2 (-\cos(\theta_0 + h_4) + \cos(\theta_0)) \right]
 \end{aligned}$$

Equation F.9

To simplify this a little the following substitutions are made

RI = r_0	TJ = θ_0	PK = ϕ_0
RIP = $r_0 + 2h_3$	TJM = $\theta_0 - 2h_2$	PKM = $\phi_0 - 2h_5$
RIM = $r_0 - 2h_1$	TJP = $\theta_0 + 2h_4$	PKP = $\phi_0 + 2h_6$

$$HIM = RI - RIM = r_0 - r_0 - 2h_1 = -2h_1$$

$$RM = (RI + RIM) / 2 = r_0 - h_1$$

$$HIP = RIP - RI = r_0 + 2h_3 - r_0 = 2h_3$$

$$RP = (RI + RIP) / 2 = r_0 + h_3$$

$$HJM = TJ - TJM = 2h_2$$

$$TM = (TJ + TJM) / 2 = \theta_0 - h_2$$

$$HJP = TJP - TJ = 2h_4$$

$$TP = (TJ + TJP) / 2 = \theta_0 + h_4$$

$$HKM = PK - PKM = 2h_5$$

$$COM = (\cos(TM) - \cos(TJ))$$

$$HKP = PKP - PK = 2h_6$$

$$COP = (\cos(TJ) - \cos(TP))$$

$$\begin{array}{lll}
U(I, J, K) = U_0 & U(I-1, J, K) = U_1 & U(I+1, J, K) = U_3 \\
U(I, J-1, K) = U_2 & U(I, J-1, K) = U_2 & U(I, J, K-1) = U_5 \\
U(I, J, K+1) = U_6 & &
\end{array}$$

and

$$\begin{aligned}
LO &= -\ln\left(\cos\left(\frac{TJ}{2}\right)\right) + \ln\left(\sin\left(\frac{TJ}{2}\right)\right) \\
LOM &= -\ln\left(\cos\left(\frac{TM}{2}\right)\right) + \ln\left(\sin\left(\frac{TM}{2}\right)\right) \\
LOP &= -\ln\left(\cos\left(\frac{TP}{2}\right)\right) + \ln\left(\sin\left(\frac{TP}{2}\right)\right)
\end{aligned}$$

Using these substitutions Equation F.9 may be expressed as

$$\begin{aligned}
& U_1 \left[\frac{\sigma_1}{HIM} (RM)^2 COM \frac{HKM}{2} + \frac{\sigma_4}{HIM} (RM)^2 COP \frac{HKM}{2} + \right. \\
& \left. \frac{\sigma_5}{HIM} (RM)^2 COM \frac{HKP}{2} + \frac{\sigma_8}{HIM} (RM)^2 COP \frac{HKP}{2} \right] + \\
& U_3 \left[\frac{\sigma_2}{HIP} (RP)^2 COM \frac{HKM}{2} + \frac{\sigma_3}{HIP} (RP)^2 COP \frac{HKM}{2} + \right. \\
& \left. \frac{\sigma_6}{HIP} (RP)^2 COM \frac{HKP}{2} + \frac{\sigma_7}{HIP} (RP)^2 COP \frac{HKP}{2} \right] - \\
& U_0 \left[\frac{\sigma_1}{HIM} (RM)^2 COM \frac{HKM}{2} + \frac{\sigma_2}{HIP} (RP)^2 COM \frac{HKM}{2} + \right. \\
& \frac{\sigma_3}{HIP} (RP)^2 COP \frac{HKM}{2} + \frac{\sigma_4}{HIM} (RM)^2 COP \frac{HKM}{2} + \\
& \frac{\sigma_5}{HIM} (RM)^2 COM \frac{HKP}{2} + \frac{\sigma_6}{HIP} (RP)^2 COM \frac{HKP}{2} + \\
& \left. \frac{\sigma_7}{HIP} (RP)^2 COP \frac{HKP}{2} + \frac{\sigma_8}{HIM} (RM)^2 COP \frac{HKP}{2} \right]
\end{aligned}$$

Equation F.10

This algorithm has resulted from the development of the first term. The remaining two terms of this equation may be similarly developed integrating the second term at a constant angle (θ) and the third at a constant angle (ϕ) along the outer boundaries of the 'cubes'.

The second term then becomes

$$\begin{aligned}
 & U_2 \left[\frac{\sigma_1}{HJM} (\text{Sin}(TM)) \left(\frac{HIM}{2} \right) \left(\frac{HKM}{2} \right) + \frac{\sigma_2}{HJM} (\text{Sin}(TM)) \left(\frac{HIP}{2} \right) \left(\frac{HKM}{2} \right) + \right. \\
 & \left. \frac{\sigma_5}{HJM} (\text{Sin}(TM)) \left(\frac{HIM}{2} \right) \left(\frac{HKP}{2} \right) + \frac{\sigma_6}{HJM} (\text{Sin}(TM)) \left(\frac{HIP}{2} \right) \left(\frac{HKP}{2} \right) \right] + \\
 & U_4 \left[\frac{\sigma_3}{HJP} (\text{Sin}(TP)) \left(\frac{HIP}{2} \right) \left(\frac{HKM}{2} \right) + \frac{\sigma_4}{HJP} (\text{Sin}(TP)) \left(\frac{HIM}{2} \right) \left(\frac{HKM}{2} \right) + \right. \\
 & \left. \frac{\sigma_7}{HJP} (\text{Sin}(TP)) \left(\frac{HIP}{2} \right) \left(\frac{HKP}{2} \right) + \frac{\sigma_8}{HJP} (\text{Sin}(TP)) \left(\frac{HIM}{2} \right) \left(\frac{HKP}{2} \right) \right] - \\
 & U_0 \left[\frac{\sigma_1}{HJM} (\text{Sin}(TM)) \left(\frac{HIM}{2} \right) \left(\frac{HKM}{2} \right) + \frac{\sigma_2}{HJM} (\text{Sin}(TM)) \left(\frac{HIP}{2} \right) \left(\frac{HKM}{2} \right) + \right. \\
 & \frac{\sigma_3}{HJP} (\text{Sin}(TP)) \left(\frac{HIP}{2} \right) \left(\frac{HKM}{2} \right) + \frac{\sigma_4}{HJP} (\text{Sin}(TP)) \left(\frac{HIM}{2} \right) \left(\frac{HKM}{2} \right) + \\
 & \frac{\sigma_5}{HJM} (\text{Sin}(TM)) \left(\frac{HIM}{2} \right) \left(\frac{HKP}{2} \right) + \frac{\sigma_6}{HJM} (\text{Sin}(TM)) \left(\frac{HIP}{2} \right) \left(\frac{HKP}{2} \right) + \\
 & \left. \frac{\sigma_7}{HJP} (\text{Sin}(TP)) \left(\frac{HIP}{2} \right) \left(\frac{HKP}{2} \right) + \frac{\sigma_8}{HJP} (\text{Sin}(TP)) \left(\frac{HIM}{2} \right) \left(\frac{HKP}{2} \right) \right] +
 \end{aligned}$$

Equation F.11

and the third becomes

$$\begin{aligned}
 & U_5 \left[\frac{\sigma_1}{HKM} (LO-LOM) \left(\frac{HIM}{2} \right) + \frac{\sigma_2}{HKM} (LO-LOM) \left(\frac{HIP}{2} \right) + \right. \\
 & \left. \frac{\sigma_3}{HKM} (LOP-LO) \left(\frac{HIP}{2} \right) + \frac{\sigma_4}{HKM} (LOP-LO) \left(\frac{HIM}{2} \right) \right] + \\
 & U_6 \left[\frac{\sigma_5}{HKP} (LO-LOM) \left(\frac{HIM}{2} \right) + \frac{\sigma_6}{HKP} (LO-LOM) \left(\frac{HIP}{2} \right) + \right. \\
 & \left. \frac{\sigma_7}{HKP} (LOP-LO) \left(\frac{HIP}{2} \right) + \frac{\sigma_8}{HKP} (LOP-LO) \left(\frac{HIM}{2} \right) \right] - \\
 & U_0 \left[\frac{\sigma_1}{HKM} (LO-LOM) \left(\frac{HIM}{2} \right) + \frac{\sigma_2}{HKM} (LO-LOM) \left(\frac{HIP}{2} \right) + \right. \\
 & \frac{\sigma_3}{HKM} (LOP-LO) \left(\frac{HIP}{2} \right) + \frac{\sigma_4}{HKM} (LOP-LO) \left(\frac{HIM}{2} \right) + \\
 & \frac{\sigma_5}{HKP} (LO-LOM) \left(\frac{HIM}{2} \right) + \frac{\sigma_6}{HKP} (LO-LOM) \left(\frac{HIP}{2} \right) + \\
 & \left. \frac{\sigma_7}{HKP} (LOP-LO) \left(\frac{HIP}{2} \right) + \frac{\sigma_8}{HKP} (LOP-LO) \left(\frac{HIM}{2} \right) \right]
 \end{aligned}$$

Equation F.12

If Equations F.10, F.11, F.12 are added together and we the terms are rearranged we have

$$U(I, J, K) = \frac{\left(FR_1 * U(I-1, J, K) + FR_2 * U(I, J-1) + FR_3 * U(I+1, J, K) + \right.}{\left(FR_1 + FR_2 + FR_3 + FR_4 + FR_5 + FR_6 \right)} \left. \left(FR_4 * U(I, J+1) + FR_5 * U(I, J, K-1) + FR_6 * U(I, J, K+1) \right) \right)$$

Equation F.13

where

$$FR_1 = \left[\begin{aligned} & \frac{\sigma_1}{HIM} \frac{HKM}{2} (RM)^2 COM + \frac{\sigma_4}{HIM} \frac{HKM}{2} (RM)^2 COP + \\ & \frac{\sigma_5}{HIM} \frac{HKP}{2} (RM)^2 COM + \frac{\sigma_8}{HIM} \frac{HKP}{2} (RM)^2 COP \end{aligned} \right]$$

$$FR_2 = \left[\begin{aligned} & \frac{\sigma_1}{HJM} (\sin(TM)) \frac{HIM}{2} \frac{HKM}{2} + \frac{\sigma_2}{HJM} (\sin(TM)) \frac{HIP}{2} \frac{HKM}{2} + \\ & \frac{\sigma_5}{HJM} (\sin(TM)) \frac{HIM}{2} \frac{HKP}{2} + \frac{\sigma_6}{HJM} (\sin(TM)) \frac{HIP}{2} \frac{HKP}{2} \end{aligned} \right]$$

$$FR_3 = \left[\begin{aligned} & \frac{\sigma_2}{HIP} \frac{HKM}{2} (RP)^2 COM + \frac{\sigma_3}{HIP} \frac{HKM}{2} (RP)^2 COP + \\ & \frac{\sigma_6}{HIP} \frac{HKP}{2} (RP)^2 COM + \frac{\sigma_7}{HIP} \frac{HKP}{2} (RP)^2 COP \end{aligned} \right]$$

$$FR_4 = \left[\begin{aligned} & \frac{\sigma_3}{HJP} (\sin(TP)) \frac{HIP}{2} \frac{HKM}{2} + \frac{\sigma_4}{HJP} (\sin(TP)) \frac{HIM}{2} \frac{HKM}{2} + \\ & \frac{\sigma_7}{HJP} (\sin(TP)) \frac{HIP}{2} \frac{HKP}{2} + \frac{\sigma_8}{HJP} (\sin(TP)) \frac{HIM}{2} \frac{HKP}{2} \end{aligned} \right]$$

$$FR_5 = \left[\begin{aligned} & \frac{\sigma_1}{HKM} (EOM - EMM) \frac{HIM}{2} + \frac{\sigma_2}{HKM} (EOM - EMM) \frac{HIP}{2} + \\ & \frac{\sigma_3}{HKM} (EPM - EOM) \frac{HIP}{2} + \frac{\sigma_4}{HKM} (EPM - EOM) \frac{HIM}{2} \end{aligned} \right]$$

$$FR_6 = \left[\begin{aligned} & \frac{\sigma_5}{HKP} (EOM - EMM) \frac{HIM}{2} + \frac{\sigma_6}{HKP} (EOM - EMM) \frac{HIP}{2} + \\ & \frac{\sigma_7}{HKP} (EPM - EOM) \frac{HIP}{2} + \frac{\sigma_8}{HKP} (EPM - EOM) \frac{HIM}{2} \end{aligned} \right]$$

and

$$-\ln \frac{(\cos(\theta_0))}{2} - \ln \frac{(\sin(\theta_0))}{2} = EOM$$

$$-\ln \frac{(\cos(\theta_0 - h_2))}{2} - \ln \frac{(\sin(\theta_0 - h_2))}{2} = EMM$$

$$-\ln \frac{(\cos(\theta_0 + h_4))}{2} - \ln \frac{(\sin(\theta_0 + h_4))}{2} = EPM$$

Equation F.13 is the solution to Laplace's equation in three dimensions and is applied in succession to each of the nodes in the passive volume of the model.

Appendix G Source code for three-dimensional numerical model

The two-dimensional numerical model source code was modified to encompass the developed three-dimensional algorithms. Only the units that were modified are shown.

```
program Doslak;

uses
  Forms,
  Main in 'Main.pas' {Form1},
  Angle in 'Angle.pas',
  Membrane in 'Membrane.pas',
  Radius in 'Radius.pas',
  MathUnit in 'Mathunit.pas',
  Display2 in 'Display2.pas',
  Average in 'Average.pas',
  Dimension in 'Dimension.pas',
  Setup in 'Setup.pas';

begin
  Application.Initialize;
  Application.CreateForm(TForm1, Form1);
  Application.Run;
end.
```

```
unit Main;
```

```
interface
```

```
uses
```

```
  WinProcs, Wintypes, Messages, SysUtils, Classes, Graphics, Controls, Forms, Dialogs,
  StdCtrls, Setup, Display2, Radius, Angle, Dimension, Mathunit, ExtCtrls, Membrane,
  ComCtrls, Average;
```

```
type
```

```
  TForm1 = class(TForm)
    Edit1: TEdit;
    Edit2: TEdit;
    Edit3: TEdit;
    Edit4: TEdit;
    Label1: TLabel;
    Label2: TLabel;
    Label8: TLabel;
    Label9: TLabel;
    Button1: TButton;
    Button2: TButton;
    Button3: TButton;
    RadioButton1: TRadioButton;
    UpDown1: TUpDown;
    Label3: TLabel;
```

```
{Procedure declarations in this unit}
```

```
procedure FormActivate(Sender: TObject);
procedure Button1Click(Sender: TObject);
procedure Button2Click(Sender: TObject);
procedure Button3Click(Sender: TObject);
procedure UpDown1Click(Sender: TObject; Button: TUDBtnType);
procedure Save_to_file(sender: Tobject);
```

```
private
  { Private declarations }
```

```
public
  {Public declarations}
```

```
{Conductivity values of the various regions of the model}
```

```
SigmaAqVit: Double;
SigmaSclera: Double;
SigmaExtraoc: Double;
SigmaLens: Double;
SigmaCornea: Double;
SigmaAir: Double;
```

```
{Internal and external conductivity values}
```

```
SigmaInt: Double;           {SIGI}
SigmaExt: Double;          {SIGE}
```

```
{Declarations for various parameters of the retinal membrane}
```

```
RMembraneResistance: Double;
RMembraneCapacitance: Double;
CapacitiveReactance: Double;
InverseRMembraneResistance: Double;
InverseRMembraneCapacitance: Double;
RmembraneImpedance: Complex;
PhaseA: Complex;
PhaseB: Complex;
AImageComp: Complex;
ARealComp: Complex;
BImageComp: Complex;
BRealComp: Complex;
```

```
{Arrays in 3 dimensions}
```

```
{Array of the magnitude of the calculated potentials}
```

```
inputUMag: array[1..45,1..44,1..2,1..44] of Double;
```

```
{Real part of the input array}
```

```
inputRU: array[1..45,1..44,1..44] of Double;
```

```
{Radial co-ordinate array}
```

inputR: array[1..45] of Double;

{Theta co-ordinate array}

inputT: array[1..44,1..2] of Double;

{Photoreceptor scaled array}

retina: array[1..22,1..2,1..44] of Double;
retinaI: array[1..22,1..2,1..44] of Double;

{Control array}

Control: array[1..10000] of Integer;

{Batch File}

Batch: array[1..60] of Double;

{Zeroed potential input array}

inputU: array[1..45,1..44,1..2,1..44] of Complex;

{Display array}

Display: array[1..45,1..44,1..44] of Integer;

{Two arrays of double node retinal potentials}

UA: array[1..22,1..2,1..44] of Complex;
UB: array[1..22,1..2,1..44] of Complex;

{Array containing conductivity values}

SIG: array[1..7] of Real;
fname: string;
binvalue: array[0..9] of Double;

{Arrays for the number of slices required, i.e.the 3D bit}

inputPhi: array[1..44,1..2] of double;
Pixelvalue: array[1..45,1..44,1..44] of longint;

{Integer variables}

Run_No,Program_No,No_of_loops,Voltage_Flag,Theta_Flag,Toggle,Iterations,Programs,ZoomFlag,SolidFileFlag,RunFlag,RunFlag2: Integer;
N1,N2,N3,N4,NA1,NA2,NA3,NA4,NB1,NB2,NB3,NB4: Integer;

Average_FlagIMinus,Average_FlagIP,Average_FlagJM,Average_FlagJP,Average_FlagKM,Average_FlagKP: Integer;
I,IMinus,IP,J,JM,JP,K,KM,KP: Integer;
half,JMBorder,JPBorder,V2Border,V4Border: Integer;

Maximum_Iterations,QV: Integer;
graph_scale_factor,graph_shift_factor,Slice_No: Integer;
Average_flag: Integer;

{Double variables}

TAU,Ima,Iteration_No:Double;
SIGA,SIGB,SIGC,SIGD,SIGE,SIGI,SIGW,SIGX,SIGY,SIGZ: Double;
W,C2L,C2H,C3L,C3H,C4,C5,CRL,CRH,CCL,CCH,FL,FH: Double;
LO,LOM,LOP,HIM,HIP,RM,RP,TJ,TJP,TJM,HJM,HJP, TM,TMP,TP,TPP,PTJ,COM,COP: Double;
PTJP,TMPPP,TPPPP: Double;
PK,PKM,PKP:Double;
PTJPCOS,PTJPSIN,TMPPCOS,TMPPSIN,TPPPCOS,TPPPSIN:Double;
SOM,SOP,PM,PP,HKM,HKP: Double;
D1,D2,D3,D4,CA,CB,CC,CD,CE,CF: Double;
SIG1,SIG2,SIG3,SIG4,SIG5,SIG6: Double;
RR,RC,RXC,YR,YXC: Double;
Frequency: Double;
RI,RIM,RIP: Double;
maxval,minval: Double;
binlevel,binincrement: Double;
A,B,C,D,E,F,G: Double;
temp1,temp2,temp3,temp4,temp5,temp6: Double;

{Complex variables}

tempc,tempc2,tempc3,tempc4,tempc5,tempc6,tempc7,tempc8,tempc9,tempc10,tempc11,tempc12,
tempc13,tempc14,tempc15,tempc16,tempc17,tempc18,tempc19,tempc20: Complex;
Ref_value: Complex;
CAC,CBC,CCC,CDC,CEC,CFC: Complex;
FR1,FR2,FR3,FR4,FR5,FR6,FRA,RY: Complex;
RMN,ANA,ANB,AD,BNA,BNB,BD: Complex;
V,V1,V2,V3,V4,V5,V6,WC,Sum,SumC: Complex;
SigmaExtC,SigmaExtCMinus,SigmaIntC,TauC,oneC: Complex;

{Long Integer variables}

Node_value,Maxnode: Longint;
Control_position: Longint;

{Boolean variables}

setupflag: boolean;

{Extended variables}

ECOM,ESOM,ECOP,ESOP:Extended;

{Text variable}

DText,EText,FText,GText,HText,XText:Textfile;

RunStr,Convergence:string;

end;

```

var
  Form1: TForm1;

implementation

{$R *.DFM}

procedure TForm1.Button1Click(Sender: TObject);

var
  R,I,B,J,K,Iloops,L,P,U,X,Half,Mark,Pointer: Integer;
  Node_value,nodes: longint;

begin
  Mark:=0;

  {Reads in the Batch File containing number of iterations and conductivity values}

  Form1.fname:='BatchEA.txt';
  AssignFile(Form1.GText,Form1.fname);
  Reset(Form1.GText);
  read(Form1.GText,Program_No,Iteration_No);

  For K:= 1 to 150 do
    begin
      read(Form1.GText,Form1.Batch[K]);
    end;
    CloseFile(Form1.GText);

  For B:= 1 to Program_No do
    begin
      Form1.Run_No:=B;
      Form1.Edit4.Text:=IntToStr(Form1.Run_No);
      Form1.SigmaAqVit:=Form1.Batch[Mark+1];
      Form1.SigmaSclera:=Form1.Batch[Mark+2];
      Form1.SigmaExtraoc:=Form1.Batch[Mark+3];
      Form1.SigmaLens:=Form1.Batch[Mark+4];
      Form1.SigmaComea:=Form1.Batch[Mark+5];
      Form1.SigmaAir:=Form1.Batch[Mark+6];
      Mark:=Mark+6;

  Form1.Iterations:=0;
  Form1.setupflag:=TRUE;

  {Reads in Parameter values}

  Start(Sender);

  {Reads in the Retinal array (homogenous, scaled, central or peripheral spots)}

  Form1.edit3.text:='READING RETINAL ARRAY';
  Form1.refresh;
  Form1.fname:='retinaSA.txt';
  AssignFile(Form1.HText,Form1.fname);

```

```
Reset(Form1.HText);
```

```
For I:=1 to 22 do
```

```
begin
```

```
  readln(Form1.HText,Form1.retina[I,1,1]);
```

```
end;
```

```
CloseFile(Form1.HText);
```

```
For I:=1 to 22 do
```

```
begin
```

```
  Form1.retina[I,2,1]:=Form1.retina[I,1,1];
```

```
end;
```

```
For K:= 2 to 44 do
```

```
begin
```

```
Form1.retina[1,2,K]:=Form1.retina[1,1,K];
```

```
  For I:=1 to 22 do
```

```
  begin
```

```
    Form1.retina[I,1,K]:=Form1.retina[I,1,1];
```

```
    Form1.retina[I,2,K]:=Form1.retina[I,1,K];
```

```
  end;
```

```
end;
```

```
{For a homogeous retina}
```

```
{For K:=1 to 44 do
```

```
begin
```

```
Form1.retina[1,1,K]:=2;
```

```
Form1.retina[2,1,K]:=2;
```

```
Form1.retina[3,1,K]:=2;
```

```
Form1.retina[4,1,K]:=2;
```

```
Form1.retina[5,1,K]:=2;
```

```
Form1.retina[6,1,K]:=2;
```

```
Form1.retina[7,1,K]:=2;
```

```
Form1.retina[8,1,K]:=2;
```

```
Form1.retina[9,1,K]:=2;
```

```
Form1.retina[10,1,K]:=2;
```

```
Form1.retina[11,1,K]:=2;
```

```
Form1.retina[12,1,K]:=2;
```

```
Form1.retina[13,1,K]:=2;
```

```
Form1.retina[14,1,K]:=2;
```

```
Form1.retina[15,1,K]:=2;
```

```
Form1.retina[16,1,K]:=2;
```

```
Form1.retina[17,1,K]:=2;
```

```
Form1.retina[18,1,K]:=2;
```

```
Form1.retina[19,1,K]:=2;
```

```
Form1.retina[20,1,K]:=2;
```

```
Form1.retina[21,1,K]:=2;
```

```
Form1.retina[22,1,K]:=1;
```

```
Form1.retina[1,2,K]:=2;
```

```
Form1.retina[2,2,K]:=2;
```

```
Form1.retina[3,2,K]:=2;
```

```
Form1.retina[4,2,K]:=2;
```

```
Form1.retina[5,2,K]:=2;
```

```

Form1.retina[6,2,K]:=2;
Form1.retina[7,2,K]:=2;
Form1.retina[8,2,K]:=2;
Form1.retina[9,2,K]:=2;
Form1.retina[10,2,K]:=2;
Form1.retina[11,2,K]:=2;
Form1.retina[12,2,K]:=2;
Form1.retina[13,2,K]:=2;
Form1.retina[14,2,K]:=2;
Form1.retina[15,2,K]:=2;
Form1.retina[16,2,K]:=2;
Form1.retina[17,2,K]:=2;
Form1.retina[18,2,K]:=2;
Form1.retina[19,2,K]:=2;
Form1.retina[20,2,K]:=2;
Form1.retina[21,2,K]:=2;
Form1.retina[22,2,K]:=1;
end; }

```

{The input potential array is set to zero}

```

For I:=1 to 45 do
begin
  For J:=1 to 44 do
  begin
    For K:=1 to 44 do
    begin
      For Half:=1 to 2 do
      begin
        CMake(0,0,Form1.inputU[I,J,Half,K]);
      end;
    end;
  end;
end;
end;

```

{The retinal double nodes are set to zero}

```

For K:=1 to 44 do
begin
  For I:=1 to 22 do
  begin
    CMake(0,0,Form1.UA[I,1,K]);
    CMake(0,0,Form1.UB[I,1,K]);
    CMake(0,0,Form1.UA[I,2,K]);
    CMake(0,0,Form1.UB[I,2,K]);
  end;
end;

```

```

Repeat
Form1.Refresh;
Form1.Edit1.Text:=IntToStr(Form1.Iterations);
Runflag:=0;

```

{Initiates the display routine to see the final few iterations}

```
{If Form1.Iterations > 1995 then
begin
  Eye2(Sender);
end;}
```

```
{Work out the value of the before and after slices}
```

```
For U:=1 to 44 do
begin
  Form1.K:=U;
  Form1.KM:=U-1;
  Form1.KP:=U+1;
```

```
If (Form1.KM=0) then Form1.KM:=2;
If (Form1.KP=45) then Form1.KP:=43;
```

```
{Setting the initial conductivity values}
```

```
Form1.SIGA:=Form1.SIG[1];
Form1.SIGB:=Form1.SIG[1];
Form1.SIGC:=Form1.SIG[1];
Form1.SIGD:=Form1.SIG[1];
Form1.SIGW:=Form1.SIG[1];
Form1.SIGX:=Form1.SIG[1];
Form1.SIGY:=Form1.SIG[1];
Form1.SIGZ:=Form1.SIG[1];
```

```
{Calculate first node at [1,1,1] in 3D}
```

```
Cadd(Form1.inputU[2,1,1,Form1.K],Form1.inputU[2,5,1,Form1.K],tempc);
Cadd(Form1.inputU[2,10,1,Form1.K],tempc,tempc2);
Cadd(Form1.inputU[2,37,1,Form1.K],tempc2,tempc3);
Cadd(Form1.inputU[2,44,1,Form1.K],tempc3,tempc4);
```

```
Cadd(Form1.inputU[2,1,2,Form1.K],Form1.inputU[2,5,2,Form1.K],tempc5);
Cadd(Form1.inputU[2,10,2,Form1.K],tempc5,tempc6);
Cadd(Form1.inputU[2,37,2,Form1.K],tempc6,tempc7);
Cadd(Form1.inputU[2,44,2,Form1.K],tempc7,tempc8);
```

```
Cadd(tempc4,tempc8,tempc9);
Cmake(10,0,tempc10);
Cdiv(tempc9,tempc10,Form1.V);
```

```
{U[I,J]:=(W*V)+((1-W)*U[I,J]);}
```

```
Cmake(Form1.W,0,Form1.WC);
Cmult(Form1.WC,Form1.V,tempc);
Cmake(1,0,tempc2);
Csub(tempc2,Form1.WC,tempc3);
Cmult(tempc3,Form1.inputU[1,1,1,Form1.K],tempc4);
Cadd(tempc,tempc4,Form1.inputU[1,1,1,Form1.K]);
```

```
Form1.inputU[1,1,1,Form1.K]:=Form1.inputU[1,1,2,Form1.K];
```

```
For X:=1 to 2 do
```

```

begin
Form1.half:=X;
Runflag:=1;
Runflag2:=1;

Dimension.Phi(Sender);

Pointer:=1;
lloops:=0;

Repeat {Repeat loop for the Control array = 74}

lloops:=lloops+1;

Form1.I:=Form1.control[Pointer]; {Pointer value = I value}
If Form1.I<>99 then {99 is code for Membrane routine}
begin
Form1.IMinus:=Form1.control[Pointer+1]; {IM value}
Form1.IP:=Form1.control[Pointer+2]; {IP value}

{Calculates the Radial component of potential}

Radial(Sender);

{Number of nodes at a specific I value controlled by pointer value in control array}

No_of_loops:=control[Pointer+3];
Pointer:=Pointer+5;

For L:=1 to Form1.No_of_loops do
begin
Form1.J:=Form1.control[Pointer]; {J value}
Form1.JM:=Form1.control[Pointer+1]; {JM value}
Form1.JP:=Form1.control[Pointer+2]; {JP value}

{If averaged node then use appropriate Voltage_Flag routine}

Form1.Voltage_Flag:=Form1.control[Pointer+3];

{If Theta routine done then will be flagged with Theta_Flag}

Form1.Theta_Flag:=Form1.control[Pointer+4];

{For change in conductivity values for different nodes}

If Form1.control[Pointer+2] > 100 then
begin
Form1.SIGA:=Form1.SIG[Form1.Control[Pointer+5]];
Form1.SIGB:=Form1.SIG[Form1.control[Pointer+6]];
Form1.SIGC:=Form1.SIG[Form1.control[Pointer+7]];
Form1.SIGD:=Form1.SIG[Form1.control[Pointer+8]];
Form1.JP:=Form1.control[Pointer+2]-100;
Form1.SIGW:=Form1.SIGA;
Form1.SIGX:=Form1.SIGB;
Form1.SIGY:=Form1.SIGC;

```

```

Form1.SIGZ:=Form1.SIGD;
Pointer:=Pointer+9;
end
else
begin
Pointer:=Pointer+5;
end;

```

{Use specific voltage routine when node averaging required}

```

If Form1.Voltage_Flag > 0 then Average.Calculate_Average(Sender);

```

{Calculation of Theta component of node}

```

If Form1.Theta_Flag > 0 then
begin
Angle.Theta(Sender);
end;
end; {end for J loops at this I value}
end {end for this I value}

```

else {For 'If' statement regarding $I < 99$ therefore do membrane routine}

```

begin {Calculation of the double node potentials at the retina}
Membrane.Retina(Sender);
Pointer:=Pointer+1;
end;

```

until Iloops=75; {end of 75 I loops repeat}

end; {End of one half}

If Form1.K=1 then

```

begin
For I:=1 to 45 do
begin
For J:=1 to 44 do
begin
Form1.inputU[I,J,2,1]:=Form1.inputU[I,J,1,44];
Form1.inputU[I,J,2,44]:=Form1.inputU[I,J,1,1];
Form1.UA[J,2,1]:=Form1.UA[J,1,44];
Form1.UB[J,2,1]:=Form1.UB[J,1,44];
Form1.UA[J,2,44]:=Form1.UA[J,1,1];
Form1.UB[J,2,44]:=Form1.UB[J,1,1];
end;
end;
end;
end;

```

For P:=1 to 22 do

```

begin
Form1.inputU[20,P,1,Form1.K]:=Form1.UA[P,1,Form1.K];
Form1.inputU[22,P,1,Form1.K]:=Form1.UB[P,1,Form1.K];

Form1.inputU[20,P,2,Form1.K]:=Form1.UA[P,2,Form1.K];
Form1.inputU[22,P,2,Form1.K]:=Form1.UB[P,2,Form1.K];

```

```

end;

end; {End of one slice of three dimensional model}

Ref_value:=Form1.inputU[44,35,1,1];
For K:=1 to 44 do
begin
For J:=1 to 44 do
begin
For I:=1 to 45 do
begin
CSub(Form1.inputU[I,J,1,K],Ref_value,Form1.inputU[I,J,1,K]);
CSub(Form1.inputU[I,J,2,K],Ref_value,Form1.inputU[I,J,2,K]);
end;
end;
end;

For J:=1 to 22 do
begin
For K:=1 to 44 do
begin
CSub(Form1.UA[J,1,K],Ref_value,Form1.UA[J,1,K]);
CSub(Form1.UB[J,1,K],Ref_value,Form1.UB[J,1,K]);
CSub(Form1.UA[J,2,K],Ref_value,Form1.UA[J,2,K]);
CSub(Form1.UB[J,2,K],Ref_value,Form1.UB[J,2,K]);
end;
end;

Form1.Iterations:=Form1.Iterations+1;

{If Form1.Iterations=500 then
Save_to_File(Sender); }

{If Form1.Iterations=2000 then
Save_to_File(Sender); }

until Form1.Iterations=Form1.Iteration_No; {Number of iterations required}

Save_to_file(Sender);

end;
CloseFile(Form1.DText);
CloseFile(Form1.EText);
CloseFile(Form1.FText);
end;

{Procedure to save potentials along axis to text file }
procedure TForm1.Save_to_file(Sender: Tobject);
var
I,J,U,K: integer;

begin
RunStr:=InttoStr(Form1.Run_No);
Convergence:=InttoStr(Form1.Iterations);

```

```
Form1.fname:='top'+Convergence+RunStr+'.txt';
AssignFile(Form1.DText,Form1.fname);
Rewrite(Form1.DText);
```

```
Form1.fname:='bottom'+Convergence+RunStr+'.txt';
AssignFile(Form1.EText,Form1.fname);
Rewrite(Form1.EText);
```

```
Form1.fname:='surface'+Convergence+RunStr+'.txt';
AssignFile(Form1.FText,Form1.fname);
Rewrite(Form1.FText);
```

```
{Form1.fname:='imtop'+Convergence+RunStr+'.txt';
AssignFile(Form1.MText,Form1.fname);
Rewrite(Form1.MText);
```

```
Form1.fname:='imsurface'+Convergence+RunStr+'.txt';
AssignFile(Form1.NText,Form1.fname);
Rewrite(Form1.NText);}
```

```
{Form1.fname:='phase'+Convergence+RunStr+'.txt';
AssignFile(Form1.XText,Form1.fname);
Rewrite(Form1.XText); }
```

```
{ For I:=Rmax downto 1 do
  begin
    write(Form1.EText,' ',Form1.inputU[I,1,1,1].Re);
  end;
  For I:=2 to RMax do
    begin
      write(Form1.EText,' ',Form1.inputU[I,44,1,1].Re);
    end;}
```

```
{Procedure to plot every real potential in top half to file}
```

```
For I:=1 to 44 do
  begin
    For J:=1 to 43 do
      begin
        write(Form1.DText,' ',Form1.inputU[I,J,1,1].Re);
      end;
    writeln(Form1.DText,' ',Form1.inputU[45,44,1,1].Re);
  end;
```

```
{Procedure to plot every real potential in bottom half to file}
```

```
For I:=1 to 44 do
  begin
    For J:=1 to 43 do
      begin
        write(Form1.EText,' ',Form1.inputU[I,J,2,1].Re);
      end;
    writeln(Form1.EText,' ',Form1.inputU[45,44,2,1].Re);
  end;
```

```
{Procedure to plot every real potential on the surface}
```

```
For K:=1 to 44 do
```

```

begin
For J:=1 to 44 do
  begin
    write(Form1.FText,' ',Form1.inputU[29,J,1,K].Re);
    end;

  For J:=1 to 44 do
    begin
      write(Form1.FText,' ',Form1.inputU[29,J,2,K].Re);
      end;
    writeln(Form1.FText,' ');
end;

{Procedure to plot every imaginary potential in bottom half to file
For I:=44 downto 1 do
  begin
    For J:=1 to 43 do
      begin
        write(Form1.MText,' ',Form1.inputU[I,J,2,1].Im);
        end;
      writeln(Form1.MText,' ',Form1.inputU[45,44,2,1].Im);
    end;

{Procedure to plot every imaginary potential on the surface
For K:=1 to 44 do
  begin
    For J:=1 to 44 do
      begin
        write(Form1.NText,' ',Form1.inputU[29,J,1,K].Im);
        end;

      For J:=1 to 44 do
        begin
          write(Form1.NText,' ',Form1.inputU[29,J,2,K].Im);
          end;
        writeln(Form1.NText,' ');
    end;

    {write(Form1.XText,' ',Form1.PhaseA.Im,' ',Form1.PhaseB.Im);}

  end;

  {begin
For I:=45 downto 1 do
  begin
    write(Form1.EText,' ',Form1.inputU[I,1,1,1].Re);
    end;
  For I:=2 to 45 do
    begin
      write(Form1.EText,' ',Form1.inputU[I,44,1,1].Re);
      end;
    end;
  end;

  {This procedure activates the zoom control Button 2}
procedure TForm1.FormActivate(Sender: TObject);

```

```

begin
Form1.setupflag:=TRUE;
Form1.K:=1;
runflag:=0;
runflag2:=0;
Setup.start(sender);
Eye2(Sender); {In display2 unit}
end;

procedure TForm1.Button2Click(Sender: TObject);

begin
ZoomFlag:=1-ZoomFlag;
If ZoomFlag=1 then Form1.Button2.Caption:='Zoom ON';
If ZoomFlag=0 then Form1.Button2.Caption:='Zoom OFF';
Form1.Refresh;
Eye2(sender);
end;

procedure TForm1.Button3Click(Sender: TObject);
begin
SolidFillFlag:=1-SolidFillFlag;
If SolidFillFlag=1 then Form1.Button3.Caption:='Fill';
If SolidFillFlag=0 then Form1.Button3.Caption:='Point';
Form1.Activate;
end;

procedure TForm1.UpDown1Click(Sender: TObject; Button: TUDBtnType);
begin
Form1.edit2.text:=InttoStr(Form1.Updown1.position);
Form1.slice_no:=Form1.Updown1.position;
Eye2(Sender);
end;

end.

```

```

unit Setup;

```

```

interface

```

```

uses

```

```

WinProcs, Wintypes, Messages, SysUtils, Classes, Graphics, Controls, Forms, Dialogs,
StdCtrls;

```

```

procedure Start(sender: TObject);

```

```

implementation

```

```

uses Main, Mathunit;

```

```

procedure Start(Sender: TObject);

```

```

var
R,X,I,J,K,L,P,U,VZ,xval,Pointer,No_of_loops:Integer;
tempc,tempc2: Complex;

begin
{If the Setup Flag is true then set up the conductivities etc}
  If Form1.setupflag=TRUE then
    begin
      Form1.Edit2.Text:='1';
      Form1.Label8.visible:=False;
      Form1.toggle:=0;

{The relaxation factor}
      Form1.W:=1.80;

{Conductivity Values of specific regions}
      {Form1.SigmaAqVit:=1;
      Form1.SigmaSclera:=0.01;
      Form1.SigmaExtraoc:=0.06;
      Form1.SigmaLens:=1;
      Form1.SigmaCornea:=0.01;
      Form1.SigmaAir:=0.06;}
      Form1.RMembraneResistance:=1.67;
      Form1.RMembraneCapacitance:=43.3;

{Conductivity Values}
      Form1.SIG[1]:=Form1.SigmaAqVit;
      Form1.SIG[2]:=Form1.SigmaSclera;
      Form1.SIG[3]:=Form1.SigmaExtraoc;
      Form1.SIG[4]:=Form1.SigmaLens;
      Form1.SIG[5]:=Form1.SigmaCornea;
      Form1.SIG[6]:=Form1.SigmaAir;
      Form1.SIG[7]:=0;

{Equation manipulation of retinal parameters}
      Form1.Frequency:=5;
      If Form1.Frequency>0.01 then
      Form1.CapacitiveReactance:=Form1.RMembraneCapacitance/Form1.Frequency;
      Form1.InverseRMembraneResistance:=1/Form1.RMembraneResistance;
      If Form1.Frequency<0.01 then Form1.InverseRMembraneCapacitance:=0;
      If Form1.Frequency>0.01 then Form1.InverseRMembraneCapacitance:=1/Form1.CapacitiveReactance;
      CMake(Form1.InverseRMembraneResistance,Form1.InverseRMembraneCapacitance,Form1.tempc);
      CInv(Form1.tempc,Form1.RMembraneImpedance);
      {CMake(0,0,Form1.RMembraneImpedance);}

{Internal and External conductivity values}
      Form1.SigmaInt:=Form1.SigmaAqVit;
      Form1.SigmaExt:=Form1.SigmaSclera;

      Form1.Graph_scale_factor:=60;
      Form1.Graph_shift_factor:=0;

{Three blocks of code follow depending on the state of the Read_from_Disc RadioButton}

{If the RadioButton is checked TRUE or FALSE

```

the radial input array (inputR) and
the theta input array (inputT) are read from disc}

{Radial array read from disc}

```
Form1.edit3.text:='READING RADIAL ARRAY';  
Form1.fname:='inputR.txt';  
AssignFile(Form1.EText,Form1.fname);  
Reset(Form1.EText);
```

```
For I:=1 to 45 do  
  begin  
    readln(Form1.EText,Form1.inputR[I]);  
  end;  
CloseFile(Form1.EText);
```

{Theta array calculated}

```
Form1.edit3.text:='READS THETA ARRAY';  
  
Form1.inputT[1,1]:=0;  
For J:=2 to 9 do  
  begin  
    Form1.inputT[J,1]:=Form1.inputT[J-1,1]+(Pi/16);  
  end;  
Form1.inputT[9,1]:=85*(Pi/180);  
Form1.inputT[10,1]:=90*(Pi/180);  
Form1.inputT[11,1]:=96*(Pi/180);  
Form1.inputT[12,1]:=101.25*(Pi/180);  
Form1.inputT[13,1]:=104*(Pi/180);  
Form1.inputT[14,1]:=107*(Pi/180);  
Form1.inputT[15,1]:=108.5*(Pi/180);  
Form1.inputT[16,1]:=110*(Pi/180);  
Form1.inputT[17,1]:=110.5*(Pi/180);  
Form1.inputT[18,1]:=111*(Pi/180);  
Form1.inputT[19,1]:=111.5*(Pi/180);  
Form1.inputT[20,1]:=111.75*(Pi/180);  
Form1.inputT[21,1]:=112*(Pi/180);  
Form1.inputT[22,1]:=112.5*(Pi/180);  
Form1.inputT[23,1]:=113*(Pi/180);  
Form1.inputT[24,1]:=113.4*(Pi/180);  
Form1.inputT[25,1]:=113.8*(Pi/180);  
Form1.inputT[26,1]:=114.2*(Pi/180);  
Form1.inputT[27,1]:=114.6*(Pi/180);  
Form1.inputT[28,1]:=115*(Pi/180);  
Form1.inputT[29,1]:=116*(Pi/180);  
Form1.inputT[30,1]:=117*(Pi/180);  
Form1.inputT[31,1]:=120*(Pi/180);  
Form1.inputT[32,1]:=123.75*(Pi/180);  
Form1.inputT[33,1]:=126*(Pi/180);  
Form1.inputT[35,1]:=129*(Pi/180);  
Form1.inputT[34,1]:=Form1.inputT[35,1]-(0.01/Form1.inputR[29]);  
Form1.inputT[36,1]:=Form1.inputT[35,1]+(0.01/Form1.inputR[29]);  
Form1.inputT[37,1]:=135*(Pi/180);  
Form1.inputT[38,1]:=141*(Pi/180);  
Form1.inputT[40,1]:=146.25*(Pi/180);  
Form1.inputT[39,1]:=Form1.inputT[40,1]-(0.01/Form1.inputR[14]);
```

```
Form1.inputT[41,1]:=Form1.inputT[40,1]+(0.01/Form1.inputR[14]);
Form1.inputT[42,1]:=157.5*(Pi/180);
Form1.inputT[43,1]:=168.75*(Pi/180);
Form1.inputT[44,1]:=Pi;
```

```
Form1.fname:='ttop.txt';
AssignFile(Form1.EText,Form1.fname);
Rewrite(Form1.EText);
For I:=1 to 44 do
begin
  writeln(Form1.EText,Form1.inputT[I,1]);
end;
CloseFile(Form1.EText);
```

```
Form1.inputT[1,2]:=(2*Pi)-0;
Form1.inputT[2,2]:=(2*Pi)-(Pi/16);
Form1.inputT[3,2]:=(2*Pi)-(Pi/8);
Form1.inputT[4,2]:=(2*Pi)-((3*Pi)/16);
Form1.inputT[5,2]:=(2*Pi)-(Pi/4);
Form1.inputT[6,2]:=(2*Pi)-((5*Pi)/16);
Form1.inputT[7,2]:=(2*Pi)-((3*Pi)/8);
Form1.inputT[8,2]:=(2*Pi)-((7*Pi)/16);
Form1.inputT[9,2]:=(2*Pi)-85*(Pi/180);
Form1.inputT[10,2]:=(2*Pi)-90*(Pi/180);
Form1.inputT[11,2]:=(2*Pi)-96*(Pi/180);
Form1.inputT[12,2]:=(2*Pi)-101.25*(Pi/180);
Form1.inputT[13,2]:=(2*Pi)-104*(Pi/180);
Form1.inputT[14,2]:=(2*Pi)-107*(Pi/180);
Form1.inputT[15,2]:=(2*Pi)-108.5*(Pi/180);
Form1.inputT[16,2]:=(2*Pi)-110*(Pi/180);
Form1.inputT[17,2]:=(2*Pi)-110.5*(Pi/180);
Form1.inputT[18,2]:=(2*Pi)-111*(Pi/180);
Form1.inputT[19,2]:=(2*Pi)-111.5*(Pi/180);
Form1.inputT[20,2]:=(2*Pi)-111.75*(Pi/180);
Form1.inputT[21,2]:=(2*Pi)-112*(Pi/180);
Form1.inputT[22,2]:=(2*Pi)-112.5*(Pi/180);
Form1.inputT[23,2]:=(2*Pi)-113*(Pi/180);
Form1.inputT[24,2]:=(2*Pi)-113.4*(Pi/180);
Form1.inputT[25,2]:=(2*Pi)-113.8*(Pi/180);
Form1.inputT[26,2]:=(2*Pi)-114.2*(Pi/180);
Form1.inputT[27,2]:=(2*Pi)-114.6*(Pi/180);
Form1.inputT[28,2]:=(2*Pi)-115*(Pi/180);
Form1.inputT[29,2]:=(2*Pi)-116*(Pi/180);
Form1.inputT[30,2]:=(2*Pi)-117*(Pi/180);
Form1.inputT[31,2]:=(2*Pi)-120*(Pi/180);
Form1.inputT[32,2]:=(2*Pi)-123.75*(Pi/180);
Form1.inputT[33,2]:=(2*Pi)-126*(Pi/180);
Form1.inputT[35,2]:=(2*Pi)-129*(Pi/180);
Form1.inputT[34,2]:=Form1.inputT[35,2]+(0.01/Form1.inputR[29]);
Form1.inputT[36,2]:=Form1.inputT[35,2]-(0.01/Form1.inputR[29]);
Form1.inputT[37,2]:=(2*Pi)-135*(Pi/180);
Form1.inputT[38,2]:=(2*Pi)-141*(Pi/180);
Form1.inputT[40,2]:=(2*Pi)-146.25*(Pi/180);
Form1.inputT[39,2]:=Form1.inputT[40,2]+(0.01/Form1.inputR[14]);
```

```

Form1.inputT[41,2]:=Form1.inputT[40,2]-(0.01/Form1.inputR[14]);
Form1.inputT[42,2]:=(2*Pi)-157.5*(Pi/180);
Form1.inputT[43,2]:=(2*Pi)-168.75*(Pi/180);
Form1.inputT[44,2]:=(2*Pi)-Pi;

```

```

Form1.fname:='tbottom.txt';
AssignFile(Form1.EText,Form1.fname);
Rewrite(Form1.EText);
For I:=1 to 44 do
begin
  writeln(Form1.EText,Form1.inputT[I,2]);
end;
CloseFile(Form1.EText);

```

```

{Reads in the Control array}
Form1.fname:='control3.txt';
AssignFile(Form1.EText,Form1.fname);
Reset(Form1.EText);
For K:= 1 to 6223 do
  begin
    read(Form1.EText,Form1.control[K]);
  end;
CloseFile(Form1.Etext);
end;

```

```

{INITIAL INPUT ARRAYS ARE SET TO ZERO}
Form1.edit3.text:='SETTING INPUT ARRAY TO ZERO';
Form1.refresh;
For K:=1 to 44 do
  begin
    For J:=1 to 44 do
      begin
        For I:=1 to 45 do
          begin
            Form1.Display[I,J,K]:=0;
            CMake(0,0,Form1.inputU[I,J,1,K]);
            CMake(0,0,Form1.inputU[I,J,2,K]);
          end;
        end;
      end;
    end;
  end;
end;

```

```

{Retinal double nodes are set to zero}
Form1.edit3.text:='ZEROING DOUBLE NODES';
Form1.refresh;
For K:=1 to 44 do
  begin
    For I:=1 to 22 do
      begin
        CMake(0,0,Form1.UA[I,1,K]);
        CMake(0,0,Form1.UB[I,1,K]);
        CMake(0,0,Form1.UA[I,2,K]);
        CMake(0,0,Form1.UB[I,2,K]);
      end;
    end;
  end;
end;

```

```

{Used Nodes are read in}
Form1.edit3.text:='READING USED NODE ARRAY';
Form1.refresh;
Form1.fname:='usednodes.txt';
AssignFile(Form1.EText,Form1.fname);
Reset(Form1.EText);

For VZ:= 1 to 1013 do   {Number is line number in text file}
  begin
  k:=vz;
  read(Form1.EText,I);
  read(Form1.EText,J);
  Form1.Display[I,J,1]:=1;
  Form1.Display[I,J,2]:=1;

{Copy to the other 713 slices}
  For L:=2 to 3 do
    begin
    Form1.Display[I,J,L]:=Form1.Display[I,J,1];
    Form1.Display[I,88-J,L]:=Form1.Display[I,J,1];
    end;
  end;
CloseFile(Form1.EText);

Form1.edit3.text:='SYSTEM READY';
Form1.Refresh;
Form1.Refresh;
Form1.SetupFlag:=FALSE;
end;

```

Radius unit is identical to two-dimensional version

unit Angle;

interface

uses

SysUtils, WinTypes, WinProcs, Messages, Classes, Graphics, Controls,
Forms, Dialogs, StdCtrls, MathUnit;

procedure Theta(Sender: TObject);
 procedure Left(Sender: TObject);
 procedure Right(Sender: TObject);

implementation

uses Main;

procedure Theta(Sender: TObject);

var

JM,JP:integer;
 temp: Double;
 tempc,tempc2,tempc3,tempc4: complex;

```

begin
Form1.JMBorder:=Form1.half;
Form1.JPBorder:=Form1.half;
Form1.V2Border:=Form1.half;
Form1.V4Border:=Form1.half;

{TJ = To}
  Form1.TJ:=Form1.inputT[Form1.J,Form1.half];

{TJM = To - 2h2}
  Form1.TJM:=Form1.inputT[Form1.JM,Form1.JMBorder];

{TJP = To + 2h4}
  Form1.TJP:=Form1.inputT[Form1.JP,Form1.JPBorder];

If Form1.JM=Form1.JP then
begin
  If Form1.J < 22 then
  begin
    Angle.Left(Sender);
  end;

  If Form1.J > 22 then
  begin
    Angle.Right(Sender);
  end;
end;

{HJM = 2h2}
  Form1.HJM:=Abs(Form1.TJ - Form1.TJM);

{HJP = 2h4}
  Form1.HJP:= Abs(Form1.TJP - Form1.TJ);

{TM = To - h2}
  Form1.TM:=Abs((Form1.TJM + Form1.TJ)/2);

{TP = To + h4}
  Form1.TP:=Abs((Form1.TJ+ Form1.TJP)/2);

Form1.PTJ:=Form1.TJ/2;
Form1.TMP:=Form1.TM/2;
Form1.TPP:=Form1.TP/2;

{Calculates COM}
  Form1.COM:=Abs(Cos(Form1.TM) -Cos(Form1.TJ));

{Calculates COP}
  Form1.COP:=Abs(Cos(Form1.TJ) - Cos(Form1.TP));

  Form1.PTJPCOS:=Abs(Cos(Form1.PTJ));
  Form1.PTJPSIN:=Abs(Sin(Form1.PTJ));

```

Form1.TMPPCOS:=Abs(Cos(Form1.TMP));
Form1.TMPPSIN:=Abs(Sin(Form1.TMP));

Form1.TPPPCOS:=Abs(Cos(Form1.TPP));
Form1.TPPPSIN:=Abs(Sin(Form1.TPP));

If (Form1.PTJPSIN=0) then
begin
Form1.TMPPP:=(-Ln(Form1.PTJPCOS)+(55{-Ln(1)}))-(-Ln(Form1.TMPPCOS)-
Ln(Form1.TMPPSIN)));
Form1.TPPPP:=(-Ln(Form1.TPPPCOS)+(-Ln(Form1.TMPPSIN))-(-Ln(Form1.PTJPCOS)-
55{Ln(1)}));
end

else

begin
Form1.TMPPP:=(-Ln(Form1.PTJPCOS)+(-Ln(Form1.PTJPSIN))-(-Ln(Form1.TMPPCOS)-
Ln(Form1.TMPPSIN)));
Form1.TPPPP:=(-Ln(Form1.TPPPCOS)+(-Ln(Form1.TPPPSIN))-(-Ln(Form1.PTJPCOS)-
Ln(Form1.PTJPSIN)));
end;

{Calculates FR1}

temp:=(Form1.SIGA/(Form1.HIM))*(Form1.HKM/2)*(Form1.RM*Form1.RM)*Form1.COM+
(Form1.SIGD/(Form1.HIM))*(Form1.HKM/2)*(Form1.RM*Form1.RM)*Form1.COP+
(Form1.SIGW/(Form1.HIM))*(Form1.HKP/2)*(Form1.RM*Form1.RM)*Form1.COM+
(Form1.SIGZ/(Form1.HIM))*(Form1.HKP/2)*(Form1.RM*Form1.RM)*Form1.COP;
Cmake(temp,0,Form1.FR1);

{Calculates FR2}

temp:=(Form1.SIGA/(Form1.HJM))*(Abs(Sin(Form1.TM)))*(Form1.HIM/2)*(Form1.HKM/2)+
(Form1.SIGB/(Form1.HJM))*(Abs(Sin(Form1.TM)))*(Form1.HIP/2)*(Form1.HKM/2)+
(Form1.SIGW/(Form1.HJM))*(Abs(Sin(Form1.TM)))*(Form1.HIM/2)*(Form1.HKP/2)+
(Form1.SIGX/(Form1.HJM))*(Abs(Sin(Form1.TM)))*(Form1.HIP/2)*(Form1.HKP/2);
Cmake(temp,0,Form1.FR2);

{Calculates FR3}

temp:=(Form1.SIGB/(Form1.HIP))*(Form1.HKM/2)*(Form1.RP*Form1.RP)*Form1.COM+
(Form1.SIGC/(Form1.HIP))*(Form1.HKM/2)*(Form1.RP*Form1.RP)*Form1.COP+
(Form1.SIGX/(Form1.HIP))*(Form1.HKP/2)*(Form1.RP*Form1.RP)*Form1.COM+
(Form1.SIGY/(Form1.HIP))*(Form1.HKP/2)*(Form1.RP*Form1.RP)*Form1.COP;
Cmake(temp,0,Form1.FR3);

{Calculates FR4}

temp:=(Form1.SIGC/(Form1.HJP))*(Abs(Sin(Form1.TP)))*(Form1.HIP/2)*(Form1.HKM/2)+
(Form1.SIGD/(Form1.HJP))*(Abs(Sin(Form1.TP)))*(Form1.HIM/2)*(Form1.HKM/2)+
(Form1.SIGY/(Form1.HJP))*(Abs(Sin(Form1.TP)))*(Form1.HIP/2)*(Form1.HKP/2)+
(Form1.SIGZ/(Form1.HJP))*(Abs(Sin(Form1.TP)))*(Form1.HIM/2)*(Form1.HKP/2);
Cmake(temp,0,Form1.FR4);

{Calculates FR5}

temp:=(Form1.SIGA/(Form1.HKM))*Form1.TMPPP*(Form1.HIM/2)+
(Form1.SIGB/(Form1.HKM))*Form1.TMPPP*(Form1.HIP/2)+

```

(Form1.SIGC/(Form1.HKM))*Form1.TPPPP*(Form1.HIP/2)+
(Form1.SIGD/(Form1.HKM))*Form1.TPPPP*(Form1.HIM/2);
Cmake(temp,0,Form1.FR5);

```

```
{Calculates FR6}
```

```

temp:=(Form1.SIGW/(Form1.HKP))*Form1.TMPPP*(Form1.HIM/2)+
(Form1.SIGX/(Form1.HKP))*Form1.TMPPP*(Form1.HIP/2)+
(Form1.SIGY/(Form1.HKP))*Form1.TPPPP*(Form1.HIP/2)+
(Form1.SIGZ/(Form1.HKP))*Form1.TPPPP*(Form1.HIM/2);
Cmake(temp,0,Form1.FR6);

```

```
{Calculates FR1+FR2+FR3+FR4+FR5+FR6}
```

```

Cadd(Form1.FR1,Form1.FR2,Form1.FRA);
Cadd(Form1.FRA,Form1.FR3,Form1.FRA);
Cadd(Form1.FRA,Form1.FR4,Form1.FRA);
Cadd(Form1.FRA,Form1.FR5,Form1.FRA);
Cadd(Form1.FRA,Form1.FR6,Form1.FRA);

```

```
{To calculate V1}
```

```
Cmult(Form1.FR1,Form1.inputU[Form1.IMinus,Form1.J,Form1.half,Form1.K],Form1.V1);
```

```
{To calculate V2}
```

```
Cmult(Form1.FR2,Form1.inputU[Form1.I,Form1.JM,Form1.V2Border,Form1.K],Form1.V2);
```

```
{To calculate V3}
```

```
Cmult(Form1.FR3,Form1.inputU[Form1.IP,Form1.J,Form1.half,Form1.K],Form1.V3);
```

```
{To calculate V4}
```

```
Cmult(Form1.FR4,Form1.inputU[Form1.I,Form1.JP,Form1.V4Border,Form1.K],Form1.V4);
```

```
{To calculate V5}
```

```
Cmult(Form1.FR5,Form1.inputU[Form1.I,Form1.J,Form1.half,Form1.KM],Form1.V5);
```

```
{To calculate V6}
```

```
Cmult(Form1.FR6,Form1.inputU[Form1.I,Form1.J,Form1.half,Form1.KP],Form1.V6);
```

```
{To calculate V}
```

```

Cadd(Form1.V1,Form1.V2,tempc);
Cadd(tempc,Form1.V3,tempc);
Cadd(tempc,Form1.V4,tempc);
Cadd(tempc,Form1.V5,tempc);
Cadd(tempc,Form1.V6,tempc);
Cdiv(tempc,Form1.FRA,Form1.V);

```

```
{To calculate U[I,J]}
```

```

Cmake(Form1.W,0,Form1.WC);
Cmult(Form1.WC,Form1.V,tempc);
Cmake(1,0,tempc2);
Csub(tempc2,Form1.WC,tempc3);
Cmult(tempc3,Form1.inputU[Form1.I,Form1.J,Form1.half,Form1.K],tempc4);
Cadd(tempc,tempc4,Form1.inputU[Form1.I,Form1.J,Form1.half,Form1.K]);
end;

```

```
procedure Left(Sender: TObject);
```

```
var
```

```
JMBorder,JPBorder,half,X,V2Border,V4Border:integer;
```

```
begin
```

```
  If Form1.half = 1 then
```

```
  begin
```

```
    Form1.JMBorder:=2;
```

```
    Form1.V2Border:=2;
```

```
    Form1.V4Border:=1;
```

```
  end;
```

```
  If Form1.half = 2 then
```

```
  begin
```

```
    Form1.JPBorder:=2;
```

```
    Form1.V2Border:=1;
```

```
    Form1.V4Border:=2;
```

```
  end;
```

```
end;
```

```
procedure Right(Sender: TObject);
```

```
var
```

```
JMBorder,JPBorder,half,X,V2Border,V4Border:integer;
```

```
begin
```

```
  If Form1.half = 1 then
```

```
  begin
```

```
    Form1.JPBorder:=2;
```

```
    Form1.V2Border:=1;
```

```
    Form1.V4Border:=2;
```

```
  end;
```

```
  If Form1.half = 2 then
```

```
  begin
```

```
    Form1.JMBorder:=2;
```

```
    Form1.V2Border:=2;
```

```
    Form1.V4Border:=1;
```

```
  end;
```

```
end;
```

```
end.
```

```
unit Average;
```

```
interface
```

```
uses
```

```
  SysUtils, WinTypes, WinProcs, Messages, Classes, Graphics, Controls,  
  Forms, Dialogs, StdCtrls;
```

```
procedure Calculate_Average(Sender: TObject);
```

implementation

uses Main, Mathunit;

procedure Calculate_Average(Sender: TObject);

var

tempc,tempc2,tempc3,tempc4: complex;

A,B,C,D,E,F,G: complex;

begin

{If Average_Flag = 1}

If Form1.Voltage_Flag=1 then

begin

Form1.inputU[1,Form1.J,Form1.half,Form1.K]:=Form1.inputU[1,1,Form1.half,Form1.K];

end;

{If Average_Flag = 2}

If Form1.Voltage_Flag=2 then

begin

Cmake(2,0,tempc2);

Cadd(Form1.inputU[Form1.IMinus,Form1.JM,Form1.half,Form1.K],Form1.inputU[Form1.IMinus,Form1.JP,Form1.half,Form1.K],tempc);

Cdiv(tempc,tempc2,Form1.inputU[Form1.IMinus,Form1.J,Form1.half,Form1.K]);

end;

{If Average_Flag = 3 then}

If (Form1.Voltage_Flag=3) then

begin

Form1.A:=Form1.inputT[Form1.JP,Form1.half]-Form1.inputT[Form1.J,Form1.half];

Cmake(Form1.A,0,A);

Form1.B:=Form1.inputT[Form1.J,Form1.half]-Form1.inputT[Form1.JM,Form1.half];

Cmake(Form1.B,0,B);

Cmult(A,Form1.inputU[Form1.IMinus,Form1.JM,Form1.half,Form1.K],tempc);

Cmult(B,Form1.inputU[Form1.IMinus,Form1.JP,Form1.half,Form1.K],tempc2);

Cadd(A,B,tempc3);

Cadd(tempc,tempc2,tempc4);

Cdiv(tempc4,tempc3,Form1.inputU[Form1.IMinus,Form1.J,Form1.half,Form1.K]);

end;

{Integer = 4}

If Form1.Voltage_Flag=4 then

begin

Form1.C:=Form1.inputR[Form1.IP]-Form1.inputR[Form1.I];

Cmake(Form1.C,0,C);

Form1.D:=Form1.inputR[Form1.I]-Form1.inputR[Form1.IMinus];

Cmake(Form1.D,0,D);

Cmult(C,Form1.inputU[Form1.IMinus,Form1.JM,Form1.half,Form1.K],tempc);

Cmult(D,Form1.inputU[Form1.IP,Form1.JM,Form1.half,Form1.K],tempc2);

Cadd(C,D,tempc3);

Cadd(tempc,tempc2,tempc4);

Cdiv(tempc4,tempc3,Form1.inputU[Form1.I,Form1.JM,Form1.half,Form1.K]);

```

end;

{If Average_Flag = 5}
If Form1.Voltage_Flag=5 then
begin
Form1.inputU[21,Form1.J,Form1.half,Form1.K]:=Form1.UA[Form1.J,Form1.half,Form1.K];
end;

{If Average_Flag = 6}
If Form1.Voltage_Flag=6 then
begin
Form1.inputU[21,Form1.J,Form1.half,Form1.K]:=Form1.UB[Form1.J,Form1.half,Form1.K];
end;

{If Average_Flag = 7}
If Form1.Voltage_Flag=7 then
begin
Form1.C:=Form1.inputR[21]-Form1.inputR[19];
Cmake(Form1.C,0,C);
Form1.D:=Form1.inputR[19]-Form1.inputR[18];
Cmake(Form1.D,0,D);

Cmult(C,Form1.inputU[18,12,Form1.half,Form1.K],tempc);
Cmult(D,Form1.UA[12,Form1.half,Form1.K],tempc2);
Cadd(C,D,tempc3);
Cadd(tempc,tempc2,tempc4);
Cdiv(tempc4,tempc3,Form1.inputU[19,12,Form1.half,Form1.K]);
end;

{If Average_Flag = 8}
If Form1.Voltage_Flag=8 then
begin
Form1.C:=Form1.inputR[23]-Form1.inputR[22];
Cmake(Form1.C,0,C);
Form1.D:=Form1.inputR[22]-Form1.inputR[21];
Cmake(Form1.D,0,D);

Cmult(C,Form1.UB[22,Form1.half,Form1.K],tempc);
Cmult(D,Form1.inputU[23,22,Form1.half,Form1.K],tempc2);
Cadd(C,D,tempc3);
Cadd(tempc,tempc2,tempc4);
Cdiv(tempc4,tempc3,Form1.inputU[22,22,Form1.half,Form1.K]);
end;

{If Average_Flag = 9}
If Form1.Voltage_Flag=9 then
begin
Cmake(2,0,tempc2);
Cadd(Form1.UA[22,Form1.half,Form1.K],Form1.UB[22,Form1.half,Form1.K],tempc);
Cdiv(tempc,tempc2,Form1.inputU[21,22,Form1.half,Form1.K]);
end;

{If Average_Flag = 10}
If Form1.Voltage_Flag=10 then
begin

```

```

Form1.C:=Form1.inputR[21]-Form1.inputR[20];
Cmake(Form1.C,0,C);
Form1.D:=Form1.inputR[20]-Form1.inputR[19];
Cmake(Form1.D,0,D);

Cmult(D,Form1.UA[22,Form1.half,Form1.K],tempc);
Cmult(C,Form1.inputU[19,22,Form1.half,Form1.K],tempc2);
Cadd(C,D,tempc3);
Cadd(tempc,tempc2,tempc4);
Cdiv(tempc4,tempc3,Form1.inputU[20,22,Form1.half,Form1.K]);
end;
end;
end.

```

unit Dimension;

interface

uses

SysUtils, WinTypes, WinProcs, Messages, Classes, Graphics, Controls,
Forms, Dialogs, StdCtrls, MathUnit;

procedure Phi(Sender: TObject);

{procedure Posterior(Sender: TObject);}

implementation

uses Main;

procedure Phi(Sender: TObject);

var

X,k,half:integer;

temp:double;

tempc,tempc2,tempc3,tempc4: complex;

begin

{Phi array calculated}

Form1.inputPhi[1,1]:=0;

Form1.inputPhi[2,1]:=Pi/43;

Form1.inputPhi[3,1]:=2*(Pi/43);

Form1.inputPhi[4,1]:=3*(Pi/43);

Form1.inputPhi[5,1]:=4*(Pi/43);

Form1.inputPhi[6,1]:=5*(Pi/43);

Form1.inputPhi[7,1]:=6*(Pi/43);

Form1.inputPhi[8,1]:=7*(Pi/43);

Form1.inputPhi[9,1]:=8*(Pi/43);

Form1.inputPhi[10,1]:=9*(Pi/43);

Form1.inputPhi[11,1]:=10*(Pi/43);

Form1.inputPhi[12,1]:=11*(Pi/43);

Form1.inputPhi[13,1]:=12*(Pi/43);

Form1.inputPhi[14,1]:=13*(Pi/43);

Form1.inputPhi[15,1]:=14*(Pi/43);

Form1.inputPhi[16,1]:=15*(Pi/43);

```

Form1.inputPhi[17,1]:=16*(Pi/43);
Form1.inputPhi[18,1]:=17*(Pi/43);
Form1.inputPhi[19,1]:=18*(Pi/43);
Form1.inputPhi[20,1]:=19*(Pi/43);
Form1.inputPhi[21,1]:=20*(Pi/43);
Form1.inputPhi[22,1]:=21*(Pi/43);
Form1.inputPhi[23,1]:=22*(Pi/43);
Form1.inputPhi[24,1]:=23*(Pi/43);
Form1.inputPhi[25,1]:=24*(Pi/43);
Form1.inputPhi[26,1]:=25*(Pi/43);
Form1.inputPhi[27,1]:=26*(Pi/43);
Form1.inputPhi[28,1]:=27*(Pi/43);
Form1.inputPhi[29,1]:=28*(Pi/43);
Form1.inputPhi[30,1]:=29*(Pi/43);
Form1.inputPhi[31,1]:=30*(Pi/43);
Form1.inputPhi[32,1]:=31*(Pi/43);
Form1.inputPhi[33,1]:=32*(Pi/43);
Form1.inputPhi[34,1]:=33*(Pi/43);
Form1.inputPhi[35,1]:=34*(Pi/43);
Form1.inputPhi[36,1]:=35*(Pi/43);
Form1.inputPhi[37,1]:=36*(Pi/43);
Form1.inputPhi[38,1]:=37*(Pi/43);
Form1.inputPhi[39,1]:=38*(Pi/43);
Form1.inputPhi[40,1]:=39*(Pi/43);
Form1.inputPhi[41,1]:=40*(Pi/43);
Form1.inputPhi[42,1]:=41*(Pi/43);
Form1.inputPhi[43,1]:=42*(Pi/43);
Form1.inputPhi[44,1]:=43*(Pi/43);

```

```

For X:=1 to 44 do
  begin
    Form1.inputPhi[X,2]:=Form1.inputPhi[X,1];
  end;

```

```

{PK = Po}
  Form1.PK:=Form1.inputPhi[Form1.K,Form1.half];

```

```

{PKM = Po - 2h5}
  Form1.PKM:=Form1.inputPhi[Form1.KM,Form1.half];

```

```

{PKP = Po + 2h6}
  Form1.PKP:=Form1.inputPhi[Form1.KP,Form1.half];

```

```

{HKM = 2h5}
  Form1.HKM:=Abs(Form1.PK-Form1.PKM);

```

```

{HKP = 2h6}
  Form1.HKP:=Abs(Form1.PKP-Form1.PK);

```

```

{PM = Po - h5}
  Form1.PM:=Abs((Form1.PKM + Form1.PK)/2);

```

```

{PK = Po + h6}
  Form1.PP:=Abs((Form1.PKP + Form1.PK)/2);

```

end;

end.

{If Form1.KM=Form1.KP then

begin

 If Form1.K > 22 then

 begin

 Dimension.Posterior(Sender);

 end;

end;}

{procedure Posterior(Sender:TObject);

begin

 If Form1.half = 1 then

 begin

 Form1.PKP:=(Form1.inputPhi[Form1.KP,2]);

 end;

 If Form1.half = 2 then

 begin

 Form1.PKP:=(Form1.inputPhi[Form1.KP,1]);

 end;}

unit Membrane;

interface

uses

 Windows, Messages, SysUtils, Classes, Graphics, Controls, Forms, Dialogs,
 StdCtrls, Mathunit;

 procedure Retina(Sender: TObject);

implementation

uses Main;

{Calculates the complex number potentials on the double retinal nodes}

procedure Retina(Sender: TObject);

var J: integer;

begin

{Retinal Weighting Factors}

Form1.NA1:=18;

Form1.NA2:=17;

Form1.NA3:=24;

Form1.NA4:=25;

Form1.NB1:=19;

Form1.NB2:=18;

Form1.NB3:=23;

Form1.NB4:=24;

862

{Retinal Weighting Factors}

Form1.N1:=Form1.NA1;
Form1.N2:=Form1.NA2;
Form1.N3:=Form1.NA3;
Form1.N4:=Form1.NA4;

J:=0;

REPEAT

J:=J+1;

Form1.J:=J;

{Weighting Factors change depending on the value of J}

IF Form1.J>=13 then Form1.N1:=Form1.NB1;

IF Form1.J>=13 then Form1.N2:=Form1.NB2;

IF Form1.J>=13 then Form1.N3:=Form1.NB3;

IF Form1.J>=13 then Form1.N4:=Form1.NB4;

{Retinal scaling for photoreceptor density}

Form1.TAU:=Form1.retina[Form1.J,Form1.half,Form1.K];

Form1.Ima:=Form1.retinaI[Form1.J,Form1.half,Form1.K];

{Parameter calculation for retinal double nodal potentials}

Form1.D1:= Form1.inputR[21]-Form1.inputR[Form1.N1];

Form1.D2:= Form1.inputR[Form1.N1]-Form1.inputR[Form1.N2];

Form1.D3:= Form1.inputR[Form1.N3]-Form1.inputR[21];

Form1.D4:= Form1.inputR[Form1.N4]-Form1.inputR[Form1.N3];

Form1.CA:=(2*Form1.D1+Form1.D2)/(Form1.D1*(Form1.D1+Form1.D2));

Form1.CB:=(Form1.D1+Form1.D2)/(Form1.D1*Form1.D2);

Form1.CC:=Form1.D1/(Form1.D2*(Form1.D1+Form1.D2));

Form1.CD:=(2*Form1.D3+Form1.D4)/(Form1.D3*(Form1.D3+Form1.D4));

Form1.CE:=(Form1.D3+Form1.D4)/(Form1.D3*Form1.D4);

Form1.CF:=Form1.D3/(Form1.D4*(Form1.D3+Form1.D4));

{Component parts to the algorithm to calculate the double node potentials of the retina}

CMake(Form1.SigmaExt,0,Form1.SigmaExtC);

CMake(-Form1.SigmaExt,0,Form1.SigmaExtCMinus);

CMake(Form1.SigmaInt,0,Form1.SigmaIntC);

CMake(Form1.CA,0,Form1.CAC);

CMake(Form1.CB,0,Form1.CBC);

CMake(Form1.CC,0,Form1.CCC);

CMake(Form1.CD,0,Form1.CDC);

CMake(Form1.CE,0,Form1.CEC);

CMake(Form1.CF,0,Form1.CFC);

CMake(Form1.Tau,Form1.Ima,Form1.TauC);

CMake(1,0,Form1.oneC);

{ANA:=-SIGE*CD*(TAU+(RMN*SIGE*(CE*U(N3,J)-CF*(N4,J)))/(1+RMN*SIGE*CD))

CMult(Form1.CEC,Form1.inputU[Form1.N3,Form1.J,Form1.half,Form1.K],Form1.tempc);

CMult(Form1.CFC,Form1.inputU[Form1.N4,Form1.J,Form1.half,Form1.K],Form1.tempc2);

CSub(Form1.tempc,Form1.tempc2,Form1.tempc3); {CE*U(N3,J)-CF*U(N4,J)}

Cmult(Form1.RMembraneImpedance,Form1.SigmaExtC,Form1.tempc4); {tempc4= RMN*SIGE}

CMult(Form1.tempc3,Form1.tempc4,Form1.tempc5);

CAdd(Form1.TauC,Form1.tempc5,Form1.tempc6); {tempc6 is the numerator}

```

CMult(Form1.tempc4,Form1.CDC,Form1.tempc7);
CAdd(Form1.onec,Form1.tempc7,Form1.tempc8); { tempc8 is denominator}

CDiv(Form1.tempc6,Form1.tempc8,Form1.tempc9);

CMult(Form1.SigmaExtCMinus,Form1.CDC,Form1.tempc10);
CMult(Form1.tempc10,Form1.tempc9,Form1.ANA);

{ANB:=SIGI*(CB*U[N1,J]-CC*U[N2,J])+SIGE*(CE*U[N3,J]-CF*U[N4,J])}

CMult(Form1.CBC,Form1.inputU[Form1.N1,Form1.J,Form1.half,Form1.K],Form1.tempc11);
CMult(Form1.CCC,Form1.inputU[Form1.N2,Form1.J,Form1.half,Form1.K],Form1.tempc12);
CSub(Form1.Tempc11,Form1.tempc12,Form1.tempc13);
CMult(Form1.tempc13,Form1.SigmaIntC,Form1.tempc14);
CMult(Form1.SigmaExtC,Form1.tempc3,Form1.tempc15);
CAdd(Form1.tempc14,Form1.tempc15,Form1.ANB);

{AD:=SIGI*CA+(SIGE*CD)/(1+RMN*SIGE*CD)}
CMult(Form1.SigmaExtC,Form1.CDC,Form1.tempc16);
CDiv(Form1.tempc16,Form1.tempc8,Form1.tempc17);
CMult(Form1.SigmaIntC,Form1.CAC,Form1.tempc18);
CAdd(Form1.tempc18,Form1.tempc17,Form1.AD);

{BNA:=SIGI*CA*(TAU+(RMN*SIGE*(CE*U[N3,J]-CF*U[N4,J])));}

CMult(Form1.SigmaIntC,Form1.CAC,Form1.Tempc19);
CMult(Form1.Tempc19,Form1.tempc6,Form1.BNA);

{BNB:=SIGE*(CE*U[N3,J]-CF*U[N4,J])+ SIGI*(CB*U[N1,J]-CC*U[N2,J])}
Form1.BNB:=Form1.ANB;

{BD:=SIGI*CA*(1+RMN*SIGE*CD)+SIGE*CD}

CMult(Form1.tempc18,Form1.tempc8,Form1.tempc20);
CAdd(Form1.tempc20,Form1.tempc16,Form1.BD);

{PotA:=ANA+ANB/AD}
Cadd(Form1.ANA,Form1.ANB,Form1.tempc);
Cdiv(Form1.tempc,Form1.AD,Form1.UA[Form1.J,Form1.half,Form1.K]);

CMake(0,Form1.UA[Form1.J,Form1.half,Form1.K].Im,Form1.AImageComp);
CMake(Form1.UA[Form1.J,Form1.half,Form1.K].Re,0,Form1.ARealComp);

{Cdiv(Form1.AImageComp,Form1.ARealComp,Form1.PhaseA);
Ctan(Form1.PhaseA,Form1.PhaseA);
CInv(Form1.PhaseA,Form1.PhaseA);}

{PotB:=BNA+BNB/BD}
Cadd(Form1.BNA,Form1.BNB,Form1.tempc2);
Cdiv(Form1.tempc2,Form1.BD,Form1.UB[Form1.J,Form1.half,Form1.K]);

CMake(0,Form1.UB[Form1.J,Form1.half,Form1.K].Im,Form1.BImageComp);
CMake(Form1.UB[Form1.J,Form1.half,Form1.K].Re,0,Form1.BRealComp);

{Cdiv(Form1.BImageComp,Form1.BRealComp,Form1.PhaseB);

```

```
Ctan(Form1.PhaseB,Form1.PhaseB);  
CInv(Form1.PhaseB,Form1.PhaseB);}
```

```
UNTIL J=22;
```

```
end;
```

```
end.
```

Display2 unit is modified only slightly to show potential distribution on each plane
or 'slice' through the eye.
